



HAL
open science

Laser generation of nanoparticles in liquids: new insights on crystal structure control and colloidal stability

Gaétan Laurens

► **To cite this version:**

Gaétan Laurens. Laser generation of nanoparticles in liquids: new insights on crystal structure control and colloidal stability. Materials Science [cond-mat.mtrl-sci]. Université de Lyon, 2019. English. NNT: 2019LYSE1161 . tel-02339184

HAL Id: tel-02339184

<https://theses.hal.science/tel-02339184>

Submitted on 30 Oct 2019

HAL is a multi-disciplinary open access archive for the deposit and dissemination of scientific research documents, whether they are published or not. The documents may come from teaching and research institutions in France or abroad, or from public or private research centers.

L'archive ouverte pluridisciplinaire **HAL**, est destinée au dépôt et à la diffusion de documents scientifiques de niveau recherche, publiés ou non, émanant des établissements d'enseignement et de recherche français ou étrangers, des laboratoires publics ou privés.



Université Claude Bernard  Lyon 1

N° NNT d'ordre : XXX

THÈSE de DOCTORAT DE L'UNIVERSITÉ DE LYON

Opérée au sein de :

l'Université Claude Bernard Lyon 1

Ecole Doctorale ED52

Physique et Astrophysique de Lyon

Spécialité de doctorat : Physique-Chimie

Discipline : Physique

Soutenue publiquement le 24/09/2019, par :

Gaétan Laurens

**Laser generation of nanoparticles in liquids :
new insights on crystal structure control and colloidal stability**

Devant le jury composé de :

Thomas Niehaus

Professeur des Universités, Université de Lyon

Examineur

Vincenzo Amendola

Professeur des Universités, Università di Padova

Rapporteur

Tatiana Itina

Directrice de Recherche CNRS, Université de Saint-Etienne

Rapporteuse

Marcella Dell'Aglio

Chercheuse, Università di Bari

Examinatrice

Philippe Marmottant

Directeur de Recherche CNRS, Université Grenoble Alpes

Examineur

David Amans

Maître de conférence, Université de Lyon

Directeur de thèse

Remerciements

Ces trois années ont été plus qu'enrichissantes tant sur les plans scientifique et professionnel que sur le plan personnel. Je me sens grandi de cette forte expérience qui je l'espère ne sera que le début. Je dois cela en grande partie à David que je veux sincèrement remercier.

Patient, pédagogue et bienveillant sont les premiers mots qui me viennent pour toi. Ton enthousiasme et ta joie de transmission de la science se ressentent dans ton travail et dans ton encadrement. Je te remercie de m'avoir permis de travailler sur ces projets aussi pluridisciplinaires les uns que les autres et de m'avoir permis d'aborder une partie théorique qui me tenait tellement à cœur. Sur ce côté théorique, je suis très heureux d'avoir pu travailler avec Abdul. Je te remercie de m'avoir appris autant d'outils calculatoires au niveau informatique et scientifique. Tu m'as beaucoup impressionné sur tes compétences et tes connaissances de théoricien. J'espère pouvoir utiliser ce que tu m'as appris pour la suite dans autant de sujets divers et variés.

Lors de ce travail de thèse, j'ai travaillé sur beaucoup de projets collaboratifs dont je veux remercier les acteurs et actrices principaux.

Pour les travaux sur le rubis, l'aide de Tristan a été si précieuse pour aboutir à cette belle étude. Ton travail si précis et minutieux ainsi que nos échanges m'ont beaucoup apporté. Je souhaite remercier Samy avec qui nos discussions m'ont éclairé sur l'hydrodynamique des bulles et d'avoir relu mon chapitre. Un grand merci à Anna pour m'avoir donné l'opportunité de participer à cette expérience au synchrotron et à toute l'équipe de m'avoir accueilli. Je remercie également le groupe du Pr. Barcikowski qui a m'a gentiment accueilli et aidé pendant mon mois à Essen. Enfin, j'aimerais remercier Julien de m'avoir aidé et conseillé en cette fin de thèse (et pour la suite) ainsi que d'avoir relu ce manuscrit.

Ce travail de recherche s'est fait dans de bonnes conditions. Et pour cela je remercie largement les personnes que j'ai côtoyé aux deux étages du bâtiment Kastler. J'ai beaucoup apprécié la sérénité et l'efficacité de Gilles, les connaissances impressionnantes et la bonne humeur de Benoît, les conseils de Jérémie et d'Estelle et l'aide générale apportée par Julien, Florian et le reste de l'équipe Luminescence. J'ai une pensée pour les discussions aux pauses café avec Alban, Antonio, Anne et plus particulièrement pour MamAmina qui a tendrement veillé sur nous. Je remercie aussi Cécile pour les moments conviviaux que nous avons passé ensemble comme les fêtes de la science et les TPs d'optique.

Un mot en particulier pour Christophe qui, grâce à ton très bon cours de master, m'a permis de rencontrer David et d'obtenir ma thèse dans ton groupe. Tu m'as donné un bon aperçu des qualités d'un chef d'équipe. Tes bons conseils et ton aide pendant et pour la suite de la thèse m'ont été plus que précieux.

Comment parler d'une équipe de recherche sans parler des doctorants. Trois belles années à pas-

ser dans ses différents bureaux, de côtoyer tant de personnes et rythmées par ses travaux. Au début, ce fut Quentin, Darjan et Isabelle avec qui j'ai passé d'excellents moments. Puis, il y a eu Amira et Arsène et ses moments de convivialité, de discussions. Mais finalement qu'il n'y a eu qu'un seul fil rouge, Justine, un soutien pour les bons moments comme les mauvais, une collègue complice dans le travail et dans le rire. Je te remercie pour tous ces bons moments et te souhaite encore félicitation Mme Fahy.

J'ai aussi une pensée pour le cinéphile Yann, le sportif Jeff, le footeux Valentin, et cette grande voyageuse Elodie. Je vous remercie pour ces très bons moments au labo, au bar et au gymnase.

En plus des doctorants de l'équipe, je suis ravi d'avoir rencontré autant de doctorants de l'ILM venant de tous les horizons que l'on a pu regrouper avec la Team Doc'. Cette belle aventure humaine a été plus qu'enrichissante avec les bonnes personnes. Je remercie énormément Mathilde, Antony et Romain, en plus de Justine et Amira avec qui ce projet s'est réalisé. Bien entendu, je souhaite remercier la direction de l'institut qui nous a fait confiance. Que la nouvelle génération puisse faire perdurer cette team !

J'ai une grosse pensée pour l'équipe d'informaticiens de l'IPNL, Hugues et Gaël, et ces débats qui ont animé tous ces midis. Merci Hugues pour m'avoir hébergé tant de fois !

Enfin, je souhaite remercier toutes les personnes qui m'ont soutenu et suivi durant ces années et qui se sont intéressées à ma thèse. À toute ma famille, mes potes de Poitiers, de Bordeaux, de Montréal, de Lyon. Merci à la SCNF pour ce travail abattu dans ses rames et à sa ponctualité.

Et naturellement, mes dernières pensées vont à ma Clémentine. Entre cette belle région de Savoie et ces incroyables voyages, tu as toujours été là pour me soutenir, pour me motiver et m'aider. Notre avenir est prêt à affronter le monde.

Introduction	1
1 General features of Pulsed Laser Ablation in Liquids	7
1.1 Free parameters	8
1.1.1 Experimental set-ups	8
1.1.2 Before laser ablation	10
1.2 Successive physico-chemical mechanisms	12
1.2.1 Ablation process	12
1.2.1.1 Photon absorption and relaxation processes	12
1.2.1.2 Ablation mechanisms and plasma expansion	14
1.2.2 Plasma and bubble phases	17
1.2.2.1 Plasma phase and its related phenomena	17
1.2.2.2 Macroscopic bubble expansion and collapse	20
1.2.3 Nanoparticle formation	21
1.2.3.1 Nanoparticle growth mechanisms	21
1.2.3.2 Colloids aging	26
1.3 PLAL interests in synthesis methods	28
1.3.1 Advantages	28
1.3.2 Improvements	30
1.3.3 Applications	32
1.4 Conclusion	34
2 Dynamics of gas bubbles	37
2.1 Bubble dynamics monitoring by shadowgraphy	39
2.1.1 Shadowgraphy technique	39
2.1.2 Dimensionless numbers	40

2.1.3	Thermodynamic parameters	42
2.2	Fluence dependency	45
2.3	Viscosity influence	49
2.3.1	Geometrical shape	50
2.3.2	We , Re and Ca numbers	51
2.3.3	Bubble spreading power laws	52
2.3.4	High capillary numbers dynamics	54
2.4	Conclusion	58
3	Stabilized gold colloidal solutions by ionic strength	61
3.1	Theory and experimental analysis	63
3.1.1	DLVO theory	63
3.1.2	Methods of characterization	64
3.2	Colloidal stability using ionic salts	68
3.2.1	Salt concentration effect	68
3.2.2	Solution concentration effect	72
3.3	Surface chemistry of gold nanoparticles	76
3.3.1	PLEIADES beamline	76
3.3.2	XPS results	80
3.4	Conclusion	83
4	Crystal structure control by stabilizing ligands	85
4.1	Nano-rubies synthesis driven by ligands	87
4.1.1	Synthesis by PLAL	87
4.1.1.1	Challenges with aluminum oxide	87
4.1.1.2	Nano-rubies synthesis	89
4.1.2	Characterization measurements	89
4.1.2.1	Structural characterization	89
4.1.2.2	Optical characterization	93
4.2	Stability of alumina polymorphs	95
4.2.1	Theoretical methods	96
4.2.1.1	Quantum chemistry methods	96
4.2.1.2	Empirical potentials	98
4.2.2	Potentials benchmarking	99
4.2.2.1	Description of the potentials	100
4.2.2.2	Statistical analysis tools	102
4.2.3	Polymorphs stability from clusters to nanoparticles	104
4.2.3.1	Particles generation	104
4.2.3.2	Clusters size	105

4.2.3.3	Nanoparticles range	107
4.3	Mechanical structure of ligand-free and capped alumina nanoparticles	112
4.3.1	SMTBQ calculations	113
4.3.2	VASP calculations	116
4.3.2.1	Free alumina surface	116
4.3.2.2	Capped alumina structure	119
4.4	Conclusion	120
Conclusion		123
Appendix		127
A	Characterization methods	129
A.1	Concentration from absorption spectrum	129
A.2	Differential sedimentation centrifuge	131
A.3	Zeta potential measurement	133
B	Quantum chemistry methods	135
B.1	Theoretical basis	135
B.2	Density Functional Theory	137
B.2.1	DFT outlines	137
B.2.2	Exchange-correlation functionals	139
B.2.3	Atomic orbitals basis set	140
B.3	The Vienna Ab initio Simulation Package	142
B.3.1	The plane waves basis	142
B.3.2	Pseudopotentials	143
B.3.3	VASP parameters	144
C	Empirical potentials benchmarking	145
C.1	Isomers	145
C.2	Nanoparticles	148
D	SMTBQ and VASP calculations	151
D.1	Theoretical analysis of local pressure	151
D.2	$\Delta a/a_0$ -P- $\Delta\lambda$ relation	152
D.3	SMTBQ free alumina surface	154
D.4	VASP slabs	155
Bibliography		157
Résumé en français		197

List of publications

203

The world of the infinitely small generally remains unknown for the large majority of the society. For instance, a web search with the words "nanoparticles" or "nanomaterials" leads to article titles such as "What are nanoparticles ?" or "Why are nanomaterials important?". Everyone can define a particle or a material, however, the combination with the prefix *nano-* makes these words mysterious. The General Conference on Weights and Measures officially adopted the prefix nano as a standard in 1960. From the greek word *nânos* meaning *dwarf*, the modern definition refers to the nano-scale where particles are considered nanometric when at least one dimension is less than 100 nm. Even if the nano-world was popularized with the nanosciences and nanotechnologies in the XXth century, such particles have always existed in nature¹⁻³. Inorganic nanoparticles are found mainly in the air since weather conditions and volcano eruptions produce metallic, silicate and hydroxyde nanostructures. Organic bodies secrete by microbial processes nano-elements as proteins and viruses.

Nanoparticles exist in the human production since a long time⁴. The most famous example is the Lycurgus cup fabricated by Romans in the IVth century. Its green color is attributed to the light scattering of silver nanoparticles while the red color in transmission is due to the light absorption by the gold nanoparticles⁵. IXth century Mesopotamian ceramics were found to be composed of two silver nanoparticles size slices where the bright color is due to the interference of the scattered light⁶. Awareness of the existence of such particles appears with the scientific and industrial expansion from the XVIIIth century. The conjecture of elementary species as well as the quantum physics principles allowed to lay the foundations of the nano-world in the first half of the XXth century. However, synthesis and manipulations of such nanomaterials were achieved in the second half of this century⁷ following the development of novel experimental system such as the Transmission Electronic Microscope (TEM) by Knoll and Ruska in 1932⁸.

Nowadays, nanomaterials are extensively used in any industrial sectors: information, energy, environmental science, medicine, biology, food and agriculture, transportation, cosmetics, optical and electronic devices, among many others^{3,9}. A rapid expansion of the use of nanomaterials in indus-

try was recorded in the last decades, although research is still ongoing on their potential effects to the environment and human health. Vance *et al.* reported 54 products containing nanostructures in 2005, two years after the launch of the Nanotechnology Consumer Products Inventory¹⁰. 9 years later, 1814 products were listed.

The strong interest in nanomaterials is explained by their original physico-chemical properties due to their size. Indeed, interesting and original physico-chemical properties arise with the increase of the surface-to-volume ratio with the decreasing particle size. In addition to the size reduction, optical and mechanical properties as well as electrical conductivity and chemical reactivity performances are tuned, and enhanced properties can be obtained with respect to those of the bulk^{11,12}. As a consequence of this research motivation, numerous ways to produce nanoparticles have been developed from the 50s. From nature ways, new biological methods have been very recently defined as green chemistry methods. Metal nanoparticles have been already produced using bacteria, fungi and yeast, algae and plants¹³. From artificially production, top-down techniques refer to the size reduction of a bulk material to smaller particles. Among others, grinding, milling, sputtering as well as ultra-sonication, microwave irradiation and electrochemical methods are classified in this category. The wet-chemical synthesis, such as co-precipitation, sol-gel, micro-emulsion, hydro- or solvo-thermal routes, are bottom-up methods where the molecular precursors nucleate and grow in nanoparticles^{14,15}. In bottom-up methods, we can include physical techniques such as the thermal/laser ablation.

Since the first functional ruby laser made by Maiman in 1960¹⁶ and the development of laser systems, laser ablation in gas atmosphere or in vacuum was the core of interest in several processes. Thin film preparation, surface cleaning, microelectronic device fabrication, analytical chemistry, and nanocrystal or cluster sources growth revolutionized the industrial processes for plenty of applications. Semiconductors as CdSe were produced for optics where their photoluminescence play an important role for new LED devices^{17,18}. First nanotubes¹⁹ and fullerenes²⁰ systems were generated by laser ablation and their very broad range of electronic, thermal and structural properties make them industrial key products.

As the first laser ablation experiments were performed in vacuum or in vapor phase, it was only a matter of time before first tries in a liquid phase were attempted. Since 1987, iron and tungsten metastable phase structures were synthesized using a ruby laser by a so-called *Pulsed-Laser-Induced Reactive Quenching* (PLIRQ) method at solid-liquid interfaces by Ogale *et al.*^{21,22}. Shortly after, Lida *et al.* developed *Laser Ablation in a Liquid Medium* (LALM)²³ as a way to prepare colloid samples for an Inductively Coupled Plasma Atomic Emission Spectroscopy (ICP-AES) experiment. This novel technique was found simple and convenient to produce suspension of Cu/Zn sub-micrometer particles and to overcome some general issues encountered in the gas-phase laser ablation for ICP-AES

measurements. So far, the synthesized products were not defined as nanoparticles. Only carbon-based microparticles were reported in several studies, ablating a graphite target immersed in benzene or toluene^{24,25}. In 1993, nanoparticle colloidal solutions of numerous metals were synthesized by Neddersen *et al.* in different solvents for Surface-Enhanced Raman Spectroscopy (SERS) experiments²⁶. They reported the production of Ag nanoparticles of 20 nm. These pioneers predicted the potential of this novel synthesis route: "*A new and highly promising method for preparing metal colloids is described that eliminates some of the problems associated with the chemical procedures. Advantages of this method include the simplicity of the procedure, its versatility with respect to metals or solvents, and the absence of chemical reagents or ions in the final preparation.*" A few years later, in 1997, Prochazka *et al.* addressed the size-controlled of Ag nanoparticles by fragmentation and addition of anions in the solution²⁷. These first studies laid the foundations of the Laser Ablation in Liquid (LAL).

As for gas-phase laser ablation, LAL was used for machining and manufacturing at the micro- and nano-scale as well as the generation and the processing of nanomaterial colloids. By immersing a workpiece into a liquid, the machining processes, as cutting, drilling or microstructuring, are largely improved by confining the reaction spot and its products, lowering the heat on the target and reducing the produced debris²⁸. When the interesting products are the removal material, the Laser Synthesis and Processing Colloids method combines several processes²⁹. All the techniques, which refer to LAL, belong to the Laser Ablation (Synthesis) in Liquid (Solution) (LAL/LASIS) category. This includes the Pulsed Ablation in Liquid (PLAL) as well as the Reactive Laser Ablation in Liquid where the aim is to induce reactions between the ablated matter and the liquid. In parallel, Laser Fragmentation in Liquid (LFL) and Laser Melting in Liquid (LML) are designed as Laser Processing of Colloids (LPC) methods. These processes allow the size reduction or increase of particles, already generated by LAL or another synthesis route. In the scientific community, the Pulsed Laser Ablation in Liquid (PLAL) is the most common method and is under the scope of this thesis. Therefore, I will refer only to PLAL afterward.

The PLAL reaction is a physico-chemical process where several mechanisms occur successively to finally produce nanomaterials. Laser ablation is defined as the ejection of matter from a solid target induced by a light-matter interaction. A laser beam is thus absorbed by the target immersed in a liquid media and after complex relaxation processes, the matter is removed from the target surface. A dense and hot plasma is created and is composed of the ablated matter. When the plasma cools by being quenched by the liquid, its energy transfers into the liquid, which evaporates by producing a gas bubble mainly composed of the liquid. This bubble expands and collapses sometimes several times. The release of the materials, *i.e.* of the produced nanoparticles, in the liquid mainly occurs during the first collapse. Colloids thus formed may age and be subject of some transformations. Large overview about PLAL can be found in available reviews²⁹⁻³².

PLAL remains an active research topic since this method appears promising at the industrial scale, both for the production process and the products. Moreover, it proposes an alternative for the production of nanoparticles colloids compared to traditional synthesis methods. This method is versatile due to the wide range of accessible materials, as well as numerous solvents. The nanoparticles are directly produced in the solvent, thus referring this synthesis method as an one-step process, advantageous for industrial production. Colloids can be produced in standard organic or aqueous solvents or more original matrix such as viscous oils or polymers. However, various processes can occur during the synthesis and accordingly PLAL involves complicated mechanisms.

At last but not least, the nanoparticles are generally stabilized in the liquid without using complexing agents and they are therefore described as ligand-free. While its main advantage is the production of bare surface nanoparticles, this is also the origin of the lack of control of the nanoparticles morphology and their crystal structure. Numerous improvements have been proposed since these last decades to a better control of the nanoparticles production. The use of adsorbates, such as ions and organic ligands, leads to a better colloidal stability, a production of mono-dispersed nanoparticles in size and in shape and may induce metastable crystal structure. Even if these methods are quite common, some fundamental mechanisms remain questioned.

This thesis work aims to give new insights about the mechanisms leading to a better control of the PLAL reaction and the laser-induced nanoparticles in colloidal solutions. I used methods from different domains of expertise to probe the physical and the chemical mechanisms involved in the nanoparticles production. My thesis work ties in with the team's objectives to investigate the fundamental aspects of the PLAL mechanisms and its ability to produce nanomaterials, and more specially with the PhD of Julien Lam (2012-2015)³². In previous works, plasma spectroscopy was used to track the kinetics of the reactive species at the early stage of the plasma. Shadowgraphy technique set-up using an ultra-fast camera and an iCCD camera has been developed since several years to observe the bubbles and plasma dynamics as well as the shockwaves. In addition, the ability of our group to produce large amount of nanoparticles was used in various collaborative projects. For instance, the surface chemistry of ligand-free gold nanoparticles was probed in a first run of XPS experiments, or CeO₂ nanoparticles have been produced to assess their activity in the degradation of organophosphorus compounds (decontamination of warfare agents). Finally, such experimental studies are usually reinforced with theoretical calculations, thanks to collaborations with the "Modeling of Condensed Matter and Interfaces" team and the "Theoretical Physical Chemistry" team of the institute, *i.e.* computational quantum chemistry, empirical potentials, statistical physics, numerical methods. My own work benefits from this background.

The general outlines, which define the PLAL synthesis, will be developed in the chapter 1. The free parameters, which are susceptible to influence the mechanisms, will be listed and briefly related to their effect on final products. Then I will describe each successive mechanism occurring during the ablation process as well as the nanoparticle formation phenomena. Improvements of

this technique will be presented in the context of the interests of PLAL nanoparticles in future applications. The features of the PLAL method will be thus viewed in the actual state of art. This first chapter will bring into light the intrinsic and extrinsic factors that impact the reaction and the produced nanoparticles.

In the chapter 2, I will describe the dynamics of the laser-generated bubbles for which their originality are relevant for the field of fluid mechanics. Especially, the motivation to produce in an one-step process nanoparticles in engine oils leads to study the dynamics of bubbles induced in high viscosity solvents thus resulting in high capillary numbers. The shadowgraphy technique developed by our team was used in order to track the bubbles. An automatic treatment was also developed to evaluate the hydrodynamics regimes of the bubbles thanks to their driving forces identification.

In the two last chapters, I will focus on the influence of stabilizing agents added in the solution before the ablation. The studied adsorbates are from two categories.

In chapter 3, the addition of complexing ions for the synthesis of gold colloids will be discussed in light of both salt and solutions concentrations. X-Rays Photoelectron Spectroscopy (XPS) experiments have been performed to probe the surface chemistry of the laser-generated gold nanoparticles, as well as the origin of charge carriers leading to the electrostatic repulsion forces between gold nanoparticles.

In chapter 4, I will emphasize the use of organic ligands as adsorbates stabilizing ruby nanoparticles. The ruby corresponds to chromium doped alumina in the corundum crystal structure. An experimental approach will present how we investigated the influence of the ligands on the nanoparticles size, crystal structure and their luminescence properties. Then, a complete theoretical study will demonstrate the stabilization effect of such organic molecules on the structure of alumina nanoparticles, after having delimited regions of alumina polymorphs stability. This work was performed using Density Functional Theory (DFT) based calculations and empirical potentials approach.

CHAPTER 1

GENERAL FEATURES OF PULSED LASER ABLATION IN LIQUIDS

Contents

1.1 Free parameters	8
1.1.1 Experimental set-ups	8
1.1.2 Before laser ablation	10
1.2 Successive physico-chemical mechanisms	12
1.2.1 Ablation process	12
1.2.2 Plasma and bubble phases	17
1.2.3 Nanoparticle formation	21
1.3 PLAL interests in synthesis methods	28
1.3.1 Advantages	28
1.3.2 Improvements	30
1.3.3 Applications	32
1.4 Conclusion	34

Ablation in liquids puts into play complex physico-chemical mechanisms, which generate nanoparticles. The spatial and temporal scales make difficult the direct control of the reactions. Though, numerous parameters influence the synthesis and need to be taken into account. Indeed, elements specific to the PLAL process technique or to the materials used can perturb the system and either lead to a better control of the final products or to destabilize the solutions.

This chapter aims to describe the actual knowledge of the physico-chemical mechanisms that define the PLAL synthesis and how the synthesis parameters might influence the nanoparticles formation. The successive steps occurring before and after ablation will be integrated in the current state of art. The interests about this merging technique for industry will be related for both fundamental research and industrial applications.

1.1 Free parameters

1.1.1 Experimental set-ups

On the pioneering work of Nedderson *et al.*²⁶, an experimental set-up was designed to prepare metal nanoparticles colloids for SERS measurements. Ablation in water and organic solvents was performed on vertical bulk metal targets, immersed in the liquid. A Nd:YAG laser beam was brought horizontally and focused with a convergent lens. This simple picture of this pioneer set-up underlies the general PLAL experiments.

Nowadays, a simple and convenient configuration is widely used by the scientific community. Comparable to Nedderson's set-up, a container is partially filled with a solvent, stirred by a magnetic stirrer. The container type depends on the final solution volume desired and can be a small beaker or a large crystallizer. In a different manner, the target stands horizontally on the bottom of the container in the focal plan of a convergent lens. Figure 1.1(a) schemes the characteristics of the set-up used in this work.

The development of LAL synthesis to generate continuously colloidal solutions brings into light the capacity of this new method to produce nanoparticles at large scale with a high productivity yield^{33,34}. Experimental installations have been built to produce high scale and to perform continuous nanoparticles synthesis, based on a liquid flow system. A similar set-up has been adopted in our group where a flow cell was made by 3D printing (see figure 1.1(b)). A peristaltic pump brings the liquid from the source tank to the bottom of the cell. The bulk target, which was inserted vertically in the cell, is ablated by the horizontal laser beam. As the liquid travels from the bottom to the top of the cell, the produced objects as well as the persistent bubbles are removed from the target and evacuated outside the cell. Finally, the final colloidal solution can be stored in a large container.

For the two configurations, a large rectangle of the target needs to be ablated for a better yield efficiency. Two options can be considered: either the target support may be moved by a 2D-directions translation stage, or the laser beam is directly controlled with steering mirrors. The second option has been preferred by performing a zigzag scanning because of the more rapid time of execution

(≈ 1 ms) and the easier triggering of the laser and the experimental tools. In the liquid flow circuit, the laser is turned off at the end of each scan in order to let the flow removed the produced matter. Finally, two ablation laser systems were used. The first one is a UV beam ($\lambda = 355$ nm), using the third harmonic of a 5-ns Nd:YAG laser ($f = 9$ Hz) and reaching a maximum laser energy of 36.7 mJ/pulse. The second laser system is more dedicated for the nanoparticle synthesis thanks to its high repetition rate of 1 kHz. The laser system was elaborated by the Fibercryst company and was designed to operate in the near-IR range ($\lambda = 1064$ nm). Basically, the laser beam from a passively Q-switched kilohertz Nd:YAG laser is amplified using a Taranis laser gain module. The Taranis module consists of a diode-pumped Nd:YAG single crystal fiber. The final maximum energy per pulse is 2 mJ/pulse with a pulse duration of 500 ps.

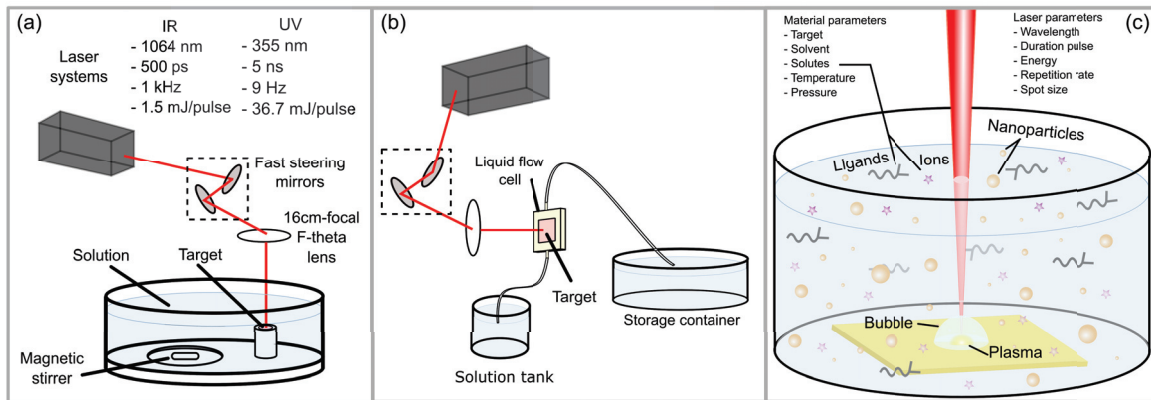


Figure 1.1 – PLAL experiment systems and characteristics used in this thesis work: (a) in a beaker or crystallizer and (b) in a liquid flow cell set-up. Nanoparticles are synthesized through a multi-step process including plasma and bubble formation, optimized by adjusting material or laser parameters listed in (c).

Like any new process, parameters optimization of the synthesis according to the desired final products is primordial. Parameters involved in the laser ablation in liquid are numerous and can be arranged in two large categories, as summarized in figure 1.1(c). These parameters will be discussed in the following in the light of their effects in the different stages of the ablation process.

- **Light parameters:** the first important parameters to take into account are the intrinsic characteristics of the laser used. Lasers are defined by their pulse duration τ_L , their wavelength λ_L , their energy, their repetition rate f and their beam or spot size. Nowadays, a large panel of lasers is commercially available for PLAL^{29,30}. These lasers can be found from the femtosecond to the millisecond pulse duration ($10^{-15} - 10^{-6}$ s), with wavelength from ultraviolet (UV) to infrared (IR), energy per surface area or fluence between 0.1 - 100 J/cm² and with a large frequency range between the Hz to the MHz. The laser energy per pulse controls essentially the productivity yield as shown in figure 1.2 (a).

Others parameters relative to the ablation process should be taken into account such as the ablation time³⁵, the interpulse distance^{36,37} (respectively figures 1.2 (b) to (c)) and the number of pulse per spot³⁸. The number of pulse per spot is related to scanning and laser frequencies and may have important consequences on the bubble phase dynamics during the reaction³⁶.

- **Matter parameters:** this category groups together the material parameters and the environment conditions. First, the solution is composed of the solvent and solutes, *i.e.* all the objects added in the solvent as ions or ligands. The solvent and the solute concentrations are thus essential and can modify physico-chemical properties of the liquid and change the ablation conditions. Factors as the density, viscosity, refractive index or surface tension are important parameters regarding the laser interaction with the liquid and the dynamics of the mechanisms involved in the reaction^{29,30}. In figure 1.2(d), the ablation rate has been measured for iron ablation in different solvents³⁸. Moreover, there are also extrinsic factors linked to the process. A stationary liquid media will rapidly saturate while a liquid movement, only stirred circularly or due to a flow, will evacuate the produced objects from the ablation spot^{39,40}. The thickness layer between air and the target is controlled by the absorption of the light by the liquid³⁷ (Fig. 1.2(e)).

Similarly, the physico-chemical properties of the target material play also a role on the reaction and on the final produced particles. In addition of the intrinsic chemical composition of the material, which is the main parameter to take into account, the physical properties as the shape or the thickness of the target could be significant⁴¹. Figure 1.2(f) displays an example of the mass removal as a function of the thickness of a gold target. In a lesser extent, the pressure and temperature thermodynamic conditions of the system are far from the extreme conditions during the PLAL reaction, reducing their role in the process.

1.1.2 Before laser ablation

On its way, the light needs to pass through the liquid layer and its content before reaching the target, such as the solutes and the previous ablated particles.

First, the beam travels through the solvent and solute molecules where absorption and scattering phenomena reduce the energy beam. The solvent and the additives should be chosen and concentrated according to the wavelength-dependent absorption coefficient. Yan *et al.* measured the transmittance of solution with different adsorbates species and concentration using a 248-nm excimer laser⁴². Results showed that beam energy can be transmitted from 87 % at low surfactant concentration to 30 % for the highest. In the same way, the thickness of the liquid layer is thus important as the optical penetration depth decays with the absorption coefficient³⁷.

Liquid depends also on the fluence. Heating, photodissociation until optical breakdown phenomena can occur with increasing fluence^{43–48} and reduce the energy beam drastically. At high intensities, non-linear effects can alter the the spatial energy distribution by causing self-focusing, filamenta-

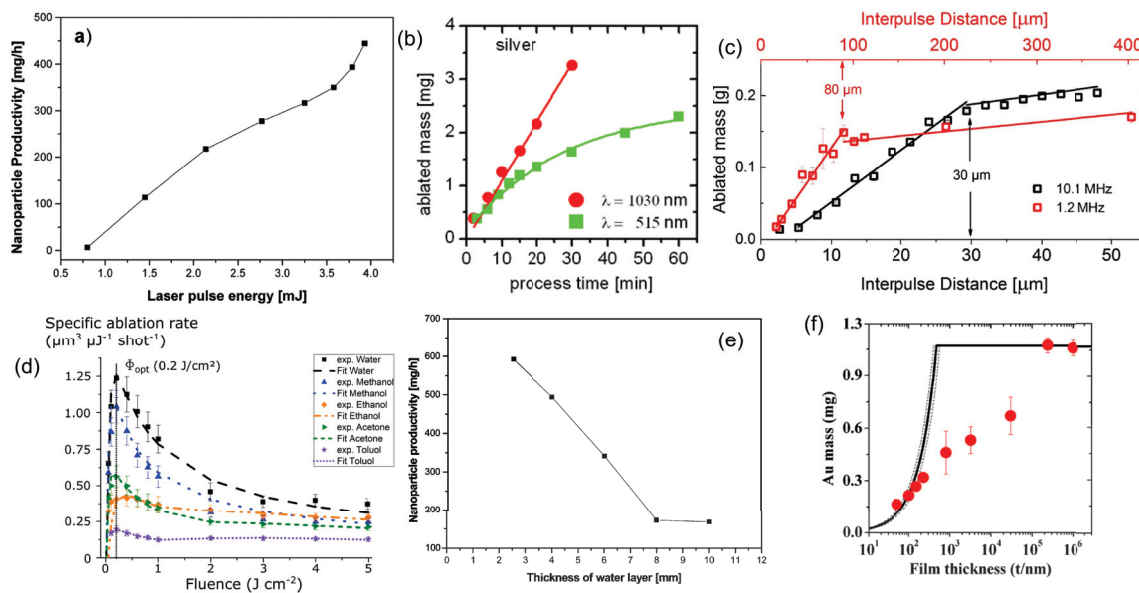


Figure 1.2 – Some parameters influencing the ablation synthesis: (a) the production productivity is controlled essentially by the laser pulse energy (Reprinted from³⁷). The mass removal can depend on (b) the process time and (c) the distance between two pulses (Reprinted respectively from³⁵ and³⁶). (d) The specific ablation takes into account the mass removed as a function of the energy and number of shot for different solvents (Reprinted from³⁸). The thickness of (e) the liquid layer or (f) the target can impact the ablation process (Reprinted respectively from³⁷ and⁴¹).

tion, white continuum or multi-photons absorption^{49,50}.

Along the optical path, the laser pulse is subject of a medium transition between the ambient air and the liquid, which is characterized by a refractive index modification. This issue can be solved by displacing the focusing lens to correct the focal point^{45,51}.

In a multipulse laser ablation processing, the early ablated material composes already the colloidal solution content. Particles in suspension, located in the optical path, absorb or scatter the beam. According to the distance from the focal point, the energy deposited on the particles leads to different processes. At low fluence, objects can be simply heated before the melting point and thermal nanobubbles are generated in their surrounding⁵². Surface or complete melting can be achieved through LML^{53–58}. At higher fluence, large nanoparticles are fragmented in smaller ones through LFL^{27,49,54–56,59}. In addition of the fluence, smaller laser wavelengths (*i.e.* 532 and 355 nm), meaning higher photon energy, are more efficient for these processes since a better absorption can be usually achieved⁶⁰. Therefore, to avoid surexposition of the as-produced colloids to the beam, a short process time (few minutes to tens of minutes) is appreciated in a small volume of stirred liquid. Otherwise, a fluid flow is necessary to evacuate the particles³⁹.

When the beam finally meets the solid target, some mechanisms can reduce the energy beam available for absorption and modify the reaction dynamics. A well polished surface can reflect more

efficiently the incident beam, while a rough surface allows an absorption leading to an inhomogeneous material removal⁶¹.

1.2 Successive physico-chemical mechanisms

The PLAL reaction is a physico-chemical process where several mechanisms occur successively to finally create nanomaterials. This section aims to describe temporally these steps and to give some insights about the impact of the synthesis parameters on the reaction and on the final products as well as the experimental analysis techniques used to probe the different mechanisms. Figure 1.3 tends to summarize and schemes these stages along a timeline.

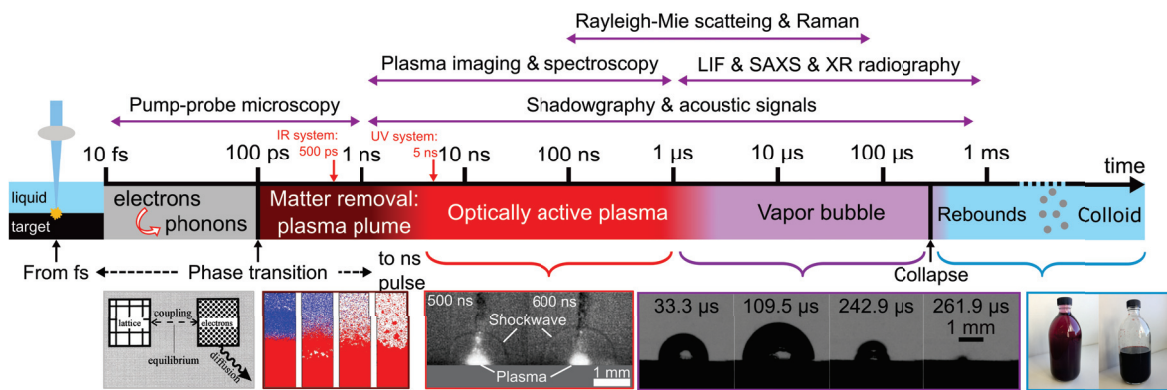


Figure 1.3 – Timeline representing the successive stages that occur during PLAL synthesis from the laser pulse interaction with the target to the release of the as-produced nanoparticles in the solution. At the top of the time scale, the analysis techniques are displayed according to their time resolution. At the bottom, from left to right: electron-phonon scattering scheme⁶², plasma plume simulation snapshot⁶³, plasma and shockwave images⁶⁴, bubble images⁶⁵ and nano-gold colloidal solution. Red arrows indicate the pulse duration of the two laser systems I used during this thesis work.

1.2.1 Ablation process

1.2.1.1 Photon absorption and relaxation processes

By reaching the solid target, the laser energy is absorbed and several mechanisms of excitation and relaxation arise depending on the pulse duration. Based on comparison between the pulse duration τ_L and the electron and lattice characteristic times to reach a thermodynamic equilibrium, respectively τ_e and τ_i , two regimes exist^{62,66} (Fig. 3.2).

- (i) **Non-thermal regime:** the laser energy is first absorbed by the electrons, which are brought to the conduction band. This excitation is more or less long depending on the material, but is generally of tens of femtoseconds (τ_{abs}). Free electrons of metals will more easily absorb the laser light, while semiconductors or dielectrics need to cross the bandgap in order to produce free electrons. The excitation of the electrons leads to an out-equilibrium state and is followed by a rapid thermalization established in a time τ_e by the electron-electron scattering. The gas

of electrons reaches an electronic temperature T_e through a Fermi-Dirac distribution. τ_e is generally on the order of tens of femtoseconds⁶⁷, while the ions from the lattice remain cold compared to T_e .

Then, the electrons transfer their energy to the ions within a time τ_i of several picoseconds^{68,69}. The lattice thermalization is thus carried out by electron-phonon coupling following a Boltzmann distribution to reach a temperature T_i in equilibrium with T_e of thousands of Kelvin. Consequently, the non-thermal regime is defined for ultrashort pulse where the different thermalizations occur successively without reheating before the first structural modifications: $\tau_L \ll \tau_e \ll \tau_i$ or $\tau_e \ll \tau_L \ll \tau_i$. Hence, the femtosecond and picosecond pulses are included in this regime.

- (ii) **Thermal regime:** this regime is characterized by pulse duration such as nanosecond pulse longer than the electron-phonon coupling and the structural modifications: $\tau_e \ll \tau_i \ll \tau_L$. From absorption to thermal phenomena such as heating and evaporation, the reheating of the target leads to consider these mechanisms to occur simultaneously. Therefore, the temperature of the system is assumed to be at the thermodynamic equilibrium between the species: $T_e = T_i = T$.

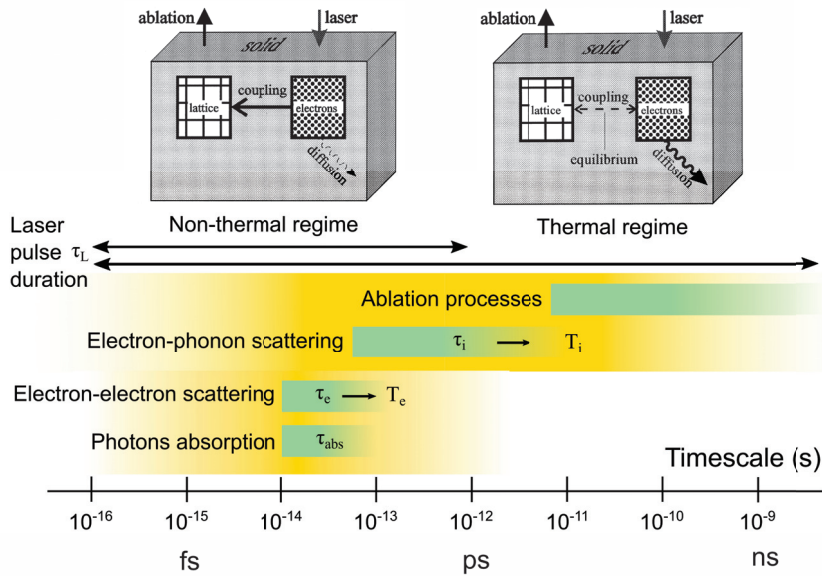


Figure 1.4 – Characteristic times of excitation and thermalizations mechanisms of electrons τ_e and lattice τ_i after the absorption of the laser beam within τ_{abs} by the target and before the ablation processes start (Figure inspired from⁶⁹). Schemes on the top panel show these mechanisms in the cases of non-thermal and thermal regimes according to the laser pulse duration (Reprinted from⁶²).

1.2.1.2 Ablation mechanisms and plasma expansion

After the phenomena of absorption and excitation of the system, which ends to the thermalization of the electrons and the lattice, the structural modifications start. This stage corresponds to the ablation process where the matter is removed and leads to the plasma expansion. At such short scales, we got information essentially from theoretical calculations. Different calculations methods have been considered for the description of the ablation process since the first experiments in the sixties. Numerical modeling including thermal and hydrodynamic models has been developed to study all the pulse duration and fluence ranges^{70–81}. Monte Carlo^{82–84} and Molecular Dynamics (MD)^{63,85–98} simulations have also been used to investigate such ablation processes. Important reviews on the history of theoretical approaches of laser ablation simulation are available in the literature^{99–101}.

In our work, we are using ns pulses (500 ps and 5 ns sources). For such pulses, MD approach is hardly usable because (i) such a time scale is too long regarding the computational cost, and (ii) the laser/matter interaction is generally not considered. The energy deposition can no more be considered as a separate initial event. The interaction between the laser pulse and the early formed plasma has to be taken into account, which leads to a screening and plasma warming.

Several ablation mechanisms have been identified according to the pulse duration and the fluence applied in the system. These different ablation mechanisms will be described through thermodynamic paths displayed on $\rho - T$ diagram (Fig. 1.5(a)). For visual considerations, molecular dynamics snapshots will also help (Fig. 1.5(b-d)). Such diagram is often used in theoretical studies, but it is important to mention that these diagrams are assumed to be locally at the thermodynamic equilibrium and depend on the studied materials. Calculated fluence (energy/area ratio) are compared with respect to the ablation fluence threshold F_{th} , characterized by a transition between an evaporation process and ejection mechanisms implying larger material amounts. These fluence regimes depend on the laser pulse and the material.

(i) **Vaporization:** the vaporization describes the phase transition from a condensed phase (solid or liquid) to the vapor phase. With enough time and at high temperature, the outer surface of the target follows sublimation and evaporate in order to form mainly atoms and small clusters (Region IV in figure 1.5(b)). As the thermal equilibrium is reached, the thermodynamic path follows the binodal line until the vapor region (green arrow in figure 1.5(a)).

(ii) **Normal boiling:** this phenomenon describes the heating of the system and the heterogeneous nucleation of vapor bubbles from a liquid. This implies an equilibrium liquid-gas where inhomogeneities of gas, solid defects or solid surface impurities lead to gas bubble formation. Even if the main bubbles form at the outer surface, they may be created in the liquid volume or at the solid-liquid interface and diffuse to the surface. This regime is seen when the temperature overrides the boiling temperature T_b . Normal boiling are the normal heating processes fol-

lowing the equilibrium liquid-vapor binodal line (I-Y path) in the $\rho - T$ diagram (green curve in figure 1.5(a)) directly from the triple point TP or after crossing the binodal line (I-J-Y red curve in figure 1.5(a)).

- (iii) **Explosive boiling:** as referred also as *phase explosion* or *homogeneous nucleation*, this is the only thermal process able to explain the ejection of the matter in short lapse time. Depending on the laser pulse regime, the heating of the target may be isochoric (A-B-Y path in figure 1.5(a)) or non-isochoric (A-I-J-Y path) and the temperature of the system may override the critical temperature point CP. This heating is characterized by an important and rapid transition to the metastable region crossing the spinodal line (Y-E-F path in figure 1.5(a)). The superheated liquid state thus formed has an high temperature, which allows to pass the gas nucleation barrier. Therefore, an high nucleation rate enables to gas bubbles to nucleate and grow (Region II in figure 1.5(b)). This homogeneous nucleation remains slow and the gas phase becomes the dominant phase while liquid droplets persist and are ejected with the gas.

- (iv) **(Trivial) Fragmentation:** fragmentation processes may explain some non-thermal ablation mechanisms at the ultrashort laser pulse. First, the heating from solid state occurs at constant volume. The stress induced by this isochoric heating is converted into an immediate strain, characterized by a rapid expansion (A-C path in figure 1.5(a)). The relaxation takes place in the supercritical liquid state (C-D path) where decomposition of the matter is carried out by creating gas voids (Region III in figure 1.5(b)). The system ends in the superheated metastable region, already decomposed. The main effect in this ablation mechanism is thus due to a mechanical fragmentation of the matter, and not to a thermal process. A different mechanism can also exist according to pulse duration and fluence. The heating becomes non-isochoric and the expansion starts already in the supercritical liquid state (A-I-K path in figure 1.5(a)). The relaxation is, however, similar to the fragmentation regime. This small difference leads the authors to consider a quasi-similar process, named *trivial fragmentation*, by opposition with the *direct fragmentation* or *nontrivial fragmentation*.

- (v) **Spallation:** at low fluence, this regime is essentially due to mechanical effect. Indeed, an internal break propagates along the solid surface and results in entire layers detachment. Such mechanism occurs when the stress applied in the system overtakes its tensile strength and creates defects and small breaks. By propagation, large pieces of matter and atomic size particles are ejected. Its relaxation ends in the solid-vapor metastable region, with a passage in the solid-liquid state (not shown here).

It is important to mention that whether these different mechanisms can be explained independently from each other, simultaneous regimes can occur during an ablation process. For instance, snapshots displayed in figure 1.5(b) show the different mechanisms which are present according

to the regions along the target depth. Indeed, the energy, which is absorbed locally from the outer surface to the target volume, will result in different ablation mechanisms, as well as from the center to the edges of the ablated spot. According to the target material type, metals are the most studied^{70,73–77,79–81,96–98} with respect to other materials such as oxides^{74,78} and graphite^{73,74}.

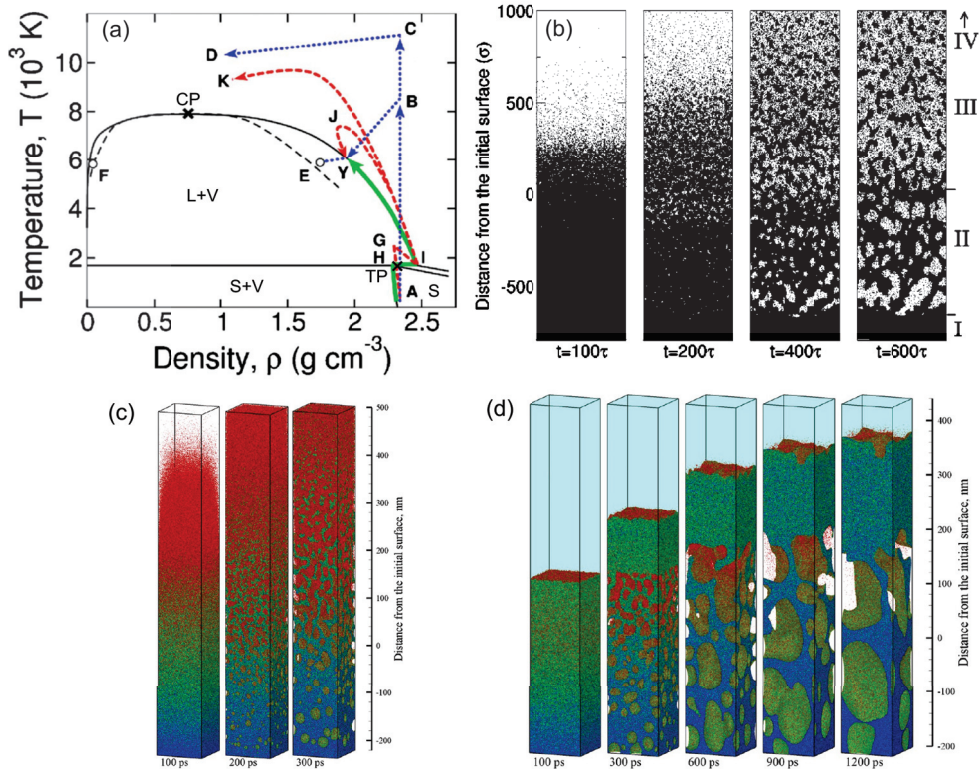


Figure 1.5 – (a) $\rho - T$ phase diagrams calculated to follow the temporal thermodynamical paths of the different ablation mechanisms (Reprinted from⁹⁵). The blue dotted curves refer to the direct fragmentation (A-B-C-D path) and the phase explosion (A-B-Y-E-F path) mechanisms. The trivial fragmentation (A-I-K) and the normal boiling (A-I-J-Y) processes are indicated by the red dashed curves. The normal boiling and vaporization occur depending on the fluence, higher the fluence and further the heating follows the binodal line (A-Y) displayed by the green solid curve. (b) Temporal snapshots of molecular dynamics simulations using a pulse duration of $\tau_L \approx 400 fs$ and with a fluence of $F = 2.8F_{th}$ (Reprinted from⁹¹). The plasma expansion is separated in four regions: (I) the non ablated matter close to the target, (II) the phase explosion state, (III) the direct fragmentation process, and (IV) the vaporization regime. Simulation snapshots of ablation of a silver bulk target ($\tau_L = 100 fs$ and $F = 400 J/m^2$) (c) in vacuum and (d) in water (Reprinted from⁹⁷).

Until now, the ablation processes were described in vacuum or in a gas media. Several studies performed also simulations of ablation in a liquid^{63,80,81,96–98}. General conclusions highlight that the physics behind the gas-phase ablation mechanisms are found to be similar in water environment, except that, the plasma plume suffers from the strong confinement effect applied by the

liquid environment. At the same fluence, these mechanisms are slowed down in expansion at the interface of the ejected layer and the target, but the cooling rate is faster.

Recently, the group of Zhigilei observed how the removed matter is mixed with the water in an explosive boiling regime. They simulated the silver target ablation with $\tau_L = 100$ fs and $F = 400$ J/m² in vacuum and in water⁹⁷. Phase explosion in vacuum is driven by the release of vapor at the surface region being in a superheated state (red Ag atoms in figure 1.5(c)). The plasma plume freely and rapidly expands thus displaying an internal region close to the target, which decomposes into vapor and small liquid droplets (green and red mix Ag atoms). When confining by a liquid, the surface is in a superheated molten state (blue molten Ag atoms in figure 1.5(d)), which slowly expands. The explosive decomposition forms a superheated vapor composed of small clusters and atoms, which is contained in a dense hot layer (green and red mix Ag atoms). At the outmost layer of this hot layer, a mixing region forms between the Ag atoms and the water molecules brought in the supercritical state. In the subsurface, a foamy structure is constituted of vapor and melt matter (blue and green Ag atoms generating voids) while the expansion slows down. The molten layer was confirmed experimentally by pump-probe microscopy, which was pointed out as the main difference with gas-phase ablation¹⁰².

Experimentally, these phenomena are difficult to probe at this time scale by *in situ* characterization. Pump-probe microscopy succeeded to get information at the early stage of the laser-matter interaction and during the ablation process¹⁰². Domke *et al.*¹⁰³ captured the reflectivity and the Newton rings from 1 ps to few μ s that give insights about the ablation process of a Mo film in liquid. They observed excitation process with the increase of electrons temperature, and validated that no difference exists in the first ps between PLAL and gas-phase ablation. They confirmed the confinement effect of the liquid on the plasma plume and they identified the ablation regime as phase explosion.

1.2.2 Plasma and bubble phases

1.2.2.1 Plasma phase and its related phenomena

During the expansion of the material, a hot and dense plasma contains highly charged and neutral species as atoms, ions, molecules and electrons, and can be mixed with melted droplets and small clusters. This plasma plume is considered at the non-equilibrium state as it is characterized by high temperature ($T_{electrons} > 1000$ K), pressure (1-10 GPa) and density (10^{22-23} atoms/cm³)^{64,104-106}. From this plasma plume, several phenomena have been reported:

Plasma light emission.

Excitation and photo-ionization occur in the plasma phase due to the high energy involved. Electron density was measured on the order of 10^{18-19} electrons/cm³^{107,108}. Relaxation of the highly ionized

species leads to a light emission from the plasma. The optically active plasma spectrum can be decomposed into two elements: (i) a continuous background exists due to electron-ion radiative recombinations as well as bremsstrahlung phenomenon and (ii) discrete lines are emitted from the de-excitation of atomic species first and from molecular content, as well as black body^{104,105,107,109-113}. These light emissions reveal important informations about the plasma composition and formation dynamics of the particles inside the plasma phase. Optical plasma spectroscopy (developed as Laser-Induced Breakdown Spectroscopy (LIBS) for metrology) is extensively used as an experimental technique to capture the emission lines of atoms and molecules, and to access to the electron density as well as the temperature of the system. An example of spectrum coming from the ablation of an alumina target is displayed in figure 1.6(a).

The group of Sakka extensively studied the molecules formed in the plasma during the first μs of the ablation. In particular, they tracked the emission lines evolution from the ablation of a graphite and boron nitride target immersed in different aqueous and organic liquids. Molecule and ion emission lines as C_2 , CN, BO and B^+ were captured at $\approx 100 \text{ ns}$ after the pulse shot when the strong continuous background is reduced to reveal the discrete lines^{104,109}. Oxidation of aluminum ions during the plasma was also observed by plasma spectroscopy^{107,111}. All these studies reveal that first chemical reactions with the solvent occur during the plasma phase and more especially during its quenching by the liquid media.

Maintenance of the plasma.

Time-resolved plasma images can also be tracked by fast plasma imaging to observe the dynamics of the plasma plume and to obtain thermodynamical parameters¹¹²⁻¹¹⁶. Similarly, shadowgraphy can also distinguish the plasma^{106,117-120}. Plasma images captured with an iCCD camera are presented in figures 1.3 and 1.6(b)(left) as well as shadowgraphy picture in figure 1.6(b)(right).

From these techniques, plasma lifetime has been estimated from a tens of ns to a few μs , depending on the laser parameters and the liquid environment^{105,114}. For ns laser pulse duration, the plasma coexists with the laser pulse. Therefore, the plasma is still maintained by absorption of the pulse energy, which leads to an increase of its temperature and its lifetime^{115,120,121}. Lifetimes of a few μs have been already measured for laser pulses longer than 100 ns, which allow a better and longer emission lines measurements. In return, the so-called *plasma shielding* effect reduces the energy deposited on the target^{118,122,123} and at the same time, the ablation yield¹²⁰.

Shockwaves generation.

From the ablated material detachment, energy released by the system is partially used in the plasma formation and expansion of the matter. The excess energy causes a so-called *recoil pressure*, which results in the generation of a shockwave. This shockwave travels in all directions, both in the target and in the liquid (Fig. 1.3). It can be defined as a pressure wave propagating in a medium, which involves a gradient flow of physical quantities such as matter density or temperature. Prac-

tically, shockwaves have been observed during the first hundreds of nanoseconds by following the refractive index fluctuations of the liquid captured by fast-imaging implemented in shadowgraphy^{43,118,120,124}, Schlieren^{112,113} and laser scattering^{106,119} set-ups, complementary with acoustic signal measurements^{118,125,126}. In liquids, the shockwave propagates at a velocity higher than 1000 m/s and dissipates its energy by heat and producing cavitation bubbles in the multipulse disturbed solution. The energy evacuated by the shockwave was estimated between 10 and 50 % according to the experimental conditions^{43,127,128}, though the experiments were performed in the case of liquid optical breakdown studies. With such high energy and speed, matter hit by the pressure wave may be deformed, fractured and even ejected from the target. Phase transition was observed from graphite to diamond structure achieved by compression wave¹²⁹.

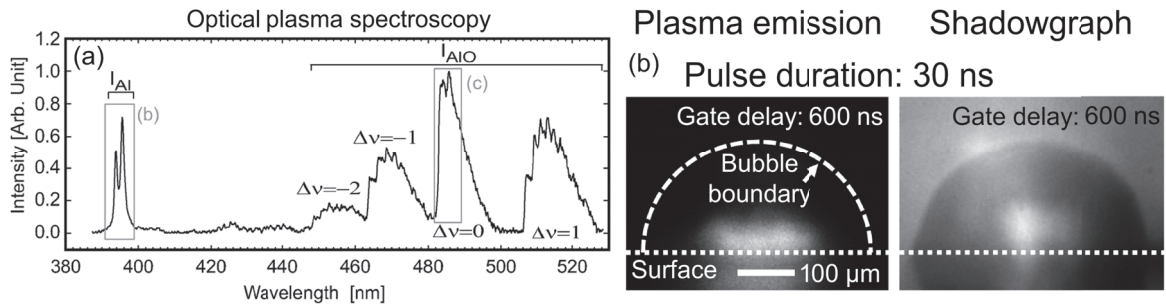


Figure 1.6 – (a) Emission lines of Al atoms and AlO molecules recorded by plasma spectroscopy (Reprinted from¹⁰⁷). (b) Plasma imaging and shadowgraphy techniques used to capture plasma coupled with a nascent bubble during the ablation of a copper target using a laser pulse of 30 ns (Reprinted from¹²⁰).

Nascent bubble phase.

In addition to the shockwaves, the energy dissipation occurs through the strong interaction of the plasma with the liquid, which leads to the vaporization of the liquid molecules. In the works of Shih *et al.*, the mixing region between the molten layer and the supercritical water was assumed to serve as a precursor for the formation of the cavitation bubble. Recent experimental studies tend to demonstrate that the expansion of the plasma is coupled with the growth of a nascent vapor bubble^{120,121}. At short pulse of 30 ns, Tamura *et al.*¹²⁰ recorded plasma images and shadowgraphs showing that the optical plasma plume was larger than the boundary of a cavitation bubble (Fig. 1.6(b)). They thus supposed that the plasma and the nascent bubble are related during their expansion while species of the plasma are injected in the bubble. Then, the plasma is rapidly quenched in contact with the water from its edges to its center. *A contrario*, a longer laser pulse of 100 ns presents a larger bubble volume compared to that of the plasma thus leaving the two phases expand independently from each other. Authors explained that this relation is induced by the time and the speed at which the bubble grows relative to the plasma maintained by the laser pulse duration¹³⁰. The balance between the energy used to create the phase and to warm the plasma favors the heat-

ing and then the following water vaporization.

1.2.2.2 Macroscopic bubble expansion and collapse

From the energy transfer between the plasma and the liquid media, the vapor bubble expands rapidly. In almost 1 μ s, a sub-millimeter bubble becomes visible^{130–134} (Fig. 1.7(a)). Its shape is hemi-spherical and totally smooth compared to some bumped-like shapes seen at the early stage of the plasma corresponding to droplets ejection¹²⁰. The temperature and the pressure conditions within the vapor bubble begin at several hundreds of Kelvin and bar¹³³. These quantities decrease while the gas bubble expands rapidly (Fig. 1.7(a)). Then, its front slows down and the bubble reaches a maximum radius in the millimeter range in most of the cases, which corresponds to a minimum in temperature and pressure. The liquid pressure compresses then the bubble, which starts to collapse by accelerating. This bubble shrinking increases suddenly the temperature and the pressure. This first bubble lasts hundreds of μ s, depending on the laser and the liquid parameters^{119,131,132,135–137}. Its hemi-spherical shape depends also on the wettability with the target, marked by the contact angles, and the liquid temperature.

From the violent collapse, a shockwave can be emitted and be visible due to a gradient density wave in the liquid^{106,112}. Other so-called *rebound bubbles* follow the first large one by decreasing in amplitude and each rebound collapse may be accompanied by a lower shockwave. These numerous collapses and shockwaves may be the new source of the removal of macroscopic fragments, or may fragilize the target in the case of multipulse ablation processes^{106,112,113}. Rebound number depends essentially on the liquid viscosity and the solutes in the solvent. Moreover, some persistent bubbles may remain close to the ablation spot, which can shield the next energy pulse in a multipulse ablation process¹³⁸. At the end, the bubble content is released in the liquid phase, producing thus a colloidal solution of nanoparticles.

Gas bubble phase was extensively studied since its lifetime scale is large enough to enable numerous experimental techniques to follow its dynamics (Fig. 1.3). The fast imaging is widely used in shadowgraphy^{108,118,124,130,132,135,139,140} or Schlieren^{112,113} set-ups. The former technique enables to capture bubble dynamics by following the bubble shadow in front of a bright background (examples of images are displayed in figures 1.3 and 1.7(b)), while the refractive index deformations are tracked with the latter method, without possibility to see inside the vapor phase. Laser scattering methods such as Rayleigh^{106,119,141,142} and Raman¹⁴³ scattering allow to probe matter inside the bubble by lighting the bubble content, which scatters the light. With this technique, formation and growth of particles can be followed. More recently, X-rays (XR) experiments were performed by the group of Plech^{137,144–146}. XR Radiography is sensitive to the phase modification and to the light transmission fluctuation, similar to the Schlieren technique. It allows to capture images of the bubble by phase contrast. Small Angles X-Rays Scattering (SAXS) was also

used to probe the particles inside the bubble. Indeed, this technique has the advantages to be sensitive to the nanoscale sizes and the obtained signal intensity is proportional to the particle volume and mass. Temporal and spatial information on the particle size distribution can be obtained from these complementary techniques along the bubble evolution. Finally, in the continuity of LIBS measurements, luminescence of the species inside the bubble can be tracked by re-exciting them with a delayed laser. This so-called *Light Induced Fluorescence* (LIF) has, however, not been reported for PLAL investigation.

From these experimental measurements, the bubble dynamics have already been analyzed and modeled thanks to some hydrodynamic models: the Keller-Miksis model^{119,135}, the Gilmore model⁴³ and the Rayleigh-Plesset equation¹³² (Fig. 1.7(a)). Thermodynamic parameters as temperature and pressure are deduced from the evolution of the bubble radius, volume and speed as well as an estimation of the molecular density. The Rayleigh-Plesset model was used by Lam *et al.* to estimate the number of molecules inside the bubble¹³². They showed that molecules from the solution are mostly present inside the bubble, which may react during the gas phase. This last model will be described in details in the chapter 2.

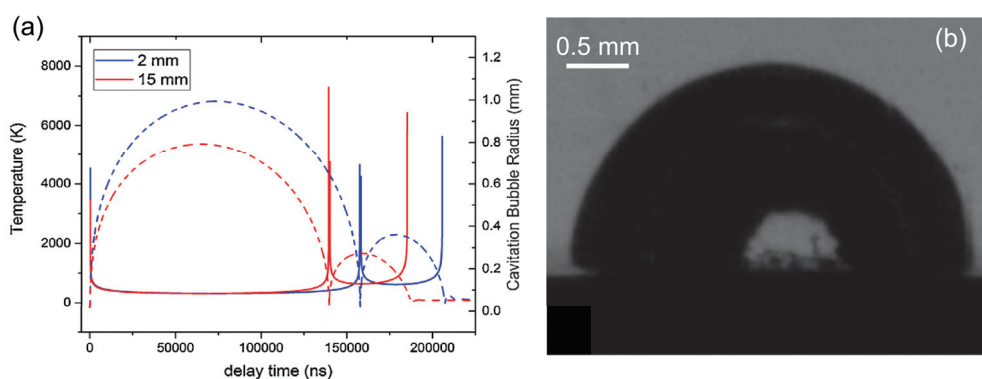


Figure 1.7 – (a) Calculated temperature and radius of laser-induced cavitation bubbles for two water heights above a gold target (Reprinted from¹³⁶). (b) Typical shadowgraphy image of a bubble produced in water.

1.2.3 Nanoparticle formation

1.2.3.1 Nanoparticle growth mechanisms

As a result of these successive steps during the PLAL reaction, the nanoparticles formation is achieved at the end of the synthesis. As the matter removal leads to the plasma phase, first investigations focused on the plasma expansion and quenching as well as its coupling with the initial vapor phase. As seen above, plasma spectroscopy and shadowgraphy reveal that particles are already present in the early stage of the vapor bubble^{120,121}, and chemical reactions occur during the

plasma phase^{104,105,111}. However, a lack of evidence of the nanoparticles nucleation needs to be overcome.

Different studies observed nanoparticles inside the bubble^{131,142} but no evidence were brought about their size and their growth dynamics. Recently, the group of Plech was able to probe inside the gas bubble using SAXS and XR radioagraphy^{137,144–147}. Two particle size categories were found to already coexist within the bubble. The bimodal size distribution is well-known since the early PLAL experiments^{51,148–150} (typical size distribution is displayed in figure 1.8(a)). At the maximum bubble height, small primary nanoparticles between 8-10 nm fill the whole bubble volume while larger secondary nanoparticles from 40 to 60 nm are located in the center and in the upper parts of the bubble (Fig. 1.8(b)). However, the apparatus resolution limits the nanoparticle detection to about few nm. Then, the primary particles seem to be pushed during the bubble collapse and agglomerate to the surface with the secondary particles. The mass analysis reveals that the large nanoparticles are weakly present in the first bubble, but in the rebound after the first collapse. This indicates that the primary particles may agglomerate during the bubble collapse (Fig. 1.8(b)). However, in all the measurements, no significant size modifications were reported. In addition, a small fraction of the primary particles was detected outside the bubble during its expansion, whereas the agglomerates are confined inside the bubble and are released during the collapses. That means that the bubble walls are not impermeable to the small nanoparticles. These results are in agreement with Rayleigh laser scattering made by Soliman *et al.*¹⁴², which concluded that some particles were ejected in the liquid during the bubble expansion even if the main portion remains in the gas phase. They also showed that the growth speed of the nanoparticles in PLAL is higher than in gas-phase ablation. With Raman scattering, Takeuchi *et al.* saw that Ti metallic nanoparticles oxidize and crystallize slowly during bubble phase¹⁴³.

Even if the capture of the two size populations within the bubble is a major step, the fundamental mechanism of formation is still unclear. Some explanations were proposed. Multiple factors must play a role in the formation of the nanoparticles. The thermal heating of the plasma and the mechanical erosion produced by bubble collapse have been suggested as the dominant mechanisms^{51,151}. The former phenomenon would favor evaporation to produce the primary particles. Agglomeration of the small particles combined with target fragmentation during the bubble collapse and shockwave propagation may form the secondary nanoparticles. From a thermodynamic point of view, differences in ablation mechanisms may lead to this bimodality⁶¹. Thermal vaporization favors the primary particles while the explosive boiling with the ejection of melted droplets produces the larger ones, though some people suggested that the large liquid droplets could evaporate during the plasma quenching¹²⁰. By studying the ablation crater morphology, different areas were observed according to the fluence, the pulse duration and the number of pulses^{152,153}. Center of the spot is attributed to the ablation area where the primary particles could be ejected (Red dashed

circle in figure 1.8(c)) while edges of the crater, which receive less energy, are considered as a modification area (Ring between the blue and green dashed circles). An intermediary ring between the center and edges is named as the annealing area (Ring between the red and green dashed circles), where the energy received can only melt the region and produce large liquid droplets. These regions imply that the ablation regimes are different according to the received energy from the laser focal point.

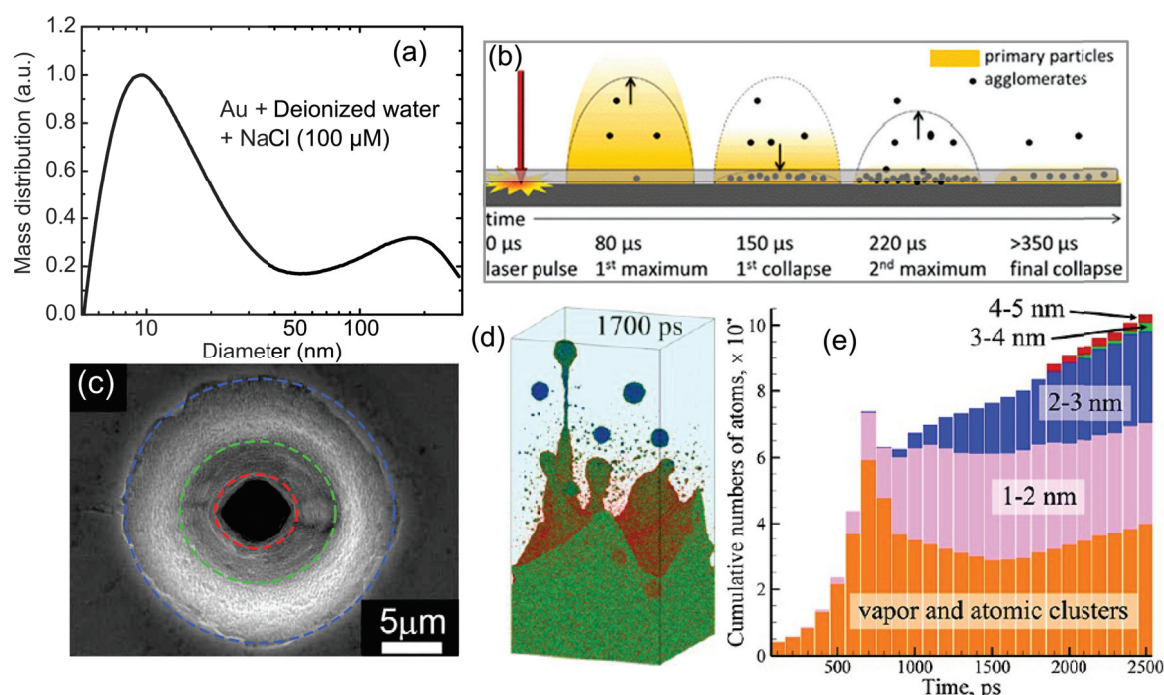


Figure 1.8 – (a) Relative weight distribution of a gold nanoparticles solution produced in an aqueous solvent composed of $100 \mu\text{M}$ of NaCl salt. It shows the two size populations encountered frequently in PLAL products. (b) Scheme of the primary and secondary particles formation during the bubble phase and its multiple collapses (Reprinted from¹³⁷). (c) SEM picture of a crater made by a fs laser on a silicon target. Its morphology reveals three regions: the ablation center leads to primary particles (internal red dashed circle), the annealing ring ejects secondary particles due to melting (between green and red dashed circles) and the edges of the crater suffer from structural modifications (between blue and green dashed circles)(Reprinted from¹⁵²). (d) Simulation snapshot of an ablation process on a Ag target in water (100 fs, 400 J/m^2) leading to the (e) formation of clusters and nanoparticles size (Reprinted from⁹⁷).

Theoretically, insights about the nanoparticle formation were reported by molecular dynamics simulations. As described above, Shih *et al.*^{96–98} simulated the ablation of a Ag target immersed in water for fluence leading to explosive boiling regime under femtosecond laser pulse (100 fs , 400 J/m^2)(Fig. 1.8(d)). They observed the formation of a superheated layer at the interface with the target and a mixing region where the water, in a supercritical state, hosts atomic vapor and small

clusters. A time-resolved analysis of these formed particles showed that they grow from Ag vapor and clusters of few atoms until size of few nm (Fig. 1.8(e)). The small blue dots present in the simulation snapshot displayed in figure 1.8(d) shows these predicted primary particles. A second mechanism reveals the production of larger particles. Indeed, the superheated layer at the interface with the solid becomes unstable and decomposes into large nanoparticles: (i) due to the density difference and water confinement, Rayleigh-Taylor instabilities induce roughness at the interface between the molten layer and the mixing region. The liquid layer is thus decelerated and rebounds on the solid target surface. (ii) The impulsion given to the molten layer at the rebound creates ejection of large nanojets due to Richtmyer-Meshkov instabilities (green droplets in figure 1.8(d)). (iii) Spherical spheres finally detach from the liquid layer by Plateau-Rayleigh capillary instabilities. In contact with the water in the mixing region, the nanoparticles cool and solidify with a cooling rate calculated at 10^{12} K/s⁹⁶ (blue particles in figure 1.8(d)). The rapid quenching may explain some metastable crystal structures^{22,154} as well as amorphous phase obtained during some ablation experiments¹⁵⁵. At the final time of the simulation, the largest nanoparticles were measured above 10 nm and the frozen structures reveal polycrystallinity of the particles, with crystal domains separated by stacking faults and twin boundaries. Finally, such calculations should be considered carefully because of the short simulation time and cannot allow the generalization for all the ablation processes, which depend on the laser and material parameters.

Based on theories developed for wet-chemical synthesis, different mechanisms have been found to explain the nucleation as well as the growth of nanostructures. Firstly, the nucleation step consists to create nuclei that remain stable and irreversible if the size is larger than a critical size. Applied to PLAL synthesis, the LaMer mechanism seems the most convenient model to describe nucleation. This mechanism was developed originally by LaMer in the 50s to explain the nucleation on various oil aerosols and sulfur sols¹⁵⁶. The basic idea is to consider the nucleation and the growth separately. The nucleation evolution is predicted as a function of material concentration, followed by a growth step with no additional nucleation, as shown in the inset of figure 1.9. The first stage (I) shows an important and rapid increase of the atom or monomer concentration until a critical concentration C_{crit} where the self-nucleation or *burst nucleation* occurs (II). The atoms thus nucleate homogeneously and their concentration reduces while the seeds grow (III) and remain stable to a finite concentration value C_{inf} .

Then, these seeds grow into nanocrystals. These steps can be described by several mechanisms, which are both complementary and competitive.

- (i) **Coalescence:** due to the dominant Brownian motion (the gravitationnal and thermocapillary motions are neglected), a high collision rate between the atoms, nuclei and clusters leads to larger particles. This process is often preceded by coagulation, agglomeration or aggregation

mechanisms (see figure 1.9(a)). When particles of the relatively same size get close to each other, they agglomerate or aggregate. When they are from different size, they start to fuse (*i.e.* coagulate) and create anisotropic spheres before totally coalescing. This mechanism occurs naturally during the PLAL reaction or caused by a LML second laser processing. The particles are irradiated during the ablation process far from the focusing point in the liquid or can deliberately be melted to produce larger and more monodispersed particles^{157,158}. By playing with energy surfaces between two solids and the heating of the particles due to the deposited laser energy, segregated, biphasic and core-shell alloy structures can be synthesized^{159–162}.

- (ii) **Ostwald ripening:** due to their higher surface energy, the small particles are less stable than the bigger ones. Consequently, the small particles dissolve and their atoms redeposit on the large particle surface through a heterogeneous nucleation mechanism. Ostwald ripening, also called *coarsening*, thus favors the large particles at the expense of the small ones¹⁶³. Jendrzey *et al.* showed that the Pt nanoparticles formation is due to the competition between coalescence and Ostwald ripening¹⁶⁴, as schemed in figure 1.9(a).
- (iii) **Particle attachment:** Alignment of crystalline particles along their crystallographic planes due to Van der Waals, Coulombic and dipolar interactions is referred as Particle Oriented Attachment (OA). Alignment may not be oriented or partially oriented, without a certain crystallographic organisation. In the case of amorphous nanoparticles or poorly crystal structures, they attach to finally crystallize in bulk symmetry¹⁶⁵. OA of Ti¹⁶⁶ and Te¹⁶⁷ was observed in organic solvents and in water. High temperature favors thermodynamically the attachment of the particles, complementary with a low charge and uncoordinated surface. Therefore, a long-period ablation, which can enhance the nanoparticle charge surface, will heat the liquid around the laser path and allow a better attachment.

These nucleation and growth mechanisms are considered intrinsic to the ablation process. External factors can be used to control the final products. Adsorbates are the most used to have a positive effect on the desired particle shape and size. Indeed, by adding ligands at the particle surface, we may control their stability¹⁶⁸, size^{169,170}, shape¹⁷¹ as well as the crystal structure¹⁷² and the surface state¹⁷³ during the ablation process. Even during the aging, ligands stabilize more efficiently the particles compared to ligand-free particles¹⁶⁸. Adsorbates facilitate the formation of complex structures as nanospindle after several days¹⁷⁴, and nanotube, nanorod or nanoplatelet after few hours^{175,176}. Amans *et al.* synthesized Y_2O_3 with organic ligands¹⁶⁹ and found that the size distribution peak was reduced and narrowed more than 4 times. The size of nanoparticles can also be tuned according to the surfactant concentration added in the solution^{170,173,177}. In our group, we synthesized $Al_2O_3:Cr^{3+}$ nanoparticles using ligands to tailor the size and the crystal structure of the nano-rubies¹⁷⁸, as it will be presented in the chapter 4, section 1. Moreover, additive ions have been extensively used to control the particles size, shape and stability due to the increase of electrostatic repulsion of enhanced surface charge^{179–181}. Such ions can also serve to dope directly oxide nanoparticles using the solvent as our work done with Gd_2O_3 nanoparticles doped with europium

ions¹⁸². In chapter 3, the interaction and effects of the added ions in the liquid during the synthesis will be described in details.

Finally, reaction-induced growth can occur through *in situ* chemical reactions during the PLAL synthesis. When a multipulse process is performed, each pulse supplies new atomic species that interact between them, with solvent and adsorbates, and with previous formed particles. Oxidation is the most common reaction in aqueous environment modifying the surface state of particles^{61,151}. Marzun *et al.* showed that oxidation reactions during the synthesis are mainly driven by the reactive oxygen molecules originating from the water molecules decomposition¹⁸³ and, to a lesser extent, by the dissolved oxygen from the ambient air. Oxydo-reduction reactions might be purposefully induced by introducing metal salts in the liquid media. Metallic composites and alloys are thus produced. According to the ablation rate and the solute concentration, alloy with tuned species ratio can be achieved. Jiménez *et al.* were able to synthesis Au and Ag nanoparticles capped with a SiO₂ shell in one step¹⁸⁴. CoPt¹⁸⁵ and PdCu¹⁸⁶ nano-alloys were produced in K₂PtCl₄ and CuCl₂ solutions, respectively. In organic solvent, the main effect is the graphitization where a carbon shell forms around the particles^{183,187,188}. Novel structures may also be achieved by *in situ* chemical reaction between different atomic species ablated from an alloy target. AgGe graphen-like microspheres were successfully synthesized from an Ag-doped Ge wafer¹⁸⁹. The germanium atoms serve as nuclei for silver atoms thanks to galvanic reactions. A supply in new ions after each pulse leads to the nanoparticles growth in large microspheres.

1.2.3.2 Colloids aging

At the end of the bubble phase, its content is released in the liquid. Nanoparticles remain in suspension in the liquid and form thus a colloidal solution. Agglomeration may occur and lead to precipitation, except when stabilization is controlled by the use of ions or ligands. Moreover, classical chemical and colloidal mechanisms might modify the particle characteristic evolution in the solution. Indeed, by applying external factors or aging the solution, particle morphology and stability can be tuned.

Intrinsically to the obtained solution, growth may still continue by the mechanisms described above. These growth processes can lead to the instability of the solution, which is characterized by an important increase of the particle size. The solution can intentionally be aged to obtain particular size or morphology due to the liquid temperature, pH or *via* phase transition. Liu *et al.* followed the evolution of Te particles ablated in several solvents where different stages of growth occur in a large scale of time¹⁶⁷. In the first seconds after the PLAL process, spherical nanoparticles smaller than 10 nm were produced. Within the next minutes, they crystallized and attached to form nanochains that self-assemble to obtain nanocubes in some cases or aggregate into large structures by a slow growth stage process, *i.e.* lasting few hours to days. At the end, spheres of few micrometers are

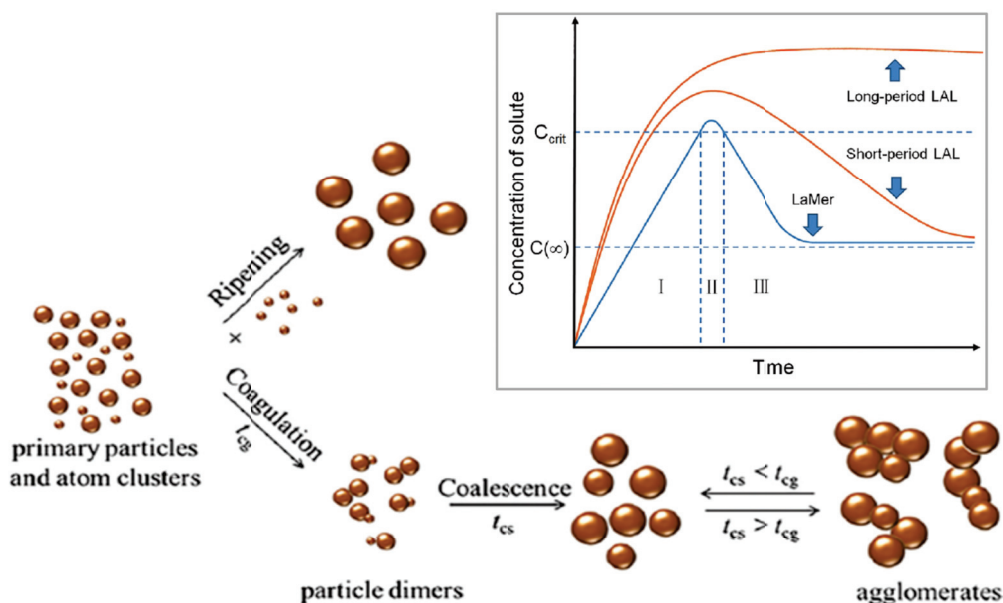


Figure 1.9 – Complementary and competitive growth mechanisms leading to nanoparticles formation during PLAL synthesis. Inset refers to the classical (blue curve) and PLAL-adapted (red curves) LaMer mechanisms (Reprinted from¹⁹⁰).

obtained by an extremely slow recrystallization of these assemblies in few days or weeks. Aging allows also to observe phase transition from as-produced metastable crystal structure or amorphous phase particles^{154,155}. In addition, shape can be tailored according to the aging time. Zhang *et al.* observed the formation of leaf-like nanoplatelets of WO_3 after two days of aging¹⁹¹ and Huang *et al.* obtained GaOOH nano-spindles one week after the synthesis of amorphous nanoparticles¹⁵⁵. Even if the plasma and the bubble phases host the main chemical reactions between the produced objects and the surrounding molecules, some reactions may continue after the synthesis. Surface oxidation generates oxide nanoparticles or passivated shell formation at the surface¹⁸³.

In parallel to the aging processes, some external factors can bring structural modifications. With adsorbates on the surface, the nanoparticles remain usually stable in a longer time than without ligands. Sobhan *et al.* showed that gold colloids synthesized with cetyl trimethylammonium bromide (CTAB) molecules remain stable for several months while the colloids in pure water show a decline after the first month¹⁶⁸. Adding salts in the liquid allows also the stabilization of the particles once synthesized. Since the highly charge surface state enhances the repulsion between the particles, aggregation is thus avoided and the colloidal solution remains stable over a long time. In addition, Kwon *et al.* demonstrated that, in the case of gold nanoparticle colloids, addition of salt before and after the synthesis leads to the same stability because of the already strong stable colloidal solution of nano-gold in pure water¹⁸⁰. Stable solutions are achieved as long as the right salts and concentration are chosen^{180,192}.

Electric or magnetic field have been used to assist the PLAL synthesis. Electrochemistry-assisted PLAL was developed by Liu *et al.* to produce nanorods of $\text{Cu}_3(\text{OH})_2(\text{MoO}_4)_2$ ¹⁹³ and GeO_2 nanospindles or nano-cubes by varying the electrical field¹⁹⁴. The principle is the ablation of a target in an electrolytic cell where electrochemical reactions occur at the vicinity of two copper electrodes, due to the highly charged surface of the produced nanoparticles. This mechanism is also used for Electrophoretic Deposition (EPD) in order to perform thin film coatings¹⁹⁵. By applying a magnetic field coupled with the PLAL synthesis of magnetic particles, they are oriented in the direction of the field and nanochains are formed in an one-step process¹⁹⁶.

In addition, second laser processing may, on purpose or not, interact with the particles in suspension, located in the optical path. The energy deposited on the particles leads to post-irradiation treatment, which leads to shape and size tailoring⁵⁴⁻⁵⁶. LML was extensively studied and used for either reshaping or sintering particles to produce versatile large structures. Nanospheres were obtained after melting and reshaping of nanorods^{53,197}, sintering of smaller nanospheres^{57,58,157,158,198} or more complex structures¹⁹⁹. By increasing the fluence, vaporization may start to remove atoms or small fragments from the particles, yielding to a reduced particle size^{57,158}. At high fluence, Coulombic explosion causes the fragmentation of the particles and the reduction of their size^{27,49,54,55,59}. Temperature and pressure are external parameters that influence intrinsic characteristics of the liquid state as the viscosity, density or compressibility. Applied high pressure has been seen to mainly reduce the bubble size and lifetime that may alter the nanoparticle formation¹³⁹. Supercritical fluid is reached by increasing the temperature and the pressure and one thus produce nanoclusters via a dry process²⁰⁰. Finally, modification of the temperature can perturb the spherical shape of particles. For instance, ZnO nanoparticles transform into nanorods above 60°C¹⁷⁶. It should be mentioned that the content released at the end of the vapor phase is already formed. Hence, the initial nucleation and growth of the nanoparticles during the plasma and vapor phases remain the most important steps to fully understand in order to produce controlled objects.

1.3 PLAL interests in synthesis methods

1.3.1 Advantages

PLAL synthesis method appears in the nineties²⁰¹ and joined the numerous synthesis techniques designed to produce nanomaterials. PLAL has its own advantages compared to chemical or other physical processes. PLAL enables to produce ligand-free surface nanoparticles. Here are classified in different categories the interesting features of PLAL.

Convenience. As described above, the different available set-ups are simple to mount and to use. A fixed laser with its optics are necessary to bring the energetic light beam into a container, as

simple as a beaker, where a bulk target is immersed in a liquid. Even for more complex system such as a liquid flow, the set-up can be designed and mounted once. The exchange of the consumable items is also easy and fast to achieve since only the target and the liquid need to be removed manually. Consequently, this ease-of-use system allows to handle simply and safely the final solution and the nanoparticles compared, for instance, to pulsed laser deposition (PLD) where the particles are generated on a substrate.

One of the great pro of PLAL is to offer the possibility to form and integrate nanoparticles in an one-step process. Functionalization with molecules, proteins, DNA or polymers to produce instantaneously bioconjugate particles has been experimented²⁰²⁻²⁰⁴, as well as embedding directly in an appropriated matrix as polymers to form composites²⁰⁵ or in engine oils for lubricating^{206,207}. PLAL final products have already been used to introduce them directly in a second set-up experiments such as catalysis^{208,209} and electrochemical reactions processes^{193,194}, ICP-AES²³ or SERS²⁷.

Versatile. Thanks to the numerous adjustable parameters, a large range of bare particles can be synthesized according to their size, their shape, their composition and their structure. A wide range of particles size from few nm to several μm has been already achieved. Various solvents were explored from classical aqueous or organic liquids, such as acetone, alcohols, alkene, alkane, to supercritical fluid. Some studies compared the effect of different solvents on the formation of the nanoparticles^{26,38,152,167,183}.

A plenty of material has been explored over the three last decades and covers almost all the periodic table of elements, such as metals^{26,51,181,192,210,211}, alloys including core-shell structures^{159-162,184-186}, magnetic nanoparticles^{212,213}, doped oxides^{169,178,182,214}, semiconductors^{194,215-217}, carbon-based particles^{25,64,218,219}, chalcogenides²²⁰⁻²²², complex stoichiometries^{223,224}, and composites^{196,225-227}. In addition, according to the experimental conditions and parameters, shape can be tuned according to the confinement dimensions of the nanostructures. Some examples are presented in the table 1.1. In 0D particles, spheres are the most synthesized since it is energetically favorable^{160,161,185,186}. Nanocubes^{42,167,179,194,228} and hollow particles^{37,42,199} can be also produced. Nano-rods^{175,176,179,229}, -tubes^{228,230}, -spindles^{176,231} and -chains^{167,196} were generated by use of adsorbates or by oriented attachment process. 2D nanomaterial formation yields to sheets^{179,232}, disks²³³, layers^{175,234}, platelets⁴² and leaves^{191,235,236}. Finally, more complex and exotic structures can be obtained as flower^{193,199,236,237}, tetrapod²³⁷ and tree-like²³⁶ shapes. Of course, the growth and assembly of the lower dimension structures to larger ones are the general mechanism of formation^{167,236}. In addition, crystal phases are tailored using adsorbates¹⁷⁸ and amorphous phase^{154,155} as well as metastable crystal structures^{22,154} of specific size have already been fabricated.

One of the advantages of PLAL remains the high purity of as-produced colloidal solution. Indeed, by avoiding the use of molecular precursors and additive species in the solution, only suspended and naked nanoparticles are obtained without other pollutant. This feature is important for various applications, which will be described in the next section.

Ecology and Health. It is well-known that the nanoparticles have a bad effect on health and environment due to their size where almost no living organic barriers can stop them. Inhalation of nano-size aerosols is the main cause of important damages in a living body²³⁸⁻²⁴⁰. Therefore, the production of aerosols is extremely dangerous. Thanks to the confinement with the liquid media, PLAL is thus an one-step process that allows a safer generation of nanostructures directly embedded in a liquid or even solid matrix.

The actual environmental problems lead to revise the synthesis production of products, especially in the chemistry. Green Chemistry emerged at the beginning of the 1990s and is defined as "*the design of chemical products and processes to reduce or eliminate the use and generation of hazardous substances*"²⁴¹. 12 based-principles have been set to determine if a synthesis method can be considered as a green process. The PLAL technique appears to validate all these principles and is considered conform as green synthesis. The main advantages of ablation in liquid is the ability to perform synthesis with no precursors that may be toxic and generate waste. Bulk target is lesser dangerous and toxic than molecular precursors and the possible unablated material during the PLAL process can be retreated by second laser processing afterwards to reduce residues.

Economically. The convenient set-up as well as the simple consumable items make ablation in liquid affordable. Bulk target cost is usually lower than molecular active agents, used for instance in wet-chemical synthesis. Without using precursors in the synthesis, only the liquid and the bulk target are used and less consumable items are necessary, reducing thus the cost of a synthesis. PLAL is a long-term viable method, where the high investment on the laser and optical systems is compensated in a long time run, depending on the productivity yield²⁹. According to Jendrzej *et al.*²⁴², PLAL becomes economically interesting for a productivity yield higher than 500 mg/h in the case of gold nanoparticles (Fig. 1.10(d)).

1.3.2 Improvements

Unfortunately, the fabrication of surfactant-free nanostructures makes difficult the control of the size and morphology of the particles. As seen above, PLAL final products show a broad polydispersity, which is an important issue in order to compete with monodispersed and size controlled nanoparticles synthesized by the chemical techniques. Kabashin *et al.* studied the size distribution of gold colloids produced with a femtosecond laser as a function of the fluence⁵¹. They showed that narrow and almost monodispersed particle size can be obtained at low fluence while at high fluence, a broad distribution was measured. Between the two fluences, a bimodal distribution reveals the transition between two ablation regimes. Moreover, the crystal structure as well as the composition of the final objects are difficult to tailor since the extreme thermodynamic conditions of the ablation cause complex chemical reactions and structural modification. As a result, the composition and crystal phase of the nanoparticles are not necessarily those of the target. Undesired

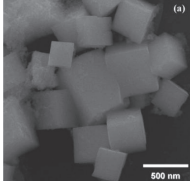
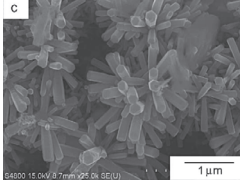
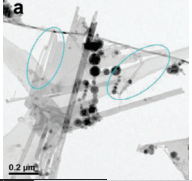
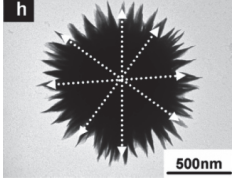
Dimension	Morphology	Material	Images
0D	Spheres Hollow Cube	Ag/Cu ¹⁶⁰ , Fe/Au ¹⁶¹ , PdCu ¹⁸⁶ , CoPt ¹⁸⁵ MgO ⁴² , Al₂O₃ ³⁷ , Fe₁₉Ni₈₁ ¹⁹⁹ , Mn₃O₄ ¹⁷⁹ GeO₂ ¹⁹⁴ , AgCl ⁴² , Te ¹⁶⁷ , [PbS, NiO, MgO, Ag₂O] ²²⁸	
1D	Rods Tubes Spindles Chains	ZnO ¹⁷⁶ , Mg(OH)₂ ¹⁷⁵ , CN ²²⁹ , Mn₃O₄ ²⁴³ PbS ²²⁸ , BN ²³⁰ ZnO ¹⁷⁶ , GeO₂ ¹⁹⁴ , CuO ²⁴⁴ Fe₃C ¹⁹⁶ , Te ¹⁶⁷	
2D	Sheets Disk Layers Plates Leaf	Ag ²³² , Mn₃O₄ ²⁴³ Au/Ag ²³³ Zn(OH)₂ ¹⁷⁵ , AgBr ²³⁴ Ag₂O ⁴² ZnO ²²⁹ , CN ²³⁶	
3D	Flower Tetrapods Tree	CN ²³⁶ , Cd(OH)₂ ²³⁷ , Zn(OH)₂ ¹⁹⁹ , CuVO₇ ¹⁹³ Cd(OH)₂ ²³⁷ Zn/ZnO ²³⁶	

Table 1.1 – Examples of nanoparticle shapes. Pictures refer to the materials and references indicated in bold.

crystal structure, metastable or amorphous phases can be obtained as well as heterogeneous particle assemblies of different phases, compositions and morphologies. In addition, defects, failures or extraneous elements usually perturb the particles surface. Hence, the stability of the colloidal solution might not be guarantee.

Solutions have been experimented to overcome these drawbacks. The use of adsorbates, as ligands or complexing ions, is one of the most improving method to stabilize and control the nanoparticle solution, as described previously. Quenching induced by ligands or ions at the early stage in the plasma and bubble phases allows to reduce drastically the size. An example of size quenching of Y_2O_3 nanoparticles by organic ligands is shown in figure 1.10(a). Colloidal stability is also reached thanks to steric or electrostatic repulsion. Surface chemistry state is thus tailored by the choice of the adsorbates. They can modify the charge state as well as the active sites of the surface. Second laser processes have been also extensively studied as an effective method to control the particle characteristics: reshaped and resized are achieved by LFL and LML. According to the experimental set-up, the ablation and residence times¹⁷⁹ as well as the flow of the liquid²⁴⁵ play a role on the solution.

Productivity yield is certainly the second important drawback. While the spray pyrolysis method has a productivity rate of hundreds of gram per hour²⁴⁶, PLAL productivity rate needs to be improved in order to be competitive. While ablation in liquid was a young and in-development method in nineties, an important breakthrough improved PLAL to industrial scale. Barcikowski's group developed a research branch dedicated to the upgrading of the productivity yield. Recently, gram-scale synthesis was performed continuously, using a high power and a high repetition rate ultrafast laser. From 2010 to 2016, production rate was enhanced from 1.3 to 4 g/h and thus reaching the multigram-scale synthesis^{36,37}. Streubel *et al.* published two articles where they achieved 4 g/h productivity yield for platinum⁴⁰ and a production yield above 1 g/L for Au, Ag, Al, Cu and Ti³⁶ (shown in figure 1.10(b)). They performed synthesis of these different elements for one hour, using a 500 W high power, 10.1 MHz high repetition rate and 3 ps laser. The main issue to reach such high production rate is that the usual slow laser motion compared to the repetition rate induces a screening of the previous bubble with the next pulse. The energy beam is absorbed by the remaining bubble on the target and the amount of removed matter is thus reduced. To overcome this difficulty, a high-speed scanner composed of a galvanic mirror and a polygon mirror scanning system was developed to reach a speed of almost 500 m/s in order to move the laser beam faster than the repetition rate. However, this system is still limited by the slower horizontal galvanometric mirror. Scheme of the set-up is displayed in figure 1.10(c). A liquid flow with a rate of 330 mL/min was chosen in order to avoid screening with the blocked bubbles in the chamber and a plausible re-irradiation process^{39,247}. The colloidal solution contained Pt nanoparticles with a size distribution narrowed at around 7 nm. Such progress in nanoparticle production is promising for the future of PLAL in the industry.

The expensive cost of the laser system is also important to take into account. The investment on such equipment can be an obstacle to the PLAL perspective, but as discussed in the pros section, this cost can be absorbed in a long-period run (Fig. 1.10(d)).

Despite all these advanced works, a general disadvantage is the unclear understanding of several aspects during the ablation process. As mentioned above, the main research work should be addressed to clarify the nucleation and growth processes of the nanoparticles during the successive stages. In addition, all the different parameters, optical in one side and material in the other, prevent to the numerous research groups to follow an universal procedure as well as to obtain reproducible and repeatable results.

1.3.3 Applications

Development of novel synthesis routes as PLAL, which bring new advantages, opens up new and exciting possibilities to tailor the chemical and physical properties of nanomaterials in order to improve or design applications.

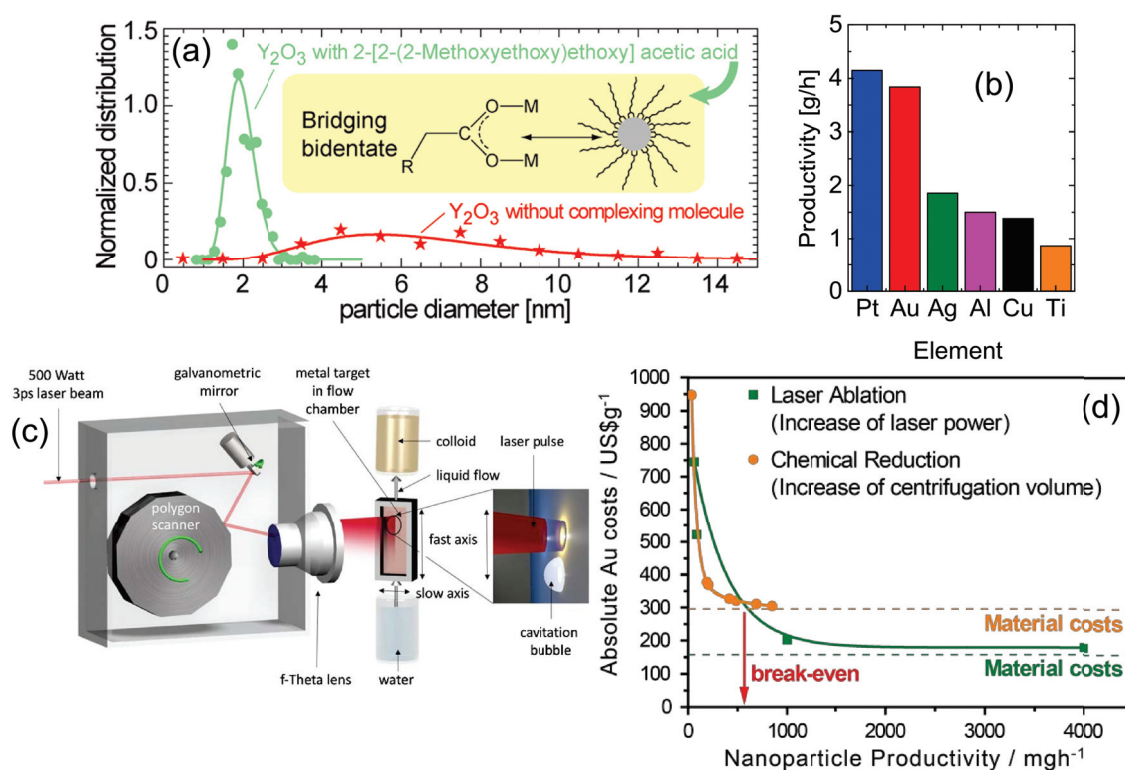


Figure 1.10 – (a) Quenching effect of organic ligands on Y_2O_3 nanoparticles size distribution (Reprinted from ¹⁶⁹). (b) Metal nanoparticles produced with a gram-per-hour rate using (c) a multi-gram continuous set-up developed by Streubel *et al.* using a high-speed scanner and high power laser (Reprinted from ³⁶). (d) Absolute manufacturing and labor costs per ablated mass relative to the productivity yield of gold nanoparticles synthesized by PLAL in water and chemical reduction (Reprinted from ²⁴²).

The main advantage of PLAL is the possibility to obtain ligand-free nanoparticles. Their reactive surface, combined with a high purity of the final product, allows to enhance the performance of numerous applications. Catalysis is, of course, the first application where free surfaces are needed for a maximum of efficiency and where the ligand-free products show a better catalytic performance than the chemical capped particles^{208,248}. Zhang *et al.* compared the catalytic efficiency of an alcohol and the CO molecule by coupling gold nanoparticles made by PLAL or by standard chemical process on CeO_2 nanorods²⁴⁸. Kinetics of reaction were 5 to 10 times higher for the PLAL nanoparticles than for the chemical counterparts. In addition, the carbonization of organic solvent, which creates a carbon shell around inorganic nanoparticles, contributes also to the enhancement of the catalytic reaction¹⁸⁷. In analytical chemistry methods, the ratio signal-to-noise is increased by naked nanoparticles in the case of SERS²⁴⁹. In biomedicine, the free surface of the nanoparticles enables to enhance the MRI imaging combined with a low toxicity²⁵⁰. The PLAL nanoparticles were also incorporated in solar cells to promote photo-conversion since ligands quench excitons according to Kymakis *et al.*²⁵¹. In the same study, they showed that capped nanoparticles in solar

cell matrix allows the same photo-conversion yield than without ligands. Similarly, efficient *in situ* or *ex situ* functionalization with any bio-molecules can be performed to obtain selective sensors according to the surface-chemistry sensitive environments²⁵² and to be used in biological or medical applications.

For some PLAL nanostructures, the surface charge is naturally high and their colloidal stability is maintained through electrostatic forces. Due to electrostatic attraction, high adsorption efficiency is reached and particles are used, for instance, for pollution decontamination²⁵³. Coupled with an electric field in electro-phoretic deposition process, electrodes or thin films may be coated and used in various applications, such as electrochemical detection²⁵⁴ or long-term neural activity record²⁵⁵. As-produced PLAL-generated nanoparticles can contain a large amount of defects, which facilitate photoluminescence emission, useful in optical devices²⁵⁶ and in photocatalyze process for pollutant degradation²⁵⁷.

Finally, numerous applications have been explored for the integration of PLAL nanoparticles. The main ones are related to the fields of magnetism, optics and plasmonics, biology and medicine, catalysis and energy as well as environment protection²⁹. With this scalable and multivalent process, the as-produced nanomaterials will be integrated in any industrial applications in order to improve the desired chemical or physical properties. Consequently, industry has shown interest in PLAL and its derivatives with the creation of three start-ups, Particular GmbH (Germany), i-Colloid in-house branch of IMRA (USA) and Hamamatsu Nanotechnology (Japan). The distributor Strem Chemicals, Inc. (USA) sells PLAL-generated colloidal solutions. For instance, colloidal solution of metals such as Au, Ag, Pt and Ti are prepared by Particular GmbH at different concentrations in several solvents and with particles sizes either below 20 nm or between 50 and 70 nm.

1.4 Conclusion

Pulsed Laser Ablation in Liquid is a physical way to synthesize a plenty of different nanoparticles according to their composition, shape, crystal phase and size. This convenient, simple and scalable process hides complex physico-chemical mechanisms, which are related to numerous experimental parameters. Several advantages are reported to overcome issues coming from other synthesis routes and hit the interest of industry. Ligand-free nanoparticles are the most attractive feature in this method, however, a high productivity yield combined with a monodispersed and adjustable size has, for now, not been achieved.

To improve the synthesis of nanomaterials, the understanding of the nanoparticles formation and reaction with their environment have been challenging in the last previous years. We saw that the gas phase is the longest stage of the ablation process where nanoparticles are already introduced from the plasma. Important progress was made to analyze the plasma and bubble dynamics and to probe their content.

In parallel, studies have reported that the addition of adsorbates in the solution before the ablation

process leads to a better control of the colloidal stability and the particles crystal structure. Yet, the effects of such ligands during the reaction are not fully understood yet. These different features will be investigated in the following by using ions and ligands as examples of stabilizing agents for gold colloids and nano-rubies synthesis, respectively.

CHAPTER 2

DYNAMICS OF GAS BUBBLES

Contents

2.1 Bubble dynamics monitoring by shadowgraphy	39
2.1.1 Shadowgraphy technique	39
2.1.2 Dimensionless numbers	40
2.1.3 Thermodynamic parameters	42
2.2 Fluence dependency	45
2.3 Viscosity influence	49
2.3.1 Geometrical shape	50
2.3.2 We , Re and Ca numbers	51
2.3.3 Bubble spreading power laws	52
2.3.4 High capillary numbers dynamics	54
2.4 Conclusion	58

As described in the chapter 1, after an initial stage of nucleation and growth of a few microseconds, the laser-generated nanoparticles are trapped in a cavitation bubble during a few hundreds of μs . Primary nanoparticles spend a long time with respect to the characteristic time of their generation in the bubble, which can be considered as a "reactor". The dynamics of the bubble can influence the aggregation and the maturation of the particles. Tomko *et al.* observed a relation between nanoparticles size and the maximum radius and lifetime of bubbles¹³⁶. Hence, the dynamics of the bubble shape can give information about thermodynamic conditions, influencing nanoparticles formation. However, SAXS experiments have shown that most of the bubble content is ejected in the solution after the first collapse¹³⁷. They have also shown that the nanoparticles are formed at the early stage of the bubble. Therefore, we have focused our work on the first oscillation of the laser-generated bubble. Effects related to the fluid compressibility can be ignored and simple model used as we will show.

Historically, our group has developed a shadowgraphy technique set-up to record the bubble dynamics and deduced the thermodynamic conditions during the lifetime of the bubbles. In particular, they deduced that the bubble is essentially composed of the molecules of the solvent compared to the ablated matter¹³². The team has also aimed at characterizing the thermodynamic path experienced by matter inside the bubble (temperature/pressure/density) as well as the extreme conditions reached during the collapse. Thanks to these former studies, we became aware that the conditions, and more specifically the very short time scale of the processes, are intrinsically relevant for the field of fluid mechanics. Even if the issue remains tightly linked to laser generation of nanoparticles in liquids, we will mainly reported in this chapter experiments devoted to original condition for the field of fluid mechanics, *i.e.* highly viscous liquids leading to huge capillary numbers. This study has been conducted in the framework of a collaborative project with the Barcikowski's group of the Essen-Duisburg University. Barcikowski's group aims to produce well controlled colloids to reach the fine chemicals market and the industrial applications. The one-step synthesis of nanoparticles in engine oils, including highly viscous polyolefins, would be a breakthrough. Nanoparticles as additives in engine oil are relevant for engineering industry. For example, nanoparticles are often used to enhance the tribological properties of the lubricant in the automotive industry^{258,259}. However, it is still mostly unknown how viscosity and surface tension influence shape, lifetime and size of the laser-generated bubbles.

In this chapter, laser-induced cavitation bubbles are captured using shadowgraphy technique and an ultra-fast camera. After a description of the experimental set-up and the theoretical tools, bubbles are studied according to the injected laser energy as well as the solvent viscosity. In the case of low viscosity, the thermodynamic conditions are investigated by solving a simplified Rayleigh-Plesset equation. Then, hydrodynamic regimes are evaluated in order to clarify the forces that drive the bubbles motion according to the experimental conditions. While at low viscosity, the inertial

forces drive the vapor system, an increase of the viscosity leads to a drastic increase of the capillary number Ca , which indicates a change of regime to a domination of viscous forces. Interestingly, our systems at high capillary numbers cannot be interpreted with models from fluid mechanics.

2.1 Bubble dynamics monitoring by shadowgraphy

2.1.1 Shadowgraphy technique

The shadowgraphy system was designed to capture the shadow of the bubble induced by a vertical ablation laser beam on a horizontal target (Fig. 2.1). A small vessel is filled with 6 mL of a static liquid. The vessel is moved using a XY translation stage. The immersed target is fixed in the bottom of the vessel in order to get around 1 cm of liquid thickness above the solid surface. The laser beam is initially expanded by a lenses system and passes through a selective optical density filter to control the injected laser power. Finally, the beam is focused on the target surface thanks to a 15-cm convergent lens moved by a vertical translation stage.

The light source was first carried out by a continuum HeNe laser (632.8 nm, P=13 mW) coupled with lenses and a diffuser in order to obtain a large and homogeneous bright background. However, the homogeneity of the background was not completely achieved since the diffuser is pixelised, as can be seen in bubble images in figure 2.1. For this purpose, we replaced the continuum laser by a pattern of ultra-bright white LEDs. A perfect light and homogeneous source was thus obtained (see bubbles images in figure 2.5).

To record the bubble shadow, an ultra-fast camera (Phantom v711 from Vision Research) coupled with a zoom lens system (Zoom 6000 from Navitar) collects images at high frame rate. This rate depends on the resolution of the image view and the exposure time. In the following results, different image resolutions were recorded between $128 \times 128 \text{ px}^2$ and $256 \times 128 \text{ px}^2$, leading to different time intervals and frame rates comprised between 4.6 and $6.7 \mu\text{s}$, and 215 800 and 150 000 frames per second (fps), respectively. Such speed of recording enables to track bubble dynamics since its lifetime is a few of hundreds of μs . The magnification of the optical system of the Zoom 6000 is 0.65. According to its performance specification, the resolution limit of the optical assembly is then $31 \mu\text{m}$, which also corresponds to the image of a single pixel ($20 \mu\text{m}$ in size divided by the magnification). It leads to an overall resolution of $44 \mu\text{m}$ ($\sqrt{2} \times 31 \mu\text{m}$). The camera and the laser are both triggered externally. The temporal resolution of the trigger is 5 ns, which has no consequences on the overall time resolution regarding the frame rate.

Finally, two ablation laser systems were used as mentioned in figure 1.1. The first one is a UV beam ($\lambda = 355 \text{ nm}$), using the third harmonic of a 5-ns Nd:YAG laser. The laser energy reaches a maximum of 36.7 mJ/pulse. The second laser system is dedicated to the nanoparticle synthesis thanks to its high repetition rate of 1 kHz. In the near-IR range ($\lambda = 1064 \text{ nm}$), its energy per pulse is 2 mJ/pulse with a pulse duration of 500 ps.

For a selected material and laser system, statistics are performed on series of several individual laser-generated bubbles. An example of bubble snapshots is shown in figure 2.1 in the case of Gd_2O_3 ablation, using the UV system. Recording characteristics are described in the figure legend. In a multipulse process, secondary cavitation bubbles may be produced in the surrounding of particles located in the laser path, in addition to the absorption and scattering of the incident beam. They usually perturb the geometry and the dynamic of the primary bubble at the target surface, and make difficult the image treatment. Moreover, matter deposition on the target has also an impact on the bubble dynamics. Hence, the liquid was replaced by fresh one and the target cleaned between each series, and only the first bubble was recorded.

Depending on the material and the laser power, the size of bubbles varies and for a better image treatment, the magnification of the optical system is tuned accordingly. Images are thus calibrated with a scale for every series. As shown in figure 2.1, the first image bounded by a red square serves as a calibration in the treatment process before the first laser impact. The second image is marked by the presence of the confined plasma between the liquid and the target, and corresponds to the starting time, $t = 0 \mu\text{s}$. The third image shows the first bubble image. The following images show the bubble dynamics from the growth to the collapse with the corresponding time on the top of each picture. Even if the successive collapses and rebounds could be interesting for what concern the material removal and the nanoparticles productivity, as described in the last chapter, I will only focus on the first bubble.

2.1.2 Dimensionless numbers

The collected images were analyzed automatically by a Python code I developed. The automatic data processing is able to extract and to fit the contour of the bubble shape and to compute geometrical parameters image per image. Figure 2.2 displays results of the bubble contour processing and lists the calculated parameters used for bubble analysis. During growth and shrinking stages, the bubble shape may change. As we will see below, the bubble can have either a hemispherical geometry or a two-part shape composed of a spherical cap at the top of the bubble and a conical interface layer close to the target foot, leading to an apparent rim (Fig. 2.2(a)). The cap is characterized by its height, which remains equal to the radius of curvature and will be referred as the bubble radius R in the following. Regarding the interface layer, its footprint radius x is used to quantify the bubble progression and recession on the target and will be called the bubble foot. The interlayer has also a variable thickness e , which corresponds to the rim height. We also focused on the three-phase contact line looking at its angle and velocity. The contact angle is defined in figure 2.2(a) (The convention is consistent with the one used for droplet, *i.e.* $\theta = 0^\circ$ corresponds to perfect wetting). In the case of bubbles presenting a clear interface layer, the horizontal radius of the rim L can also be determined. In order to easily calculate these geometrical parameters, the contour is fitted as illustrating in the inset of figure 2.2(b). An equation of a hemisphere combined with two straight lines allows to fit any shapes.

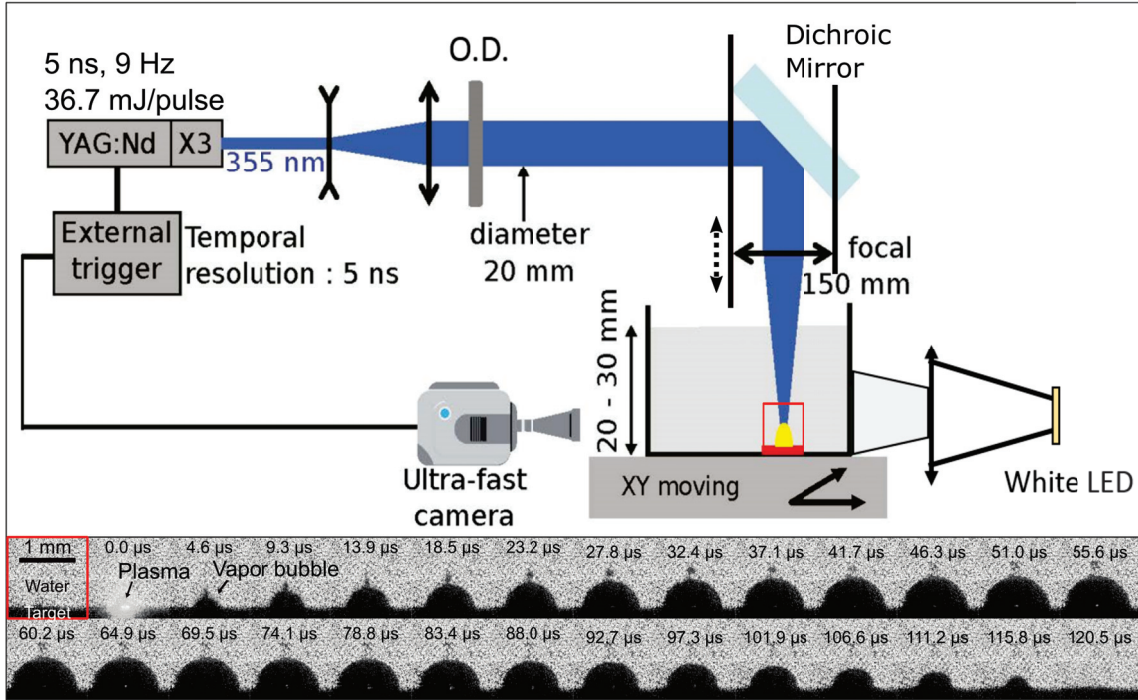


Figure 2.1 – (Top) Scheme of the shadowgraphy set-up mounted with the UV ablation laser system to capture (bottom) images of the bubble dynamics in the frameworks of Gd_2O_3 ablation. Resolution of each picture is $128 \times 128 \text{ px}^2$ and the exposure time is $4.63 \mu\text{s}$, corresponding to a frame rate of 215 800 fps. The time delay from the laser pulse is displayed on each snapshot.

From these different geometrical parameters, dimensionless numbers used in fluid mechanics can be calculated. Indeed, by following the bubble dynamics at the top of the bubble, the rim edge and the interlayer foot, local velocities are obtained and referred as V_t , V_e and V_{cl} , respectively (displayed in figure 2.2(a)). Weber (We), Reynolds (Re) and Capillary (Ca) numbers are quantities used to compare forces that compete and then identify which ones are driving the dynamics. Their expressions are given in equation 2.1. We corresponds to the ratio between the surface tension forces and the inertial forces. γ corresponds to the surface tension, ρ to the solvent density. V refers to the velocity of the bubble, namely V_t , V_e and V_{cl} , calculated from the length X , which corresponds to their respective radius, R , L and x . Re compares inertial and viscous forces characterized by the dynamic viscosity η . Finally, Ca evaluates the balance between the surface tension and the viscous forces.

$$We = \frac{\rho X V^2}{\gamma} \quad Re = \frac{\rho X V}{\eta} \quad Ca = \frac{\eta V}{\gamma} \quad (2.1)$$

As an example, figure 2.3 presents the evolution of these different parameters calculated during gadolinia ablation. 33 bubbles were analyzed and one of these bubbles is shown in figure 2.1. For

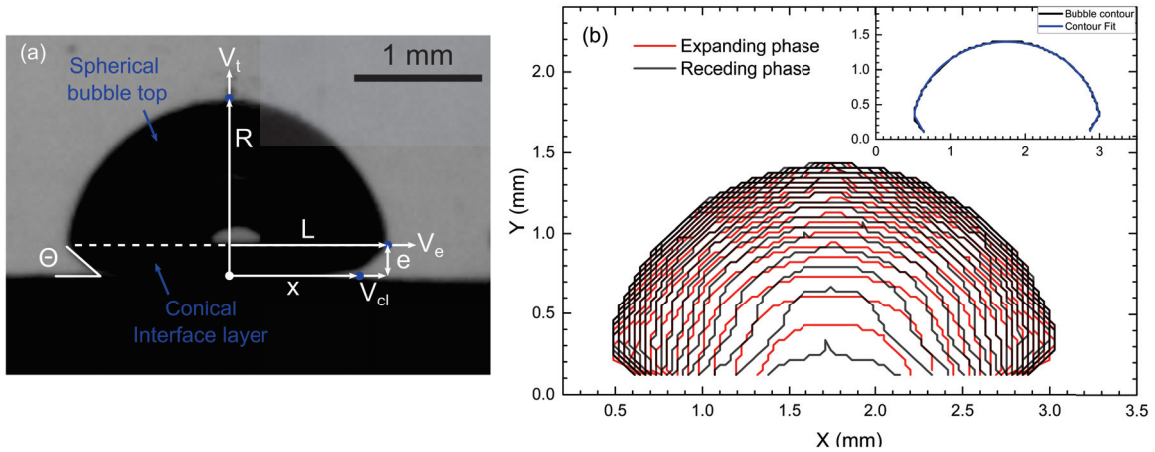


Figure 2.2 – The automatic data processing provides (a) geometrical parameters for each bubble by (b) fitting its contour.

each bubble, the radius R is plotted with respect to the time in figure 2.3(a). Radii vary between about 0.2 and 0.6 mm while the lifetime of the bubbles evolves from about 100 to 150 μs . By normalizing the time for each bubble by its lifetime, we can see that the velocity of the bubbles and the three numbers are quite similar for all the studied bubbles, emphasizing the reproducibility of the dynamics even if there is a large uncertainty on the bubble lifetime.

2.1.3 Thermodynamic parameters

Several models have been used in the past years to predict the laser-induced bubble dynamics in PLAL. The Gilmore model is one of the most comprehensive model since it takes into account the compressibility of the liquid necessary to describe the rebounds after the first bubble oscillation²⁶⁰. However, we are only interested in the first oscillation because: (i) the nanoparticles are mainly released after the first collapse, and (ii) information about the ratio between the ablated matter and the vaporized solvent (*i.e.* bubble composition) can be obtained from the dynamics of the first bubble¹³². Therefore, we chose the Rayleigh-Plesset (RP) equation that appears more relevant and easier to solve, and describes perfectly the first bubble dynamics. The RP model described the movement of a liquid-gas interface for a given pressure difference between the gas pressure and the liquid pressure. Solving RP equation can then give insight on the inner pressure in the bubble. This was our main goal.

Initially, the RP model has been developed to consider the liquid point of view in the sense that the composition of the vapor bubble is not taken into account. The bubble dynamics are thus driven by the liquid characteristics. Some assumptions are provided concerning the liquid and the bubble. The liquid is considered infinite with a pressure $P_L = P_{\text{inf}}$, and incompressible. The bubble is assumed spherical and homogeneous with a pressure P_B . Between the two phases, no mass transfer is also

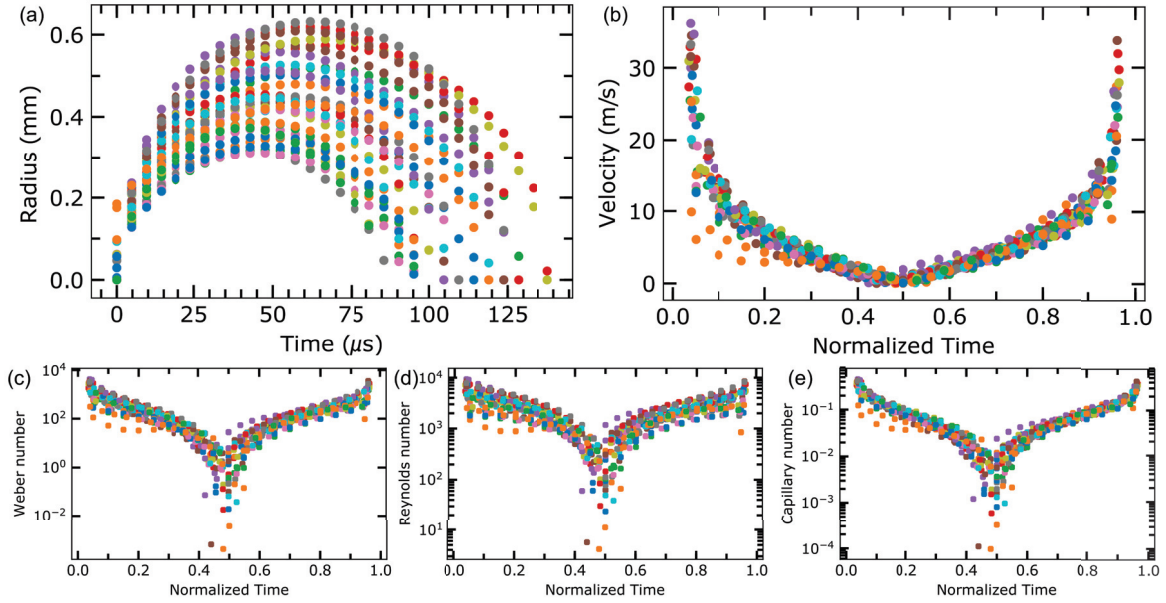


Figure 2.3 – (a) Radius of $^{33}\text{Gd}_2\text{O}_3$ laser-generated PLAL bubbles in water as a function of time. (b) Velocity of the cap, (c) We , (d) Re and (e) Ca quantities were calculated as a function of time. For each bubble, the time is normalized with respect to its lifetime.

assumed. The evolution of the bubble is similar to that made in PLAL since the growth and collapse reveal a volume change through oscillations. However, the two systems differ in several points. The main difference is the presence of the solid target. The nascent bubble expands and leads to a hemispherical shape. Since the ablation processes eject solid particles and vaporize solvent molecules, the homogeneity of the system is not guaranteed. Soliman *et al.* proposed first to introduce the Rayleigh-Plesset equation in the case of PLAL bubble²⁶¹. By taking into account the limitations of the model in the case of PLAL, they successfully described the size dynamics of the bubble, as well as pressure and temperature thermodynamic parameters. In the case of low viscous solvents such as water, our group suggested a simplified RP equation thanks to appropriated assumptions^{32,132}. The development of the simplified RP equation begins with the complete RP model, which is demonstrated elsewhere³²:

$$R\ddot{R} + \frac{3}{2}\dot{R}^2 = \frac{1}{\rho} \left(P_B - P_L - \frac{2\gamma}{R} - \frac{4\eta\dot{R}}{R} \right) \quad (2.2)$$

The inertial term at the left of the equation competes with the last terms, including Laplace pressure and the viscous forces. As seen in figures 2.3(c) and (d), in water, We and Re numbers are in the range of 10^2 and 10^3 , respectively. With such high values, inertial forces are thus favored compared to the considered forces, *i.e.* the surface tension for the former and the viscosity for the latter. The system is driven by inertia and the Laplace pressure and the viscous forces can be neglected. RP equation is then simplified:

$$R\ddot{R} + \frac{3}{2}\dot{R}^2 = \frac{P_B - P_L}{\rho} \quad (2.3)$$

Moreover, the system is assumed isentropic, *i.e.* without energy and mass exchange with the liquid. The mass transfer was already neglected in the initial RP model. In addition, as shown in figure 2.3(a), the bubble evolves symmetrically with respect to time, as expected for an isentropic process. The energy conservation can be estimated by comparing the possible dissipated energy with the injected energy. The heat transfer from the bubble to the liquid media is mostly driven by convection. The transferred power is calculated from $\Phi = hS_B\Delta T$, with $h = 100 \text{ W.m}^{-2}.\text{K}^{-1}$, $S_B = \pi R^2 + 2\pi R^2$ and $\Delta T = T_B - T_o \approx 10^3 \text{ K}$. With a radius in the range of a millimeter, the transferred power is estimated at around 0.9 W. For a bubble lifetime of $10^2 \mu\text{s}$, the energy dissipated is about 0.09 mJ for one pulse. This is far below the 36.7 mJ/pulse of the laser source. Consequently, the system is considered adiabatic and the bubble process isentropic. By taking the bubble as an ideal gas, the thermodynamic Laplace's law is given by:

$$P_B = \frac{C}{R^{3\gamma_h}} \quad (2.4)$$

where C is a constant and $\gamma_h = \frac{C_p}{C_v}$ is the heat capacity ratio between the isobaric heat capacity C_p and the isochoric heat capacity C_v . The isentropic system assumption is validated by the linearity of the logarithm form of the relation 2.4, $\ln P_B = \ln C - \gamma_h \ln R^3$, leading to values of γ_h consistent with theoretical values¹³².

In order to integrate equation 2.3, the left inertial part is modified in order to suppress the second derivative, and P_B is replaced by expression 2.4:

$$\begin{aligned} \frac{1}{2R^2\dot{R}} \frac{d(R^3\dot{R}^2)}{dt} &= \frac{1}{\rho} \left(\frac{C}{R^{3\gamma_h}} - P_L \right) \\ \frac{d(R^3\dot{R}^2)}{dt} &= \frac{2}{\rho} (CR^{2-3\gamma_h}\dot{R} - P_LR^2\dot{R}) \end{aligned} \quad (2.5)$$

This last relation is integrated with respect to time and leads to calculate the bubble pressure P_B :

$$\begin{aligned} R^3\dot{R}^2 &= \frac{2}{\rho} \left(\frac{C}{3-3\gamma_h} R^{3-3\gamma_h} - \frac{P_LR^3}{3} \right) + K \\ \dot{R}^2 &= \frac{2}{3\rho} \left(\frac{P_B}{1-\gamma_h} - P_L \right) + \frac{K}{R^3} \\ P_B &= (1-\gamma_h) \left(P_L + \frac{3\rho}{2} \left(\dot{R}^2 - \frac{K}{R^3} \right) \right) \end{aligned} \quad (2.6)$$

The integration constant K is thus determined at $\dot{R} = 0$, *i.e.* at the bubble maximum radius R_{max} , which reduces equation 2.3 as $P_B = \rho R_{max}\ddot{R}_{max} + P_L$. Finally, by using the second relation of equation

2.6, K is found to be equal to:

$$K = \frac{-2R_{max}^3}{3\rho} \left(\frac{P_B}{1 - \gamma_h} - P_L \right) \quad (2.7)$$

$$K = \frac{2R_{max}^3}{3(\gamma_h - 1)} \left(R_{max}\ddot{R}_{max} + \frac{\gamma_h P_L}{\rho} \right)$$

The bubble pressure is thus calculated through the last relation in equations 2.6 where only the first derivative is necessary to compute P_B . This is an advantage if few points are recorded due to the camera frame rate. For this purpose, direct fits of R^2 and R^3 are carried out with polynomial regressions. From mathematical differentiation, \dot{R} is computed, as well as \ddot{R}_{max} . Since we considered the system as an ideal gas, the temperature T_B and the number of molecules in the vapor N_B can also be estimated thanks to the isentropic relation and the ideal gas relation, respectively:

$$\frac{T_B}{T_o} = \left(\frac{P_B}{P_o} \right)^{\frac{\gamma_h - 1}{\gamma_h}} \quad P_B V = N_B k_B T_B \quad (2.8)$$

with T_o and P_o , the initial temperature and pressure à $t = 4.75 \mu s$, V the bubble volume and the Boltzmann constant $k_B = 1.38 \cdot 10^{-23} \text{ J.K}^{-1}$.

The pressure and temperature for laser-generated bubbles in water were calculated and are plotted in figures 2.4(a) and (b), respectively. The target is gadolinia. Their profiles appear symmetric, similar to the bubble radius dynamics displayed in the inset of figure 2.4. Extreme conditions are present at the early stage of the bubble growth. These hundreds of bar and thousands of kelvin decrease until reaching ambient conditions at the maximum size of the bubble. The sudden collapse is then characterized by a recovering of the initial extreme values of pressure and temperature. The temporal profiles and the values of these thermodynamic quantities are in agreement with previous studies, performed with various experimental conditions and material ^{119,132,135,136}.

2.2 Fluence dependency

As described in the first chapter, the laser power is one of the main parameters that influences the ablation dynamics, especially the vapor bubble. Indeed, by injecting an increasing energy in the system, more energy is transferred into the liquid during its interaction with the plasma. Several studies have deduced from bubble analysis that the size and the lifetime are increased with the laser fluence ^{136,262–264}. Reich *et al.* ²⁶³ investigated bubble dynamics from 1 to about 200 J/cm² and noticed a linear increase of the bubble volume after crossing a threshold at 40 J/cm². However, all these works focused on the geometrical and thermodynamic quantities evolution and do not address the hydrodynamic of the bubble during ablation. In the following work, both thermodynamic and hydrodynamic parameters have been determined according to the deposited fluence on target

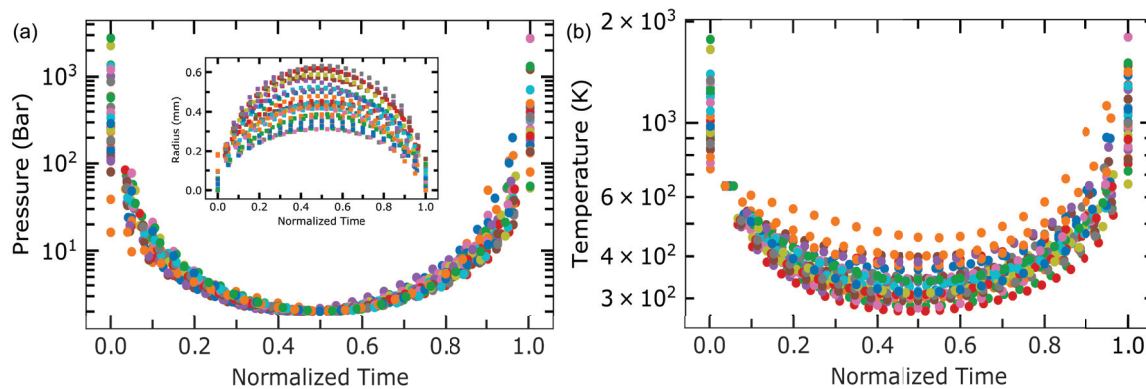


Figure 2.4 – (a) Pressure and (b) temperature profiles of 33 laser-generated bubbles in water calculated from the modified RP equation 2.6 as a function of normalized time. The target is gadolinia. Inset shows the bubble height dynamics.

immersed in water.

The UV laser was used due to its higher power, allowing to tune more easily the fluence. Gold target was ablated at 26.0, 7.6 and 2.4 mJ/pulse, which correspond to fluences of 49.0, 14.3 and 4.5 J/cm² with a spot size measured at 260 μm . Each ablation will be referred as Au_50, Au_15 and Au_5, respectively. A target of yttrium-iron-garnet (YIG), Y₃Fe₅O₁₂, was ablated with the same fluence than Au_15 in order to compare the two target materials and will be noted YIG_15. For each ablation, three bubbles have been recorded with a resolution of 128 x 128 px², a frame rate of 210 000 fps and a time interval of 4.76 μs .

Figure 2.5 shows the bubble sequences for each sample, ordered as a function of the laser energy. The yellow squared images show the collapse of the first bubble. The enhancement of the bubble size and lifetime due the increasing energy can be clearly seen from these snapshot sequences. The bubbles shape remains hemispherical in water for the whole dynamics until the last step of the shrinking stage. Size of the highest bubbles, indicated by green squares, decreases from top to bottom sequences with the lowering ablation energy, as well as the time of these maximum bubbles. This trend is quantified in figure 2.7(a) by plotting the bubble radius and in figure 2.6 by showing bubbles lifetimes as a function of their respective maximum radius. Their lifetimes can also be easily compared with the bar graph, placed in the left-top inset of figure 2.6. Ablations of gold at different energies show an increase of the bubble radius from 1 mm for Au_5 to about 2.5 mm for Au_50, corresponding to a longer lifetime from almost 200 μs to 400 μs . The bubble generated during the YIG ablation is found to be larger (+ 0.3 mm) and longer (+ 50 μs) than the Au_15 bubble, for a same energy. Size increase is also visible when volumes are calculated (right-bottom inset in figure 2.6). From low to high energies, volumes increase by two orders of magnitude from around 0.2 mm³ to 12 mm³.

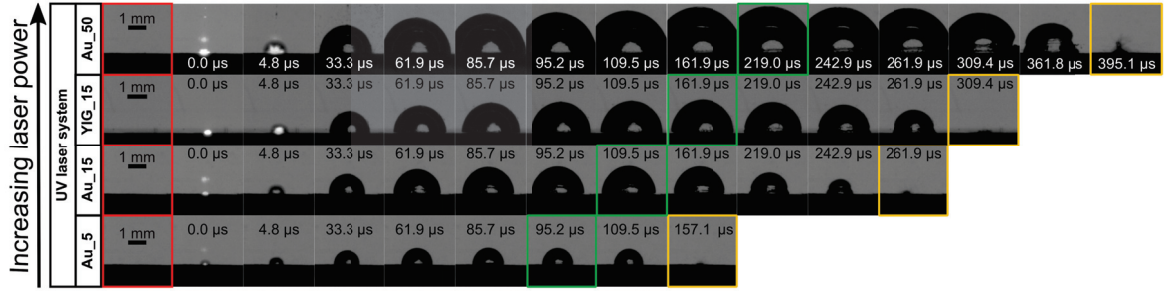


Figure 2.5 – Snapshot sequences of one bubble of each ablation condition, ordered by increasing laser energy. The red squared pictures is the last picture before ablation, green squares show the maximum radius of each bubble and yellow squares show the first collapse of the bubble.

Theoretically, the Rayleigh Collapse Time (RCT) is derived from the complete Rayleigh-Plesset equation, which describes the collapse of a cavitation bubble in an incompressible liquid. It corresponds to the collapse time duration from a maximum size R_{max} . As PLAL bubble follows a two-stage process, *i.e.* growth and collapse, the RCT needs to be doubled in order to compare RCT prediction with the measured bubble lifetime: $t_{RCT} = 2 \times 0.915 R_{max} \sqrt{\frac{\rho}{P_L}}$ with the liquid density $\rho = 10^3 \text{ kg.m}^{-3}$ and the external pressure $P_L = 101 \text{ kbar}$. The linear curve in figure 2.6 shows the evolution of the RCT as a function of the bubble maximum size. Experimental values agree with their calculated counterparts, at least for the low fluence. At the highest fluence for Au_50, the bubbles are shorter by almost $50 \mu\text{s}$. Therefore, the agreement with the RCT, despite the fact that the experimental system differs from the theoretical one, confirms that the Rayleigh-Plesset equation enables the description of the first cavitation bubble produced by PLAL when the isentropic case is assumed. In the case of the full dynamics of the bubbles, including multiple rebounds, the description needs to be extended using the Gilmore model²⁶⁰.

Figures 2.7(b) and (c) show the pressure and temperature parameters with respect to the normalized time for all the samples. Hydrodynamic quantities are also displayed in figures 2.7(d)-(f) showing the evolution of We , Re and Ca , respectively. In a general manner, bubbles dynamics are similar for all energies, and present the same range of values. As described previously, the system experiences extreme conditions at the early stage of the growth and at the final collapse with hundreds of bar and kelvin, while near-ambient conditions (2 atm and around 300 K) are reached most of the time of the bubble phase. Close to the maximum height, the temperature observed in the different conditions only differs from each other by about 150 K, largely smaller than the highest temperatures reached. Concerning the different forces in competition, inertia dominates the bubble motion since high values of We and Re allow to neglect the surface tension and the viscous forces. The capillary numbers, calculated below unity, indicate that the surface tension is slightly higher than the viscous forces. The fast velocity of the boundaries indicates that the expansion process is inertially driven.

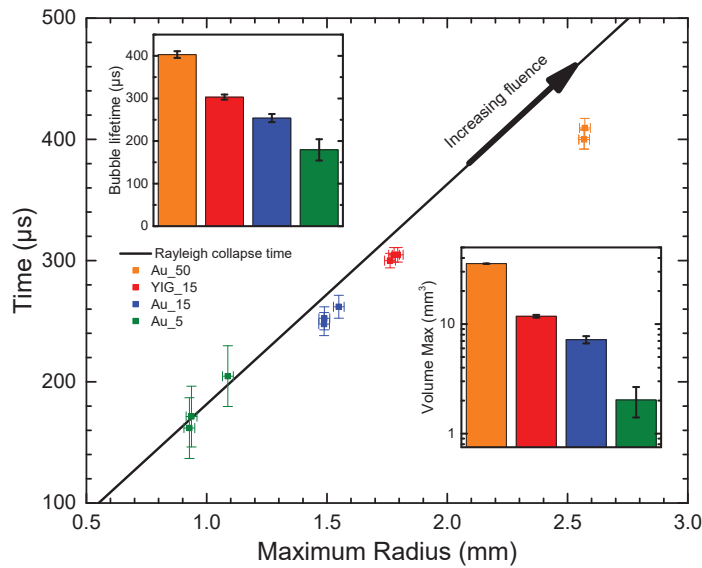


Figure 2.6 – Bubble lifetime with respect to the maximum radius of each analyzed bubble. The solid straight line represents the Rayleigh Collapse Time (RCT). Bar charts display bubble lifetimes (top-left inset) and volumes (bottom-right inset) according to the ablated material and applied laser power.

In conclusion, an evident increase of bubbles size and lifetime is related to the augmentation of laser power used for PLAL experiments. By increasing the energy available in the system, a larger proportion of solvent can be vaporized, leading to a longer vapor phase. Interestingly, the dynamics of the bubbles presented with the evolution of the dimensionless numbers and the thermodynamic parameters are the same for every laser energy since the velocity remains roughly unchanged. Moreover, we can supposed that the pressure and temperature are found similar since the energy differences from low to high fluences lead to vaporize the solvent molecules instead of increasing the thermodynamic conditions in bubbles.

Consequently, the nanoparticles formation could be affected by the duration of their stay in the cavitation bubble, where the bubble lifetime can be controlled thanks to the laser energy. However, most of the time the ambient conditions inside the bubble may have a small impact on the nanoparticles formation. The more likely moments where nanoparticles can be subject to modification remain during the extreme condition periods at the collapses, in agreement with the works of Plech's group^{137,144,145,147,263}. The collapse of the bubble is characterized by a drastic increase of the pressure, the density and the temperature, which would lead to a maturation of the produced particles, at least aggregation and certainly some effects on the crystal structure. Finally, these results prove as well that bubble dynamics are not affected by the target matter for nanosecond pulse

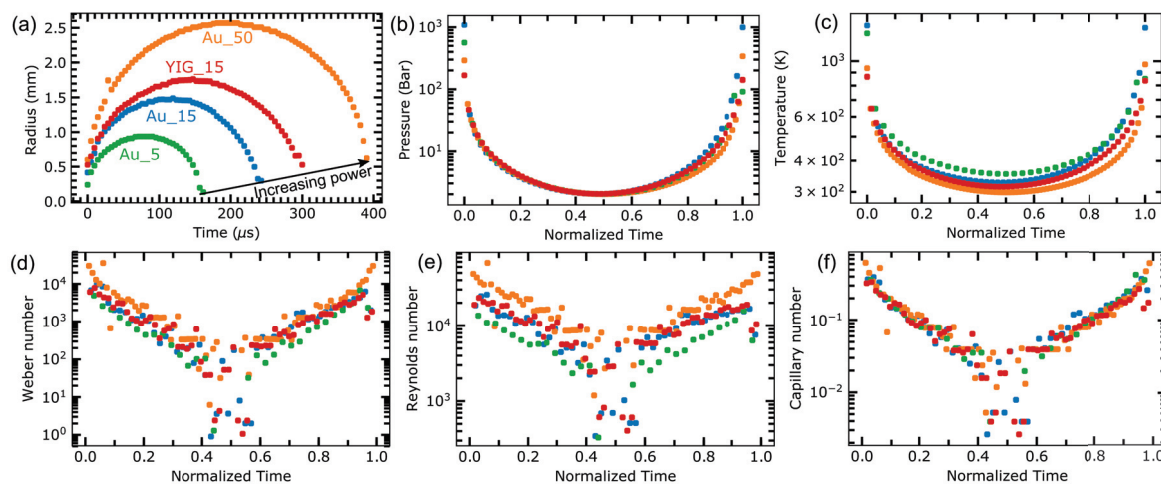


Figure 2.7 – (a) Radius evolution of energy dependent bubbles enables to calculate thermodynamic quantities as the internal (b) pressure and (c) temperature, as well as (d) Weber, (e) Reynolds and (f) Capillary numbers.

duration. Indeed, the long pulse duration favor the plasma warming and then the vaporization of the solvent, with a limited effect of the target material. However, further investigations should be addressed in order to clarify the impact of the ablated material on the bubble size and lifetime, such as the differences observed between Au_15 and YIG_15, the two target materials ablated at the same energy.

2.3 Viscosity influence

First chapter gives an overview of different PLAL conditions where laser as well as material parameters were largely explored. The vapor phase has been extensively studied since the time and size scales of the bubbles are large enough to be able to easily observe them. However, no systematic observation of laser-induced bubbles is performed, because the interest remains final nanoparticles. Consequently, there is a lack of literature investigating cavitation bubbles in versatile targets and solvents, and especially, in highly viscous liquids. PLAL offers the possibility to produce colloidal solution in a one-step process, including in oils^{258,265} or monomers²⁶⁶ at high viscosity. Such solvent is suspected to have a strong effect on bubble dynamics but it is still unknown how viscosity and surface tension influence shape, lifetime and size of the laser-generated bubble, and how they influence the nanoparticle growth and distribution inside the bubble. A deeper understanding could offer new ways to ultimately improve the overall PLAL process, *i.e.* repeatability and productivity.

In this section, the bubble morphology and its dynamics will be investigated at the light of the influence of the viscosity. For this purpose, two highly viscous polyalphaolefin (PAO) oils were used and water served as reference. Experiments were carried out in commercially available Spectrasync

PAO6 and PAO40 oils supplied by Exxon Mobile. Characteristics of each solvent are summarized in table 2.1. Note that oil densities ρ are approximately the same than water whereas the surface tension γ of water is the double of those of PAOs. More importantly, the dynamic viscosities η of PAO6 and PAO40 are, respectively, 1 and 2 orders of magnitude higher than the water viscosity. Ablations were performed on gold and YIG targets by the UV laser system with an energy of 7.6 mJ/pulse. Recording parameters and numbers of bubbles images are similar than the Au_OD3 and YIG_OD3 bubbles presented in the last section.

The bubbles dynamics have been studied by considering geometrical changes of the bubbles shape and the dynamics revealing different hydrodynamics regimes.

Parameters	Water	PAO6	PAO40
ρ (kg.m ³)	997	830	850
η (Pa.s)	0.001	0.067	0.649
γ (N.m ⁻¹)	0.0720	0.0297	0.0315

Table 2.1 – Density, dynamic viscosity (at 293 K) and surface tension parameters of the three solvents.

2.3.1 Geometrical shape

The influence of viscosity on cavitation bubble is clearly visible thanks to the snapshot sequences collected during the ablation of gold in the three solvents, displayed in figure 2.8(a). The shape is strongly modified by the two PAOs: the bubble does not present a hemispherical shape anymore, but it composes of two parts. At the top of the bubble, the cap remains hemispherical. In the solid target vicinity, the bubble foot forms an interface layer of thickness e . Its shape was considered conical as a first approximation, even though in the case of PAO40, a curved shape could be more appropriated. The definition of the geometrical parameters is displayed in section 2.1.2 and in figure 2.2(a).

By comparing the bubble radius R and the foot size x in figure 2.8(b), two dynamics emerge. In water, the contact line and radius grow equally, leading to an overlap of the two curves and to the hemispherical shape of the cap. By increasing the viscosity, the foot is quickly slowed down during its growth and reaches a maximum length while the cap continues to grow. Hence, the vertical increase of the bubble drives the interlayer thickness e . At the end of bubble lifetime, its foot and its height curves intersect before the collapse. The foot is described by an abrupt decrease compared to the bubble radius. This indicates a sudden flip of the contact angle from low to high angles where the intersection corresponds to $\theta = 90^\circ$.

In addition of the shape change, the viscosity tends to decrease the lifetimes and the volumes of the bubbles. Between water and PAO40, a reduction of about 1.5 of the bubbles lifetimes can be observed in figure 2.8(c), independently of the ablated material. Similarly, the volumes of the

bubbles in PAO40 are reduced by about 2.5 and 3.3 times compared to bubbles volumes in water when Au and YIG are ablated, respectively (Fig. 2.8(d)).

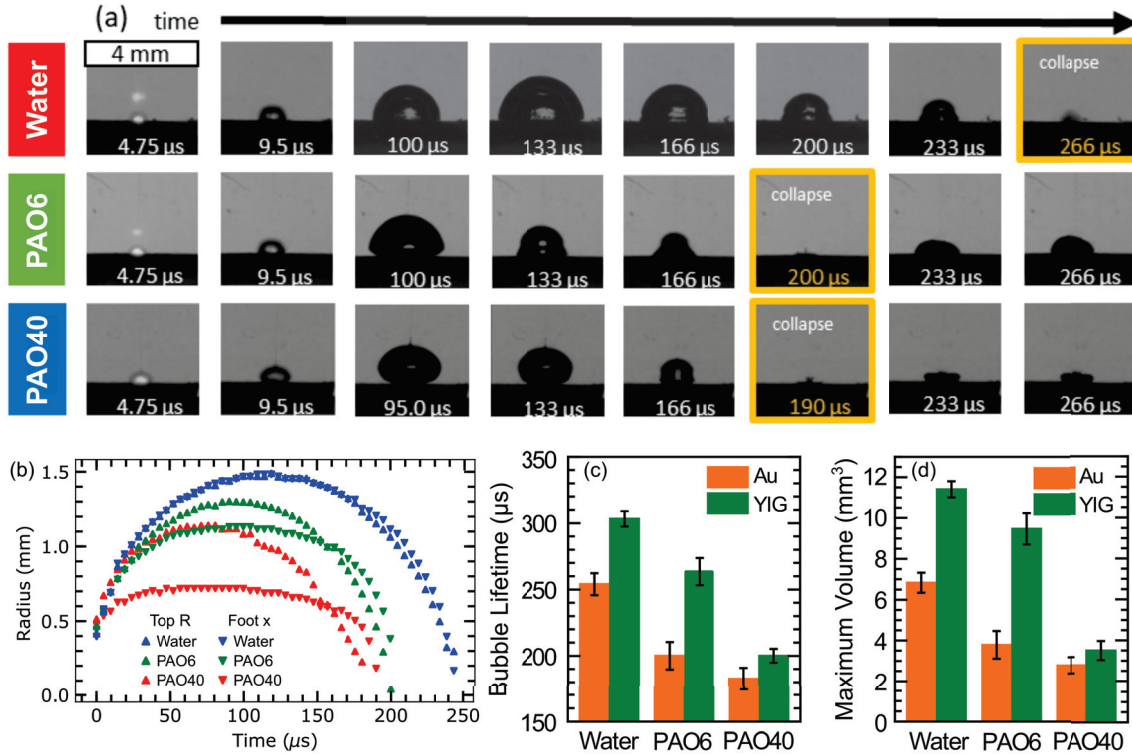


Figure 2.8 – (a) Snapshot sequences of one bubble produced by gold ablation in three solvents. (b) Bubble (vertical) and foot (horizontal) radii, R and x , are compared for the three solvents as well as (c) the bubble lifetimes and (d) the maximum volumes for Au and YIG targets ablation.

2.3.2 We , Re and Ca numbers

By increasing the viscosity, the Weber, Reynolds and Capillary numbers drastically change, as can be seen in figure 2.9. These numbers were calculated at the top of the bubble and at the bubble foot. As the viscosity is not taken into account in We formula, the same evolution of We occurs for the three solvents, with high values from 10^4 at the early stage of the bubble to a minimum of 10^2 (Fig. 2.9(a)). Only the bubble foot in PAO40 begins to move with We of about 10^3 , since the initial velocity of the bubble in this oil is slightly lower than for the other liquids. In any case, inertia still dominates the motion compared to surface tension for the cap and the foot.

On the contrary of We , Re and Ca scale with the viscosity where three regimes are clearly distinguishable in figures 2.9(b) and (c), respectively. By comparing viscous forces with inertial forces, Re shows decreasing values with viscosity. From water to PAO6 and PAO40, Re is reduced by 2 and 3 orders of magnitude, respectively, and reaches the unity for the highest viscous oil. Therefore, viscosity cannot be neglected anymore when compared with inertia.

This trend is confirmed by the Ca evolution where the values increase with the viscosity. In water,

Ca is less than unity in the first μs before reaching 10^{-2} at the maximum bubble size. In PAO6 and PAO40, the same trend is shifted by 2 and 3 orders of magnitude towards high Ca , respectively. On the opposite of the water regime, the viscous forces are now the dominant forces over the surface tension. In addition, figure 2.9(d) displays Ca curves calculated at the top of Au and YIG bubbles in the three solvents and shows that dynamics are once again independent of the target material. Therefore, viscosity and inertia are the only forces in competition in order to drive the bubble motion.

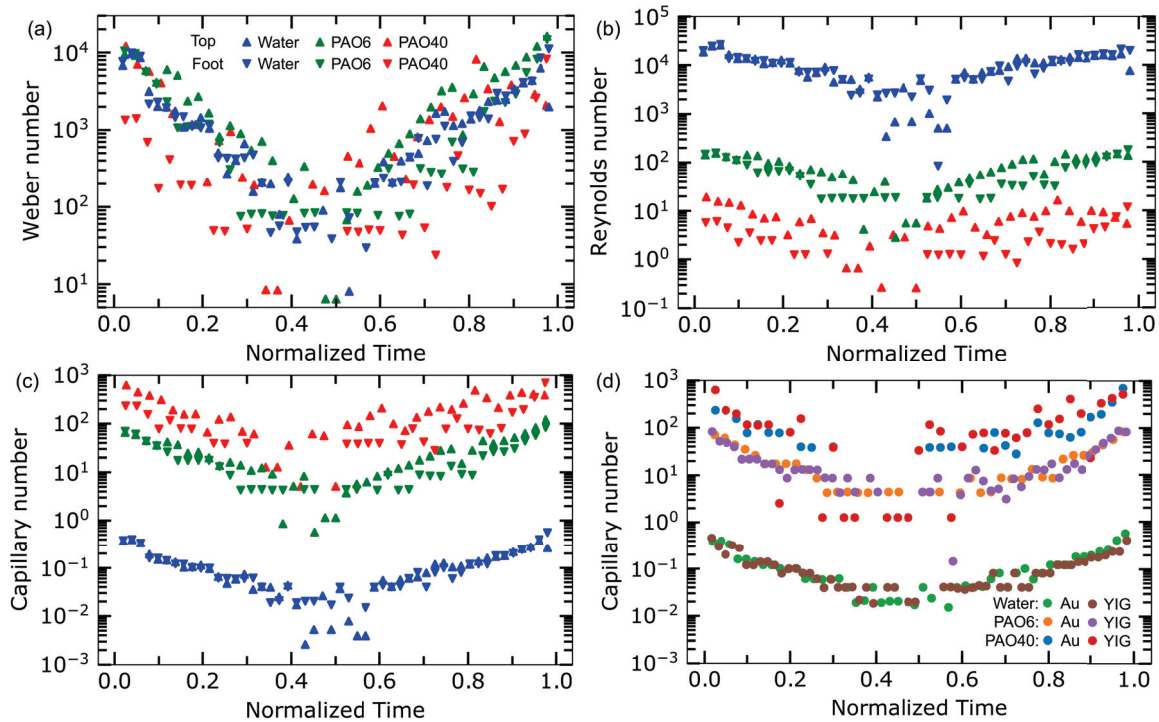


Figure 2.9 – Gold bubble dynamics are evaluated at the top and at the foot by (a) Weber, (b) Reynolds and (c) Capillary numbers as a function of normalized bubbles lifetime for the three solvents. (d) Capillary numbers are also compared for bubbles induced in the three solvents on Au and YIG targets.

2.3.3 Bubble spreading power laws

A way to define the successive regimes is to determine the power law that describes the spreading of a bubble or a drop. Indeed, in the hydrodynamic community, advancing and receding sessile droplets^{267,268} or spreading bubbles^{269,270} follow a power law under the form $x(t) = At^n$ with A a constant and n the power exponent, which characterizes the spreading regime^{268,270–272}.

For a bubble characterized by a constant volume, inertio-capillary regimes lead to theoretical time evolution between $t^{1/2}$ and $t^{1/3}$ depending on the driving force, *i.e.* the gravity or the capillary strength, respectively, which counterbalances the inertia, and if the bubble footprint radius is larger

or smaller than the capillary length, leading to a flattened or a spherical shape respectively. The capillary length is defined as a length scaling factor when the gravity and the surface tension force are in equilibrium: $a = \sqrt{\frac{\gamma}{\rho g}}$. For a droplet characterized by a constant volume, when inertia is marginal, the balance between the surface tension and the viscous dissipation leading to friction at small scale is described by the Tanner's law with $t^{1/10}$.

In the case of laser-generated bubbles, the bubbles behavior is substantially different during its early expansion in addition to have a variable volume. The driving force is identified as the bubble inner pressure P_B . In water, we saw that simplified Rayleigh–Plesset equation applies and reflects the balance between inertia and inner pressure:

$$\rho v^2 = \rho \frac{R^2}{t^2} = P_B \quad (2.9)$$

with v the bubble velocity at the boundaries.

According to the isentropic relation 2.4, it leads to the balance:

$$R = \frac{A}{\rho} t^{\frac{2}{3\alpha+2}} \quad (2.10)$$

with A a constant. As the heat capacity ratio α is 1.33 for water and tends to 1 for larger molecules, we expect a power law coefficient $n = 1/3$ for water and $n = 2/5$ for the oils.

By plotting the radius and the foot of the different bubbles with respect to time in logarithm scale, the growth part are fitted by one or two linear curves where the n exponents are displayed directly on the graphs (Fig. 2.10). From figure 2.10(a), it appears that the spherical cap is driven by inertio-capillary regime for every solvent since every calculated n is comprised between 0.3 and 0.4, which is consistent with theoretical exponent $n = 1/3$.

At the bottom of the bubble, more interesting features appear, as shown in figure 2.10(b). As for the cap, bubble foot growth in water is described by one linear slope equals to 0.37, corresponding to the inertio-capillary regime. For the viscous oils, two trends emerge. The first part describes the inertio-capillary regime where the bubbles grow with n around 0.3-0.4. Then, a second reduced slope is achieved with n comprised between 0.1 and 0.2. This indicates a change of regime with the contribution of the viscous forces, as described by Tanner's law. Close to the surface, friction has to be included in the resistance forces along with inertia. In the case of PAO6, this transition coincides with the dynamic separation between the top radius and the foot at around 30 μs , indicated by the dash line in the inset of figure 2.10(b).

These results are consistent with theoretical predictions but some deviations remain. They can be explained because these power laws have been developed for systems different in comparison with ours. For instance, in Tanner's theory, a droplet wets almost completely its target, leading to

a spherical cap shape. In addition, power laws have been derived for low capillary numbers $Ca \ll 1$, which is only the case for water. To our best knowledge, there is no study available in the literature describing a droplet or bubble spreading in such high capillary number regime. Moreover, a constant bubble volume during spreading is typically assumed for the theoretical derivation of n in literature. For laser-generated bubbles, the volume is not constant and this leads to a deviation from the theory developed for droplets. However, the measured values are close to the literature and, in the case of high viscosity, reflect qualitatively the expected trend.

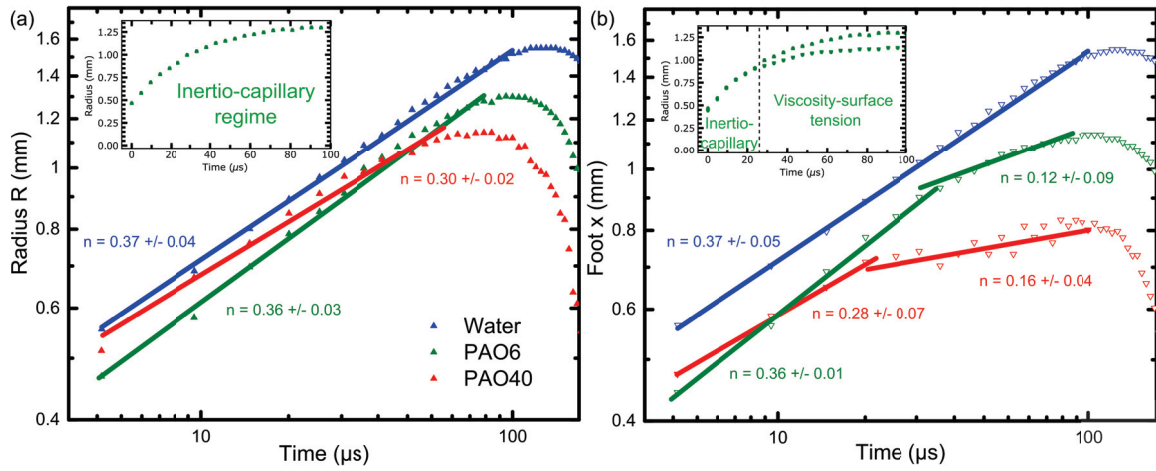


Figure 2.10 – (a) Radius and (b) foot evolutions according to time, plotted in logarithm scale and (insets) in linear scale. Fitted linear curves display the n exponents, which relate to forces regimes, summarized in insets.

2.3.4 High capillary numbers dynamics

In viscous oils, two-step regimes observed at the foot differ with the inertio-capillary regime occurring at the top. This difference cannot be only explained by the liquid viscosity resistance that bubbles encounter. Combined with the fact that the foot is slowed down compared to the bubble radius, the solid target has thus an obvious role in bubble dynamics. Blake *et al.* have proposed a molecular-kinetic theory (MKT) model^{273,274} in the case of a droplet spreading on a solid, in air. The velocity at the contact line V_{cl} depends essentially on the dynamic θ and equilibrium θ^0 contact angles, respectively:

$$V_{cl} = 2\kappa\lambda \sinh \left[\frac{\gamma}{nk_B T} (\cos\theta - \cos\theta^0) \right] \quad (2.11)$$

κ is the exchange rate of molecules at an absorption site on the target surface, λ is the average distance between absorption sites, n is the number of affected absorption sites per unit area at the solid-liquid interface and γ represents the surface tension.

They considered that the contact line is driven by the statistical motion of the liquid molecules at

the triple point and introduced activation energies of molecules adsorption and desorption at the surface of the solid. This concept deals with the idea that the contact line motion is determined by local perturbations induced by the triple point flow. With this three-phase zone movement, adsorption or desorption sites are disturbed from equilibrium and hence, local surface tensions balance is modified. The out-of-balance surface tension force thus drives the driving force and the dynamic contact angle θ as a consequence. Therefore, this theory describes the solid/liquid interactions or in other words, the contact line friction. At the end, the dynamic contact angle depends on the contact line velocity and on a friction term, and is proportional to the liquid viscosity and the equilibrium work of adhesion, $W_a^0 = \gamma(1 + \cos\theta^0)$ with θ^0 the equilibrium contact angle.

Simplest hydrodynamic theories have been developed to describe wetting dynamics. Cox-Voinov model^{275,276} gives the dynamic contact angle θ relative to the capillary number Ca at the contact line, *i.e.* its velocity:

$$g(\theta) = g(\theta_m) + Ca \ln\left(\frac{L}{L_m}\right) \quad (2.12)$$

$$\text{with } g(\theta) = \frac{1}{2} \int_0^\theta \left(\frac{x}{\sin x} - \cos x\right) dx$$

L and L_m are appropriately chosen macroscopic and microscopic length scales, respectively. The model assumes that the dynamic contact angle is controlled by the viscous bending applied on the vapor/liquid interface. The contact line deformation is supposed to form at a mesoscopic scale due to viscous flow. This intermediate scale deals with a microscopic angle θ_m , assumed to be equal to θ^0 , in contact with the solid, which differs with the macroscopic dynamic contact angle.

Some theoreticians have combined the hydrodynamic theory with MKT model to take into account the viscosity η and the contact line friction ζ . The resulting relation leads to the contact line velocity inversely proportional to the viscosity and to the friction term²⁷⁷:

$$V_{cl} = \frac{\gamma(\cos\theta - \cos\theta^0)}{\zeta + \frac{3\eta}{\theta} \ln\left(\frac{L}{L_m}\right)} \quad (2.13)$$

$$\text{with } \zeta = \frac{\eta v_L}{\lambda^3} \exp\left(\frac{W_a^0}{nk_B T}\right)$$

with v_L is the molecular flow volume of the liquid. Such a relation implies that the bubble motion near the target surface is controlled by the viscosity both with the viscous vapor/liquid interaction and with the solid/liquid friction. At the top of the bubble, only the liquid viscosity resistance may act on the bubble interface due to the absence of the target. This is what we observe in our experiments since the cap and the foot dynamics of the bubble are not similar in the case of viscous oils. Friction combined with viscous forces cause the triple point motion quenching, which propagates

along the contact line until creating an interface layer, while only the liquid viscous resistance limits the inertial cap growth in a hemispherical shape smaller than in lower viscous liquid. By increasing the viscosity and consequently friction and viscous resistances, such limitations occur sooner than in low viscous liquids.

However, all these theoretical models assumed small capillary numbers ($Ca \ll 1$), unsuitable to interpret our results. High viscosities have already been studied, but at low velocities, corresponding to low Ca . A combination of high viscosity and high velocity is necessary to obtain high Ca . To our knowledge, such high Ca (> 100) have never been reported, highlighting the originality of these bubble dynamics, which combined extreme speeds in high viscous liquids. However, large Ca numbers are achieved in the context of high-speed coating, up to 1000 for the coating of optical fibers^{278,279}.

Despite this lack of unified model, some phenomena, which belong to experiments in normal conditions, are observed in our systems.

Contact angle hysteresis. Figure 2.11(a) shows absolute velocity of the contact line V_{cl} as a function of dynamic contact angles θ of bubbles generated in PAO6 and PAO40. Growth and collapse directions are indicated by black arrows. The rapid growth is characterized by angles below 90° , except at the early stage of the PAO6 bubble, before reaching a critical angle $\theta \approx 50^\circ$ at $V_{cl} = 0$. When bubbles attain their maximum size, velocity remains null while angles start to increase. When bubbles velocity increases again, angles are already far from their smallest values, to about 65° , and increase until values superior to 130° at the collapse. This hysteresis reveals that the surface is not homogeneous and delays the receding movement of bubbles. Interestingly, both liquids have the same hysteresis of around 15° . During growth process, bubble transfers its inertial energy into a liquid pressure until they equal and the contact line freezes. Then, the liquid pushes back the bubble inward in two steps. As the applied pressure is not enough compared to the work of adhesion of the liquid molecules on the solid, only the part of the contact line far from the solid is first repelled, causing an increase of the contact angle. When the driving force is superior to the adhesion work, the whole contact line is moved inward, which induces the bubble foot movement and the enhancement of its velocity. Similar hysteresis behavior was observed for a moving liquid droplet or a dynamic sessile drop at small Ca numbers^{268,273,280}.

Interlayer thickness. Another similarity with small Ca system exists for the thickness e of the interface layer, which grows with the whole bubble (see inset of figure 2.11(b)). Here we consider only PAO6 bubble since the round shape of the bubble for PAO40 would lead to an arbitrary definition of the interface layer parameters, L and e . For low capillary numbers, Ouwerkerk *et al.* predicted hemispherical bubbles lying on a microlayer^{281,282}, similar to the interlayer seen in

PAO6, in the case of bubbles generated on a hot surface in boiling liquids. Dynamics of the microlayer thickness was modeled by a boundary layer relation, assuming a constant shape of the bubble: $e = Z_b \sqrt{\nu L / V_e}$. V_e is the velocity of the liquid/vapor interface at the edge of the bubble, ν is the kinematic viscosity and L is the radius of the rim. By plotting e as a function of quantities inside the square root (Fig. 2.11(b)), the slope of the regression lines is represented by the dimensionless constant Z_b . For ablation on Au and YIG targets, Z_b exhibit close values, $Z_{b,Au} = 0.9$ and $Z_{b,YIG} = 1.1$, indicating a low dependency in the target material, and consistent with the theoretical value $Z_{b,th} = 0.9$ calculated by Ouwerkerk *et al.*

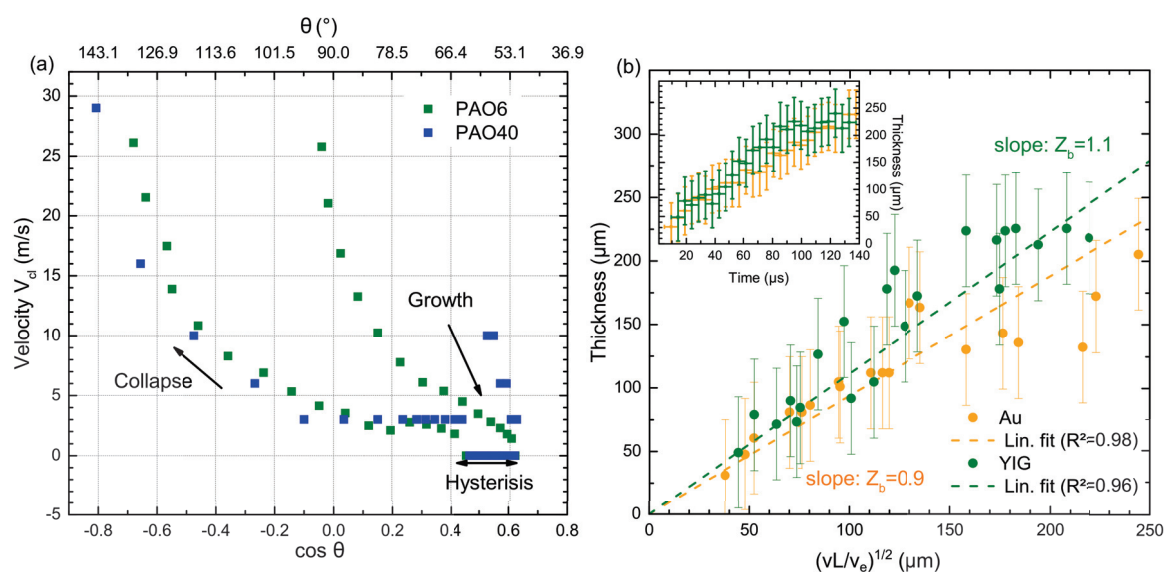


Figure 2.11 – (a) Relation between the absolute contact line velocity and the dynamic contact angle plotted for PAO6 and PAO40 bubbles. (b) Interface layer thickness of bubbles in PAO6 for Au and YIG targets as a function of (inset) time and the kinematic viscosity ν , the rim radius L and the front velocity of the rim V_e included in the square root of the boundary layer equation.

Finally, thermodynamic parameters should be calculated in order to estimate viscosity effect. On the contrary of ablation in water, the conditions, assumed to establish the simplified RP equation, are not respected in the case of viscous liquids. Indeed, viscous forces cannot be neglected anymore and the full RP equation should be thus used. However, bubbles shapes are no more hemispherical and liquid compressibility and solid friction should be included in a new model. Gilmore equation considers the compressibility. The Gilmore model is known to describe more accurately than RP equation the bubbles oscillation and shockwaves prediction²⁸³. However, the equation resolution is more complex and friction is not included. Therefore, a more general model should be developed in order to predict the thermodynamic parameters of bubbles in any experimental conditions.

2.4 Conclusion

We reported in this chapter the original dynamics of the laser-generated bubbles recorded experimentally with an ultrafast camera used in a shadowgraphy set-up. The influence of the laser energy was first investigated for Au and YIG targets in water. A simplified model of the Rayleigh-Plesset equation developed previously by our team was used to compute the temperature and the pressure all along the bubbles lifetime. These thermodynamic paths are found similar to previous works and appear independent of the laser fluence. In particular, extreme conditions are reached at the early stage and at the collapse of the bubbles. At low viscosity, the system is also found to be driven by inertia forces.

Afterwards, an increase of the viscosity leads to a drastic increase of the capillary number. It appears that there is no model available yet to explain the dynamics of laser-induced cavitation bubbles during when an extremely high capillary number is achieved ($Ca > 100$). Increasing the viscous forces, and hereby Ca up to 100, has a significant impact on the bubble shape and results in a very pronounced rim. The bubble is separated in a spherical cap driven by inertia and an interface layer close to the target where the shape differs from a sphere when the contribution of the viscous forces to the friction drastically increases. Interestingly, our data cannot be interpreted with simplified hydrodynamic (Cox-Voinov) or molecular-kinetic theory models thus highlighting the originality of the dynamics reported when extremely high capillary numbers are achieved.

To go further, we would continue to observe the bubbles dynamics by exploring a broader range of viscosity values. The interest is to relate such dynamics and the bubbles shape induced by the viscous forces with the nanoparticles morphology. As the nanoparticles suffer from the extreme conditions in the first oscillation, their maturation may be influenced by damped collapses as seen from bubbles dynamics in the highest viscous solvent. At the end, a control of the nanoparticles could be considered through the bubbles and the solvent, in addition to the one-step process interest.

CHAPTER 3

STABILIZED GOLD COLLOIDAL SOLUTIONS BY IONIC STRENGTH

Contents

3.1 Theory and experimental analysis	63
3.1.1 DLVO theory	63
3.1.2 Methods of characterization	64
3.2 Colloidal stability using ionic salts	68
3.2.1 Salt concentration effect	68
3.2.2 Solution concentration effect	72
3.3 Surface chemistry of gold nanoparticles	76
3.3.1 PLEIADES beamline	76
3.3.2 XPS results	80
3.4 Conclusion	83

As seen in the chapter 1, laser or materials parameters can be chosen in order to contribute to a better control of the final products. However, because of the inherent transient nature of the ablation processes, a satisfactory control of the final product properties is not always achieved only using laser parameters as adjustable parameters. A more straight way is the use of adsorbates, such as molecular ligands or ions, which adsorb to nanoparticles atoms thus allowing to tune the stability and the morphology of nanoparticles in solution. Usually the effect of these adsorbates is observed on the final products *via* the characterization of the nanoparticles, but their mechanisms of stabilization during the PLAL synthesis are still unclear.

In gold colloids synthesized by PLAL, electrostatic interactions have been found to be the origin of the stability of such solutions. Gold nanoparticles have been measured with a large negative zeta potential implying negative charged particles in solution. The colloidal stabilization is classically explained by the DLVO theory where the affinity of anions for gold nanoparticles surfaces leads to the formation of an electrostatic double layer. While most of studies consider that the negative charges are carried by the anions adsorbed at the nanoparticles surface^{151,192,284}, a new assumption appears recently, far to favor the role of ions. Palazzo *et al.* suppose that an excess of electrons embedded in the nanoparticles during the plasma stage of the PLAL process is the origin of the negative charges²⁸⁵.

For this purpose, we aimed to understand the stabilization of gold colloids when ions from salts are added in the solvent before PLAL synthesis. The two assumptions should lead to different surface chemistry of gold nanoparticles where the charge carrier should be different. We participated to a collaborative project that aimed to probe the surface chemistry of gold nanoparticles produced in saline solutions by performing X-rays Photoelectron Spectroscopy (XPS) experiments on a free-standing beam of PLAL-synthesized nanoparticles. For the needs of the XPS measurements, we were in charge to provide highly concentrated (> 1 g/L) and stable colloids synthesized by PLAL. We then mainly focus on the way to produce such highly concentrated colloids.

In this chapter, I will first present the preliminary results we conducted to study the stability of gold colloids synthesized with different salts. On the one hand, the influence of the salt concentration on the as-produced solutions stability was investigated. Then, the solutions were concentrated by evaporating the solvent and their stability was controlled according to the gold concentration. Finally, the first results of the XPS measurements will be presented showing that the approach considering that the charge is carried out by the anions is called into questions.

3.1 Theory and experimental analysis

The stability of gold colloids is supported by electrostatic interactions implying repulsion forces to avoid aggregation. In the DVLO theory, repulsive forces are described in term of the double layer formed by ions. I will first present in the following the theoretical features of the basic background that describes the colloidal stability. Then, the methods used to characterized systematically our gold colloids synthesized by PLAL will be described.

3.1.1 DLVO theory

The DVLO theory²⁸⁶ (named after Derjaguin, Landau, Verwey and Overbeek) describes the stability of colloidal solutions. Interactions of nanoparticles in suspension in a liquid media are modeled by a potential V_T composed of the attractive potential V_a due to the van der Waals forces and the repulsive potential V_r due to the double layer formed by ions. For spherical colloids of radius r , the attractive potential can be approximated by²⁸⁵:

$$V_a \approx -\frac{H}{6} \left(\frac{2r^2}{h^2 - 4r^2} + \frac{2r^2}{h^2} - \ln \left(\frac{h^2}{h^2 - 4r^2} \right) \right) \quad (3.1)$$

H refers to the Hamaker constant that relates the interactive van der Waals energy to the distance of separation between two particles h . In the case of gold colloids in water²⁸⁵, $H \approx 100k_B T$.

To avoid aggregation, the attractive interactions need to be balanced by repulsive forces, described by the double layer (DL) theory (Fig. 3.1). This theory has been developed with the first work of Hermann von Helmholtz in the XIXth century, until the XXth century with the Gouy-Chapman model and the works of Otto Stern.

First, the DL theory supports the fact that the nanoparticles surfaces show an affinity for anions in the solution¹⁵¹. Thus a first monolayer of anions surrounds the gold nanoparticles, called the Stern layer (region 1 in figure 3.1). By electrostatic attraction, the counter-ions are attracted. The system forms a capacitor with high concentrated charges. The anions and the cations from the bulk liquid are then attracted in the vicinity of the nanoparticle, leading to a concentration gradient. Hence, the ions concentration follows an exponential decay from the surface, c_{surf} , until recovering the averaged concentration of the solution c_{sol} . A Coulomb potential Ψ is induced by the charges, but the potential is exponentially screened by the medium, over a distance of the Debye length λ_D thus forming the diffuse layer (region 2 in figure 3.1).

The combination of the Stern and diffuse layers gave the name of the DL theory. In electrochem-

istry, λ_D is related to the ions concentration c_i (in ions.m⁻³) by:

$$\lambda_D = \sqrt{\frac{\epsilon_0 \epsilon_r k_B T}{\sum_i c_i q_i^2}} = \frac{0.3nm}{\sqrt{c_{sol}(mol/L)}} \quad (3.2)$$

with the vacuum permittivity $\epsilon_0 = 8.85.10^{-12}$ F.m⁻¹, the relative permittivity of the solvent (water here) $\epsilon_r = 78.5$, the Boltzmann constant $k_B = 1.38.10^{-23}$ J.K⁻¹, T the room temperature and q_i the ion charge of specie i . For simple electrolyte, the equation simplifies in the right expression in equation 3.2.

Then, the repulsive potential V_r can be approximated in the case of $r/\lambda_D \ll 1$ and written as follows:

$$V_r \approx \frac{\epsilon_r \epsilon_0 r \Psi_0^2}{\frac{h}{r} + 2} \exp\left(-\frac{h}{\lambda_D}\right) \quad (3.3)$$

Ψ_0 corresponds to the surface potential.

Finally, the total potential $V_T = V_a + V_r$ relative to thermal energy $k_B T$ as a function of the inter-particle distance h results in an energy barrier represented by the curves calculated by Palazzo *et al.*²⁸⁵ and displayed in figure 3.1(b).

Therefore, the nanoparticles stability is directly linked to the Debye length and so the ionic strength, *i.e.* the salt concentration for monocharge electrolyte. At the lowest concentration, *i.e.* ionic strength of 10⁻⁷ M (or mol.L⁻¹) of deionized water due to self-ionization, λ_D is large and the Coulomb repulsion between the particles is not screened by the medium. The high repulsive barrier enables to repel efficiently the particles. By increasing the ionic strength, the Debye length becomes thinner thus reducing the energy barrier. Then, crossing the barrier leads to aggregation of the particles and the colloidal stability is no more ensure. For gold nanoparticles of 5 nm with a surface potential $\Psi_0 = -60$ mV, an ionic strength of around 1 mM has been calculated to equal the thermal energy²⁸⁵ (Fig. 3.1(b)).

Finally, as the nanoparticles are in solution, they diffuse in all the volume by dragging a certain layer of liquid with them. The limit of the layer is referred as the slipping plane at which the applied potential is called the zeta potential. This potential is easily measured but its interpretation in terms of surface charge of the particle remains tricky since both surface charge and ions inside the slipping layer contribute to its value.

3.1.2 Methods of characterization

Synthesis were performed using the IR laser system (1 kHz, 500 ps, 1064 nm, 2 mJ/pulse) coupled with the flow cell system. This laser source is preferred for with respect to the UV laser system

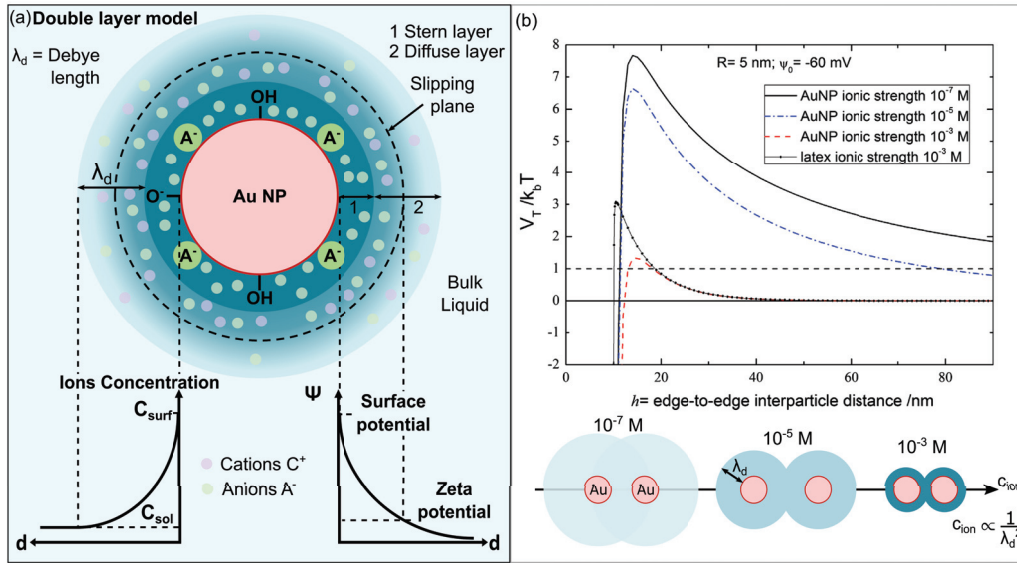


Figure 3.1 – Stabilization of gold nanoparticles in saline solution may be explained by the van der Waals attractive forces and (a) the repulsive double layer characterized by the combination of the Stern and diffuse layers. (b) Total interaction potential V_T relative to the thermal energy $k_B T$ as a function of interparticles distance calculated in the work of Palazzo *et al.* (Reprinted from²⁸⁵). At fixed nanoparticles size and surface potential, the energy barrier depends on the ionic strength related to the Debye length λ_D . Calculations have been performed by considering gold and latex nanoparticles of 5 nm with $\psi_0 = -60$ mV. Critical concentration of 1 mM reaches the thermal energy leading to aggregation of particles.

(9 Hz) due to its high repetition rate (1 kHz) ensuring a drastic increase of the production rate. The ablation has been performed on a gold target ($10 \times 20 \times 5$ mm) since the gold colloids can be easily characterized (large atomic number for HRTEM, large plasmon resonance for absorption). We used an ultra-pure water (18.2 M Ω) in order to be able to screen ions concentrations from μ M to mM. More details will be brought below, according to experiments. A scanning of the laser beam using steering mirrors ablates a rectangle of 7 x 17 mm on the target. The ablation scanning was fixed to allow 5 pulses/point with a distance between two points of $10 \mu\text{m} \times 30 \mu\text{m}$. The time between two pulses (1 ms) is shorter than the bubble lifetime. Thus, the successive bubbles do not screen the laser pulses. The produced particles are removed from the laser spot thanks to the combination of the liquid flow and the movement of the laser spot. The liquid flow is set at 5.85 mL/min. The final gold concentration was estimated at 0.14 ± 0.02 g/L for every solution synthesized in this work, thus revealing that additive ions do not affect significantly the production rate in the range of the screened concentrations.

Each colloidal solution was then systematically characterized by at least three methods of characterization that inform about different physical quantities: the concentration of the smallest nanoparticles, the size distribution and the zeta potential. These measurements were done within the hour

following the synthesis except for the zeta potential, which was measured at the end of the day.

Absorption spectroscopy. Absorbance is an easy way to characterize routinely the stability and the concentration of gold nanoparticles colloidal solutions. The absorption spectrum of gold nanoparticles below 20 nm presents a plasmonic resonance peak at about 525 nm (Fig. 3.2(a)), which shifts toward the higher wavelengths with the increasing nanoparticles size. Moreover, the peak intensity is related to the small gold nanoparticles concentration by the Beer-Lambert law. It can be shown that the absorbance at the resonance wavelength is proportional to the smallest nanoparticles concentration since the extinction coefficient remains proportional to the particles diameter below 20 nm (see Appendix A.1). The concentration c for the small nanoparticles will be thus calculated following the relation: $c [g.L^{-1}] = 0.0442 A(525)$ with $A(525)$ the absorbance at 525 nm.

Moreover, the absorption spectrum allows also to quantify the colloidal stability thanks to an empirical parameter introduced by the Barcikowski's group^{192,284}. The Primary Particle Index (PPI) is defined as the ratio between the absorbances at 380 nm and 800 nm, as displayed in figure 3.2(a). The numerator refers to the interband from all particles, *i.e.* whatever their sizes, and then gives an information about the total amount of matter. The denominator (absorption at 800 nm) increases with the increase of the individual particles sizes as well as with the amount of aggregates particles (plasmon coupling). As a result, the higher the PPI is, the more stable is the colloidal solution.

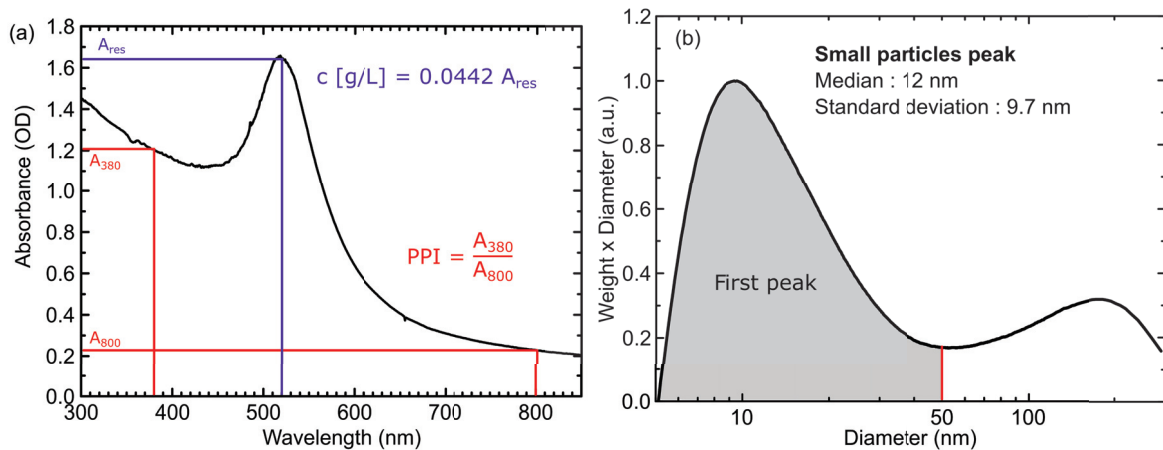


Figure 3.2 – Our synthesis were systematically characterized by measuring the (a) absorption spectrum (in optical density (OD)) to deduce the small nanoparticles concentration and the Primary Particles Index (PPI), and the (b) relative weight distribution measured with the disc centrifuge system. The gold colloidal solution synthesized using 400 μ M of NaBr in water is presented as an example.

Size distribution. The nanoparticles size distribution can be determined by two methods. Transmission Electron Microscopy (TEM) allows to record direct images of nanoparticles. For this

purpose, a droplet of the as-produced colloidal solution is poured onto a 400-mesh copper grid covered with ultrathin carbon on carbon holey support film (from Ted Pella, inc.). TEM analysis were carried out on a JEOL 2100HT microscope operating at 200 kV. Images are acquired using a Gatan Orius 200 camera at different magnifications. The resulting pictures are treated either manually using the *ImageJ* software, or automatically with the *Particle Sizer* plugin of *ImageJ* software (Fig. 3.3(a)).

The centrifugal sedimentation particle size analyzer, developed by CPS Instruments, is a routine method with respect to TEM. The principle is based on the differential sedimentation of the particles in a sucrose density gradient using a disc centrifuge system DC24000 (see Appendix A.2). A calibration is performed before each measurement using a calibration standard of 263 nm PVC spheres dispersed in water (from CPS instruments). 100 μ L of the colloidal solution is injected in the disc centrifuge system for each measurement. Sizes down to 5 nm can be detected.

As shown in figure 3.3(d), CPS and TEM methods are consistent with median sizes and standard deviations equal to 6.8 ± 3.5 nm and 6.9 ± 4.2 nm, respectively. In the following, the CPS analyzer was used systematically to deduce the size distribution, while the TEM was used occasionally since this method is time consuming. In our study, the relative weight distribution is plotted as a function of the diameters in a logarithm scale for a better legibility over a wide size range (Fig. 3.2(b)). However, for diameters displayed in log scale, the contribution of a size range to the total weight corresponds to the area under the curve (visually relevant) only if the y-axis displays the weight distribution times the diameter of the particles (see Appendix A.2). The median size and standard deviation of the relative weight distribution are calculated and only the predominant peak was considered in the case of bimodal distribution (Fig. 3.2(b)).

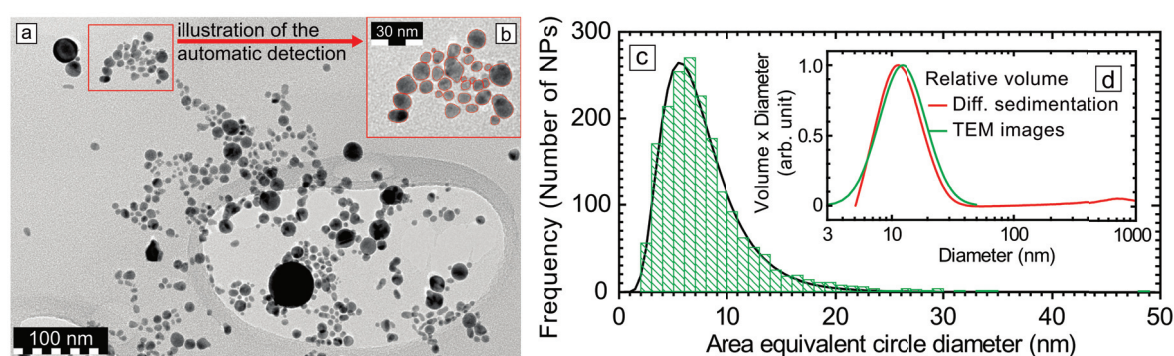


Figure 3.3 – (a) Representative TEM images used to (b) automatically detect the gold nanoparticles using the *ImageJ* software and (c) to deduce the frequency of the particle diameters (1847 particles, median size 6.9 nm, standard deviation 4.2 nm). The distribution is fitted assuming a log-normal distribution (black curve, adjusted $R^2=0.99$, median size 6.8 nm, standard deviation 3.5 nm). This fit is used to calculate (d) the relative volume distribution times the particle diameter (green curve), which is consistent with that deduced using the CPS system (red curve).

Zeta potential. As described above, the zeta (ζ) potential informs about the global ionic charge surrounding the nanoparticles, *i.e.* inside the slipping plane. The measurements are carried out using a Zetasizer apparatus from Malvern. An electrophoresis cell of volume of 750 μL is filled with the colloidal solution and an electric field is applied thanks to two electrodes. Consequently, the charged nanoparticles move toward the cathode or the anode according to their charge. Finally, the zeta potential is measured by varying the field strength and by measuring the particles velocity (see Appendix A.3). Indeed, the ions velocity depends on the field strength, which is regulated experimentally, the known values of the dielectric constant and the viscosity of the liquid, and the zeta potential. The Hückel model is more appropriate for PLAL-synthesized nanoparticles. It favors the small nanoparticles by considering that their radius is small compared to the Debye length²⁸⁷ (see Appendix A.3). A distribution of zeta potentials (in mV) is thus obtained and the median value combined with the standard deviation are determined. The sign of the zeta potential indicates the global charge sign of the nanoparticles. Therefore, lower is the zeta potential absolute value, the worst is the colloidal stability. In practice, values below $|30|$ mV refer to unstable solution for which particles aggregate.

3.2 Colloidal stability using ionic salts

The stability of the PLAL-synthesized gold colloids has been extensively studied as a function of the salts concentration^{60,177,180,192,284,288}, but not so much as a function of the nanoparticles concentration. We report in the following the results obtained from synthesis of gold nanoparticles solutions by (i) varying the concentration of different salts, (ii) by investigating the aging of these solutions, and (iii) by increasing the gold concentration.

3.2.1 Salt concentration effect

The aim of this first part is to investigate the colloidal stability of gold solutions prepared with four different salts at several concentrations. Such work has been performed previously by Merk *et al.*¹⁹² also on laser-generated gold nanoparticles in water with seven different salts, but no systematic evaluation of the size distribution was reported. They showed that the efficient ions have a chaotropic nature, defined as weakly solvated ions, on the opposite of the kosmotropic ions, which are strongly hydrated by solvent molecules. Consequently, we have selected three chaotropic salts, NaBr, NaCl and NaI, as well as the NaOH base in order to tune the pH. Concentrations from 50 to 500 μM were tested separately for each salt. The salt powder was dissolved in the deionized water before each ablation synthesis.

Figures 3.4(a-c) show the effect of the salinity on the relative weight distributions of the colloidal solutions. The synthesis in pure deionized water leads to the formation of aggregates or larger particles, which is reflected by the broad band of the 0 μM curve defined by a median value of 34.7 nm and a standard deviation of 44 nm. In general, the addition of salt results in a shift

and a sharpening of the relative weight distribution toward the smaller sizes when increasing the concentration. A second size population also exists above 100 nm. A bimodal size distribution is currently reported for laser-generated nanoparticles in liquids^{51,148–150}. The salt concentration does not appear to drastically modify the secondary particles population, which can let us to consider only the primary particles peak.

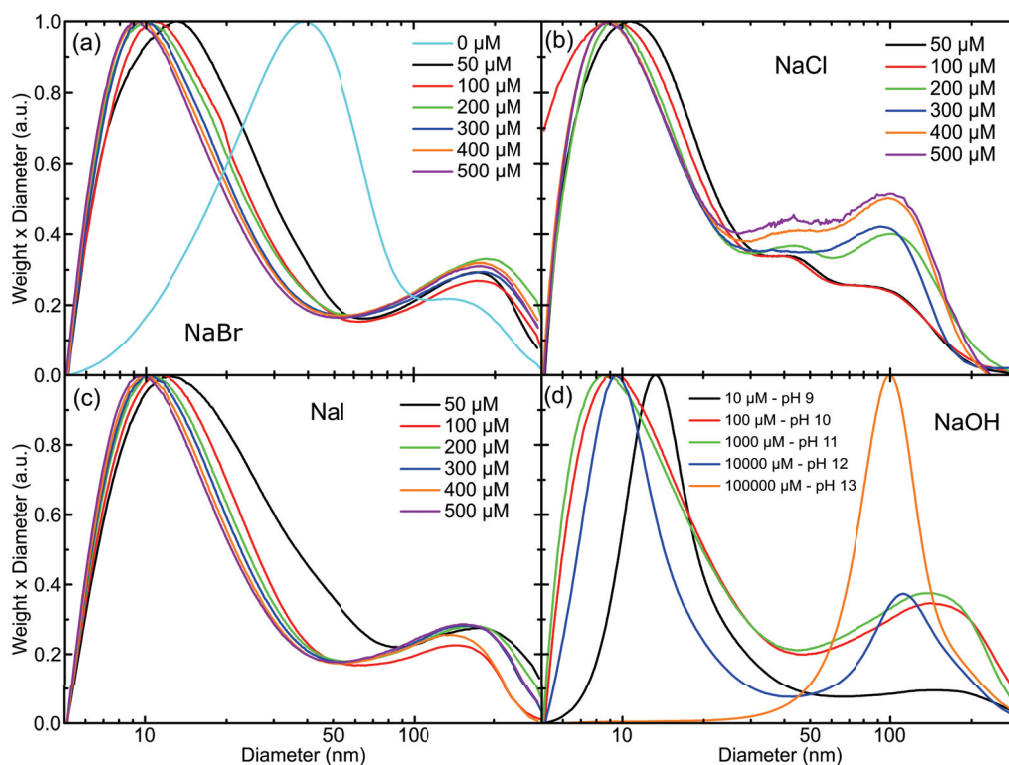


Figure 3.4 – Relative weight distribution as a function of the gold nanoparticles diameters measured for solution synthesized in pure deionized water (0 μM) and with four salts at different concentrations.

The median sizes of the primary particles mass peak are thus reported in figure 3.5(a) as a function of the concentration of the added NaBr, NaCl and NaI salts. The addition of salts seems to have the same effect, where the increase of the concentration stabilizes the nanoparticles size about 12 nm and reduces their dispersion. By increasing the pH, a concentration range of NaOH is widely explored resulting in a size stabilization of the particles until a threshold observed at pH 12 beyond which the sedimentation of the solution starts, as can be seen in the inset of figure 3.4(a).

The same trend is observed when we calculate the PPI, displayed in figure 3.5(c). The PPI slowly increases with the salts concentration, up by 2 for the chaotropic anions. The NaCl solution seems to be slightly less stable than its counterparts, which reflects the formation of secondary nanoparticles more abundant than in the other synthesis. Indeed, while the largest particles are around 200

nm in size in the case of NaBr and NaI solutions (Fig. 3.4(a) and (c)), the NaCl solution is characterized by a larger polydispersity with the presence of two mixed bands centered around 45 nm and 100 nm (Fig. 3.4(b)). In addition, these populations seem to increase with the salt concentration indicating a less stable solution than the other synthesis.

The zeta potentials measurements of these solutions support also this tendency, showing higher negative values with the increasing concentration (Fig. 3.5(b)). It confirms that the enhancement of negative charges around the particles enables to repel them from each other more efficiently. However, such as the weak PPI evolution, the zeta potentials vary slowly from -45 mV until values around -50 and -55 mV.

In the case of the NaOH solution, the PPI shows a trend different from that of the relative weight distribution (inset of figure 3.5(c)). From 10 μM to 1000 μM , the solution stability is consistent with the other saline solutions with a PPI of about 6 at 100 μM . A maximum of 7.5 is reached at pH 11, before it drastically drops to almost 2 at pH 12. The zeta potential is characterized by a drastic change at pH 12, concomitantly with a drastic increase of the size distribution observed in CPS measurements. The zeta potential displays a minimum of -80 mV before the charge collapses below -40 mV at pH 13 (purple dots in inset of figure 3.5(c)).

When we look at the whole relative weight distribution of the pH 12 (Fig. 3.4(d)), the two bands of the primary and secondary populations are sharper than the lower concentrations curves. It can indicate that nanoparticles may agglomerate or aggregate, or grow by Oswald ripening. Our measurements by CPS are not able to distinguish the two cases. The smallest sizes peak is then sharper due to the increase of particles size ranging between 20 and 50 nm. The secondary nanoparticles ranging between 50 and 300 nm also grow or aggregate until sub-microscopic sizes larger than 300 nm. At pH 13, the total aggregation results in the increase of the smallest sizes to largest diameters around 100 nm. This suggests that the secondary particles population peak was also shifted toward highest values. Unfortunately, at the time the work has been conducted, we did not have the proper equipment to probe the larger size scale.

This work shows that the salt has an effect on the stability of the gold colloidal solutions. In the studied concentration range, the higher is the concentration, the more stable is the solution, until a critical value is reached such as in the case of pH solutions. Therefore, more synthesis should be performed in the mM range to evaluate the critical concentration. For instance, the sedimentation of solutions synthesized with NaCl and KCl salts occurs above 10 mM in the work of Sylvestre *et al.*¹⁵¹.

Until now, the gold colloidal solutions were characterized directly after being synthesized. However, we were also interested to evaluate their stability over time. Such requirement is necessary to be able to produce large volumes, which can be reused within a long period of time, or even for a commercial purpose.

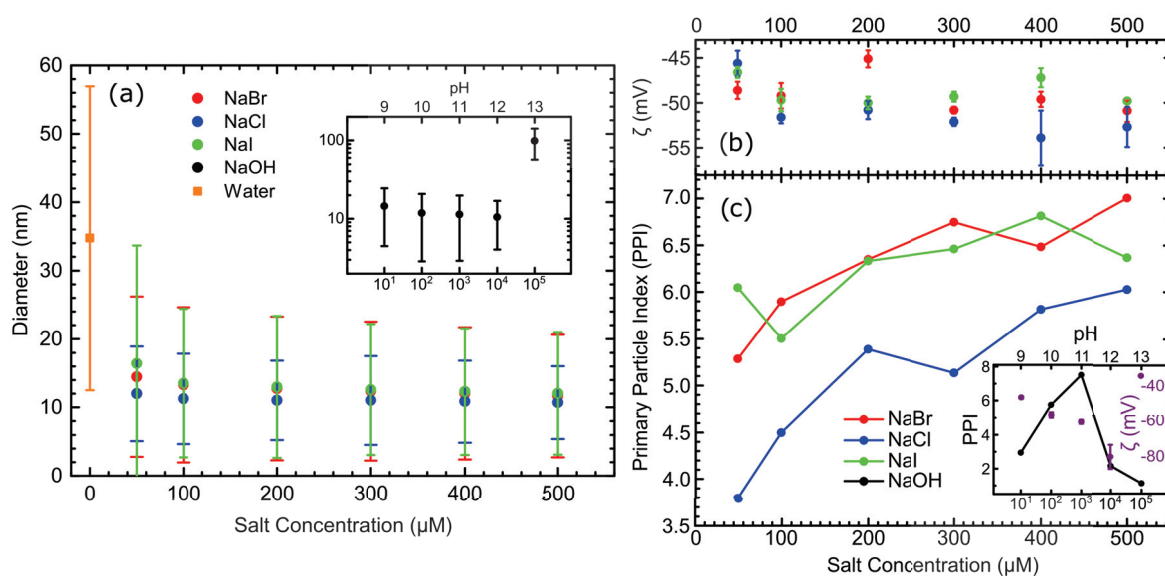


Figure 3.5 – The effect of the four salts on the gold colloidal solutions is evaluated according to their concentrations with the use of: (a) the median size and their standard deviation from the primary particles population peaks measured by CPS, (b) the zeta potential and (c) the PPI deduced from the absorption measurement. Insets refer to the NaOH solutions evaluation where the pH is linked to the concentration values.

Hence, some synthesized solutions were monitored over time. NaBr, NaCl and NaI solutions prepared with salt concentration of 50, 200 and 500 μM have been investigated, as well as the NaOH solutions at pH 9, 11 and 12. Figures 3.6(a)-(c) give insights about the stability of these solutions over a period of a few weeks.

From a general point of view, the solutions remain stable for at least one month, being composed of abundant primary particles of sizes comprised between 10 and 15 nm (Fig. 3.6(a)). Only the NaI solutions and the NaOH solution at pH 12 are destabilized immediately after the synthesis, confirmed by the PPI drops (Fig. 3.6(c)). For instance, the NaI solutions see their PPI values, starting from about 6, decreased below 3, or 2 for the highest concentrated solution. Visually, the red color of the colloidal solutions turned to darkest colors within a few hours after the synthesis. After one month, the smallest nanoparticles population seems to stabilize around 60 nm. Moreover, the zeta potential decreases slowly between -48 and -31 mV after two weeks (Fig. 3.6(b)). Finally, the NaBr salt allows a better stabilization of the gold colloidal solutions in the same period range. Even if we did not perform systematic characterization after one month, the color of the synthesized solutions is still currently (produced in mars 2018) red with a very small material sedimentation.

Recently, several studies deal with the stabilization of gold colloids using anions^{151,192,284}. But they only explored the impact of different salts and their concentration while, to our best knowledge, no work has been done on the increase of both gold and salt concentrations. Therefore, we

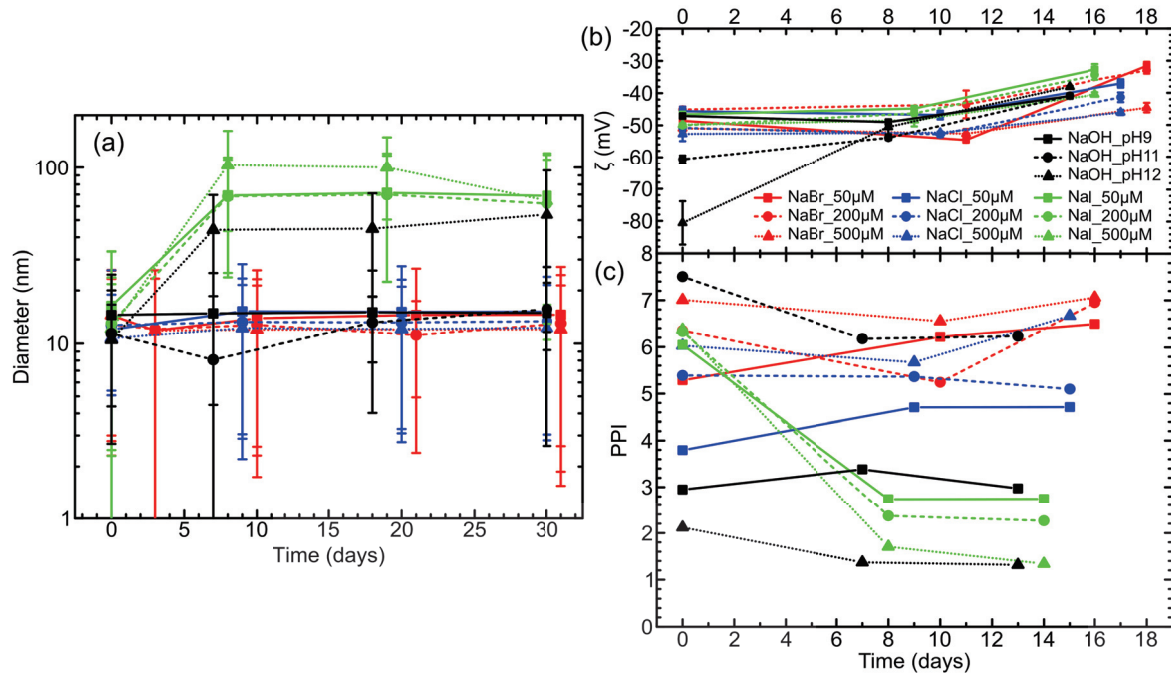


Figure 3.6 – Gold solutions synthesized in the four salts are evaluated for three initial concentrations over time. (a) Median sizes of the primary particles peak, (b) the zeta potentials and (c) the PPI are thus considered.

achieved such experiments by evaporating the solvent of several gold colloidal synthesis prepared in different saline solutions.

3.2.2 Solution concentration effect

For this series of experiments, a larger volume of gold solution is necessary in order to easily concentrate it and to perform the characterization analysis. Therefore, the synthesis were done in the same conditions than previously, except that the ablation lasted approximately 1h30 to obtain a volume of around 500 mL. Solutions have been tested for two concentrations, namely 50 and 300 μM for NaBr and NaCl salts, and at pH 9 (10 μM) and 11 (1000 μM) for the NaOH salt. Synthesis with NaI was not attempted since its stability over time was not guarantee.

Then the evaporation step was achieved by partly removing the solvent with a rotary evaporator. The whole solution is placed in a round-bottom flask, which is rotated in a bath heated at 60°C. A partial vacuum of 120 mbar is applied, leading to the slow evaporation of water. The vapor condensates outside the flask in a column cooled at 10°C and is collected in an external container. The extracted solvent conductivity was measured in order to check that no salt was removed. To follow the evolution of the solution stability, the same characterization measurements than presented above were carried out every time the volume of the solution was approximately divided by two. Finally, each solution was concentrated beyond 1 g/L, unless the solution was visually destabilized,

passing from the characteristic red color to purple. Only the NaOH solutions did not reach concentration superior to 1 g/L.

Just after the synthesis, the solution was composed of the solvent, a known concentration of salt and the ablated gold nanoparticles. The concentration of gold was measured thanks to the mass loss of the target and the final volume. Consequently, by removing the solvent, both the salt and the particles were concentrated in a restrained volume. Figure 3.7 summarizes the evolution of the zeta potentials and the PPI with the increasing concentration of gold nanoparticles and salts. Please note that the initial concentration of all the solutions was around 0.14 g/L, as seen above.

First, the general trend, which stands out, is the lowering of the zeta potential (Fig. 3.7(a) and (b)) when the solvent is removed. All the NaCl and NaBr solutions have reduced zeta potential values below -40 mV for concentrations above 1 g/L. The zeta potential of the NaOH solution also decreases as the volume decreases. These trends are consistent with those of the PPI (Fig. 3.7(c)), except in the case of NaOH and NaBr solutions initially concentrated at 10 and 300 μM , respectively. Indeed, their PPI remain constant all along the evaporation steps while their zeta potentials slowly decrease. However, the NaOH solution at pH 9 shows already a weak stability with a PPI of around 4.

The PPI displayed in figure 3.7(c) reveals that the solutions stability can be improved according to its concentration, since some maxima are visible. This is more clear in figure 3.7(d) where PPI are plotted as a function of the salt concentration. PPI maxima at around 200, 300 and 800 μM are respectively observed for the NaBr solution at 50 μM and NaCl solutions at 50 and 300 μM , before they drastically decrease. Finally, the stability of the NaOH solution at pH 9 can be understood since the salt concentration is kept low, even though its zeta potential values drop from -50 to below -30 mV (Fig. 3.7(b)). Moreover, the most surprising result remains the stability of the NaBr solution at 300 μM over a large range of concentration, reaching almost 10 mM, while its counterpart at 50 μM becomes unstable since 300 μM . It means that the salt concentration is not the only parameter defining the colloidal stability, *i.e.* one has to consider the particle concentration and then the average distance between the particles. At the end, almost all the solutions saw their salt concentrations increased to an order of magnitude, except for the NaOH solutions.

Except for the NaOH solution at pH 9, relative weight distributions displayed in figures 3.8(a)-(c) and their respective insets present the same evolution between each saline solution when increasing their concentration. A scheme of this trend is proposed in figure 3.8(d) where rectangles colors and heights represent the three nanoparticles populations defined in section 3.2.1:

1. Below 0.40 g/L, the same bimodal distribution profile with two large peaks describes the primary (red rectangle) and the secondary (purple rectangle) nanoparticles populations. Only the NaCl solutions show a peak at smallest sizes, which tends to separate in two sizes categories around 6.5 and above 10 nm (Fig. 3.8(b)).

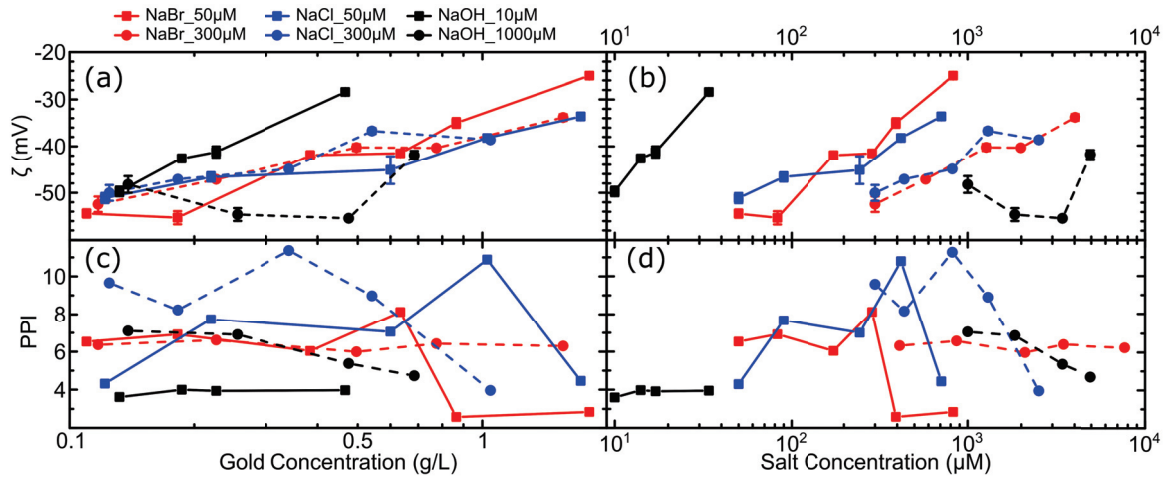


Figure 3.7 – Gold colloids synthesized in NaBr, NaCl and NaOH at two starting concentrations are characterized by the zeta potential and the PPI measurements as a function of the gold concentration, respectively (a) and (c), and the salt concentration, respectively (b) and (d).

2. Between 0.40 and 0.70 g/L, nanoparticles from 20 nm start to aggregate or grow thus shifting all the diameters toward larger sizes. As the peak of the secondary particles population above 100 nm appears reduced despite the aggregation of medium size nanoparticles, we could suspect that they grow or aggregate beyond the CPS measurements window by forming sub-microspheres or large aggregates (yellow rectangle). Consequently, as the smallest particles remain stable, the peaks of their relative weight distribution undergo a sharpening that causes the shift of the median size below 10 nm.
3. Beyond a critical concentration depending on the salt, all the smallest nanoparticles grow or aggregate at the same time, resulting on the shift of the sharp peak toward the largest sizes. At the same time, the large nanoparticles continue to grow and create more sub-microparticles.

Moreover, the results observed in the relative weight distributions seem consistent with the PPI and zeta potentials measurements. Indeed, the decrease in PPI coincides with the third step of destabilization mechanism when the primary particles peak shifts toward largest sizes. The NaBr solution at 50 μM becomes unstable between 0.63 and 0.83 g/L, and between 0.48 and 0.69 g/L in the case of NaOH at pH 11. The aggregation appears to start above 1 g/L in NaCl solutions. Only the PPI of the NaBr solution starting at 300 μM do not seem consistent in comparison to the relative weight distributions.

Finally, the decrease of the zeta potentials supports the decrease of the Coulomb repulsion and then a decrease of the stability (step 2 in figure 3.8(d)).

Relative weight distributions should be considered cautiously, since we have no information on the particles/aggregates larger than 300 nm. A larger window of observation should be necessary in

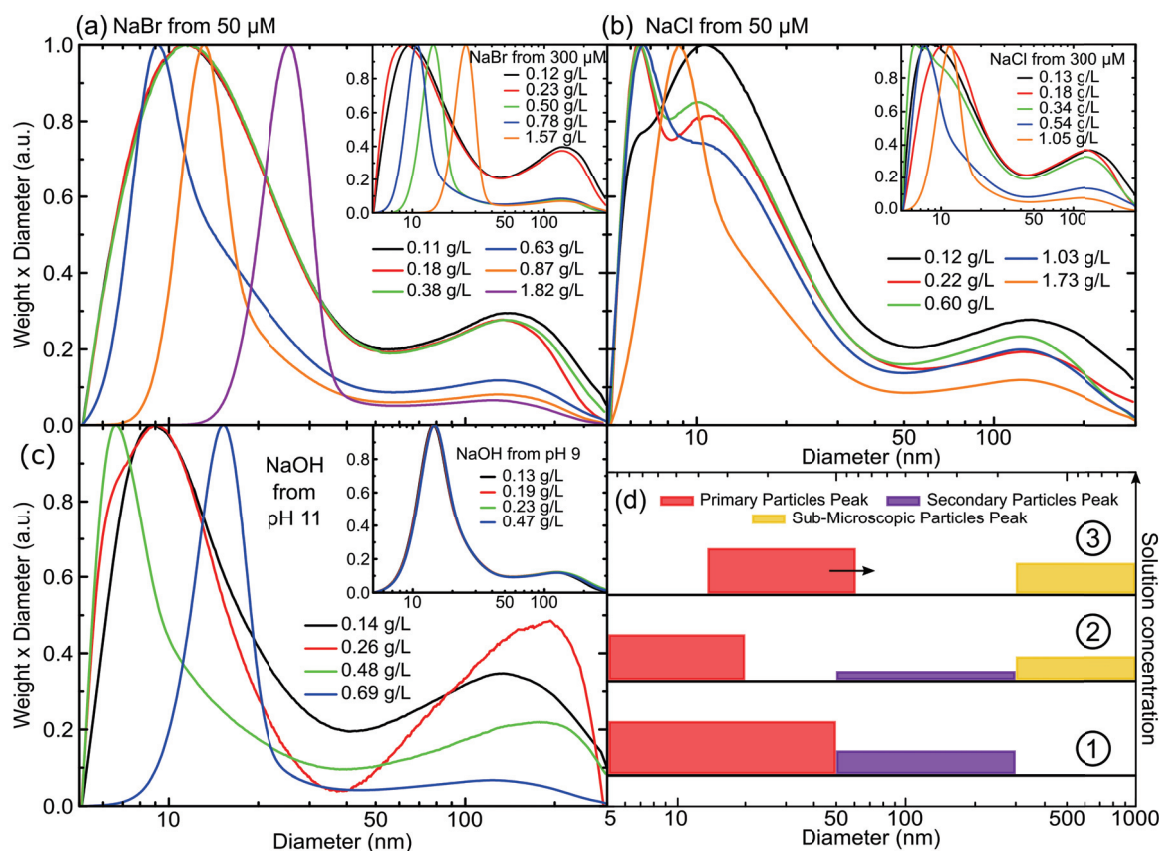


Figure 3.8 – Relative weight distributions of solutions for which their concentrations increase. We started from low salt concentrations for (a) NaBr, (b) NaCl, and (c) NaOH solutions, and higher starting salt concentrations, displayed in the respective insets. (d) Scheme of the three-step mechanism of colloidal solution destabilization.

order to confirm these assumptions. However, even if the PPI parameter is a qualitative parameter, the micronic particles contribute to its drop. Therefore, when the PPI value drop drastically as in the case of the NaBr solution starting at 50 μM , passing from 8 to almost 2, the amount of large nanoparticles can be considered to be important compared to the total material quantity.

In this study, the interesting observation is that the destabilization behavior seems to be similar starting either at low or at higher salt concentration. For instance, no significant differences are observable for NaBr and NaCl solutions, as can be seen between figures 3.8(a) and (b) and their respective insets. Hence, the destabilization appears to be independent of the initial salt concentration. When the solution volume is reduced, the mean distance between each nanoparticle is thus decreased, as well as the Debye length due to the salt concentration enhancement. Therefore, when particles are pushed to close from each other, whatever the Debye length and the charges of the particles, they have no choice than aggregate.

However, we aimed to study the mechanisms of stabilization of gold colloids from anions adsorbed

at the nanoparticles surface. In our analysis experiments, only the overall charge felt at the slipping plane are measured through the zeta potential, which differs from the charge state at the gold nanoparticles surface. A possible way to get information about the surface chemistry is then to perform X-rays Photoelectron Spectroscopy (XPS) measurements.

3.3 Surface chemistry of gold nanoparticles

3.3.1 PLEIADES beamline

Few groups carried out XPS experiments on PLAL gold nanoparticles to deduce the surface charge state, but numerous contradictions in the results make unclear their net charge. The different assumptions found in the literature are summarized in figure 3.9.

1. Sylvestre *et al.* have observed XPS signals of oxidized gold atoms located at the surface of laser-induced nanoparticles in deionized water¹⁵¹. Au⁽⁺¹⁾ and Au⁽⁺³⁾ oxide states were estimated to correspond to a total percentage of around 11 %, in agreement with coverage rates found by Merk *et al.* for particles generated in saline solutions¹⁹². The presence of oxidized Au on the surface of the laser-generated Au nanoparticles in deionized water is usually interpreted in terms of surface oxide. But such a large amount of surface oxide for gold is surprising. Mechanisms of surface charge generation were proposed when increasing the pH or adding ions^{151,284}. In the first case, surface charge is tuned by the protonation/deprotonation of hydroxide groups, already formed during PLAL synthesis.
2. The adsorption mechanism of the anions, which would lead to an increase of the surface charge, is usually assumed to be involved by surface oxides Au₂O. The charge is then localized on the oxygen atoms. A second mechanism considers the adsorption of anions on the gold surface. The anions either lose their charge by transferring to the nanoparticle or they keep their charge. In order to assess the relevancy of such mechanisms, one would precisely quantify the amount of surface oxides or anions available on the particles. XPS measurements performed on free and dry nanoparticles, without subtract or solvent effect, is then highly relevant
3. On the opposite, some studies did not observe XPS signals of oxidized Au atoms¹⁷⁷. In this sense, a third and totally different hypothesis has been considered by Palazzo *et al.*. They assume that the negative charge is already carried by an excess of electrons trapped in the gold nanoparticles²⁸⁵. Indeed, the electron density generated during the plasma phase at the early stage of the ablation process could remain embedded in the gold matrix thus limiting the ions effect to a minor role.

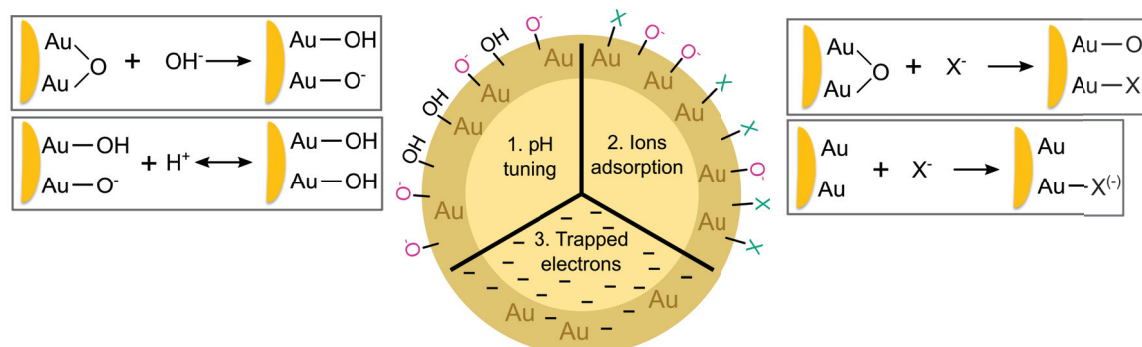


Figure 3.9 – Mechanisms of charge generation where the nanoparticle charge can be carried by oxygens due to (1) a pH tuning or because of (2) halogens adsorption. (3) Trapped electrons at high density in the nanoparticle are also envisaged.

Consequently, it becomes necessary to clarify the origin of the gold nanoparticles charge by determining surface chemistry and the origin of the "net" surface charge. For this purpose, we contributed to an international collaboration, led by Dr. Anna Levy from the NanoSciences Institute of Paris, which aimed to investigate the surface chemistry of gold nanoparticles. XPS studies on gold nanoparticles were usually performed on particles dropped on a substrate, which is known to have an influence on the surface properties. We thus aimed to probe gold nanoparticles surface in free standing conditions at the PLEIADES beamline of the SOLEIL synchrotron facility. Experiments were performed during one week, in December 2017.

This synchrotron line was designed to study by photoelectron spectroscopy isolated species from molecules to nanoparticles²⁸⁹ (Fig. 3.10(a)). In order to produce a free-standing beam of gold nanoparticles, the colloidal solution is first placed in an atomizer. Nanoparticles are thus extracted from the solution and the residual solvent is removed from the formed aerosol thanks to a silica gel dryer. The nanoparticles beam passes through an aerodynamic lens system in a carrier gas of He or Ar. Through successive apertures of decreasing diameters, the aerodynamic lens allows to produce a rather collimated beam of particles ranging from 20 to 150 nm. Then, the central part of the beam is selected with a 3-mm diameter skimmer when entering in the vacuum chamber ($< 10^{-5}$ mbar) and before being hit by the X-UV synchrotron radiation beam. Photon energies $h\nu$ at 210, 525 and 650 eV were successively selected using a monochromator and enable to eject core level electrons from atoms located at different distances from the surface (see below for details) and at 100 eV for the valence electrons. The removed electrons are captured in a hemispherical photoelectron energy analyzer. The measured quantity is thus the kinetic energy KE of the arriving electrons, which varies as a function of the atoms nature, the type of the electronic levels (valence or core electrons), their environment (chemistry), and the spin-orbit splitting. Finally, the interesting quantity remains the binding energy relative to the vacuum level BE_v , deduced by subtracting the kinetic energy KE to the X-rays photon energy $h\nu$: $BE_v = h\nu - KE$. BE_v is also related to the binding energy relative to

the Fermi level BE_F by the work function ϕ : $BE_v = BE_F + \phi$.

In our experiments, a photon energy of 210, 525 and 650 eV was successively used to probe variable surface thickness. Indeed, an ejected electron from an atom located in the nanoparticles may interact with the crystal before reaching the vacuum level. The Inelastic Mean Free Path (IMFP) λ reflects the distance for which the electron can travel before starting to scatter inelastically, namely losing its energy. A quasi-universal curve gives the general trend of the IMFP as a function of the kinetic energy of the electrons (Fig. 3.10(b))²⁹⁰. This curve is marked by a minimum ranging from 50 to 100 eV where the kinetic energy of the electrons in the 4f level of the Au atoms lies when a X-ray energy of 210 eV is selected. The corresponding IMFP is 0.44 nm for an x-ray photon energy of 210 eV. By increasing the photon energy, a longer IMFP can thus be reached, *i.e.* 0.75 and 0.89 nm at 525 and 650 eV, respectively. The maximum thickness for which electrons contribute to 95 % of the XPS signal is then considered as being $3 \times$ IMFP. Consequently, a surface thickness from 1.3 to 2.67 nm was probed by tuning the photon energy.

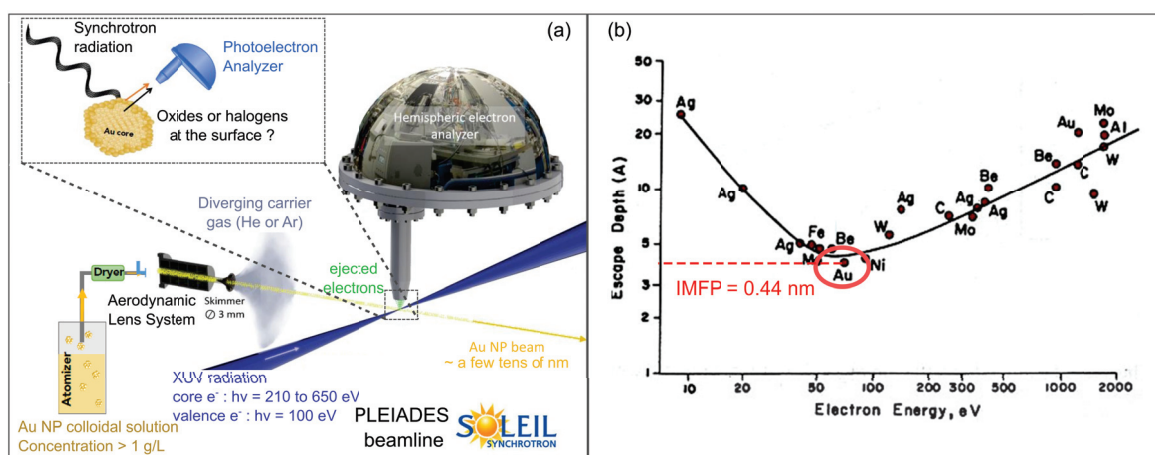


Figure 3.10 – Surface charge state of gold nanoparticles is probed in free-standing conditions using the (a) PLEIADES beamline set-up. (b) The IMFP, which allow to know the probed surface thickness, were determined thanks to the quasi-universal curve according to the kinetic energy. Data come from reference²⁹⁰.

In this collaboration, we were in charge to provide colloidal solutions of gold nanoparticles stabilized by salts and synthesized by PLAL since bare particles are necessary for such surface-sensitive diagnostic. We had to produced colloidal solution with a minimum concentration of 1 g/L. The solution has to remain stable without ligands since a thick layer of carbon would quench the XPS signal. These major constrains led to the work introduced in the previous sections. Ablations were thus performed in saline solution in the same conditions than previously, but on a longer time (from a few hours to a few days). Then, the solvent was evaporated using a rotary evaporator to reach the desired solution concentrations. Finally, three volumes of 136 and 148 mL

with gold concentration superior to 1 g/L have been obtained using NaBr and NaOH salts, respectively. The salt concentrations before ablation were fixed at 50 μM for the former synthesis and at pH 10 for the latter. The gold concentrations were determined from mass loss of the target, taking thus into account all sizes particles. Samples information are summarized in table 3.1. Absorption and size distribution analysis were also performed to control the solution quality.

	NaOH		NaBr	
	Synthesized	Concentrated	Synthesized	Concentrated
c_{salt} (μM)	100	700	50	2420
c_{Au} (g/L)	0.17	1.18	0.14	6.77
Volume (L)	1.034	0.148	6.55	0.136
Diameter (nm)	17.0 ± 6.1	-	12.7 ± 9.5	14.3 ± 9.5

Table 3.1 – Characteristics of solutions synthesized by PLAL, concentrated by solvent evaporation and analyzed in XPS measurements.

The two solutions were used during the week of XPS measurements and the stability of the samples was punctually checked by absorption. The colloidal stability was also controlled after the last run and a few months later. The nanoparticles concentration was found from resonance peak of the absorption spectra, differing from the total gold concentration measured by the target mass loss. Figure 3.11 displays the smallest nanoparticles concentration and the PPI evolution of the three samples analyzed after the PLAL synthesis, after the evaporation step, after the last XPS run and five months later.

Before the synchrotron experiments, the stability of the as-produced solutions was preserved during the concentration process, regarding the small modification of their PPI. It should be noted that the NaOH solution was less stable here with a PPI between 2.5 and 3.5 than in our previous study described in section 3.2.1. The large particles portion could have come from the small nanoparticles instability during the synthesis. Regarding the NaBr solution, the nanoparticles concentration reached around 2 g/L with a high stability corresponding to a PPI of around 7. As the absorption spectra give the concentration of small nanoparticles and that the PLEIADES set-up uses nanoparticles up to 100 nm, the total concentration of gold prevails. From a synthesis point of view, these samples fulfilled the conditions required for the XPS measurements.

During the runs on the PLEIADES beamline, the whole solution was injected in the atomizer and drier system and the solvent was removed. Consequently, the gold particles concentrations increased during the XPS measurements (not shown here). In the case of the NaBr solution, the PPI and small nanoparticles concentration dropped drastically at the end of the analysis, which means that the solution was no more stable. In the case of NaOH solution, the small particles concentration increased during the whole experiment, even if its stability started to decrease. Few months later, its PPI and its small particles concentration felt to almost 1 and 0.25 g/L, respectively.

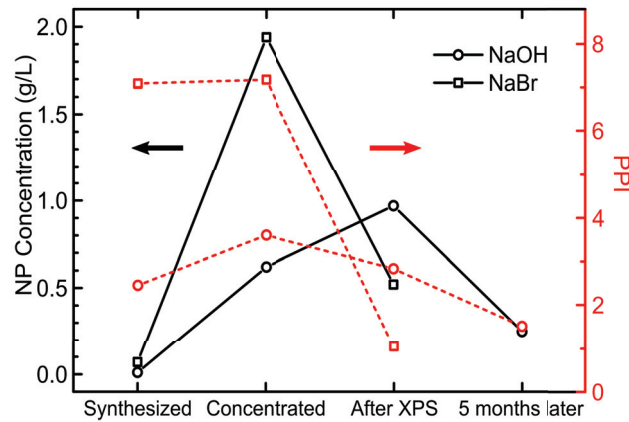


Figure 3.11 – The two synthesized solutions have been analyzed by absorption before and after the XPS experiments. The nanoparticles concentration from the absorption resonance peak (black curves) and the PPI (red curves) were thus deduced.

3.3.2 XPS results

For each solution, the 4f and 3d electrons core levels of Au and Br atoms and valence bands of the systems were respectively probed by accumulating data from several sweeps. Typically doublet peaks are found in electrons core levels spectra corresponding to the spin-orbit splitting of the electron orbital observed. Then, the experimental data have been treated by a Bayesian statistics process, described elsewhere²⁹¹, where the peaks are fitted by Voigt functions. Two models were thus compared in order to deduce the presence of oxidized Au atoms at the nanoparticles surface. In one hand, only the contribution from neutral atoms Au⁽⁰⁾ was taken into account in each doublet peak. On the other hand, the contributions from oxidized surface Au⁽⁺¹⁾ and Au⁽⁺³⁾ atoms were added in the second model. At the end, the calculated Bayesian evidence gives the relative probability that supports one model over the other.

The common element in the three solutions is the gold atoms for which the Au4f electrons have been probed (Fig. 3.12(a)). One doublet of binding energy peaks relative to the vacuum level has been reported, corresponding to the non-oxidized Au4f_{7/2} and Au4f_{5/2} spin-orbit splitting. No peaks of oxidized Au atoms have been evidenced in any solutions. This confirms results from previous XPS measurements performed on gold nanoparticles solutions made by the same collaboration two years before in the PLEIADES beamline¹⁸¹ for PLAL-synthesized gold nanoparticles in acetone. The Bayesian evidence concludes that the gold oxide presence can neither be confirmed nor exclude. So even if some oxide groups were effectively present, a coverage of less than 2 % could exist, which is insufficient to attribute the negative charge to oxidation.

A relative shift of 0.16 eV is also visible between the Au4f doublet of the NaOH and the NaBr solutions, measured respectively at (88.64 eV, 92.29 eV) for the NaOH solution and at (88.80 eV, 92.46

eV) for the NaBr solution. This small shift could be attributed to adsorbate/substrate interactions, *i.e.* halogen/gold, investigated in electrochemistry studies²⁹². The binding energy of the substrate (gold here) is expected to be slightly shifted due to the halogen adsorption because of two competing phenomena. The polarization of the substrate opposes to the adsorbate electric field and the charge transfer to the substrate, and consequently, these effects partially cancel each other.

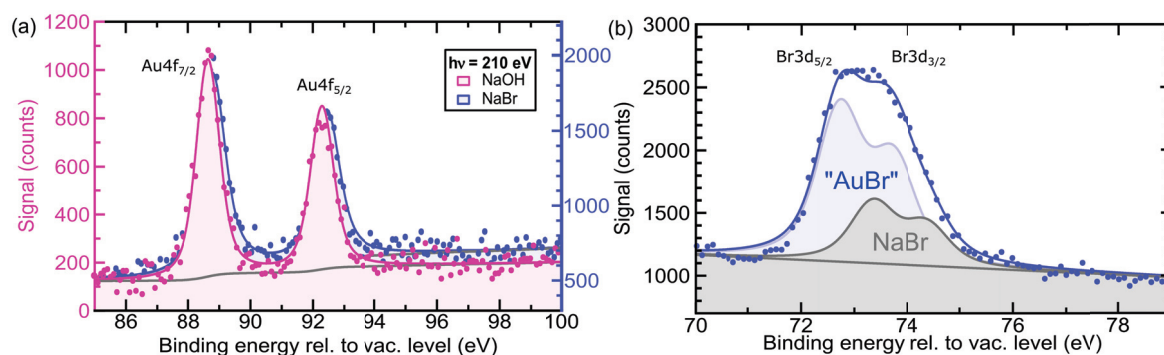


Figure 3.12 – (a) Au4f core level peaks relative to the vacuum level for both samples recorded with a 210 eV photon energy. The peaks have been fitted with Voigt functions within a Bayesian treatment. (b) The total signal of Br3d core level peaks relative to vacuum level is composed of two Br signals coming from adsorbed Br at the surface of gold nanoparticles and two other peaks from crystallized NaBr salt. The salt crystallized during the drying procedure on the PLEIADES beamline. The signal was collected independently by using NaBr solution free of gold nanoparticles.

The inner electrons of the Br3d orbitals were also tracked both in gold colloidal solutions and in saline solutions without nanoparticles. The salt concentration was adjusted in the second case to reproduce that of the first one. When passing in the dryer, the solvent evaporates leaving the dissolved ions aggregated and crystallized in salt nanoparticles.

In figure 3.12(b), the Br signal originating from the gold solution is the highest and the most broadened peak, which dissimulates two close peaks attributed to the Br3d_{5/2} and Br3d_{3/2} spin-orbit splitting. The pure nanocrystals of salt correspond to two smaller peaks shifted but included in the total signal. After a fitting treatment and a signal differentiation, we deduced that the total peak is composed of the summation of the Br contributions from the salt nanoparticles and from the Br ions attached to the gold nanoparticles, called "AuBr". This is the first evidence of the bonding of Br adsorbates on gold nanoparticles surface.

Moreover, the halogen signal seems to depend strongly on their environment. This is shown in figure 3.12(b) by a shift of 0.63 eV between the two signals. Similarly to the slight substrate shift, adsorbate binding energy suffers also from the influence of its environment. Previously, the two physical phenomena compete. This time, it was shown that the two effects become additive²⁹², meaning that the adsorbate binding energies are highly modified depending on the atoms where Br anions adsorb.

The partial coverage of Br ions was also calculated according to the following relation:

$$Br/Au = \frac{A_{Br}^{norm}}{A_{Au}^{norm}} = \frac{A_{Br}}{\sigma_{Br}} \times \frac{\sigma_{Au}}{A_{Au}} \quad (3.4)$$

A_i corresponds to the XPS peak area of the atom of specie i , already normalized by the respective accumulation time and σ_i is the surface cross-section of the electrons core level of the probed atoms. Typically, cross-sections at 210 eV are equal to 2.76 and 5.31 Mbarn for Au4f and Br3d core levels, respectively. Finally, the coverage rate for Br/Au was comprised between 42 and 51 % by increasing the photon energy. That means that halogen anions are still present when probing deeper into the nanoparticles surface.

Finally, the signal of the valence electrons of gold atoms was measured for every solution to deduce the work functions ϕ (Fig. 3.13). The work function is defined as the energy difference between the vacuum level and the last occupied electron level. Therefore, by removing the valence electrons with the X-rays beam, the apparition of the signal indicates the beginning of the electron density of states. As noted on the graph, the work functions determined from these measurements show the following order: $\phi(NaOH) = 4.2 \text{ eV} > \phi(NaBr) = 2.9 \text{ eV}$.

However, information are difficult to extract from work functions without reference values. Indeed, these physical quantities depend on many parameters, such as the dipole moment induced by the Br/Au interactions, the charge transfer from the Br to the gold atoms and the coverage rate of adsorbate.

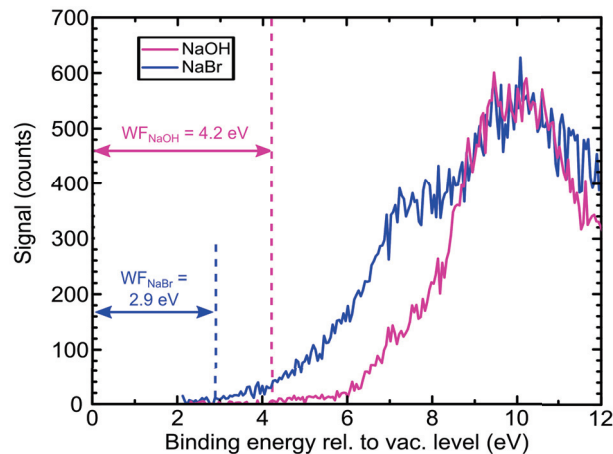


Figure 3.13 – Valence band of the nanoparticles probed at 210 eV showing the work function. The work function appears to depend on the salt.

3.4 Conclusion

In conclusion, we saw that the stability of gold nanoparticles colloidal solutions can be achieved thanks to dissolved ions. Destabilization of the synthesis seems to originate from the increase of the gold particles concentration rather than the salt concentration. However, nanoparticles aggregate beyond a critical salt concentration. Such electrostatic stabilization is addressed to the double layer generated by ions around particles. However, we aimed to understand the stability mechanisms of the anions adsorbed in the Stern layer.

Therefore, we performed XPS measurements to probe the surface chemistry of gold nanoparticles synthesized with salts. The adsorption of the half of the surface of gold nanoparticles by halogen ions has been evidenced in a free-standing nanoparticles beam. On the opposite, no oxidation proof has been reported in Au4f binding energy spectra. Thus, the adsorption mechanism of halogen anions usually assumed, which involves an oxygen atom, appears unlikely. As work functions are sensitive to the surface charge state, we may obtain interesting information about the surface chemistry, but at the current state, no explanation allows to properly conclude.

In addition, more questions remain after these first results. Firstly, even though the Br ions adsorb on gold surface nanoparticles, the type of bonds is not elucidated yet, namely Au-Br or Au-Br⁻ bonds, which could bring insights about the charge carrier. Secondly, even if non-oxidized gold atoms have been observed, it does not indicate that oxygens were not present in solution at the nanoparticles surface. Oxygen may desorb during the atomizer/dryer steps. Thirdly, if we consider that the halogen ions fix to the gold atoms through Au-Br bonds, and the oxygens disappear during the free-standing beam process generation, how can we deduce where the charge carrier is? The charges could have gone with the oxygens, or they have been transferred in the nanoparticles to contribute to the excess of electrons assumed by Palazzo *et al.*²⁸⁵.

Theoretical calculations have been initiated in order to answer these questions. Indeed, we expect that the VASP calculations could assign the binding energy peaks of the bromium atoms to either the Au-Br or Au-Br⁻ configurations. More generally, different scenarios with different ions need to be calculated to estimate which ion is susceptible to adsorb and to evaluate the most likely adsorption mode. The influence of adsorbate and substrate on binding energy and work functions leading to the observed shifts could be evaluated also by electronic calculation methods.

CHAPTER 4

CRYSTAL STRUCTURE CONTROL BY STABILIZING LIGANDS

Contents

4.1 Nano-rubies synthesis driven by ligands	87
4.1.1 Synthesis by PLAL	87
4.1.2 Characterization measurements	89
4.2 Stability of alumina polymorphs	95
4.2.1 Theoretical methods	96
4.2.2 Potentials benchmarking	99
4.2.3 Polymorphs stability from clusters to nanoparticles	104
4.3 Mechanical structure of ligand-free and capped alumina nanoparticles	112
4.3.1 SMTBQ calculations	113
4.3.2 VASP calculations	116
4.4 Conclusion	120

Inorganic materials may exist in various polymorphs according to the temperature and pressure conditions as well as the particles size. Bulk polymorph corresponds to the crystal structure with the lowest volume free energy. Structures minimize their total energy in order to gain in stability. At nanoscale, the surface energy of crystals becomes predominant over the bulk free energy due to a large surface-to-volume ratio. Polymorphs with low surface energy may thus be stabilized at the nanoscale, even though they are metastable in the bulk. Therefore, several crystal structure transitions may occur during the nanoparticles growth until reaching the bulk equilibrium. Among numerous materials presenting phase transitions at nanoscale, alumina nanoparticles are a prime example of material experiencing crossovers in polymorph stability, with two polymorphs crossover identified. Using calorimetry experiments, previous studies have shown that alumina crossovers occur from amorphous solid to cubic crystal (γ) at about 4 nm, in one hand, and from cubic to the hexagonal phase (α , *i.e.* corundum) at almost 12 nm, in another hand. Moreover, the surface energy of crystals is also governed by the surface chemistry depending on the nanoparticles environment. Adsorption of ligands could lead to the stabilization of metastable polymorph in addition to particles size and colloidal stability control. For alumina, organic ligands could stabilize alumina nanoparticles in the α -Al₂O₃ crystal phase for sizes below 10 nm, which is unexpected according to the calorimetry measurements. The use of PLAL is particularly suitable to investigate ligands effect since we can synthesis bare or capped nanoparticles.

In this chapter, we will first investigate the influence of ligands on PLAL-synthesized nanoparticles from a ruby (α -Al₂O₃:Cr³⁺) target. Then, we studied theoretically the influence of ligands on alumina mechanical structures. In a first project, we were interested to investigate the alumina crystal structures by reproducing the polymorphs stability regions deduced by calorimetry experiments. From the numerical point of view, addressing such transition requires a numerical method sustainable (computational time) and reliable (reliability of the computed energy) from a few atoms to a few hundred thousand of atoms, *i.e.* from small cluster to nanoparticles. In this context, we chose to use empirical potentials for which their reliability and accuracy need to hold from the molecular level to almost bulk-like systems. Surprisingly, we found that while complex potentials have been usually employed to model alumina, the most reliable potential was the simplest in its form, which fulfilled the description of alumina polymorphs stability over a large range of sizes. In a second project, we aimed to study the mechanical structure of the α phase of uncapped alumina nanoparticles using a charge variable empirical potential. Finally, we performed electronic calculations on ligand-free and capped α alumina surfaces, since empirical potentials are not able to take into account ligands in nanoparticles calculations. The calculations based on empirical potentials are described as well as the DFT-based calculations specifically performed for the treatment of the surfaces. We then observed a strong stabilization effect of the ligands on the mechanical structure of alumina.

We investigated the Cr^{3+} luminescence R-lines that surprisingly do not appear significantly shifted with respect to the bulk in our experimental measurements. Indeed, the chromium emission in corundum alumina is an efficient structural probe. Series of atomistic simulations using both classical molecular dynamics and Density Functional Theory (DFT) techniques were conducted to support the interpretation of the experiments. We found that surface relaxations induce a negative pressure inside the free $\alpha\text{-Al}_2\text{O}_3$ nanoparticles where the chromium atoms tend to localize. However, the presence of ligands almost annihilates the surface relaxations and restores a bulk-like structure consistently with the measured luminescence lines.

4.1 Nano-rubies synthesis driven by ligands

Crossover in polymorph stability was reported for several materials including TiO_2 ^{293–296}, ZrO_2 ^{297–299}, Fe_2O_3 ³⁰⁰, Gd_2O_3 ³⁰¹, GeTe ³⁰², Y_2O_3 ³⁰³ or Al_2O_3 . The latter material is under the scope of this work where $\alpha\text{-Al}_2\text{O}_3\text{:Cr}^{3+}$ nanoparticles below 10 nm are deemed thermodynamically unfavorable. In the following, the effect of ligands on nanoparticles will be investigated by synthesizing alumina colloids with and without ligands. The experimental protocol will be presented as well as the characterization analysis.

4.1.1 Synthesis by PLAL

4.1.1.1 Challenges with aluminum oxide

Aluminum oxide is of a great interest to its optical properties. By doping a matrix of Al_2O_3 with different ions, the resulting luminescent properties are useful in several applications. Doped with titanium, alumina crystal has been used to develop Ti-sapphir laser. $\text{Al}_2\text{O}_3\text{:C}$ shows photostimulable properties, and is used as an optically stimulated luminescence (OSL) dosimeter in radiation protection applications or in environmental dosimetry³⁰⁴. $\alpha\text{-Al}_2\text{O}_3\text{:Cr}^{3+}$ or ruby is widely employed as a pressure gauge in diamond anvil cell³⁰⁵. Indeed, the chromium luminescence in corundum is characterized by two sharp peaks that shift to higher wavelength (red-shift) as the external pressure is increased. As can be seen in the inset of figure 4.1(b), these R-lines are defined at $R1 = 694.2$ nm (14405 cm^{-1}) and $R2 = 692.76$ nm (14435 cm^{-1})³⁰⁶. With the current trend in reducing size of the studied systems, designing nanoscale pressure sensors based on nano-rubies should be of a great interest.

However, various alumina polymorphs exist according to pressure and temperature conditions as well as the size³⁰⁷. The hexagonal phase ($\alpha\text{-Al}_2\text{O}_3$), commonly called corundum, is the thermodynamic stable phase of crystalline aluminum oxide in the bulk until high temperature and pressure. Regarding size effects, McHale *et al.*^{308,309} measured experimentally that the corundum phase remains the most stable polymorph for particles as large as 12 nm. A first transition occurs between

the hexagonal phase and the cubic phase ($\gamma\text{-Al}_2\text{O}_3$) below this critical size. In figure 4.1(a), this crossover is represented by the evolution of the enthalpy of the considered polymorph relative to that of corundum as a function of the surface area (or the diameter of particles). A second transition was measured by Tavakoli *et al.*³¹⁰ at smaller size and they have shown that the alumina particles become amorphous ($a\text{-Al}_2\text{O}_3$) below 4 nm.

In addition, the sharpened luminescence lines of ruby exist only from chromium inserted in $\alpha\text{-Al}_2\text{O}_3$, while a weak broad band is observed in the case of ions incorporated in $\gamma\text{-Al}_2\text{O}_3$ ³⁰⁶ (Fig. 4.1(b)). Therefore, the synthesis of ruby at small sizes remains challenging.

Alumina was extensively synthesized by PLAL where different polymorphs have been produced such as $\gamma\text{-Al}_2\text{O}_3$ ^{107,311–315}, $\theta\text{-Al}_2\text{O}_3$ ³¹³ and hydroxydes^{315–317}. This synthesis is convenient to carry out by ablating a target of alumina or aluminum solid in water.

PLAL has already demonstrated its versatility to overcome the thermodynamic related issue. Sajti *et al.* succeeded to synthesize alumina nanoparticles with an average size larger than 30 nm³⁷. Kumar *et al.* also reported PLAL synthesis of spherical Al_2O_3 nanoparticles with an average size of 23 nm, without mentioning any crystallographic phase. To our best knowledge, no evidence of $\alpha\text{-Al}_2\text{O}_3$ nanoparticles with sizes smaller than 10 nm have been reported in PLAL at all, even including previous PLAL-synthesized alumina in bulk water.

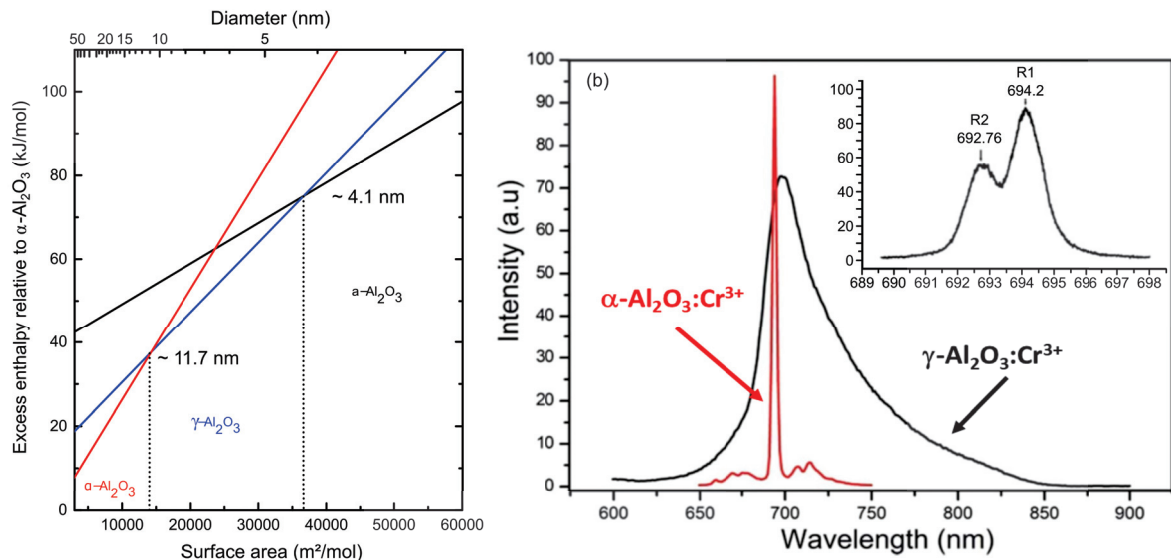


Figure 4.1 – (a) Polymorphs stability ranges of alumina according to their enthalpy relative to corundum as a function of the particle surface area and diameter (Reproduced from³⁰⁸ and³¹⁰). (b) Luminescence spectra of chromium ion incorporated in $\alpha\text{-Al}_2\text{O}_3$ and $\gamma\text{-Al}_2\text{O}_3$ matrix. Sharp peak of Cr-doped alumina reveals (inset) the two characteristics R-lines at high resolution (Reprinted from³⁰⁶).

4.1.1.2 Nano-rubies synthesis

In this study, a $\alpha\text{-Al}_2\text{O}_3:\text{Cr}^{3+}$ target has been ablated with and without organic ligands in deionized water. In order to favor the Al_2O_3 stoichiometry, the ablation was performed on a 2 mm thick Cr-doped sapphire crystal grown by the Czochralski technique, elaborated by Kheirredine Lebbou's team in our institute^{318,319}. The final Cr concentration in the grown crystals is about 1.5%. The PLAL synthesis was done during 60 min using the IR laser system and by passing 500 mL of a solution of deionized water containing 10^{-2} mol.L⁻¹ of 2-[2-(2-methoxyethoxy) ethoxy] acetic acid (MEEAA) (from Sigma-Aldrich, CAS Number 16024-58-1) in the flow cell circuit. The ligands structure is shown in inset of figure 4.3. For comparison, the same experiment was performed without ligands. Final solutions were estimated to be produced with an ablation rate of around 0.13 g/h, deduced from the weighting of the target. But we know that such a value largely overestimated the amount of nanosized materials. Nanoparticles powder is then obtained following a washing process. The whole colloidal solution is first frozen in a freezer before being dried using a freeze-drier. Then, the dried powder mixed with the remaining unreacted MEEAA is diluted in 5 ml of deionized water. A smooth centrifugation is performed to remove the biggest particles at 966 RCF (3000 RPM) during 10 min. The limpud supernatant is then subjected to a wash cycle to remove most of the free ligands. The limpud supernatant is diluted in 50 mL of acetone, leading to the precipitation of the nanoparticles. A second centrifugation is performed at 21036 RCF (14000 RPM) during 10 min. The precipitate is then withdrawn and dried.

In order to check the reproducibility, a second synthesis was performed independently one year apart by a PhD student, Arsène Chemin, in our group (synthesis called "ILM2" in figure 4.2). Moreover, a last synthesis was also reproduced by Dr. Julien Lam in the Barcikowski's group from Duisburg-Essen university (synthesis called "Essen" in figure 4.2). This latter ablation was carried out with MEEAA at the same concentration in deionized water with a diode pumped Nd:YAG laser from Ekspla operated at 1064 nm. The laser has a pulse duration of 10 ps, a repetition rate of 500 kHz, and an average power of 10 W.

4.1.2 Characterization measurements

4.1.2.1 Structural characterization

Transmission Electron Microscopy. As not enough material was produced to characterize the nanoparticles by X-Rays Diffraction (XRD), the particles crystal structure and the size distribution were deduced from images captured by Transmission Electron Microscopy (TEM). The experimental methods and conditions are similar to those described in section 3.1.2.

Low resolution TEM pictures show that addition of MEEAA results in homogeneous and monodispersed nanoparticles, separated uniformly in a large area. Figures 4.2(a) and (c),(d) display the low resolution TEM pictures for the ILM2 synthesis and the synthesis I reproduced. Without sta-

bilizing agents, particles are particularly polydispersed with sizes from a few nanometers and sub-micrometer objects, and also aggregated (inset in figure 4.2(f)). This is a first proof that ligands attached to the nanoparticles surface enable to avoid aggregation, as was already demonstrated for other doped oxides¹⁶⁹ including $\text{Y}_2\text{O}_3:\text{Eu}^{3+}$, $\text{Gd}_2\text{O}_3:\text{Eu}^{3+}$, and $\text{Y}_3\text{Al}_5\text{O}_{12}:\text{Ce}^{3+}$.

In the ILM2 synthesis, crystal phases of nanoparticles were deduced by analyzing electronic diffraction patterns from the fast Fourier transforms (FFT) of high resolution images using the Digital Micrograph software from Gatan (Fig. 4.2(b)). Thanks to international diffraction databases such as the International Centre for Diffraction Data (ICDD) or the Inorganic Crystal Structure Database (ICSD), crystallographic planes (using the miller indices (hkl)) and zone axis (noted [uvw]) were measured. (113) planes were found to correspond to the inter-reticular distance $d_{(113)} = 0.2085$ nm of the α phase (ICDD file 00-046-1212) for the solutions synthesized with the ligands (Inset of figure 4.2(a) for the ILM2 synthesis and figure 4.2(d)). Without ligands, the particles were in majority characterized by the γ phase (ICDD file 04-005-4662) (Fig. 4.2(f)).

Nanoparticles diameters were measured manually from different large field TEM images using ImageJ software and the deduced size distributions were fitted by log-normal distribution curves (Fig. 4.2(e)). In this work, nanoparticles diameters of 3.2 ± 1.3 nm were measured for capped nanoparticles, which are consistent with the reproducibility assay where size distributions are centered around 4 nm with standard deviation around 1 nm. Size distributions for the uncapped nanoparticles were difficult to carry out since the small particles aggregate as we can see in figure 4.2(d). Measuring the distinct particles would lead to biased distribution toward the large sizes.

Infrared spectroscopy. As revealed by the TEM pictures, ligands functionalized to the nanoparticles surface, leading to their stabilization. A more direct evidence of the ligands bonding is revealed by Fourier Transform Infrared (FTIR) spectroscopy. FTIR spectra correspond to absorption in the infrared range due to bond vibrations, and can then reveal the nature of the coordination of the ligands to the surface (*i.e.* of the carboxylic group to the metal ions). Spectra were recorded with a *spectrum 65* FT-IR spectrometer from Perkin-Elmer, with an universal attenuated total reflectance (ATR) sampling accessory. Dry matter was deposited on a silicon substrate and placed in the focal plan of a microscope objective. The surface observed was $100 \mu\text{m} \times 100 \mu\text{m}$ and the spectral resolution is 2 cm^{-1} .

Each peak highlighted in the spectra, shown in figure 4.3, corresponds to bending or stretching vibrations of the acid polar head of MEEAA molecules, protonated or not according to its environment. In the case of free ligands in water (grey curve), peaks located at 1740 cm^{-1} and 1200 cm^{-1} correspond to the stretching of C=O and C-OH bonds, respectively. The interaction of ligands at the oxide surface (black curve) results in the deprotonation of the carboxylic group and then to the coordination of the COO⁻ group to the surface. Types of coordination are known between oxygens of the carboxylic head and metal ions³²⁰ and are schemed on the top of the figure 4.3.

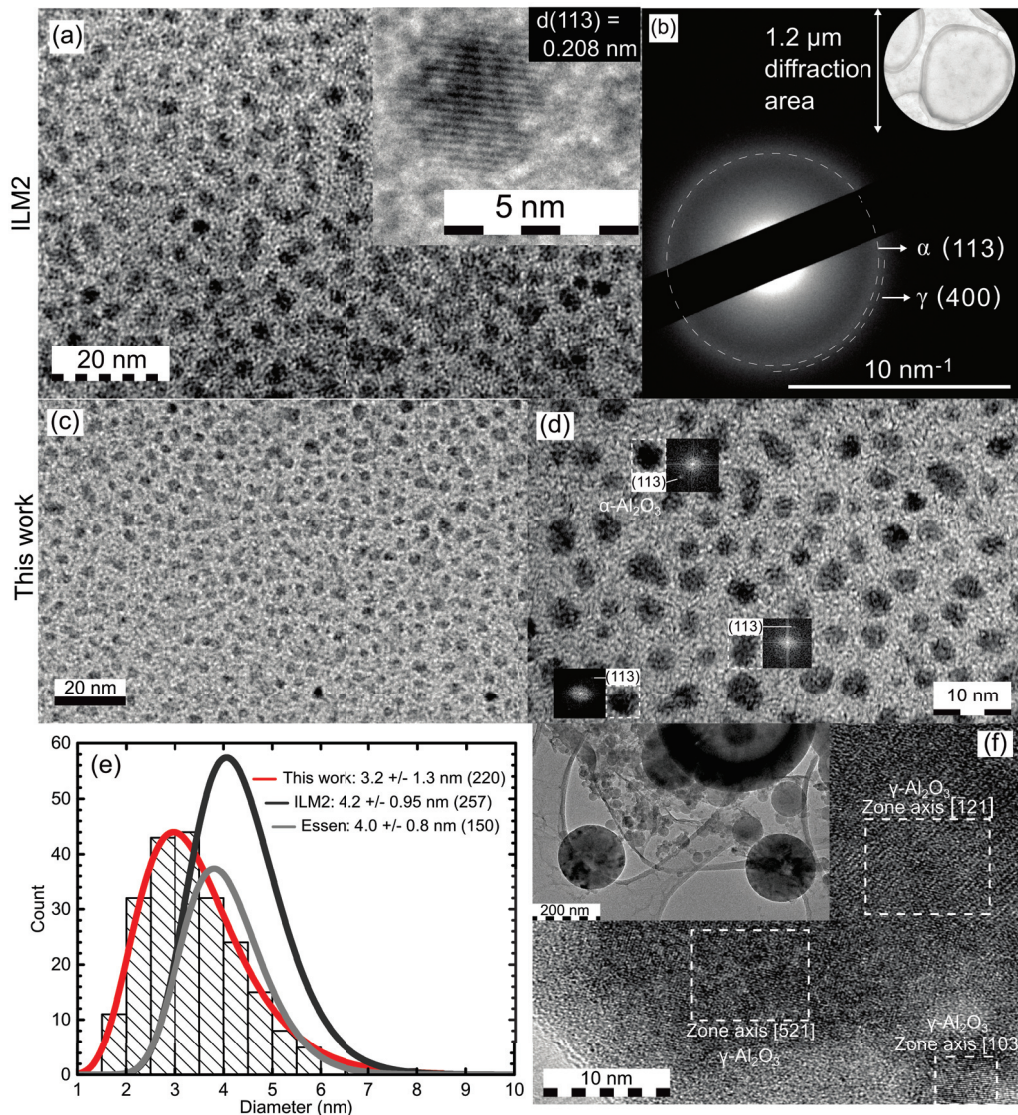


Figure 4.2 – (a) Low resolution TEM picture of the ILM2 synthesis showing a large area covered by monodispersed nanoparticles. The α phase is deduced by a (b) diffraction pattern from the large area shown in the inset. The dashed circle corresponds to the inter-reticular distance $d_{(113)}$ at 0.2085 nm of the α phase (ICDD file 00-046-1212). It is differentiated from the inter-reticular distance $d_{(400)}$ at 0.1978 nm of the γ phase (ICDD file 04-007-2479). (c),(d) Reproducible synthesis was performed in this work, which leads to the production of the same α monodispersed nanoparticles as showed by the low resolution TEM pictures and by measuring the inter-reticular distances. (e) Log-normal size distribution curves of the nanoparticles from all the synthesis. Only the histogram of this work is displayed. (f) High resolution TEM picture of alumina particles synthesized in deionized water. A low resolution TEM picture is displayed in the inset.

Hence, the coordination of the carboxylic head affects the FTIR spectrum of MEEAA ligands in the case of capped nano-rubies. When coordinated to a surface, the signals coming from the protonated carboxylic head tend to disappear, and the signatures of the coordination appear, as shown by grey arrows in figure 4.3. Among them, two main peaks located at 1584 and 1422 cm^{-1} are assigned to antisymmetric ν_{as} and symmetric ν_s stretching vibrations of COO^- group, respectively. Nara *et al.* have demonstrated that the gap between these two peaks $\Delta\nu$ is related to the interaction modes for a given metal ion³²¹. ν_{as} and ν_s frequencies have been tabulated for numerous metal acetate combinations^{322,323} and the four interaction modes have been found to be ordered according to the frequency difference $\Delta\nu$ ^{320,321}:

$$\begin{aligned} \Delta\nu(\text{chelating}) = 40 - 80 \text{ cm}^{-1} < \Delta\nu(\text{bridging}) = 140 - 170 \text{ cm}^{-1} \\ \approx \Delta\nu(\text{ionic}) < \Delta\nu(\text{unidentate}) = 200 - 300 \text{ cm}^{-1} \end{aligned} \quad (4.1)$$

In our case, $\Delta\nu$ is estimated to be 162 cm^{-1} , indicating a bridging bidentate or ionic bonding with the aluminum ions. The former mode is favored since the obtained value is in agreement with results of previous studies, which used MEEAA as ligands for several materials^{169,324}.

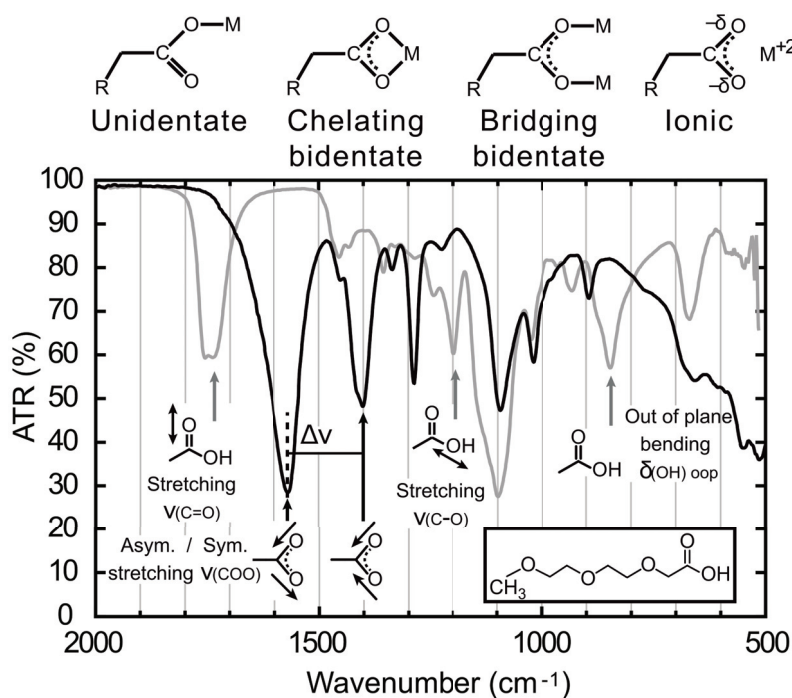


Figure 4.3 – Comparison of FTIR spectrum of ligands-capped nano-rubies (black curve) with that of the MEEAA ligands alone (grey curve). MEEAA ligand molecule is represented by the scheme in inset. It reveals that ligands attach to the nanoparticles in a bridging bidentate mode, different from the three other coordination types (top panel).

4.1.2.2 Optical characterization

Luminescence spectroscopy. High resolution luminescence spectroscopy of the final dried nanoparticles is a rapid way to confirm that α particles were obtained since it is the only structure exhibiting the R luminescence lines. Laser-generated nanoparticles were characterized by using a monochromator Ramanor U1000, from Jobin Yvon, with 1 m focal and a 1800 lines/mm grating. It had been coupled with an iStar intensified CCD (iCCD) from Andor technology. The instrumental spectral resolution is 0.05 nm. Calibration of the wavelengths was performed with two spectral calibration lamps. The optical response of the entire collection system was measured through a calibrated blackbody source and the spectra were thus corrected by the apparatus spectral sensitivity. The sample excitation is performed at 455 nm, using a collimated LED M455L2-C2 from Thorlabs.

Therefore, we recorded R-lines from our nanoparticles powder capped by ligands and with sizes below 10 nm. However in the case of the synthesis without ligands, the polydispersed distribution includes particles substantially larger than 10 nm, and larger particles are in the α phase. Nano-rubies spectrum is plotted by the dark blue curve in figure 4.4(a). For comparison, the bulk target (red curve) and microparticles powder (dark green curve) were also measured. Inhomogeneous broadening is observed only for nano-rubies spectrum, which is characteristic of the luminescence emission from doped nanoparticles when an annealing of the as-produced particles is not performed¹⁶⁹. R-lines positions were determined by fitting peaks with two Lorentzian functions, accurate at $R^2 = 0.991$ with a confidence interval of 95 %. Peaks positions are indicated on the top of figure 4.4(a), where the rectangle width represents the instrumental spectral resolution. Particles powders peaks appear slightly shifted by around 0.1 nm towards the high wavelengths, while bulk target R-lines remain close to the tabulated values, within the instrumental resolution. This small shift does not come from the experimental measurement errors since it is larger than the resolution of the spectrometer. But it can be explained by a self-absorption artifact, as this difference is only observed for particles powders. Indeed, as the refractive indexes of air and ruby are different, *i.e.* they differ by 0.76, a sample composed of powders (nano or micro) strongly diffuses the emitted light, enhancing self-absorption with respect to a bulk sample. As a very small mismatch exists between the emitted and absorbed signals, namely a Stokes shift^{325,326}, such self-absorption is asymmetric with respect to the wavelength, and leads to measure a lowered intensity and a shifted peak position, as schemed in figure 4.4(b). To ensure this assumption, luminescence measurements were performed by homogenizing the powder environment with a liquid of refractive index lowering the diffusion. We use 1-chloronaphthalene liquid with a refractive index of 1.63 at 20°C. The new luminescence peaks are this time closer to the bulk peaks positions, as shown in figure 4.4(a) by the lighter colors curves of micro- and nanoparticles wet powders.

Consequently, no shifts are observed from macroscopic size to nanoscale. This is surprising since such luminescence experiments allow for probing the environment of the emitter. Indeed, in the

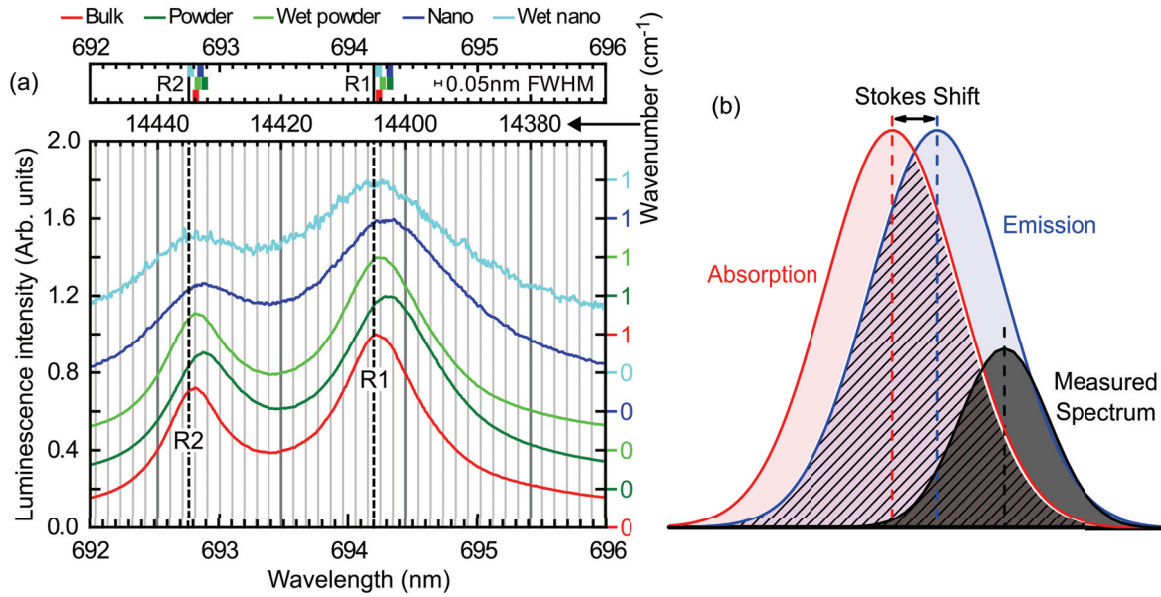


Figure 4.4 – (a) Ruby R-lines were measured by high resolution luminescence spectroscopy for dry (dark) and wet (light) powders of micro- (green) and nano-size (blue) particles as well as bulk target (red). A liquid of refractive index of 1.63 was used for the wet powders. The curves are normalized to 1. Ordinates 0 and 1 for each curve are displayed on the right vertical axis. Top panel displays their R1 and R2 lines positions where the width of the squares correspond to the instrumental spectral resolution. (b) Self-absorption combined with a weak Stokes shift results in a lowered intensity and a signal slightly shifted.

case of bulk ruby, aluminum atoms are substituted by chromium ions thus standing in trigonal site. Chromium are very sensitive to their site symmetry where the minor fluctuation due to an applied strain induced by an external pressure or the creation of an interface leads to the modification of the crystal field. Hence, the energy levels of the embedded chromium evolve, especially the energies corresponding to the luminescent R-lines. Finally, this is why the chromium emission lines are pressure sensitive in bulk. Yet, the lack of pressure shift measured in the synthesized nanoparticles seems to indicate that chromium ions remain in the symmetry of their bulk sites and there is no huge stress inside the nanoparticles.

However, recent studies have considered that an internal pressure exists inside the nanoparticles^{235,327}. Such intrinsic quantity, or also called the Laplace pressure P_{int} , was initially defined for a spherical fluid as the combination of the pressure of the surrounding media P_{ext} , plus another pressure term that relates the surface tension γ of the sphere with its curvature radius R :

$$P_{int} = P_{ext} + \frac{2\gamma}{R} \quad (4.2)$$

However, this law was used for micro-size particles of gas, liquid or isotrope metals (such as copper

agregates), on the contrary of the case of solid nanoparticles composed of iono-covalent materials (with bonds strongly oriented). If we apply Laplace relation for spherical nanoparticles, the internal pressure increases inversely proportional to the particle radius. For sizes from 3 to 4 nm as observed in TEM, our nano-rubies should sustain theoretical pressures between 2.25 and 1.70 GPa, by considering the ambient pressure and a surface tension equals to 1.69 J/m^2 ³⁰⁸. By considering a linear relation between the R1-line shift and the applied pressure^{328,329}, such pressures should be observed in our luminescence measurements and would correspond to shifts ranging between 0.8 and 0.6 nm, which are clearly not visible in our luminescence results.

To summarize, we found that the solutions synthesized with ligands lead to more controlled nanoparticles in size, and to a better colloidal stability of the alumina nanoparticles. Although all the nanoparticles cannot be systematically analyzed, most of the analyzed particles below 10 nm seem to form in α phase. On the opposite, the solution without ligands showed particles more poly-dispersed for which the γ phase appears predominant. Moreover, the synthesis of size controlled colloids using ligands seems reproducible, even with different ablation equipment. The ligands influence also the luminescence properties of nano-rubies. The expected shift of luminescence R-lines of chromium in α alumina nanoparticles is not visible in our measurements. Therefore, we performed a comprehensive theoretical study in order to investigate the polymorphs of alumina at nanoparticles size, and the influence of ligands on the mechanical structure of alumina in α phase.

4.2 Stability of alumina polymorphs

In a first project, we aimed to evaluate the crystal structures of alumina at nanoparticles size through a theoretical approach, which can give insights about the atomistic understanding of nucleation and growth of bare nanoparticles.

Calculations methods at various length scales have been developed along the XXth century since the revolution of quantum mechanics. Numerous simulation approaches allow for modeling different kinds of systems from the atomic scale using electronic approaches to the mesoscopic scales using empirical potentials. I will first briefly review the computational methods available for different ranges of size.

Then, we chose to use empirical potentials to investigate the crystal structures of alumina particles by reproducing the polymorphs stability regions from a few atoms to a few tens of thousands of atoms. We confronted four different empirical potentials that have been already employed in previous alumina studies. I will describe the empirical potentials as well as the analysis tools implemented to assess the calculation results. Finally, I will present the results obtained from this benchmarking where the polymorph stability regions predicted by each potential are compared with calorimetry measurements.

4.2.1 Theoretical methods

Numerous simulation methods exist to calculate systems from atoms to nanoparticles. We can categorize them in two groups. On the one hand, computational chemistry methods are based on the resolution of the Schrödinger equation using a wavefunction/Hamiltonian formalism. The size of systems treated by electronic calculations is limited due to the large computational cost. On the other hand, other methods have been developed to simplify the calculations by using empirical potentials.

4.2.1.1 Quantum chemistry methods

Computational chemistry is used to simulate systems at the electronic and atomic scales based on quantum mechanics. These methods are based on the wavefunction/Hamiltonian formalism derived from the Schrödinger equation in the stationary case, defined as:

$$\hat{H}\Psi(\vec{r}) = E(\vec{r})\Psi(\vec{r}) \quad (4.3)$$

with $\hat{H} = T_e + V_{ee} + V_{en}$

where \hat{H} is the Hamiltonian operator expressed under the Born-Oppenheimer approximation³³⁰. A quantum system composed of atoms is thus described by contributions attributed to electrostatic charges distributed between nuclei and electrons. Kinetic energy of electrons T_e is taken into account by the first term, while the nuclei are considered fixed compared to electrons. Coulomb interactions are described by the electronic repulsion V_{ee} , as well as the nuclei/electrons attractive term V_{en} . The state of this system is described by the wavefunction Ψ and its energy E is obtained after the resolution of the Schrödinger equation. From these quantities, it is thus possible to determine the physico-chemical properties of the system. A more detailed description is reported in Appendix B.1.

From this Hamiltonian consideration, the analytic resolution of the Schrödinger equation is prevented by the electronic interaction term V_{ee} for polyelectronic systems. From this observation, numerous calculations methods based on this wavefunction-Hamiltonian formalism have been developed according to the way to handle this problem. They include *ab initio* (or first-principles) approaches and Density Functional Theory (DFT) based calculations. However, the size of the system treated by electronic calculations is limited due to the large computational cost. Other methods have been developed to simplify the calculations by doing several approximations in the wavefunction/Hamiltonian formalism such as semi-empirical methods or describing the systems by empirical potentials.

***Ab initio* methods.** One of the earlier *ab initio* methods is the Hartree-Fock (HF) approach³³¹

for which the electronic interactions are averaged in a mean field. The wavefunction of the total system is then decoupled as the product of mono-electronic wavefunctions in the formalism of a Slater determinant³³², and the Hamiltonian is written as a sum of mono-electronic hamiltonians. In HF calculations, correlations between electrons located at short (dynamic or instantaneous correlation) and long (static or permanent correlation) distances are thus not included, leading to energy over-estimation as in the case of H₂ molecule dissociation.

In post Hartree-Fock methods, the electronic correlation is taken into account by developing the system wavefunction as a linear combination of several Slater determinants, which characterize excited electronic states. This means that some electrons of the systems are excited in unoccupied highest levels. Generally, only few orders of determinants are taken into account to avoid too exhausting calculations. Among others, the Moller and Plesset model (MPn) combines the post HF approach using a total wavefunction written according to excited Slater determinants with the perturbation theory. The total Hamiltonian H is expressed as the perturbation W^n of order n developed around an equilibrium Hamiltonian H_0 : $H = H_0 + \lambda W^n$. For instance, the MP2 model uses a perturbation of second order.

Consequently, such computational chemistry methods present a high accuracy that goes with a long calculation time. These approaches are expensive in computational cost as they are based on wavefunction with $4N$ variables, *i.e.* 3 spatial and 1 spin variables for each electron. The post HF calculations are also heavier since several Slater determinants need to be evaluated.

Density Functional Theory (DFT). This approach and its derivatives consist to substitute the wavefunction of $4N$ variables by the electronic density ρ of the system, which is composed only of 3 spatial coordinates and 1 spin variable (see Appendix B.2.1). The theorems of Hohenberg and Kohn (HK)³³³ put then the basis of the theory by demonstrating that the energy of the system is a functional of the electron density $E[\rho]$, while so far, the Hamiltonian was a functional of the wavefunction. This statement implies that the DFT formalism is equivalent to that of the wavefunction/Hamiltonian of the first-principles methods. Then, they showed that the ground state energy E_0 of the system corresponds to the global energy minimized by ρ (full description is presented in Appendix B.2.1).

However, the resolution of the Schrödinger equation is still prevented because of the electronic interaction. Kohn and Sham solved this problem³³⁴ by substituting the real system of interacting electrons immersed in an external potential V_{ext} by a fictive system of non-interacting electrons moving in an effective external potential V_s . The two systems are thus related by their energies and their electron densities, which are considered equivalent. The fictive system is then defined by:

$$E[\rho] = T_s[\rho] + \int V_s(\vec{r})\rho(\vec{r})d\vec{r} \quad (4.4)$$

$$\text{with } V_s(\vec{r}) = V_{ext}(\vec{r}) + \int \frac{\rho(\vec{r}')}{|\vec{r} - \vec{r}'|} d\vec{r}' + V_{xc}(\vec{r}) \quad (4.5)$$

Finally, the energy of the system depends on the known expression of the total kinetic energy $T_s[\rho]$ and $V_s(\vec{r})$, which includes three terms. The first one is a known external potential of the real system and the second term derives from the full classical Coulombian interaction term (see Appendix B.2.1). $V_{xc}(\vec{r})$ corresponds to the exchange-correlation term. As the expression of this functional is not mentioned in the Kohn-Sham theory, numerous functionals have been developed to approximate the exchange-correlation contribution. Among others, we can mention the PBE³³⁵ and the B3LYP functionals³³⁶ defined as a Generalized Gradient Approximation (GGA) functional and a hybrid functional, respectively (see Appendix B.2.2). As all functionals contain free parameters adjusted on theoretical results or experimental data, the DFT-based approaches cannot be considered as *ab initio* methods.

In DFT, the density simplification leads to a computational time reduced by one to several orders of magnitude compared to that of the post HF methods. It also succeeds to have a computational cost similar to the Hartree-Fock approach by integrating in addition the electronic correlation, absent in the HF model. The main problem of these quantum chemistry methods lies in the size limitation of systems. Indeed, only tens of atoms can be supported by DFT calculations, which results in new approaches considering more approximations.

In the context of solid state calculations, the computational cost can be drastically decreased by the use of plane waves basis state by the Bloch theorem³³⁷ and limited to the first Brillouin zone in crystal structures. This approach is the concept of DFT-based methods, such as the Vienna Ab initio Software Package (VASP) code^{338–340}. In this method, the contribution of the core electrons are approximated by a softer potential, called pseudopotentials, which must reproduce the exact DFT wavefunction at the valence electrons region (see Appendix B.3).

Semi-empirical approach. Other models use the accuracy of the wavefunction/Hamiltonian formalism combined with several approximations to simplify greatly the calculations. These semi-empirical methods often neglect some integrals or parametrized others with free parameters adjusted on experimental data or electronic calculations. This latter consideration implies that semi-empirical methods can be differentiated between the *ab initio* or DFT-based methods. Notably we can mention the Density Functional based Tight-Binding (DFTB)^{341,342}, which sets a parametrized Hamiltonian based on DFT.

The semi-empirical calculations allow for an effective compromise between accuracy and computational cost thus computing systems of a few hundreds of atoms but with a lower precision in comparison to DFT calculations.

4.2.1.2 Empirical potentials

Finally, by avoiding, the wavefunction/Hamiltonian formalism, analytical expression may be formulated to describe a global potential where the atoms of the system interact. Generally, the construction of such potentials is based on the summations of bonded forces between atoms, con-

sidering an attractive part at long distance combined with a repulsive contribution at short distance. For instance, the Coulomb electrostatic expression balances these two interactions according to the atoms charges. Van Der Waals forces can also be taken into account as well as charge-dipole interactions. As each contribution includes free parameters adjusted on experimental data, these approaches are referred as empirical potentials.

Two main type of models exist: (i) the pair-wise potentials where interactions between pairs of atoms are summed as implemented in the Lennard-Jones potential³⁴³ or the (Coulomb-)Buckingham expression³⁴⁴. (ii) Otherwise the many-body potentials define those that includes interactions between three or more particles. Among others, we find in particular the embedded-atom method (EAM)³⁴⁵.

As the interactions between atoms are calibrated, systems monoatomic or biatomic are favored by these potentials while the type of interactions remains unchanged. Inorganic materials such as oxides or metals involve ionic or covalent bonds, which can be easily configured. In more complex systems mixing different interactions types, these approaches are difficult to set. Moreover, such potentials can be used in molecular dynamics to simulate large systems of thousands of atoms because they are usually really simple to compute. On the contrary of quantum chemistry methods, the gain in computation cost is thus lost in the accuracy. However, it can noted that larger a system, more it behaves classically. However, we can wonder whether these potentials might be efficient in smaller size range.

4.2.2 Potentials benchmarking

Alumina polymorphs have been extensively studied theoretically^{346–348} including corundum^{348–351}, cubic phase^{352–355}, amorphous phase^{356–361} and liquid-like structure^{359,362,363}. Such studies investigated alumina structures of bulk and surfaces^{348,364,365}, or clusters size^{111,366–369} by first-principle calculations as well as by molecular dynamics^{352,356,370} and surface energies relaxations^{371,372}. However, no calculations were performed over a large range of particle size. Numerically, calculating particles from a few atoms to hundreds of thousands of atoms requires large scale simulations, which are only accessible with reliable empirical potentials. With oxide materials, the task exhibits additional complexities because of the oxygen bonding and the complex structural and stoichiometric landscape.

Recently, Erlebach *et al.* combined *ab-initio* and MD calculations to study the structure evolution of the hematite $\alpha - \text{Fe}_2\text{O}_3$ particles³⁷³, close to the alumina structure. An interatomic potential was used to performed conformational research on $(\text{Fe}_2\text{O}_3)_n$ clusters with $n=1-10$ validated by DFT optimization and MD calculations on particles as large as 5 nm. To our best knowledge, such work on a large range of size for alumina structures has not been reported yet.

Therefore, we performed a benchmarking using empirical potentials dedicated to the description of alumina in order to study the phase transitions from alumina clusters to nanoparticles as large as 12 nm.

4.2.2.1 Description of the potentials

The selected four potential models were developed and used over the past decades to study alumina nanoparticles and bulk, essentially by molecular dynamics calculations. Here are presented the potentials used for this benchmarking, where r_{ij} and q_i correspond to the inter-ionic distance and the effective charge, respectively. All the following expressions are written in atomic units.

1. **Alvarez.** Alvarez and coworkers have introduced a two-terms potential^{353,354} (equation 4.6), composed of a classical Coulomb term and a repulsive steric term with σ_i as the ionic radius and p an adjusted exponent parameter. This model was developed for molecular dynamics (MD) calculations done on γ -Al₂O₃ nanoparticles of 1 440 atoms³⁵³ and 11 520 atoms³⁵⁴, built in a cubic geometry.

$$V_{Alvarez} = \sum_{i < j} \left[\frac{q_i q_j}{r_{ij}} + \frac{1}{p(\sigma_i + \sigma_j)} \left(\frac{\sigma_i + \sigma_j}{r_{ij}} \right)^p \right] \quad (4.6)$$

2. **Streitz.** Streitz and Mintmire³⁷⁴ have developed a potential by including a variable charge electrostatic potential (ES) with the known empirical potential embedded-atom method (EAM), presented in equation 4.7. They named this new approach the ES+ potential. The main advantage of this approach is to take into account the modification of the local atomic charges due to the environment of each atom.

The first contribution of equation 4.7 contains the atomic energies and the electrostatic interactions. E_0 includes the neutral atomic energy and nuclear terms independent of the atomic charges. The single charge interactions are described by the χ_i term, which is composed of the atomic electronegativity χ_i^0 and the nuclear-attraction integral $[j|f_i]$ corrected by the Coulomb electronic interaction $[f_i|f_j]$. The atomic density distribution was modeled as a simple exponential of the form: $f_i(r_i) = \frac{\zeta_i^3}{\pi} \exp(-2\zeta_i r_i)$, with ζ_i a free atomic parameter. The nuclear and electronic integrals were defined by Roothaan³⁷⁵. The last term corresponds to the double charge interactions where V_{ij} contains the atomic hardness J_i^0 and the electronic interaction integral $[f_i|f_j]$.

The second term shows the two-terms embedded-atom method potential. $F_i[\rho_i]$ is the energy needed to embed an atom in the the local electron density ρ_i , which is build as a linear superposition of atomic density functions. $\phi_{ij}(r_{ij})$ is the pair potential necessary for the short-range repulsive description of the pair interactions. $A_i, B_{ij}, C_{ij}, \alpha_{ij}, \beta_{ij}, \xi_i$ and r_{ij}^* are free parameters adjusted by optimizing the experimental structural values (cohesive energy, lattice parameters, elastic constants) of the fcc aluminum bulk as well as of the bulk and numerous surfaces

of α -alumina.

$$V_{Streitz} = E_{es} + E_{EAM} \quad (4.7)$$

$$E_{es} = E_0 + \sum_i q_i \chi_i + \frac{1}{2} \sum_{i,j} q_i q_j V_{ij}$$

$$E_{EAM} = \sum_i F_i [\rho_i] + \sum_{i < j} \phi_{ij}(r_{ij})$$

$$\text{with, } \chi_i = \chi_i^0 + \sum_j Z_j ([j|f_i] - [f_i|f_j]) \quad \text{with, } F_i = -A_i \sqrt{\frac{\rho_i}{\xi_i}}$$

$$V_{ij} = J_i^0 \delta_{ij} + [f_i|f_j] \quad \rho_i = \sum_{i \neq j} \xi_j \exp[-\beta_{ij}(r_{ij} - r_{ij}^*)]$$

$$\phi_{ij} = 2B_{ij} \exp[-\beta_{ij}(r_{ij} - r_{ij}^*)] - C_{ij} [1 + \alpha_{ij}(r_{ij} - r_{ij}^*)] \exp[-\alpha_{ij}(r_{ij} - r_{ij}^*)]$$

3. **Vashishta.** Equations 4.8 describe the two- and three-body terms developed by Vashishta *et al.*^{359,376}. The two-body term $V_{ij}^{(2)}$ is an electrostatic potential composed of different terms using fixed charges. The first one is the steric repulsion with H_{ij} and η_{ij} as the steric strength and exponent parameters, respectively. The Coulomb interactions are modeled by the second term where an exponential element was included with the Coulomb screening length λ . The two last terms are the charge-dipole and the Van der Waals interactions with D_{ij} and W_{ij} as the strengths of these attractive terms, respectively, and ξ the charge-dipole screening length. The three-body term $V_{jik}^{(3)}$ includes two compounds that correct the stretching and bending of the bonds according to the phase configuration desired. Summations over i, j and k are limited to the local environment of each atom, using a cutoff r_{cut} and step functions Θ on the distances in the radial term $R^{(3)}(r_{ij}, r_{ik})$. Another cutoff θ_{cut} on the angles contributes to favor the α crystal structure. As for the Streitz potential, the strengths and characteristic length parameters as well as the free parameters ($B_{jik}, C_{jik}, \gamma, r_{cut}, \theta_{cut}$) were fitted on experimental data, satisfying structural properties values (lattice constant, cohesive energy, bulk modulus, and some elastic constants).

The development of this potential aimed to describe α , liquid and amorphous phases of bulk alumina, based on MD calculations using periodic boundary conditions. A cell of 8 640 atoms

was generated and relaxed using the Verlet algorithm³⁷⁷.

$$\begin{aligned}
 V_{Vashishta} &= \sum_{i<j} V_{ij}^{(2)}(r_{ij}) + \sum_{i<j<k} V_{jik}^{(3)}(r_{ij}, r_{ik}) & (4.8) \\
 V_{ij}^{(2)} &= \frac{H_{ij}}{r_{ij}^{\eta_{ij}}} + \frac{q_i q_j}{r_{ij}} e^{-\frac{r_{ij}}{\lambda}} - \frac{D_{ij}}{r_{ij}^4} e^{-\frac{r_{ij}}{\xi}} - \frac{W_{ij}}{r_{ij}^6} & \\
 V_{jik}^{(3)}(r_{ij}, r_{ik}) &= R^{(3)}(r_{ij}, r_{ik}) P^{(3)}(\theta_{jik}) & \\
 \text{with, } R^{(3)}(r_{ij}, r_{ik}) &= B_{jik} \exp\left(\frac{\gamma}{r_{ij} - r_{cut}} + \frac{\gamma}{r_{ik} - r_{cut}}\right) & \\
 &\quad \times \Theta(r_{cut} - r_{ij}) \Theta(r_{cut} - r_{ik}) & \\
 P^{(3)}(\theta_{jik}) &= \frac{(\cos\theta_{jik} - \cos\theta_{cut})^2}{1 + C_{jik} (\cos\theta_{jik} - \cos\theta_{cut})^2} &
 \end{aligned}$$

4. **Woodley.** The Woodley potential is based on the Matsui's potential³⁷⁸ that was used by Gutiérrez *et al.* for important work on liquid³⁷⁹ and amorphous^{357,358} phases of bulk alumina using MD simulations with periodic boundary conditions. As shown in equation 4.9, it consists on the Coulombic contribution, and the Buckingham potential terms with the interaction parameters A_{ij} , B_{ij} , and ρ_{ij} . However, some divergence issues at short distances led Woodley³⁸⁰ to add the Lennard-Jones repulsive term in r_{ij}^{-12} with its strength C_{ij} . Free parameters are adjusted on structural data, dielectric and elastic constants of alumina. Interestingly, Woodley optimized clusters structures by DFT from initial candidate structures found by using this interatomic potential as a pre-step calculation.

$$V_{Woodley} = \sum_{i<j} \left[\frac{q_i q_j}{r_{ij}} - A_{ij} \exp\left(\frac{-r_{ij}}{\rho_{ij}}\right) - \frac{B_{ij}}{r_{ij}^6} + \frac{C_{ij}}{r_{ij}^{12}} \right] \quad (4.9)$$

These potentials selected from the literature have been introduced in a home-made computational code integrating geometrical optimization and molecular dynamics processes. In order to converge structures, energy or force gradient minimization is achieved by Quasi-Newton or Conjugate-Gradient methods³⁸¹.

4.2.2.2 Statistical analysis tools

We decided to characterize our large nanoparticles by calculating the Structure Factor (S) and the Coordination number (n_c). These two elements are related through the Radial Distribution Function (RDF) $g(r)$ ^{357,359,379}.

Radial Distribution Function $g(r)$.

This function consists to calculate the evolution of the atomic density of each atom as a function of the radial distance. The RDF gives insights about the long distance order, which can be found in crystalline structure. $g(r)$ is calculated from the partial pair-distribution function $g_{ab}(r)$ (equation

4.10), which considers that an atom of species a is surrounded by an average number of atoms of species b ($a, b = \text{Al or O}$) contained in a shell of thickness $(r + \Delta r)$.

$$g_{ab}(r) = \frac{\langle n_{a,b}(r, r + \Delta r) \rangle}{4\pi r^2 \Delta r \rho c_b} \quad (4.10)$$

where ρ is the material density and c_b is defined as the ratio of partial atoms number over the total atoms number: $c_b = N_b/N$. Calculations were done with $\Delta r = 5.10^{-4}$ Å for interatomic distance ranging from 0 to almost 25 Å.

The total radial $g(r)$ and neutron $g_n(r)$ distribution functions are calculated as follow:

$$g(r) = \sum_{a,b} c_a c_b g_{ab}(r) \quad (4.11)$$

$$g_n(r) = \frac{\sum_{a,b} c_a b_a c_b b_b g_{ab}(r)}{\left(\sum_a c_a b_a \right)^2}$$

with b_a and b_b the coherent neutron scattering cross sections of atom species a and b , respectively.

Coordination number n_c .

The number of first-neighbors b surrounding an atom a corresponds to the coordination number n_c for this atom. It can be calculated from the integration of the total RDF first peak, from 0 to R_{max} ^{357,379}.

$$n_c = 4\pi\rho c_b \int_0^{R_{max}} r^2 g_{ab}(r) dr \quad (4.12)$$

The cutoff radius R_{max} was chosen to be fixed for each type of bonds in order to compare the potentials: $R_{max}(\text{Al-Al}) = 3.10$ Å $>$ $R_{max}(\text{Al-O}) = 2.43$ Å $>$ $R_{max}(\text{O-O}) = 1.76$ Å.

On the contrary of the RDF, this quantity is important for the short distance characterization of the structure. It allows to determine the nature of the crystallographic sites by their symmetry and so the crystallographic phase.

Structure Factor $S(q)$.

The static structure factor allows to characterize the long distance ordering of an object. This function is the main component of the intensity peaks of x-rays or neutron diffractograms and allows for comparison between theoretical calculations and experimental measurements. By applying the Fourier transform of the partial RDF $g_{ab}(r)$ plus a window function³⁵⁷, the partial static structure factor $S_{ab}(q)$ is obtained:

$$S_{ab}(q) = \delta_{ab} + 4\pi\rho(c_a c_b)^{1/2} \int_0^R [g_{ab}(r) - 1] \frac{r^2 \sin(qr)}{qr} \frac{\sin(\pi r/R)}{\pi r/R} dr \quad (4.13)$$

with R , the cutoff distance chosen here as the half of the box simulation length. From $S_{ab}(q)$, we

can calculate the x-rays $S_X(q)$ and neutron $S_n(q)$ structure factors:

$$S_X(q) = \frac{\sum_{a,b} (c_a c_b)^{1/2} f_a f_b S_{ab}(q)}{\sum_a c_a f_a^2} \quad (4.14)$$

$$S_n(q) = \frac{\sum_{a,b} (c_a c_b)^{1/2} b_a b_b S_{ab}(q)}{\sum_a c_a b_a^2}$$

with f_a and f_b the x-rays form factors of atom species a and b , respectively.

4.2.3 Polymorphs stability from clusters to nanoparticles

4.2.3.1 Particles generation

The benchmarking of the empirical potentials previously described was used to study two size populations of nanoparticles. First a research of conformations of most stable small clusters $(Al_2O_3)_n$ ($n=1-3$) was performed with the empirical potentials by following three steps:

- (1) $n \times 10\,000$ random isomers were built and were calculated by geometry optimization. At the end, the similar clusters are eliminated if their energies and distances are lower than 0.002 eV and 0.7 Å. The remaining structures are then ordered by energy.
- (2) For comparison, 2000 random geometries were optimized by DFT, using the Gaussian09 software. Two successive calculations using B3LYP/6-31G* and B3LYP/6-311+G* basis sets were performed and similar geometries were removed between each step.
- (3) Even if the empirical potentials are less accurate, the main advantage is to be able to perform a conformation research on a wide range of geometries on the contrary of time-consuming DFT calculations. From this observation, the last step consists to optimize by DFT the first ten most stable conformers calculated with the potentials in order to search additional geometries that were not found in step (2). This step was performed using the same previous basis sets.

Larger clusters $(Al_2O_3)_n$ with $n=4,6,8$ were also calculated following the step (1), except $n=8$ where only 60 000 geometries were computed. While the $n=4$ clusters were optimized with all the potentials, only the Alvarez's and Streit's potentials were used for $n=6$ and 8. Moreover, for the sake of computational cost, the step (2) was skipped and only the step (3) was carried out thus computing the thirty most stable structures obtained with the potentials using a tight B3LYP/6-311+G* basis set.

Secondly, larger $(Al_2O_3)_n$ nanoparticles from $n = 50$ to $n = 20\,000$ were optimized with all the potentials for the different crystal structures. To build particles of any size, we duplicated the primitive lattice cell to generate large supercells of alpha and gamma phases. $\alpha-Al_2O_3$ supercell was built from the hexagonal primitive cell of corundum (52648 ICSD file³⁸²), characterized by lattice

parameters $a = b = 4.76 \text{ \AA}$ and $c = 12.99 \text{ \AA}$, the symmetry space group $R\bar{3}c$ and composed of 30 atoms arranged in six (0001) Al_2O_3 layers. $\gamma\text{-Al}_2\text{O}_3$ is described by a cubic primitive cell (04-005-4662 ICDD file³⁸³) with a lattice parameter $a = 7.948 \text{ \AA}$ and the space group $Fd\bar{3}m$.

But the gamma phase presents a defect spinel structure where a random lack of aluminum leads to the right stoichiometry of alumina from the ideal spinel structure Al_3O_4 . However, the position of these Al vacancies from octahedral or tetrahedral sites is not clarified yet and is still under debate in the scientific community. Pinto *et al.* studied all possible configurations for the vacancies locations in the primitive cell and concluded that the octahedral sites led to the most stable primitive cell³⁵⁵. Therefore, we prepared two configurations. One configuration presents only octahedral aluminum vacancies whereas the other was made by removing randomly aluminum ions.

Finally, supercells of hundreds of thousands of atoms were built, where particles of desired size can be cut directly from them. The three crystal structures are referred as $\alpha - (\text{Al}_2\text{O}_3)$, $\gamma_{Oh} - (\text{Al}_2\text{O}_3)$ and $\gamma_{TdOh} - (\text{Al}_2\text{O}_3)$, respectively. It is important to mention that these notations correspond to the starting bulk crystal structures of the calculated nanoparticles. The optimized nanoparticles are summarized in figure C.6 in Appendix C.2, displaying the particles diameters calculated by each potential as a function of the atoms number and the units number n from $(\text{Al}_2\text{O}_3)_n$.

In order to confirm the reliability of our supercell structures and the implementation of the analysis tools, the static structure factor S was calculated for each crystal phase supercell and cross-checked with different references. Maslen *et al.*³⁸⁴ and Lewis *et al.*³⁸² characterized the alpha phase by XRD, while the groups of Zhou³⁸⁵ and Guse³⁸³ performed XRD on gamma phase. Samain³⁸⁶ studied the gamma phase on nano-size particles. As shown in the figure 4.5, green curves of our structures fit perfectly with the literature data. Red curves from the amorphous phase measured by the group of Lamparter³⁸⁷ are added for comparison.

4.2.3.2 Clusters size

Isomers of small clusters obtained with the potentials can be now compared with isomers calculated by DFT. Figure 4.6 displays the five first geometries of $(\text{Al}_2\text{O}_3)_2$ ordered as a function of their energy relative to the more stable isomer. $(\text{Al}_2\text{O}_3)_2$ was chosen since it reflects well the tendency obtained for the other sizes. $(\text{Al}_2\text{O}_3)_n$ clusters for $n=1,3,4,6$ and 8 are shown in figures C.1-C.5 in Appendix C.1. In addition, the symmetry of each structure was determined. Geometries denoted with stars correspond to clusters found in step (3) and missed in step (2).

The obtained DFT geometries have been compared with previous studies^{111,366} and found to be consistent with their results, especially with the work of the group of Li³⁶⁷ where isomers and their relative energies are perfectly coherent. For the most complex structure ($n = 8$), some differences appear due to the fewer calculations reported in the literature³⁶⁸.

Except for $(\text{Al}_2\text{O}_3)_1$ where geometries are favored from the linear 1D molecule **D_1A** to the 3D

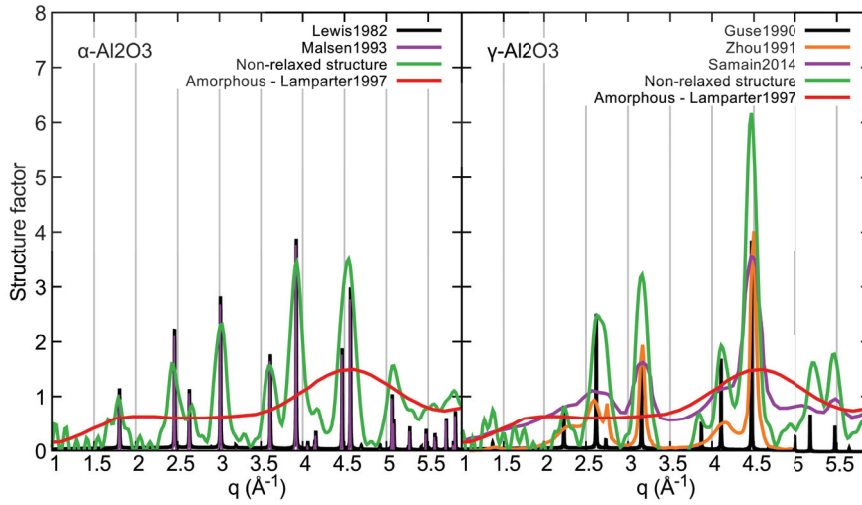


Figure 4.5 – Structure factors S of the as-build supercells (green curves) compared with experimental reference data for α ^{382,384} (left) and γ ^{383,385,386} (right) phases, as well as the amorphous phase³⁸⁷.

structure **D_1E** (Fig. C.1 in Appendix C.1), DFT calculations show that alumina structures prefer to stabilize in the highest dimensions. Indeed, the tetrahedral symmetry T_d of the first isomer **D_2A** is more stable than the higher energy particles, which tend to flatten.

The conformation research using the potentials results in diverse structures, more or less coherent with the DFT geometries. While being the most complex potentials, the Vashishta's, Streitz's and Woodley's potentials lead to structures that are qualitatively different from what is obtained in DFT. In particular, Vashishta's potential favors compact 3D-structures with regular bond lengths and angles constrained by the stretching $R^3(r_{ij}, r_{ik})$ and bending $P^3(\theta_{jik})$ terms in the three-body part of the potential. In the Woodley's potential, the very compact structures betray the overestimate of electrostatic charges.

On the opposite, the Streitz's potential favors planar structures but still fails to find the right geometries, except for Al_2O_3 . Zhou *et al.*³⁸⁸ demonstrated that the Streitz's potential gives unrealistic structures when bulk ionic configurations are highly compressed, *i.e.* the bond lengths are reduced compared to equilibrium. They showed that for sufficiently small distances between cations and anions, the Coulomb interaction predominates and E_{es} reduces by increasing the local charges, without reaching a minimum. Repulsive terms are present in the potential to avoid too close ions, but instabilities remain. They highlighted that same results could occur on non-bulk systems, such as free surfaces and interfaces, or in clusters calculations. Therefore, this explains why the Streitz's potential tends to form flat clusters in order to avoid too close bond lengths.

Surprisingly, the Alvarez's potential, which is the most simple potential, is the most efficient at predicting the correct geometries. In the case of $(\text{Al}_2\text{O}_3)_2$, almost all the DFT geometries have been found by this potential. This agreement holds even until $n = 6$ while for $n = 8$ the complexity of the

DFT structures is not retrieved.

Interestingly, the star shape **D_2C** was found in DFT after the step (3). This geometry was only predicted by the Alvarez's and Streit's models. On the opposite, it is the **D_4C** isomer that was detected by the Vashishta's and Woodley's potentials (Fig. C.3 in Appendix C.1). Hence, such calculation methods reveal that the empirical potentials can be successfully employed as a starting optimization tool thus limiting the use of computationally expensive DFT calculations. Such processes have been already used for clusters conformation researches^{373,380}, or to produce a starting configuration for *ab-initio* methods for nanoparticles larger than 50 atoms³⁵⁸.

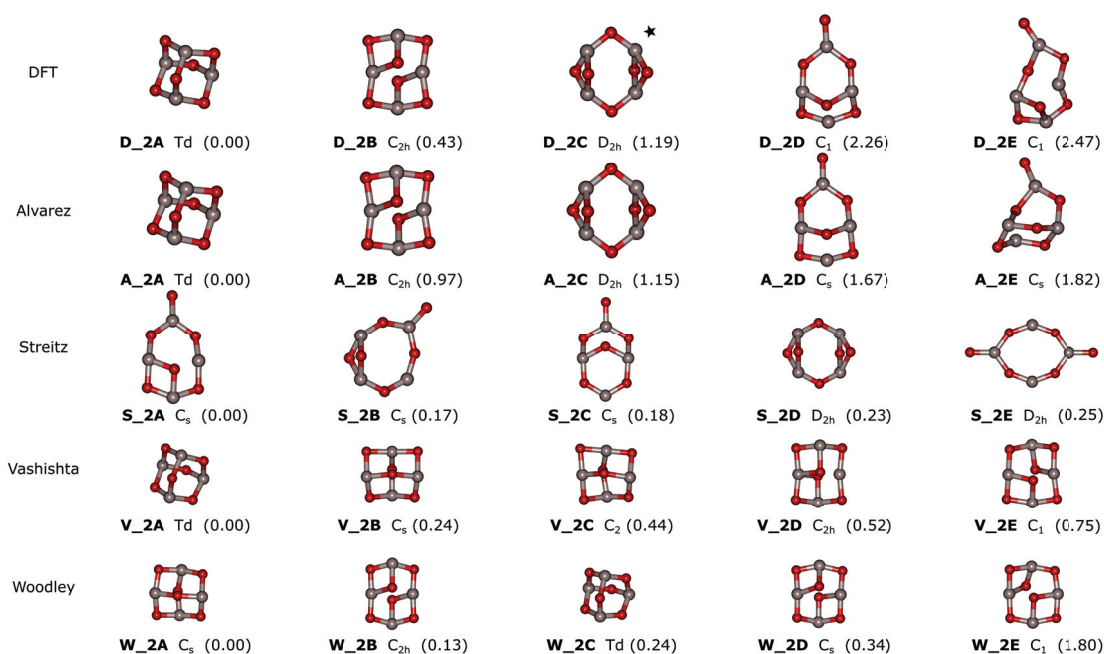


Figure 4.6 – Final isomer geometries of the $(\text{Al}_2\text{O}_3)_2$ cluster calculated in DFT and with the four empirical potentials by the conformational research method. The symmetry point groups and the energy relative to the most stable structure are added. Aluminum and oxygen ions are in grey and red, respectively. * represents the structures found by the conformation research with the potentials.

4.2.3.3 Nanoparticles range

The large nanoparticles were optimized with all the potentials for each starting crystal structure. The obtained particles were analyzed by calculating the static structure factor S , the coordination number n_c , and the energy per atom according to particles size.

Structure factor S .

Figure 4.7 displays the structure factor curves of particles calculated starting from the α phase for each potential (see figure C.7 in Appendix C.2 for the two γ phase configurations). Curves from the

bottom to the top follow the increasing size, referred by the units number n . Experimental data of the α bulk phase³⁸² and the amorphous phase³⁸⁷ (red curve) are chosen as reference on the top of each graph.

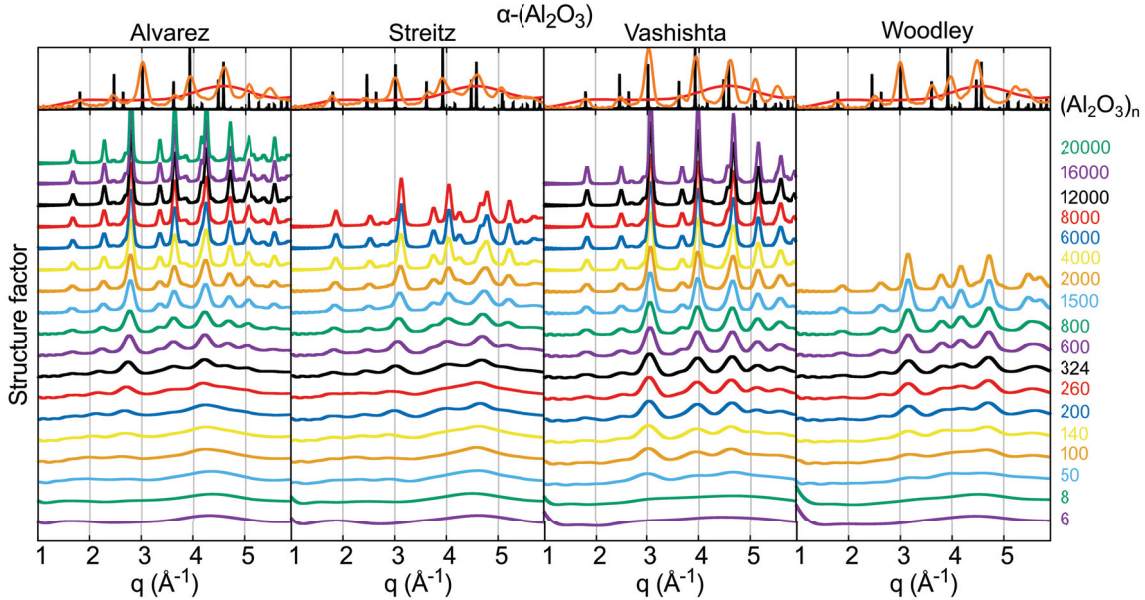


Figure 4.7 – Structure factors S computed from the relaxed $\alpha - (\text{Al}_2\text{O}_3)_n$ nanoparticles using all the potentials. For each curve, the repeat unit n is displayed on the right. Experimental data of $\alpha - (\text{Al}_2\text{O}_3)$ bulk³⁸² (black curve) and $a - (\text{Al}_2\text{O}_3)$ bulk³⁸⁷ (red curve) are displayed on top of the panel. The orange curves represent the homothety corrections applied on the $(\text{Al}_2\text{O}_3)_{1500}$ nanoparticle and designed for each potential. Similar plots for structures starting from the three crystal phases calculated with each empirical model are displayed in figure C.7 in Appendix.

Regardless of the potential, the static structure factor shows a transition from flat bands at small sizes to sharp peaks at the larger ones. The smallest particles present a large band centered around 4.5 \AA^{-1} similar to the experimental curve of the amorphous phase³⁸⁷. By increasing the size, one can observe the emergence of predominant peaks that become sharper thus characterizing the crystal organization within the system. After correcting the small shift caused by homothety in the bond lengths (orange curve in figure 4.7), a very good agreement is observed between the peaks positions and the experimental results of the α bulk phase³⁸². Furthermore, the phase transition from an amorphous phase to a crystal phase was measured at 40 \AA in calorimetry experiments³¹⁰. This crossover can be estimated starting from the $(\text{Al}_2\text{O}_3)_{100}$ and the $(\text{Al}_2\text{O}_3)_{200}$ particles, *i.e.* around 20 \AA and 24 \AA , using respectively the Vashishta's and the Woodley's potentials. Using the Alvarez's and the Streitz's potentials, the transition occurs at larger size with the $(\text{Al}_2\text{O}_3)_{324}$ particle, *i.e.* around 35 \AA and 32 \AA , respectively, close to the experimental value measured at 40 \AA ³¹⁰. Similarly to the smaller clusters, the three-body term of the Vashishta's potential favors crystal structure by

constraining bond lengths and angles in the crystal structure configuration.

Figure C.7 shows that the crystal structure evolution of nanoparticles follows the same scheme starting from both α and γ phases. Amorphous phase characterizes the small nanoparticles and a polymorph crossover at approximately the same size for each potential marks the phase transition towards the starting crystal structure.

Coordination number n_c .

For a more quantitative picture, the phase transition may be identified using local ordering measured by the coordination numbers n_c of the Al atoms. Figure 4.8(a) shows the evolution of the coordination number characterizing the octahedral sites ($n_{c,6}$) probed in the core of each particle calculated starting from $\alpha - (\text{Al}_2\text{O}_3)$, *i.e.* at $r = 5 \text{ \AA}$. The crossover thus corresponds to the slope of increasing $n_{c,6}$ percentage before 100 % of aluminum ions lie in octahedral sites symmetry, which characterizes the bulk corundum phase. Hence, the phase transition toward the α phase appears very early in the case of the Woodley's calculation. Indeed, its slope is close to that of the non-relaxed structures, except that Woodley's structures recover a bulk symmetry at larger size, namely 27 \AA . The Vashishta's crossover is more abrupt, estimated between 16 and 23 \AA , favoring rapidly a crystal structure. Finally, the crystallization predicted with the Alvarez's and Streitz's potentials seems to range from around 20 \AA to 35 \AA and 38 \AA , respectively.

To go further, the coordination distribution along the nanoparticle structure informs also about the spatial ordering. Inset of figure 4.8(a) shows the distribution profile of $n_{c,6}$ as a function of the particle distance to its center r in the case of the $(\text{Al}_2\text{O}_3)_{800}$ particle calculated with the Streitz's potential. Only at the core of the particle, all aluminum ions have the bulk coordination number thus showing that the particle surface is made of an amorphous shell. Its thickness, denoted h , is defined as the value for which we no longer have a 100 % of aluminum ions in the bulk symmetry. From Fig.4.8(b), the surface thickness h seems independent of the particles size but varies slightly from around 7.5 \AA to 13.8 \AA according to the potential used. The Vashishta's and the Woodley's potentials, which favor crystal structures at smaller sizes, present thus a thinner shell than the two other models, which predict a better reconstruction of the structure close to the surface. Please note that the non-relaxed structures display already a thin amorphous crown of 2.5 \AA , which comes from the structures of dangling atoms left after cutting in the bulk.

Therefore, this observation reveals that structures with radius r_M smaller than this surface thickness h are deformed as a whole and appear in the amorphous phase, as can be seen with the snapshots of three particles displayed in figure 4.8(c). A crystallized core region is clearly distinguishable circled by a disordered shell for the two largest $(\text{Al}_2\text{O}_3)_{2000}$ and $(\text{Al}_2\text{O}_3)_{20000}$ particles, in contrast with the first $(\text{Al}_2\text{O}_3)_{100}$ particle, which is entirely amorphized. Ultimately, the amorphous to crystal transition occurs when the shell thickness exceeds the particle radius.

Consequently, we can deduce that amorphization of the nanoparticles is due to the reorganisa-

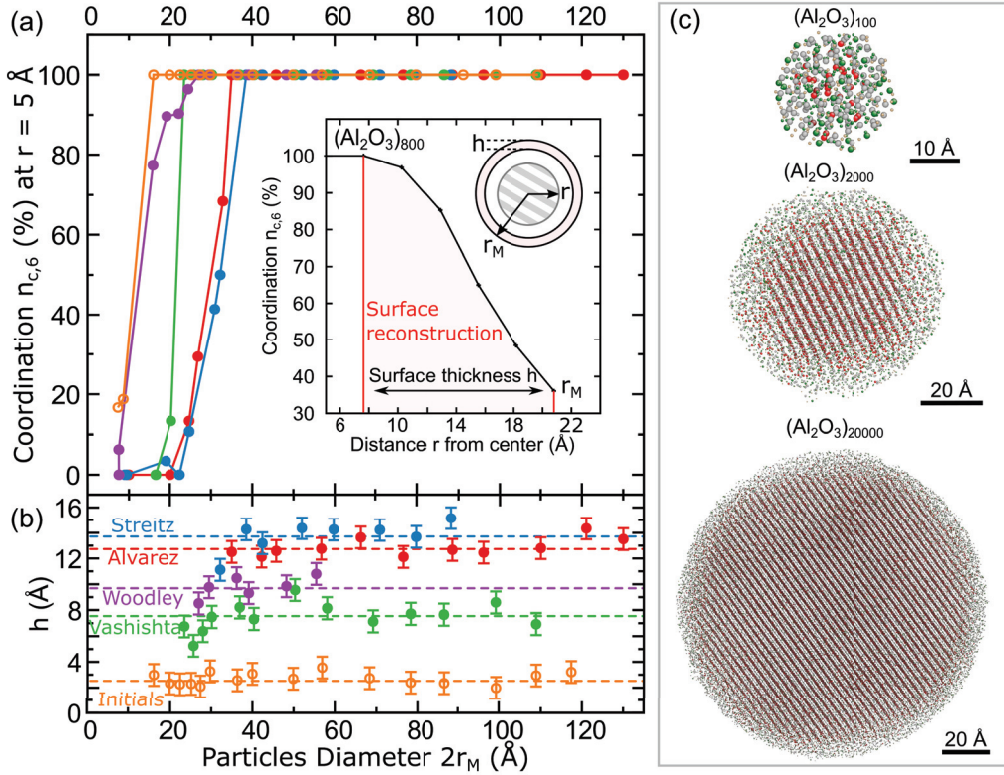


Figure 4.8 – (a) Evolution of the six coordination number ($n_{c,6}$) with the increasing particles radius r_M calculated at 5 \AA in the particles core. (Inset) Particles are subject to a surface reconstruction calculated from the $n_{c,6}$ distribution profile considering the distance r from the center of the particle. (b) The thickness of the surface shell h appears to be independent of the particle’s size. (c) Final $\alpha\text{-Al}_2\text{O}_3$ nanoparticles optimized by the Alvarez’s potential, revealing the growing crystal structure core surrounded by a constant amorphous shell.

tion of the atoms when a surface is created. The undercoordinated ions at the surface are destabilized compared to their stable symmetry in the bulk and seek to rearrange in order to lower their energy. Such process is known to induce a surface stress, different from the surface energy in the case of solid interface. Indeed, the Shuttleworth’s equation³⁸⁹ relates the surface stress to the surface energy plus an excess quantity term characterizing the energy induced by the matter deformation: $\sigma^{surf} = \gamma^{surf} + \frac{\partial \gamma^{surf}}{\partial \epsilon}$ with σ^{surf} and γ^{surf} the surface stress and the surface energy, respectively, and ϵ the surface deformation. In liquids, self-diffusion of atoms justifies the suppression of the second term, which leads to: $\sigma^{surf} = \gamma^{surf}$. Due to this equality, the Laplace-Young relation (Eqn 4.2) is valid for liquids, on the contrary of solids due to the excess surface energy. Detailed reviews clarify the difference that should be made between these quantities^{390–392}.

Energy per atom.

For now, we observed a phase transition from an amorphous phase at small sizes to a crystal struc-

ture by increasing the size. However, the final crystal structure corresponds to the starting phase. Energies of nanoparticles can then discriminate the crystal phase between α or γ , which should be the most stable phase at this particles size. Energies per atom as a function of particles diameters are reported for each polymorph in figure 4.9. Red, blue and green curves correspond to the calculated particles relaxed from the α -, γ_{Oh} - and γ_{TdOh} - (Al_2O_3) crystal structures, respectively. The phase transition ranges estimated in figure 4.8(a) are reported within the grey areas. Intersections from these energy curves refine the size of these crossover regions, marked by the dashed black lines.

First, we can observe that the amorphous region is characterized by energy curves randomly distributed. Then, the crossover coincides with a separation of the energy curves between the alpha phase and the gamma phase configurations. The γ phase appears to be the stable polymorph in the case of the Alvarez's and Streitz's calculations. This trend is in agreement with the calorimetry measurements obtained by Tavakoli *et al.*³¹⁰. On the opposite, the alpha phase is favored for the nanoparticles calculated with the Vashishta's and Woodley's potentials.

In addition, a second transition is observed at larger sizes when using the Alvarez's potential. The α energy curve crosses those of the γ phases at around 77 Å thus indicating that the former phase becomes energetically favored. This crossover differs from the experimental value of 117 Å measured by McHale *et al.*³⁰⁹. Nevertheless, this simple potential is the only one predicting both transitions. Although the largest nanoparticles sizes were not investigated due to computational limitations, the divergence of energy curves of the two phases proves the incapacity of the Streitz's to predict the second crossover.

Interestingly, both Alvarez's and Streitz's potentials lower the γ_{Oh} configuration with respect to its γ_{TdOh} counterpart, which is the expected structure according to Pinto *et al.*³⁵⁵.

To summarize, the four potentials results are reported in figure 4.10 over the wide size scale. The computed particles sizes are displayed along the scale bar, also graduated by their units numbers n . Starting from defined crystal structures, some potential optimizations result in structures consistent with experiments^{309,310}, as represented by the green regions.

First of all, we saw that the Vashishta's and Woodley's potentials are not able to predict the stable structures for the whole range of sizes. The Vashishta's potential was calibrated to calculate the bulk alpha structure, especially with its three-body term, while the Woodley's potential deviation is due to implemented over-charges.

Then, the Streitz's potential does not allow to predict the smallest clusters, an issue already reported and for which a corrected potential has been proposed³⁸⁸. However, with the increasing size, the γ phase is stabilized after a first crossover, close to the expected value. Even though largest sizes calculations were not performed due to computational limitation, the α phase does not seem to be expected by this potential.

Surprisingly, the simplest model of Alvarez *et al.* allows us to simulate the stable structures from small clusters to crystal structures at larger sizes. An optimization of the free parameters of this po-

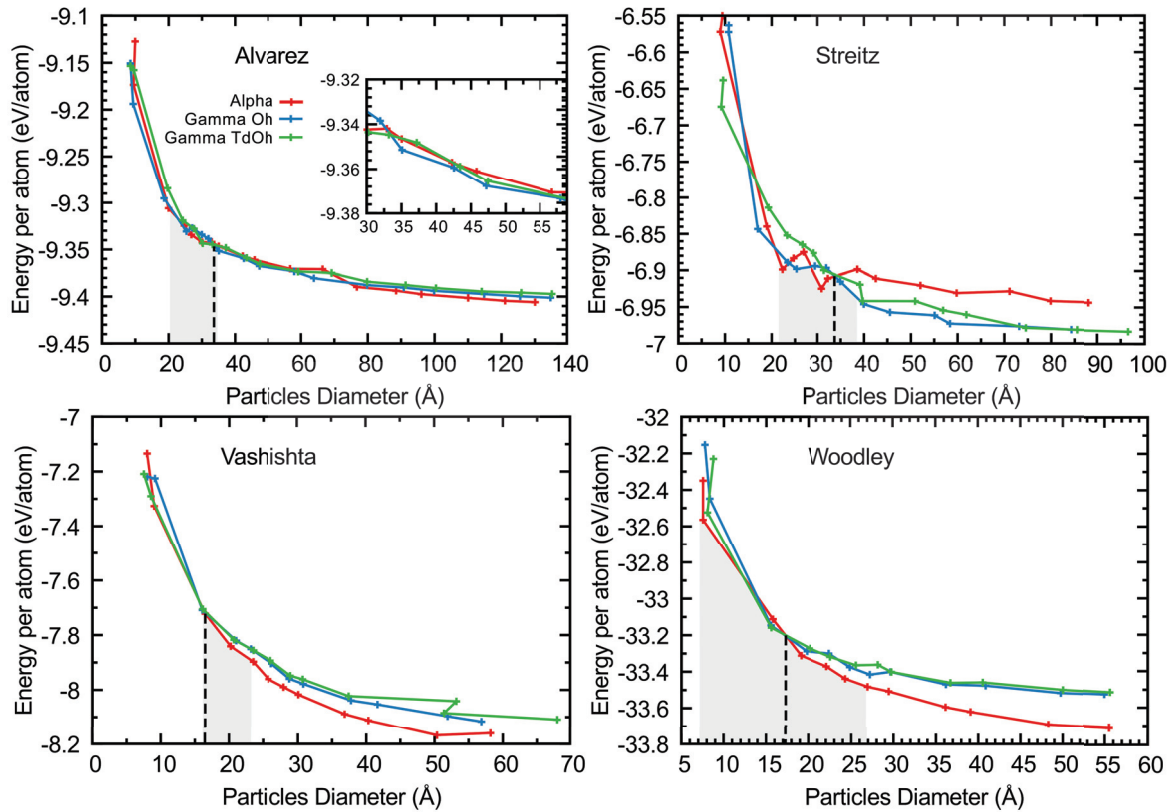


Figure 4.9 – Energies evolution over the range of nanoparticles size calculated by each potential and starting from each polymorph. Phase transition ranges estimated in figure 4.8(a) are indicated by grey areas and are confronted to the energy curves intersection (dashed black lines).

tential could correct the small shifts in size observed for the phase transitions. Generally, parameters optimization should be performed in order to fit closely each potential results to the experimental expectation.

4.3 Mechanical structure of ligand-free and capped alumina nanoparticles

In a different project, we aimed to investigate further the mechanical structure of the α phase for ligand-free and capped surfaces. For this purpose, we chose an accurate potential that enables to bring a realistic description of the mechanical structure of alumina.

To better discuss the experimental system of interest, we chose first to perform molecular dynamics (MD) calculations on α - Al_2O_3 faceted particles using the SMTBQ potential. This variable charge potential was developed for atomic interactions in oxides with an accuracy close to quantum chemistry methods while enabling the calculations of systems containing thousands of atoms.

Then, we performed calculations on ligand-free alumina surfaces using the VASP code and the

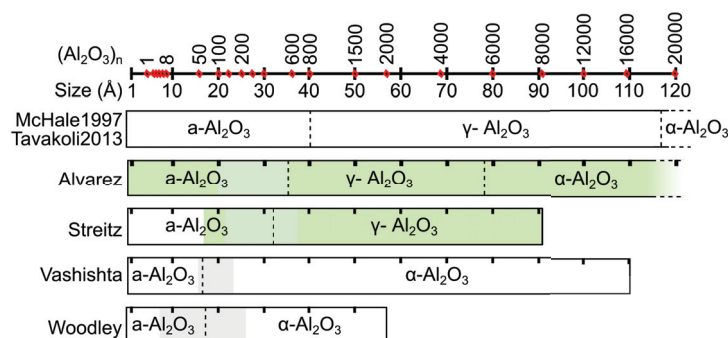


Figure 4.10 – Overview of regions corresponding to the successive stable polymorphs calculated by each potential over the large range of particles sizes. Results are compared to the crossovers deduced from calorimetry measurements^{309,310}. The computed particles sizes are displayed along the scale bar, also graduated by their units numbers n . Please note that due to computational time limitation, the larger n values (12000, 16000, 20000) have converged only for the Alvarez’s potential. Green areas show the size range where each potential describes accurately the particles according to their structures and their relative phase stability.

SMTBQ potential. We found that both approaches lead to a similar qualitative description of the mechanical structure of alumina surfaces, allowing to do a comparison with the nanoparticles structures calculated with the SMTBQ potential. Finally, we studied the influence of ligands on mechanical structure of alumina surface.

This study was the subject of a collaborative project with Dr. Tristan Albaret from the Institute Lumière Matière of the University Lyon 1.

4.3.1 SMTBQ calculations

The SMTBQ potential (for Second-Moment Tight-Binding-QEq) is a variable charge potential based on the charge equilibration (QEq) method and developed by Tétot and co-workers³⁴⁹ and available in the Large-scale Atomic/Molecular Massively Parallel Simulator (LAMMPS) code³⁹³. It was developed for describing the ionic-covalent atomic interactions in oxides like alumina. A distinct advantage of this potential is that it takes a detailed account of the charge transfer between atoms and therefore grasps the essential features of the Al-O bonding, leading to a description of surface properties with an accuracy comparable to the Density Functional approaches³⁴⁹. From this potential, a physical quantity comparable to a local pressure can be calculated. This will allow us to compare the inside pressure with the mechanical deformation of the calculated structures, as reported above for nanoparticles.

As explained in section 4.1.2.2, mechanical deformations of aluminum sites translate into an induced pressure and a shift of the luminescence lines when doped with chromium. We can demonstrate that these physical quantities are intrinsically related:

(i) Firstly, local pressures calculated following the technique described in Appendix D.1 are related to the mechanical deformations occurring inside nanoparticles. The deformations of the Al sites are evaluated considering the Al-O bond length deformation relative to the bulk: $\Delta a/a_0 = \frac{a-a_0}{a_0}$ with a and a_0 the mean bond length of Al sites of the considered system and the bulk, respectively. The deformations of the lattice under pressure were observed by different groups^{394,395} and were compared to the bond length deformations evaluated in our calculations. Finally, a linear law was found: $\Delta a/a_0 = 0.00126 \times P - 0.00011$ with P the pressure in GPa (see Appendix D.2).

(ii) Secondly, a theoretical shift of the luminescence lines relative to those from the bulk can also be linearly found from the applied pressure. From luminescence measurements under controlled pressure conditions, we obtained the following relation: $\Delta\lambda[nm] = 0.357 \times P[GPa]$ (see Appendix D.2).

The pressures calculated here reflect the applied forces on the atoms. Hence, a positive pressure indicates forces that tend to extend the atomic bonds, while a negative pressure means a compression. Experimentally, the measured pressure (strictly positive) corresponds to the application of an external pressure.

Three Al₂O₃ nanoparticles were generated with different sizes and shapes containing respectively (A) 2880, (B) 1620 and (C) 2160 atoms using the same crystallographic parameters than previously and employing a Wulff construction (Fig. 4.11(a)-(d)). Starting from α alumina bulk structure, these systems were designed from cuts along (0001), (1 $\bar{1}$ 00), (01 $\bar{1}$ 0) and (10 $\bar{1}$ 0) planes for the particles (A) and (B) and cuts along (0001), (10 $\bar{1}$ 0) and (01 $\bar{1}$ 0) planes for particle (C). These directions refer to typical planes of ruby, which were observed experimentally³⁹⁶ and theoretically^{371,372}. Calculations were assured by molecular dynamics at 300 K for all the nanoparticles and at 0 K only for the nanoparticle (A).

By partitioning the nanoparticles into shells from the surface to the center of mass (see Appendix D.1 and D.3), the examination of the pressure profiles linked to $\Delta a/a_0$ and $\Delta\lambda$ is shown in figure 4.11(e) and displays a qualitative behavior split in two regions. Figures 4.11(a)-(d) illustrate this effect by showing the high and low pressure regions in the studied clusters ($P > 0.3$ GPa or $P < -0.3$ GPa).

The outer shells of the clusters experience a positive pressure less than 1 GPa. The positive sign of these outer pressures indicates a tendency towards a surface extension, which is contrary to the Laplace expectation where the surface energy cost drives the system towards a reduction of its surface dimensions. Indeed, the bond lengths are elongated by maximum 0.1 % after 10 Å compared to bulk values. Interestingly, we note the high pressure regions on the surface of cluster (A) at 0 K, while the surface regions experience local pressure closer to zero for all the clusters at $T = 300$ K. This could be explained by noting that at finite temperature, the surface atoms will often explore regions slightly further out of the surface plane thus reducing the in-plane positive stress in

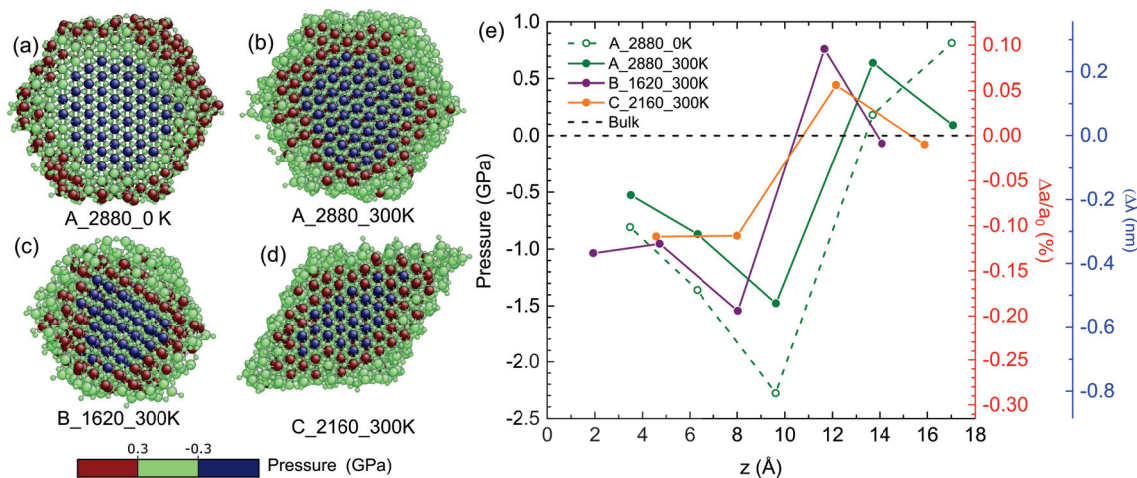


Figure 4.11 – (a)-(d) Pressure regions of three α - Al_2O_3 nanoparticle structures arranged in three pressure range, clarified by the color box. Nanoparticle (A) is composed of 2880 atoms and calculated at (a) 0 K and (b) 300 K. (c) Nanoparticle (B) is containing 1620 atoms and calculated at 300K as well as (d) the nanoparticle (C) built with 2160 atoms. Nanoparticles (A) and (B) with $(1\bar{1}00)$, $(01\bar{1}0)$ and $(10\bar{1}0)$ plane surfaces are generated by Wulff construction and the nanoparticle (C) has $(10\bar{1}0)$ and $(01\bar{1}0)$ planes. (b) Pressure profile along the inside distance from the center of mass and arranged in shells for each nanoparticle. Pressure is related to the bond lengths deformation $\Delta a/a_0$ and the luminescence shift $\Delta\lambda$ axis.

the surface region. Therefore, this positive stress is reduced at the first surface layers, but it is fed through to the sub-surface layers.

Then, since the total pressure of the isolated clusters should balance to zero, *i.e.* reaching an equilibrium with the vacuum pressure, the negative components inside the particles thus compensate the positive pressure exerted at the surface. Mechanically, the atoms in the core try to counter-balance the surface expansion by reducing their bond lengths, quantified by compression of almost 0.2 %. At ambient conditions, the local pressures do not exceed higher values than -1.5 GPa while they are larger than -2 GPa at 0 K since the core needs to compensate higher surface pressures.

Interestingly, this trend is similar between all the nanoparticles, but amplitudes of the variations appear attenuated or enhanced as a function of the nanoparticles size and shape. The cluster (B), which has almost twice less atoms than the (A) nanoparticle, seems to suffer from larger pressure variations since its radius curvature is more important and that the core atoms are closer to the surface. The smaller pressures noted for the particle (C) may come from the larger and flatter surface planes where the atoms can spread more easily and reduce the surface stress.

From our SMBTQ molecular dynamics calculations, the pressure inside the free standing α -

Al_2O_3 nanoparticles with radii between 1 and 2 nanometers appears negative and of the order of -1 GPa, while in the surface region the pressure should be positive in the 0-1 GPa range. Such pressure variations are largely within the resolution of luminescence experiments, since they correspond to shifts around 0.5 nm. However, Cr ions should be distributed in the whole alumina matrix thus canceling the pressure effect on the luminescence lines. Though, an asymmetry is still present between the amplitude of the positive and the negative pressures, which could be interpreted as the broadening of the luminescence peaks. In addition, our experimental conditions imply the use of ligands in water, which were not taken into account so far in our theoretical approach.

4.3.2 VASP calculations

4.3.2.1 Free alumina surface

Currently, empirical potentials do not allow to consider systems combining inorganic objects with organic molecules for the reasons discussed in section 4.2.1. Consequently, quantum chemistry calculations are more suited to describe ligand-capped alumina. DFT-based calculations were first performed on free (0001) $\alpha\text{-Al}_2\text{O}_3$ surface systems by using the VASP code. It provides a good parallelization and allows us to calculate systems of a few hundreds of atoms with a reasonable computational time, while preserving the DFT accuracy. For more details, the parameters used in the calculations presented below are described in Appendix B.3.3.

Aluminum oxide was investigated in the corundum phase. $\alpha\text{-Al}_2\text{O}_3$ supercell was built from the hexagonal geometry of corundum (52648 ICSD file from ref³⁸²) along the (0001) direction (labelled as z-axis) (parameters of corundum phase is recalled in section 4.2.3.1). This alumina cell was duplicated by $2 \times 2 \times 1$ along the real x, y and z cell axis directions ($x = 9.6151 \text{ \AA}$; $y = 9.6151 \text{ \AA}$; $z = 13.1148 \text{ \AA}$) (Fig. 4.12(a)). This bulk reference structure cell contains thus 120 atoms, arranged in 18 z-axis layers. 2/3 of the aluminum ions occupy an octahedral site slightly deformed in the trigonal symmetry, where the ions bond closer to one oxygen plane than the other. As a result, the atomic layers are periodically ordered in O-Al-Al planes, where the double Al layers correspond to inverted sites with long bond lengths (1.97 \AA) and short bond lengths (1.85 \AA) (Fig. 4.12(b)).

Then, the simulation of the (0001) Al_2O_3 surface was achieved by placing the bulk cell on the middle of an empty 39.3446- \AA height box (keeping the same x and y dimensions). Thus, a vacuum thickness of 26.3 \AA was fixed between the periodic images along the (0001) direction. The Al surface termination was chosen as it is known as the most stable face^{365,371,372}. All the generated slabs with their characteristics and their energy can be found in figure D.4.

Upon geometry optimization, atomic displacements occur along the z axis and lead to the relaxed structure at 0 K. At the end, the z positions of the successive Al and O layers of the final

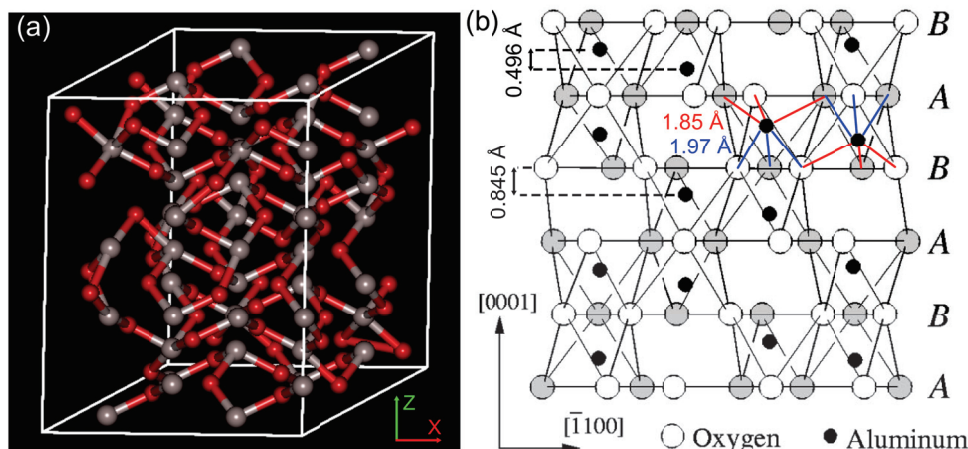


Figure 4.12 – (a) Bulk alumina slab calculated with VASP. Oxygens and aluminum are respectively red and grey. (b) Scheme of the periodic structure of corundum where the ABAB oxygen planes ordering creates successive alternated aluminum sites with long (blue) and short (red) bond lengths (Reprinted from³⁴⁸).

α -Al₂O₃ (0001) surface are compared to the bulk reference in figure 4.13. The corresponding interlayer distances and their deviation magnitudes from the bulk are summarized in table 4.1.

In the bulk cell, the planes are regularly spaced by 0.845 Å and 0.496 Å between two Al-O plans and two Al-Al plans, respectively (Fig. 4.12(b)). The first interlayer distance experiences a large relaxation (-84.6 %) where the topmost Al layer almost merges with the O underlayer. While progressing towards the center of the slab, the relaxations oscillate (between -45.6 % and +20.5 %) and stabilize after the seventh plan.

At the center of the slab, the local environment around Al atoms is close to the bulk one with a minimal deviation of the Al-O bond-length of 0.0085 Å (< 2 %). These large relaxations go along with a substantial decrease of the surface energy from 3.62 J/m² to 1.53 J/m², respectively, for the as-cleaved and optimized configurations. These results are in perfect agreement with the calculations of Ruberto *et al.*³⁴⁸ and in fair agreement with experimental results^{309,397}.

Interestingly, we note that fixing the in-plane dimensions using the bulk lattice parameters induces a net positive pressure in the system. With our calculation, the VASP code gives us access to the stress tensor σ_{ij} , which applies on the atoms according to the (x,y,z) directions. As the stress relaxation occurs in the z direction, the contribution to the pressure coming from the in-plane components of the surface stress tensor is given by: $P = \frac{\sigma_{xx} + \sigma_{yy}}{3}$. This global pressure needs to be differentiated to the local pressures seen previously in the SMTBQ calculations. Finally the pressure amounts to +1.424 GPa. Although this quantity depends on the exact cell geometry, its positive sign confirms again a tendency towards a surface extension in the in-plane dimensions, contrary to the Laplace theory.

This surface relaxation over the first layers of the alumina structure is similar to our earlier observations on the nanoparticles calculated using empirical potentials. The same bulk-like core is recovered after crossing a destabilized shell of several atomic layers. In the VASP calculations, the thickness shell is estimated to be around 5 Å, smaller than the previous thickness. It should be recalled that this calculation is limited to 2D systems where the in-plane lattice parameters are imposed at all depths along the z direction. By taking into account the nanoparticle curvature or facets shapes, these restrictions are withdrawn and more degrees of freedom allow the atoms to explore regions slightly further out of the surface in-plane. Moreover, addition of a finite temperature thermostat as in the SMTBQ calculation increases these relaxations and thus the surface shell.

Interplan	Bulk (VASP) (Å)	Surface (VASP)				Ligands (VASP)	
		(Å)	(%)	(%)	(%)	(Å)	(%)
		This work	DFT ³⁴⁸	Expt ³⁹⁷	This work	This work	
1-2	0.845	0.128	-84.8	-85	-51	0.539	-36.2
2-3	0.845	0.880	+4.1	3.2	16	0.941	11.4
3-4	0.496	0.269	-45.6	-45	-29	0.343	-30.7
4-5	0.845	1.019	+20.5	20	20	0.942	11.5
5-6	0.845	0.892	+5.5	4.8	-	0.851	0.7
6-7	0.496	0.457	-7.6	-7.1	-	0.504	1.7
7-8	0.845	0.860	+1.7	1.3	-	0.839	-0.7
8-9	0.845	0.831	-1.7	-0.8	-	0.840	-0.6

Table 4.1 – Interlayer distances (Å) and deformation magnitudes (%) along the depth of the calculated cells.

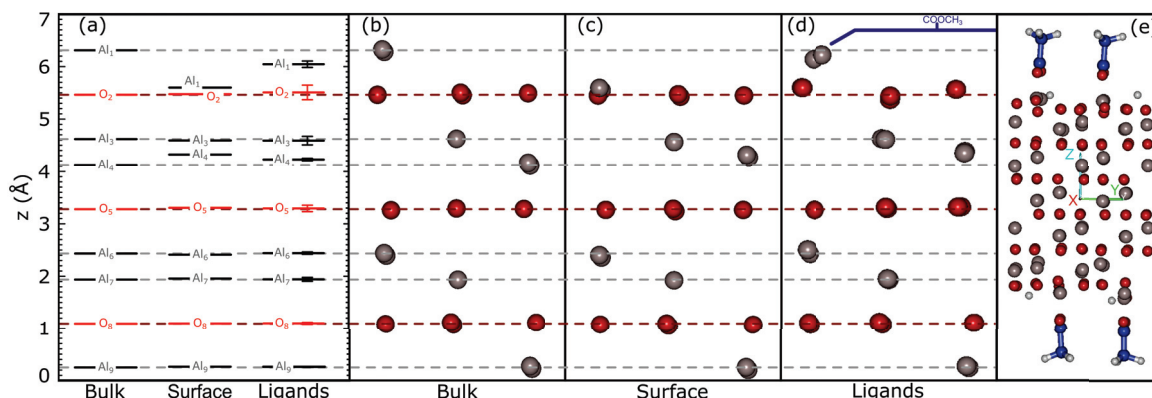


Figure 4.13 – (a) Mean z-positions of atomic layers aligned from the center of the corresponding relaxed α -Al₂O₃ cells calculated with VASP: (b) bulk, (c) free- and (d) capped-surface slabs. Ligands, sketched in blue in (d), are visible in the (e) whole 4_{bi}/0_{uni} cell. Al, O, C and H ions are in grey, red, blue and white, respectively.

Transferability between the SMTBQ and VASP methods in order to compare results was checked

by computing similar α -Al₂O₃ (0001) surface systems with the two codes (SMTBQ results are presented in Appendix D.3). On the one hand, local pressures of relaxed and unrelaxed cells served to relate the nanoparticles results with those of surfaces done only with the SMTBQ potential. In another hand, the structural results obtained on the free alumina surfaces confirm the good agreement between SMTBQ and VASP. The pressure evolution showed a similar trend than nanoparticles where a pressure discontinuity appears at the free (0001) Al₂O₃ surface. Its origin is related to the surface stress generated by the cut from the bulk and relaxations. Under the (0001) orientation the surface plane tends to extend and induced a positive stress with its in-plane components as the main pressure components. Then, the mechanical equilibrium requires a negative pressure in the bulk as a counterbalance contribution. We thus deduced that the nanoparticles computed with the SMTBQ code present the same qualitative behavior than the VASP surface. Ligands can now be added on the free surfaces to investigate their impact on the surface relaxation.

4.3.2.2 Capped alumina structure

The ligands effect is then investigated by adding molecules on the surface cells. The ligand-free (0001) α -Al₂O₃ surface is modeled as previously with a periodic 18 layers slab terminated with an Al layer on both surfaces and a vacuum thickness of 26.3 Å. The in-plane dimensions, *i.e.* the (x,y) plane, correspond to a (2 × 2) surface cell using the hexagonal bulk lattice parameters. Coated cells were made by bonding two deprotonated acetic acid molecules per surface on aluminium ions through the oxygens of the carboxylic head, as shown in figure 4.13(e). Ethanoic acid molecules (CH₃COOH) have been chosen to keep the same polar head than the MEEAA ligands but with a smaller unpolar chain thus keeping an affordable computational cost. As seen in section 4.1.2.1, the bidentate bridging mode appears to be preferred as bonding approach for the surfactant molecules on the aluminum atoms. However, four configurations were explored with different ratio of bidentate X_{bi} and unidentate X_{uni} bonding modes, with X the ligands number: (i) $4_{bi}/0_{uni}$, (ii) $3_{bi}/1_{uni}$, (iii) $2_{bi}/2_{uni}$ and (iv) $0_{bi}/4_{uni}$ (Fig. D.4). The final density coverage is then 0.025 molecules per Å². Angles and bond lengths of the ligand molecules as well as between the ligands and the surface metallic ions were initially estimated from the calculations of Nara *et al.*³²¹. Hydrogens coming from the deprotonation of ligands during the bonding were added on alumina oxygen to compensate the charge difference.

The average positions of the atomic layers in presence of ligands on the surfaces are included in figure 4.13 and relaxations are reported in table 4.1. The displayed results correspond to those of the $4_{bi}/0_{uni}$ slab being the most stable configuration. Interestingly, the energy order between all the studied slabs, which can be found in the table of the figure D.4, favors the bidentate bonding mode that confirms the experimental interpretation. Please note that the difference between covalent and ionic attach could be determined through a charge analysis using the Bader code³⁹⁸. The relaxation of the first Al-O interlayer distance is now -36.2 %, much less in comparison to the

-84.8 % of the ligand-free surface. Similarly, the bulk interlayer distances are reproduced earlier within $\pm 2\%$ after the fifth plane. Damped oscillations (from -30.7 to 11.4 %) are still visible to compensate the residual surface stress, even though the variations are less violent than previously. With ligands on the surface, the in-plane contribution to the pressure becomes +0.235 GPa with the same cell geometry as for the clean surface. This stress reduction by a factor 6.06 as well as the small variations of the interlayer distances and consequently the Al-O bond lengths show that the effect of the ligands strongly damp the relaxations of the free surface leading to a slab that almost recovers a bulk-like structure. Considering this stress reduction factor, the local pressures previously calculated for nanoparticles and reported in figure 4.11(e) should thus dip below 250 MPa and induce luminescence shift lower than 0.15 nm.

In addition, a more realistic view of the system should take into account the solvent medium as well as the hydroxylation of the surface. Numerous studies show that it is hard to obtain hydroxyl-free alumina (0001) surfaces and that the OH surfaces are obtained even for low conditions (1 Torr at 300K)^{399–401}. By covering the whole surface of the particle, the OH molecules are able to strongly bond to the Al and O layers on the first layers of the surface and could thus reduce the surface stress.

4.4 Conclusion

To summarize, we found that ligands have a clear effect on the nanoparticles size when they are used in PLAL synthesis of a $\alpha\text{-Al}_2\text{O}_3\text{:Cr}^{3+}$ target in water. Nano-rubies smaller than 10 nm have been found in synthesis with ligands. γ nanoparticles appear predominant in ligand-free synthesis, although the polydispersity of uncapped nanoparticles leads to the formation of nano-rubies with size larger than 10 nm. In addition, ligands seem to stabilize the nano-rubies leading to a lack of shift induced by Laplace pressure in the luminescence measurements.

This stabilization was investigated by different theoretical calculations:

(i) a benchmarking of empirical potentials shows that the stability of bare alumina nanoparticles at the nanoscale is mainly driven by a surface reconstruction, independent of the nanoparticles size and leading to a crystal structure core surrounded by an amorphous shell. The resulting γ polymorph is thus favored at small sizes, where, in the case of ruby, the luminescent lines are not visible.

(ii) The ability of atoms to re-arrange themselves at the nanoparticles surface in order to lower the surface energy, *i.e.* the surface stress, have been evidenced on nanoparticles using a charge variable potential (SMTBQ) as well as on free surfaces with DFT-based calculations (VASP). The system exhibits an important relaxation of the outer layers thus inducing an expansion of the atoms and a positive pressure. This thus needs to be differentiated from the Laplace's pressure. Then, the atomic perturbation caused by this stress at the surface is progressively attenuated and compensated by the atoms from the core, which tend to compress thus characterized by a negative pressure. In the case

of surface systems, the bulk configuration is recovered after a few layers from the surface.

(iii) Finally, the ligands tend to reduce the surface stress in a general manner by reducing the relaxation at the early surface, by homogenizing the damped oscillations and by stabilizing earlier the structure in the bulk configuration. The reduction of this surface stress was estimated to around 6, which decreases drastically the pressures observed in nanoparticles far below 1 GPa. The mode of bonding of the ligands on the nanoparticles surface has also been evidenced both experimentally and theoretically, preferring to adsorb in a bridging bidentate approach. Therefore, chromium ions in α alumina should experience pressures that are greatly reduced by ligands and thus emit non-shifted light, as observed experimentally.

Further theoretical investigations should be however performed. In the first study, the polymorphs stability regions were reproduced at equilibrium with geometrical optimization calculations. To simulate nucleation and growth process, molecular dynamics calculations should be carried out with the same implemented empirical potentials or with the SMTBQ potential in order to follow the out-equilibrium dynamics.

The mechanical structures of corundum have been evaluated with and without ligands. For a better comparison, the γ phase should be investigated similarly using both SMTBQ and VASP methods.

This thesis work has been conducted in order to bring new insights about the understanding of the factors influencing laser-generated nanoparticles growth and stabilization in solution. This physical method innovates by its ability to easily produce free surface nanoparticles, but the whole ablation process is composed of complex physical and chemical mechanisms thus resulting in a polydispersed and polymorphous assembly of particles. The number of adjustable parameters enables to carry out versatile experiments to synthesize nanomaterials with a plenty of material and solvent combinations. Since the first PLAL trials in the nineties, the effects of numerous factors on the formation of the nanoparticles and the final results of colloidal solutions have been explored. However, there is still a lot of work to do in order to allow a better control of the stability of the colloidal solutions, as well as on the selectivity of the nanoparticles morphology.

In the chapter 2, our efforts focused on the dynamics of the first bubble even if this stage appears less relevant for nanoparticles formation than phenomena related to the plasma. The PLAL method opens the way to explore new fundamental mechanisms induced by the extreme conditions and the very short time scale of the processes. The laser-generated bubbles have dynamics that seem similar to classical systems of bubbles or droplets spreading. Yet, the high velocities combined with high viscosities of solvents lead to consider unusual extreme conditions, relevant for fluid mechanics. Bubbles were tracked using an ultra-fast camera included in a shadowgraphy set-up. I developed a computing code to analyze automatically the bubbles pictures and to deduce the geometrical parameters as well as the dimensionless Reynolds, Weber and Capillary numbers with respect to the bubbles lifetime. For ablation in water, the analytical approach developed by our team and based on the Rayleigh-Plesset equation was used to calculate thermodynamic quantities (mostly temperature and pressure) of bubbles generated in water. Combined with the dimensionless numbers values, we confirmed that these systems are driven by inertia and remain unchanged relative to the laser fluence. The increase of laser energy leads only to a longer bubble lifetime and a larger bubble size. Afterwards, the dynamics of the bubbles were investigated with the increase of the viscosity of the

solvent. In the framework of a collaborative project, which aims to produce Au and YIG nanoparticles in engine oils, high viscous oils have been used. It appears that the viscous force cannot be neglected anymore with respect to inertia when increasing viscosity. We find that the competition between the viscous forces and the surface tension (capillary number Ca), on the one hand, and the competition between the viscous forces and inertia (Reynolds number Re), on the other hand, are both key factors. This leads to bubbles geometry different from the hemispherical shape of bubbles produced in water. The bubble shape is composed of a spherical cap driven by inertial forces and an interface layer separated by a rim. Close to the target, the friction enhanced by the viscous forces has to be included in the resistance forces along with inertia thus resulting in the interface layer. Despite some similarities between systems at low capillary numbers, *i.e.* the interlayer thickness dynamics and the contact angle hysteresis, the behavior of the contact line of our bubbles cannot be interpreted with models coming from fluid mechanics, such as the Cox-Voinov model or the molecular-kinetic theory. Our systems differentiate from classical cases by the high capillary numbers and could be relevant for field of fluid mechanics.

A straight way to control nanoparticles involves the addition of stabilizing agents on the solution before the synthesis. The first approach we saw in chapter 3 was the use of ions to stabilize gold nanoparticles in water solution. The colloidal stability is generally ascribed to the electrostatic repulsion forces generated by the ionic double layer around charged nanoparticles. However, the origin of the charge carrier is still unclear. Two distinct assumptions have been proposed. On the one hand, an excess of electrons formed during the plasma phase during the nanoparticles formation is assumed to charge the nanoparticles. On the other hand, the negative charges are supposed to be carried either by oxygen due to the deprotonation of oxide groups by tuning the pH or by the direct adsorption of anions on the surface of the particles.

In the work presented in chapter 3, we deduced from XPS measurements on a free-standing beam of gold nanoparticles produced in NaBr solution that half of their surface is covered by Br ions. However, no evidence of oxidation was found thus supporting the hypothesis of nanoparticles charged by an excess of electrons. Theoretical calculations are still in progress to explore the surface chemistry of gold nanoparticles in contact with chaotropic anions and with oxide groups.

In any case, the ions have been proved to have a real effect on the stability of gold solutions, and hence the nanoparticles size distribution. We investigated the ions concentration using salts. In general, the selected ions stabilize the solutions in a large range of concentration. A bimodal distribution of nanoparticles was measured with a dominant population from 5 to 20 nm and a second minor one around 100 nm. Unfortunately, we did not explore high concentrations where the critical amount of salt leading to destabilization can be reached. The nanoparticles aggregated for concentration higher than 10 mM only for solutions where the pH increased.

However, it appears that the gold concentration has a key role on the solution stabilization. We observed that by increasing the solution concentration from different initial salt concentrations, the

solution starts to destabilize at almost the same solution concentration. Intuitively, we can assumed that the free space between the particles are reduced with the increase of gold concentration, and independently to salt concentration, ions are then overcome when the particles have no choice than to be close.

Organic ligands are known to stabilize inorganic nanoparticles. In our case example, ligands succeed to tune the size of PLAL-synthesized nanoparticles of ruby ($\alpha\text{-Al}_2\text{O}_3\text{:Cr}^{3+}$) around 4 nm and homogenize the size distribution leading a better colloidal stability. In solutions without ligands, nanoparticles display a large polydispersity. More importantly, we found that capped nano-rubies have been produced for sizes below 10 nm whereas another polymorph (γ phase) is expected to be favored according to calorimetry experiments. Most of the ligand-free nanoparticles appear to form in the γ phase. In addition, the nanoparticles stabilized with ligands show no shift for the chromium ions lines in luminescence measurements. Indeed, the chromium emission in corundum is a sensitive structural probe. To go further, a theoretical approach has been planned to understand the influence of ligands on the structure of α alumina nanoparticles.

We pointed out that the ligands reduce drastically the stress that applies on the nanoparticles surface. Indeed, the surface stress defined as an excess energy of the surface energy is due to the atoms reconstruction when a surface is created. A surface is energetically disfavored with undercoordinated atoms and they thus seek to coordinate with those in subsurface. As a result, the surface reorganizes and the mechanical deformations lead to a positive pressure. Such deformation is progressively damped along the nanoparticle radius. A certain thickness of amorphous-like phase is then visible and appears independent of the particles size. The core of the nanoparticle counterbalances this atoms reorganization to maintain the bulk-like configuration by trying to reduce the atoms bond lengths indicated by negative pressure.

Hence, ligands have a strong impact on the surface reconstruction since they bond to undercoordinated atoms and partially prevent the collapse of this first layer. Such stabilization thus justifies the lack of luminescence shift expected for the emission lines of the chromium ions in nano-rubies.

Perspectives.

Finally, synthesis of bare nanoparticles by PLAL is of a great interest to industrial applications and promising economically in a long time run according to the productivity. However, numerous improvements need to be done to pursue toward a better control of the nanoparticles morphology and the colloidal stability. Even if the use of adsorbates allows a better control of the nanoparticles, the main advantage of PLAL compared to the other synthesis methods remains the production of colloidal solutions of ligand-free nanoparticles in an one-step process.

In this sense, chapter 3 reveals that trapped electrons can not be excluded to explain the negative charges of gold nanoparticles. Indeed, the poor amount of oxide observed raises the question of the adsorption mechanism of the anions, which are usually assumed to mainly contribute to the surface

charge of the Au nanoparticles. To confirm this assumption, we are pursuing the theoretical work launched recently. We seek to find the most likely adsorption modes of different ions on a gold surface with DFT-based calculations using the VASP software. In addition, new XPS experiments could bring final conclusion on this study. The perspective of this work would be a breakthrough in the understanding of the stabilization of metal colloids.

By using organic ligands, the stabilization seems even better. Other experiments using different molecules, laser equipment such as fs laser, and even various target materials should be interesting. Theoretically, our calculations made on corundum alumina is quite convincing on the stabilization by the ligands, but a similar study should be performed on the γ phase of alumina to confront the results obtained on the two polymorphs.

Finally, the chapter 2 remains a first exciting study whose one the final goal is to investigate how the nanoparticles growth and maturation may be influenced by high viscous oils. This study allows to observe the dynamics of the bubbles in two high viscous liquid where the conditions could be different from system such as ablation in water. To go further, we consider to explore a broader range of viscosity values and to relate the bubbles dynamics, described by hydrodynamic and thermodynamic parameters, with the nanoparticles morphology characteristics. At the end, a control of the nanoparticles could be considered through the bubbles and the solvent, in addition to the one-step process interest.

APPENDIX

A.1 Concentration from absorption spectrum

Absorption spectrum expresses the absorbance in optical density (OD) as a function of the absorbed laser wavelength. By crossing a sample of thickness h , the intensity of the incident laser beam I_0 is attenuated due to absorption and scattering related to the encountered particles. The transmitted beam has a remaining intensity I , which is recorded by a detector. Absorbance A defines the extinction variation between the two light beams:

$$A[OD] = -\log_{10} \left(\frac{I}{I_0} \right) \quad (\text{A.1})$$

A follows the Beer-Lambert law relating the attenuation of the light with the material features:

$$A = h \sum_{\{i\}} \varepsilon(i) c(i) = \frac{h}{\ln(10)} \sum_{\{i\}} \sigma(i) n(i) \quad (\text{A.2})$$

where the concentration of a particles set $\{i\}$ c_i ($\text{mol} \cdot \text{m}^{-3}$) and the molar extinction coefficient $\varepsilon(i)$ (m^2/mol) are related to the extinction cross-section $\sigma(i)$ (m^2) and the density number $n(i)$ (m^{-3}). The absorption spectrum of gold nanoparticles is known to present a resonance peak, which shifts with particles size. However, this peak was found to be static at around 525 nm for sizes below about 20 nm. For small particles, the cross section is a simple function of the size, absorbance just depends on the concentration of these nanoparticles.

Density $n(i)$. To evaluate the gold nanoparticles concentration, we want to express the density $n(i)$ by the total gold particles concentration c_{sol} in mass per volume unit (g/L). For this purpose, we consider a weight distribution $P_m(i)$ of a set $\{i\}$ of particles centered on a diameter d . The total

mass m_T is equal to the sum of each mass fraction $m(i)$ given by:

$$m_T = \sum_{\{i\}} m_T P_m(i) = \sum_{\{i\}} m(i) \quad (\text{A.3})$$

$$\text{with } \sum_{\{i\}} P_m(i) = 1$$

$m(i)$ is thus the mass of particles $\{i\}$ of the corresponding diameter d , which can be related to the particles number $N(i)$ and the density ρ :

$$m(i) = \rho V(i) = \rho N(i) \frac{4}{3} \pi \left(\frac{d}{2}\right)^3 = \rho N(i) \frac{2}{3} d S(d) \quad (\text{A.4})$$

with $S(d)$ and $V(i)$ the surface area and the volume of the particles set $\{i\}$ associated to the diameter d , respectively.

As the concentration of the solution c_{sol} is equal to the total mass m_T divided by the total volume V , equations A.3 and A.4 become:

$$P_m(i) \frac{m_T}{V} = P_m(i) c_{sol} = \rho \frac{N(i)}{V} \frac{2}{3} d S(d)$$

$$n(i) = \frac{N(i)}{V} = \frac{3}{2} \frac{P_m(i) c_{sol}}{\rho d S(d)} \quad (\text{A.5})$$

Cross-section $\sigma(i)$. From the literature, the extinction efficiency coefficient Q_{ext} can be calculated from optical constants and Mie theory, and is related to $\sigma(i)$ by:

$$\sigma(i) = Q_{ext} S(d) \quad (\text{A.6})$$

For gold, Q_{ext}/d remains constant for size below 20 nm and is estimated at 0.067 nm^{-1} from two cross-checked references^{402,403}.

By injecting equations A.5 and A.6 in A.2, we obtain a proportionality relation between c_{sol} and A :

$$A = \frac{h}{\ln(10)} \frac{3c_{sol}}{2\rho} \underbrace{\sum_{\{i\}} P_m(i) \frac{Q_{ext}}{d} \frac{S(d)}{S(d)}}_{\langle \frac{Q_{ext}}{d} \rangle}$$

$$c_{sol} [g/L] = \frac{2}{3} \frac{\ln(10)\rho}{h} \frac{1}{\langle \frac{Q_{ext}}{d} \rangle} A[OD] = 0.0442 \times A[OD] \quad (\text{A.7})$$

In our case, the absorption cell is 1-cm size (h) and the gold density is $\rho = 19.3 \text{ g.cm}^{-3}$.

A.2 Differential sedimentation centrifuge

In our experiments, we use a CPS system to determine the size distributions of the synthesized gold solutions. The principle is to inject a small volume (100 μL) of solution containing nanoparticles and to time the arrival of particles being detected when they pass in front of a diode laser beam and induce transmittance fluctuations. Then, the setup allows to find the diameter of each particle according to their arrival time.

Particles velocity.

The principle of calculation is based on the centrifugal sedimentation of particles in a liquid of density ρ_L and dynamic viscosity η_L . Forces balance takes into account the centrifugal forces along the considered z-axis, and the friction force with the Stokes-Einstein law and considering the Archimedes' principle:

$$\begin{aligned} m \frac{d\vec{v}}{dt} &= m\vec{g}_c - 6\pi\eta_L r \vec{v} - \rho_L V_p \vec{g}_c \\ &= -\alpha \vec{v} - (\rho_S - \rho_L) V_p \vec{g}_c \\ &= -\alpha \vec{v} - \Delta\rho V_p \vec{g}_c \end{aligned} \quad (\text{A.8})$$

The particles of radius r have a mass m , which is related to the volume V_p and the density ρ_S . They move with a velocity \vec{v} . \vec{g}_c is the centrifugal acceleration defined as: $g_c = \omega^2 R = RCF \times g$ with ω the rotational speed and R the radius of rotation. RCF is the Relative Centrifuge Force and g is the gravity acceleration. This gives a differential equation of the first order to solve along the vertical axis, and the solution is given by:

$$\begin{aligned} \vec{v} &= v_{lim} \left(1 - e^{-\frac{t}{\tau}}\right) \vec{e}_z \\ \text{with } v_{lim} &= -\tau g_c \frac{\Delta\rho}{\rho_S} = -\tau g_c \left(1 - \frac{\rho_L}{\rho_S}\right) \quad \text{and} \quad \tau = \frac{m}{\alpha} \end{aligned} \quad (\text{A.9})$$

Therefore, τ refers to the time for which a particle of mass m reaches the limit velocity v_{lim} . As the α term depends on the particles radius, we can rearrange τ as follows:

$$\begin{aligned} \tau &= \frac{m}{\alpha} = \frac{\rho_S V_p}{6\pi\eta_L r} = \frac{\frac{4}{3}\pi r^3 \rho_S}{6\pi\eta_L r} = \frac{2}{9} \frac{\rho_S}{\eta_L} r^2 \\ v_{lim} &= \frac{2}{9} \frac{\Delta\rho}{\eta_L} r^2 g_c \end{aligned} \quad (\text{A.10})$$

If we take gold nanoparticles of 1 μm and 10 nm rotating in water, the time to reach v_{lim} is respectively 4.3 μs and 0.43 ns. Therefore, we can consider that the particles reach instantaneously the limit speed, i.e. at constant speed, of 0.8 m/s and 80 $\mu\text{m/s}$, respectively, with $RCF = 20\,000$.

Size measurement.

When particles are at their constant velocity, the acceleration becomes null and the forces are balanced. Then, the settling velocity v_{lim} can be restated as the first derivative of the distance from the center of rotation to the detector with respect to time:

$$\frac{dR}{dt} = \frac{2}{9} \frac{\Delta\rho}{\eta_L} r^2 \omega^2 R \quad (\text{A.11})$$

$$(\text{A.12})$$

Finally, we integrate from the center of the centrifuge disc R_o to the detector position at the edge of the disc R_f , which allow us to relate the particles radius to the arrival time t :

$$\begin{aligned} \ln\left(\frac{R_f}{R_o}\right) &= \frac{2}{9} \frac{\Delta\rho}{\eta_L} r^2 \omega^2 t \\ r &= \left(\frac{9}{2} \frac{\eta_L}{\Delta\rho \omega^2} \ln\left(\frac{R_f}{R_o}\right)\right)^{\frac{1}{2}} t^{-\frac{1}{2}} \\ r &= K t^{-\frac{1}{2}} \end{aligned} \quad (\text{A.13})$$

Consequently, it is easy to calculate the particles size from the arrival time by knowing the parameters of the measured material and the driven liquid media, as well as the setup parameters for each measurement.

Data display.

At the end, a weight distribution $\rho_m(D)$ is obtained. When we plot it as a function of a linearly scale of diameters D , the small sizes are crushed with respect to the whole diameter range from nm to μm . A logarithm scale is more appropriated but it necessitates a variable change in order to preserve the weight distribution area, which represents the relative contribution to the total weight of a given size range:

$$m_T = \int_{D_{min}}^{D_{max}} \rho_m(D) dD \longrightarrow \int_{D'_{min}}^{D'_{max}} \rho'_m(X) dX \quad (\text{A.14})$$

$$\text{with } D \rightarrow X = \log(D)$$

$$dD \rightarrow dX = \frac{d(\ln(D))}{\ln(10)} = \frac{dD}{D \ln(10)}$$

Finally, we find that the relative weight distribution $\rho'_m(X)$ by multiplying the linear weight distribution $\rho_m(D)$ by its diameters D within a constant taking into account during the CPS software

process.:

$$\rho_m(D)dD = \rho'_m(X)dX$$

$$\rho'_m(X) = \rho_m(D)\frac{dD}{dX} = \rho_m(D)D \ln(10) \quad (\text{A.15})$$

$$\rho'_m(X) \approx D\rho_m(D) \quad (\text{A.16})$$

A.3 Zeta potential measurement

The zeta potential is used to know the charge of the solvated nanoparticles at the slipping plane. The principle of the ZetaSizer apparatus is to use an electrophoresis cell in order to migrate the charged particles toward the anode or the cathode as a function of the charge sign by applying an electric field. The zeta potential ζ can then be calculated from the Henry's equation:

$$\mu_e = \frac{v_e}{F_e} = \frac{2\varepsilon\zeta f(\kappa a)}{3\eta} \quad (\text{A.17})$$

where the electrophoresis mobility μ_e ($\text{m}^2/\text{V.s}$) is the particles velocity v_e over the applied electric field F_e , ε the permittivity of the solvent and η the dynamic viscosity.

$f(\kappa a)$ is the Henry's function that balances between the Hückel and Smoluchowski limits: $1 \leq f(\kappa a) \leq 1.5$ with $\kappa = 1/\lambda_D$. The complete expression of $f(\kappa a)$ can be found elsewhere²⁸⁷. It depends essentially to the ratio $\kappa a = a/\lambda_D$ between the particles radius a and the Debye length λ_D . On the one hand, the Hückel limit ($f(\kappa a) = 1.0$) favors the small particles with a large double layer ($a/\lambda_D \ll 1$), while systems of large particles in high salt solutions ($a/\lambda_D > 1$) are better described by the Smoluchowski model with $f(\kappa a) = 1.5$.

Therefore, the zeta potential is proportional to the electrophoresis mobility μ_e . As the electric field is a controlled parameter, only the particles velocity needs to be measured. For this purpose, the laser Doppler electrophoresis technique is used. The principle is to light the solution with an incident laser beam characterized with a frequency f_{ref} and a wavelength λ . The light will be then scattered by the particles and will be captured by a detector, which forms with the incident laser beam an angle θ . As the particles move, a difference appears between the frequency of the incident beam and that of the scattered beam, noted f_{sca} . This shift in frequency is related with the particles velocity as follows:

$$\Delta f = f_{ref} - f_{sca} = \frac{2v_e \sin\left(\frac{\theta}{2}\right)}{\lambda} \quad (\text{A.18})$$

The incident and scattered signals are forced to interfere with an appropriate angle thus creating a

modulated beam with a rapid and slow oscillations frequency. The smallest "beat" frequency is then recorded by the detector that can deduce the speed of each particle. The sign of the frequency shift ($\Delta f > 0$ or < 0) indicates the sign of the zeta potential (+ or -, respectively).

B.1 Theoretical basis

Calculations methods at atomic level have been developed along the XXth century with the revolution of Quantum Mechanics. A quantum system is composed of atoms that interact thanks to electrostatic charges distributed between nuclei and electrons. The state of this system is described by the wavefunction Ψ and its energy E , which are related by the Schrödinger equation, established in 1926. From these quantities, it is thus possible to determine the physico-chemical properties. In the stationary case, the time-independent Schrödinger equation is given by:

$$\hat{H}\Psi(\vec{r}) = E(\vec{r})\Psi(\vec{r}) \quad (\text{B.1})$$

where \hat{H} is the Hamiltonian operator and is expressed as follow:

$$\hat{H} = -\sum_{i=1}^N \frac{1}{2m_e} \nabla_i^2 - \sum_{A=1}^M \frac{1}{2m_A} \nabla_A^2 + \sum_{i=1}^N \sum_{j>i}^N \frac{e^2}{4\pi\epsilon_0|r_i - r_j|} - \sum_{A=1}^M \sum_{i=1}^N \frac{Z_A e}{4\pi\epsilon_0|R_A - r_i|} + \sum_{A=1}^M \sum_{B>A}^M \frac{Z_A Z_B e^2}{4\pi\epsilon_0|R_A - R_B|} \quad (\text{B.2})$$

$$\hat{H} = T_e + T_n + V_{ee} + V_{en} + V_{nn}$$

In the following, expressions will be written in atomic units, *i.e.* $e = m_e = 4\pi\epsilon_0 = 1$.

The two first terms \hat{T}_e and \hat{T}_n are the electronic and nuclear kinetic energies, respectively. Laplacian operators ∇^2 act on the electron i of mass m_e and the nucleus A of mass m_A . Coulomb interactions are described by the electronic \hat{V}_{ee} and nuclear \hat{V}_{nn} repulsive contributions, as well as the attractive term \hat{V}_{en} . Each term takes into account the interaction induced between two charged particles, for instance, one electron i of charge e and one nucleus A of charge $Z_A e$, spaced with a distance $r_{Ai} = |R_A - r_i|$. Summations are done on all the particles, namely N electrons and M nuclei.

The analytic resolution of this equation is limited to mono-electronic cases, such as the hydrogen atom or the H_2^+ molecule. Larger polyelectronic systems cannot be solved analytically, while numerical calculations are extremely difficult due to the computational cost. To simplify the resolution, the famous Born-Oppenheimer approximation is applied for any quantum systems³³⁰. This approach considers that the mass difference between electrons and nuclei induces a difference of time between the particles movements. The nuclei are thus considered fixed compared to the electrons movement. The electronic and nuclear wavefunctions and hamiltonians are thus decoupled:

$$\begin{aligned} \hat{H} &= \hat{H}_e + \hat{H}_n & \hat{H}_e \Psi_e &= E_e \Psi_e & \text{with } \hat{H}_e &= T_e + V_{ee} + V_{en} & \text{(B.3)} \\ \Psi &= \Psi_e(\vec{r}; R) \cdot \Psi_n(R) & \hat{H}_n \Psi_n &= E \Psi_n & \text{with } \hat{H}_n &= T_n + E_e + V_{nn} \end{aligned}$$

Therefore, in order to calculate the total energy of the system, the electronic part needs to be solved at first in a fixed nuclear configuration before determining the nuclear part. You can notice that the electronic energy E_e is included in the nuclear hamiltonian \hat{H}_n , as well as the electronic wavefunction Ψ_e , which depends on the constant positions of the nuclei R . The resolution of the Schrödinger equation of the electronic system is however prevented by the electronic interaction potential \hat{V}_{ee} .

From this observation, numerous calculations methods based on this wavefunction-Hamiltonian formalism have been developed within the second half of the last century, including *ab initio* or first-principles approaches, Density Functional Theory (DFT) based calculations or semi-empirical methods.

One of the earlier *ab initio* methods is the Hartree-Fock (HF) approach³³¹ for which the electronic interactions are averaged and included in a mean field. The electrons are not correlated since the wavefunction of the total system is decoupled as the product of mono-electronic wavefunctions in the formalism of a Slater determinant³³². Consequently, the Hamiltonian will be written as a sum of mono-electronic hamiltonians. In HF calculations, correlations between electrons located at short (dynamic or instantaneous correlation) and long (static or permanent correlation) distances are thus not included, leading to energy over-estimation in some cases, such as closed electronic shells systems.

In post Hartree-Fock methods, the electronic correlation is taken into account by developing the system wavefunction as a linear combination of several Slater determinants, which characterize excited electronic states. This means that some electrons of the systems are excited in unoccupied highest levels. However, these approaches are still expensive in computational cost as they are based on wavefunction with $4N$ variables, *i.e.* 3 spatial and 1 spin variables for each electron.

The Density Functional Theory (DFT) approach consists to substitute the $4N$ variables wavefunction by the electronic density of the system, which is composed of only 3 spatial coordinates and 1 spin variable. Such calculation may decrease by one to three orders of magnitude the computational

time, according to the basis set used.

B.2 Density Functional Theory

B.2.1 DFT outlines

The principle of this method is based on the substitution of the wavefunction by the electronic density ρ . The density is taken as the density matrix restricted to its diagonal, which is the product of the wavefunction of the system with its conjugate:

$$\rho(\vec{r}_1, \dots, \vec{r}_N) = \Psi(\vec{r}_1, \dots, \vec{r}_N) \times \Psi^*(\vec{r}_1, \dots, \vec{r}_N) = |\Psi(\vec{r}_1, \dots, \vec{r}_N)|^2 \quad (\text{B.4})$$

By considering the electronic Hamiltonian \hat{H}_e as defined in equation B.3, the equation cannot be solved. From 1964, Hohenberg and Kohn (HK) put the basis of the DFT by stating two theorems³³³:

- (i) For any system of interacting particles in an external potential V_{ext} , the electronic density ρ_0 associated to the ground state of the system determines unequivocally this external potential, within a constant. In other words, the physical quantities, which describe the ground state of the system, are functionals of ρ_0 and are equivalent to the wavefunction/Hamiltonian formalism. Consequently, the electronic Hamiltonian \hat{H}_e can be rearranged for any electronic density ρ , as follow:

$$E[\rho] = T[\rho] + E_{ee}[\rho] + \int V_{ext}(\vec{r})\rho(\vec{r})d\vec{r} = F_{HK}[\rho] + \int V_{ext}(\vec{r})\rho(\vec{r})d\vec{r} \quad (\text{B.5})$$

where $T[\rho]$ is the total kinetic energy, the electronic interaction term E_{ee} and an external potential V_{ext} , which includes the nuclei attraction potential V_{en} . The two first terms are regrouped within the Hohenberg and Kohn functional $F_{HK}[\rho]$, which is universal since it depends neither on the system, nor on the external potential.

- (ii) For a particular external potential, the total energy of the system in the ground state E_0 corresponds to the global minimum of the functional $E[\rho]$ with respect to *rho*. The density, which minimizes this functional, is the ground state density ρ_0 :

$$E_0[\rho_0] = \min_{\rho} \{E[\rho]\} \quad (\text{B.6})$$

The important point here is to know the HK functional $F_{HK}[\rho]$, which is unfortunately unknown, mostly due to the electron-electron contribution. In 1965, Kohn and Sham prevented this problem with the Kohn-Sham (KS) theory³³⁴. Its main point is to substitute the real system of interacting electrons immersed in an external potential V_{ext} by a fictive system of non-interacting electrons moving in an effective external potential V_s . The two systems are related by their energies and

their electronic densities, which are considered equivalent. Finally, the fictive system is defined by the new KS Hamiltonian $F_{KS} = t_s + V_s$ and the total energy is found thanks to the new Schrödinger equation of the KS system:

$$\begin{aligned} F_{KS}\phi_i &= \left[-\frac{1}{2}\nabla^2 + V_s(\vec{r}) \right] \phi_i = \varepsilon_i \phi_i \\ E[\rho] &= \sum_i \varepsilon_i = T_s[\rho] + \int V_s(\vec{r})\rho(\vec{r})d\vec{r} \end{aligned} \quad (\text{B.7})$$

Hence, the KS equation can be solved by establishing the form of the effective potential V_s , thanks to known quantities coming from the known real system.

As the total energy is conserved between the two systems, we can write from the equations B.5 and B.7:

$$T_s[\rho] + \int V_s(\vec{r})\rho(\vec{r})d\vec{r} = T[\rho] + E_{ee}[\rho] + \int V_{ext}(\vec{r})\rho(\vec{r})d\vec{r} \quad (\text{B.8})$$

The trick to remove the unknown $F_{HK}[\rho]$ functional is to inject the fictive kinetic energy $T_s[\rho]$ in the right part of the equation, *i.e.* in the real system expression. The electronic correlation is also taken into account by inserting the full classical Coulombian interaction term $J[\rho]$, which is the difference between the electronic interaction $E_{ee}[\rho]$ and a non-classical or quantum term $E_{ncl}[\rho]$ describing the exchange and the correlation terms:

$$\begin{aligned} T_s[\rho] + \int V_s(\vec{r})\rho(\vec{r})d\vec{r} &= T[\rho] + E_{ee}[\rho] + \int V_{ext}(\vec{r})\rho(\vec{r})d\vec{r} + T_s[\rho] - T_s[\rho] + J[\rho] - J[\rho] \\ \text{with } J[\rho] = E_{ee}[\rho] - E_{ncl}[\rho] &= \frac{1}{2} \iint \frac{\rho(\vec{r})\rho(\vec{r}')}{|\vec{r} - \vec{r}'|} d\vec{r}d\vec{r}' \end{aligned} \quad (\text{B.9})$$

After reorganizing the equation, the four last terms are regrouped in the exchange-correlation functional $E_{xc}[\rho]$, while the other terms are analytically known:

$$T_s[\rho] + \int V_s(\vec{r})\rho(\vec{r})d\vec{r} = \underbrace{T_s[\rho] + J[\rho] + \int V_{ext}(\vec{r})\rho(\vec{r})d\vec{r}}_{\text{known expression}} + \underbrace{+T[\rho] - T_s[\rho] + E_{ee}[\rho] - J[\rho]}_{\text{unknown } E_{xc}[\rho]} \quad (\text{B.10})$$

By eliminating terms in excess and differentiating the remaining expression with respect to the electron density, the fictive potential is expressed as a function of the terms of the real system:

$$V_s(\vec{r}) = V_{ext}(\vec{r}) + \int \frac{\rho(\vec{r}')}{|\vec{r} - \vec{r}'|} d\vec{r}' + V_{xc}(\vec{r}) \quad (\text{B.11})$$

with $V_{xc}(\vec{r})$ the functional derivative of $E_{xc}[\rho]$.

Thus, by establishing V_s , the KS equation can be solved. From the new calculated eigenfunctions ϕ_i ,

the new electron density ρ_{out} is found and characterized by a novel energy E_{out} corresponding to the summations of the solved eigenvalues ε_i . As postulate by the second HK theorem, the ground state system is found when the total energy $E[\rho]$ is minimized with respect to ρ . In practice, the scheme process of a DFT calculation is based on a Self-Consistent Field (SCF) method where iterative steps seek to minimize the total energy until a convergence criterion is respected (Fig. XX). Between two iterations when the convergence is not achieved, a mixing step is performed in order to modify the input electron density for the next iteration: $\rho_{in}^{i+1} = \alpha\rho_{in}^i + (1 - \alpha)\rho_{out}^i$.

However, some parameters are still missing, such as the exchange-correlation functional and the type of atomic orbitals.

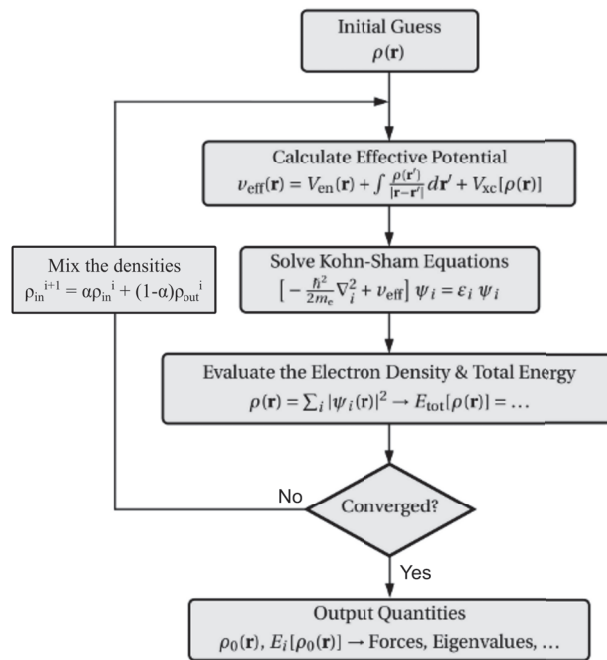


Figure B.1 – SCF iterative process applied on the electronic density in order to minimize the energy of the system by resolving the Kohn-Sham equations.

B.2.2 Exchange-correlation functionals

In order to calculate V_s , only the exchange-correlation term needs to be determined. As the expression of this functional is not mentioned in the Kohn-Sham theory, numerous functionals have been developed to approximate the exchange-correlation contribution. Such functional needs to be carefully chosen in order to ensure an efficient compromise between calculation precision and computational time. As a first approximation, E_{xc} can be separated as a sum of an exchange and a correlation terms: $E_{xc} = E_x + E_c$. The most important functionals are presented here.

LDA: Local Density Approximation. This first functional estimates that the electron density of an inhomogeneous system is locally uniform, as a homogeneous electron gas. The expression of

the correlation term is quite complex to formulate, even if quantum Monte-Carlo-based calculations resulted to an analytic form of E_c^{LDA} ^{404,405}. From the Dirac functional⁴⁰⁶, the exchange is given by:

$$E_x^{LDA}[\rho] = \int \varepsilon_x[\rho] \rho(\vec{r}) d\vec{r} = -C \int \rho(\vec{r})^{\frac{4}{3}} d\vec{r} \quad (\text{B.12})$$

GGA: Generalized Gradient Approximation. While the LDA functional considers that the global electron density varies very slowly spatially, the GGA functional⁴⁰⁷ corrects the LDA potential with a more rapid contribution depending on the density gradient $\nabla\rho$. In 1988, Becke⁴⁰⁸ built a GGA functional that corrects the LDA exchange contribution ε_x^{LDA} by adding an additional term $\Delta\varepsilon_x^{B88}$, dependent of the density gradient. Lee, Yang and Parr (LYP)⁴⁰⁹ developed a similar functional for the correlation part, and the BLYP functional is the exchange-correlation combination of both. A more complex exchange-correlation potential is the PBE functional, created by Perdew, Burke and Ernzerhof³³⁵:

$$\begin{aligned} \varepsilon_x^{PBE} &= \varepsilon_x^{LDA} \left[1 + a - \frac{a}{1 + bx^2} \right] \\ \varepsilon_c^{PBE} &= \varepsilon_c^{LDA} + H(x) \\ \text{with } x &= \frac{|\nabla\rho|}{\rho^{\frac{4}{3}}} \end{aligned} \quad (\text{B.13})$$

with a and b free parameters, and $H(x)$ the corrective term dependent of two free parameters c and d .

Hybrids Functionals. These functionals are linear combinations of exchange and correlation terms of LDA and GGA functionals, and a contribution from the exact exchange term E_x^{HF} from the Hartree-Fock theory. The most known is the B3LYP functional³³⁶, where the contribution is distributed between the exchange-correlation terms of LDA functional, the HF and B88 exchange functionals and the LYP correlation potential:

$$E_{xc}^{B3LYP} = (1 - a_0)E_x^{LDA} + a_0E_x^{HF} + a_x\Delta E_x^{B88} + (1 - a_c)E_c^{LDA} + a_cE_c^{LYP} \quad (\text{B.14})$$

with a_0 , a_x and a_c the contributions weights. Like the free parameters seen in the PBE and B3LYP expressions, all the GGA functionals mentioned above contain adjustable parameters. While the free parameters of the B88, LYP and BLYP functionals are fitted with data of rare gas atoms, those of the PBE and the B3LYP functionals are refined according to theoretical considerations and experimental data, respectively. In any case, the DFT cannot be considered as *ab initio* method since free parameters of the E_{xc} functional need to be adjusted.

B.2.3 Atomic orbitals basis set

In general for small systems with few atoms and electrons, calculations can be performed using molecular orbitals. However, they become impossible for larger systems. The common approxima-

tion for all the quantum calculations is the development of the molecular orbitals on atomic orbitals basis set. For this purpose, spatial part of the molecular orbitals φ_i are built as a linear combination of atomic orbitals (LCAO) χ_μ :

$$\varphi_i = \sum_{\mu} c_{\mu i} \chi_{\mu} \quad (\text{B.15})$$

where $c_{\mu i}$ are the contributions weights of the atomic orbitals χ_{μ} to the molecular orbital φ_i . Several atomic orbital basis sets have been developed, but only the basic basis, which are behind the recent ones, will be presented now.

- **STO: Slater Type Orbital.** The simplest basis set was elaborated by Slater⁴¹⁰: $\chi_{\mu}^{STO} = N r^l e^{-\zeta r}$, with N the normalization constant, l the orbital quantum number and ζ the exponential exponent, which characterizes the diffusivity of the function. However, we rapidly need an important number of STO functions in order to calculate properly small systems.
- **GTO: Gaussian Type Orbital.** A small difference appears in these functions where the exponential is squared: $\chi_{\mu}^{GTO} = N r^l e^{-\alpha r^2}$. This allows to reduce the number of GTO functions as the product of two functions results in a condensed GTO orbital.
- **Extended basis.** To describe accurately quantum system, more theoretical considerations need to be taken into account. Differentiation is thus made between core electrons and valence electrons. The formers strongly interact with the quasi-spherical nuclear potential, which necessitates an important number of functions to calculate finely the core energy. Far from the nuclei, several types of orbitals serve to describe the valence electrons orbitals. Typically, each valence orbital is replaced by multiple atomic orbitals of different sizes. Polarization is also considered by adding functions with higher l than the valence functions, and a diffuse shell can be described by orbitals with a small diffuse exponent, characterized by a slow decrease with distance.

Nowadays, DFT calculations used complex basis set based on the extended basis. Among others, the basis set designed by John Pople is one of the most used^{411,412}, and is written as follow: $n - n_1 n_2 n_3 \dots + + G^{**}$. n corresponds to the number of GTO functions used for the core electrons, while the number of functions to describe the valence shell is referred by the number of n_i . The value of each n_i indicates the number of GTO orbitals combined to represent the valence function. Diffuse and polarized orbitals are taken into account with the numbers of $+$ and $*$ symbols, respectively. For instance, a DFT basis set noted $6 - 311 + G^{**}$ corresponds to a system described by 6 GTO functions in the internal shell, 3 combined GTO orbitals for the first valence function and one orbital for the two others valence functions. This basis includes also one diffuse orbitals group and two polarized orbitals.

B.3 The Vienna Ab initio Simulation Package

By using the DFT method, an efficient setting between time and precision limits to study systems of tens of atoms. In the context of solid state calculations, the computational cost can be drastically decreased by the use of plane waves basis to study crystal structures. This approach is the concept of DFT-based methods, such as the VASP code.

B.3.1 The plane waves basis

In crystal structures, atoms are indefinitely arranged periodically in all the directions. The description of such periodic structure can be limited to the first Brillouin zone, where the Bloch theorem³³⁷ states that any monoelectronic wavefunction $\phi_{n\vec{k}}$ of a lattice system can be expressed as the product of a plane wave with a function $u_{n\vec{k}}$ owing the periodicity of the potential:

$$\phi_{n\vec{k}}(\vec{r} + \vec{R}) = \phi_{n\vec{k}}(\vec{r}) = u_{n\vec{k}}(\vec{r}) e^{i\vec{k}\vec{r}} \quad (\text{B.16})$$

with \vec{R} any vector from the lattice system leaving the Hamiltonian invariant, and \vec{k} the wave vector from the first Brillouin zone. n is associated to one monoelectronic band. $u_{n\vec{k}}$ can be decomposed into a sum of plane waves using a Fourier series:

$$\begin{aligned} u_{n\vec{k}}(\vec{r}) &= \sum_{\vec{G}} C_{n\vec{k}}(\vec{r}) e^{i\vec{G}\vec{r}} \\ \phi_{n\vec{k}}(\vec{r}) &= \sum_{\vec{G}} C_{n\vec{k}}(\vec{r}) e^{i(\vec{G} + \vec{k})\vec{r}} \end{aligned} \quad (\text{B.17})$$

with $C_{n\vec{k}}(\vec{r})$ the Fourier coefficients and \vec{G} the wave vector contained in the reciprocal space. Theoretically, the numbers of \vec{k} and \vec{G} to describe exactly a monoelectronic orbital remain infinite. In practice, these vectors are limited by a cutoff energy E_{cut} , as defined by:

$$\frac{\hbar^2}{2m_e} |\vec{k} + \vec{G}|^2 < E_{cut} \quad (\text{B.18})$$

Therefore, higher the cutoff energy, more extended the plane waves basis and more costly the calculation. Plane waves must be chosen in order to satisfy the calculation precision in a respectable computational time. The k -points mesh is thus essential since the reduction of the lattice system should be compensated by an increase of k -points numbers. Among others, the Monkhorst and Pack sampling method⁴¹³ allows to generate an efficient uniform k -points grid.

Such plane waves basis are practical due to the advantage to cover uniformly the probed space. However, they are rapidly limited when the number of plane waves becomes unrealistic for the description of strongly spatially localized states or the rapid oscillations of wavefunctions, as in the

case of core electrons located near the nuclei. One of the common methods to overcome this issue is the use of pseudopotentials.

B.3.2 Pseudopotentials

This approach assumes that the physical and chemical properties of a system are governed by the valence electrons, leaving the core electrons ineffective and slightly perturbed by the KS potential. From this assumption, the inner electrons and the nucleus are modeled by an effective potential interacting with the valence electrons. This denominated potential defines the so-called pseudopotential⁴¹⁴, which seeks to abrogate the description of the core electrons. Indeed, the strong attractive interaction with nucleus, represented by the V potential in figure B.2, induces rapid oscillations on the core electrons wavefunction Ψ , leading to exhausting and long calculations. Pseudopotential \tilde{V} defined from pseudo-wavefunctions $\tilde{\Psi}$ are thus developed in order to describe a softer variation in the inner localized region, characterized from the nucleus to a cutoff distance r_c (Fig. B.2). Beyond this critical radius, the valence electron pseudo-wavefunction must be equivalent to the exact atomic wavefunction Ψ . Such approximation simplifies greatly the calculations, since less plane waves are necessary to generate the pseudo-wavefunction. Several pseudopotentials have been developed, with each a different theoretical consideration based on the difference between the "all-electrons" calculations for a reference atom using the exact wavefunction Ψ and the pseudopotential calculation using the pseudo-wavefunction $\tilde{\Psi}$. Norm-conserving⁴¹⁵, Ultra-soft (USPP)⁴¹⁶ and Projected Augmented Wave (PAW)⁴¹⁷ pseudopotentials are the most used in DFT-based methods, and the two lasts ones are included for each reference atom in the VASP code library⁴¹⁸.

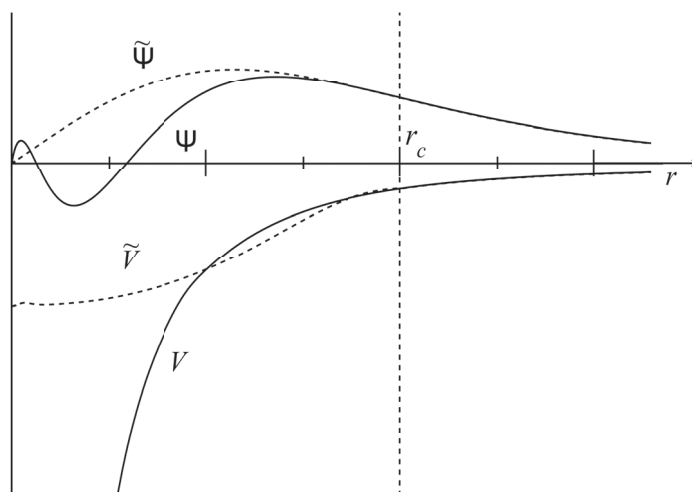


Figure B.2 – Potential V and wavefunction Ψ of the inner localized region near the nucleus are replaced by a pseudopotential \tilde{V} and a pseudo-wavefunction $\tilde{\Psi}$.

B.3.3 VASP parameters

All the calculations presented in the following were performed within the Generalized Gradient Approximation (GGA) with the PBE functional using plane waves basis set included in PAW-type pseudopotentials⁴¹⁸ (see Appendix B.3). The $2 \times 2 \times 1$ k-grid mesh is defined automatically with the Monkhorst and Pack method⁴¹³ and is centered on the middle of the Brillouin zone, *i.e.* the Γ point. A cutoff energy E_{cut} of 500 eV is fixed and the final results are obtained with an accurate precision, *i.e.* a finer second k-point grid is taken with twice larger G vectors. Typically the energy resolution per atom is less than 1 meV/atom. A self-consistent field process controlled the convergence of the calculation, ending when the energy difference of two consecutive steps becomes below the energy convergence criterion, fixed at 10^{-6} eV. At the end of the electronic optimization cycle, each atomic force is calculated thanks to the Hellmann-Feynman theorem⁴¹⁹. The ionic structure is directly minimized and finally optimized when the residual forces of each atom are lowered below 0.005 eV/atom.

APPENDIX C

EMPIRICAL POTENTIALS BENCHMARKING

C.1 Isomers

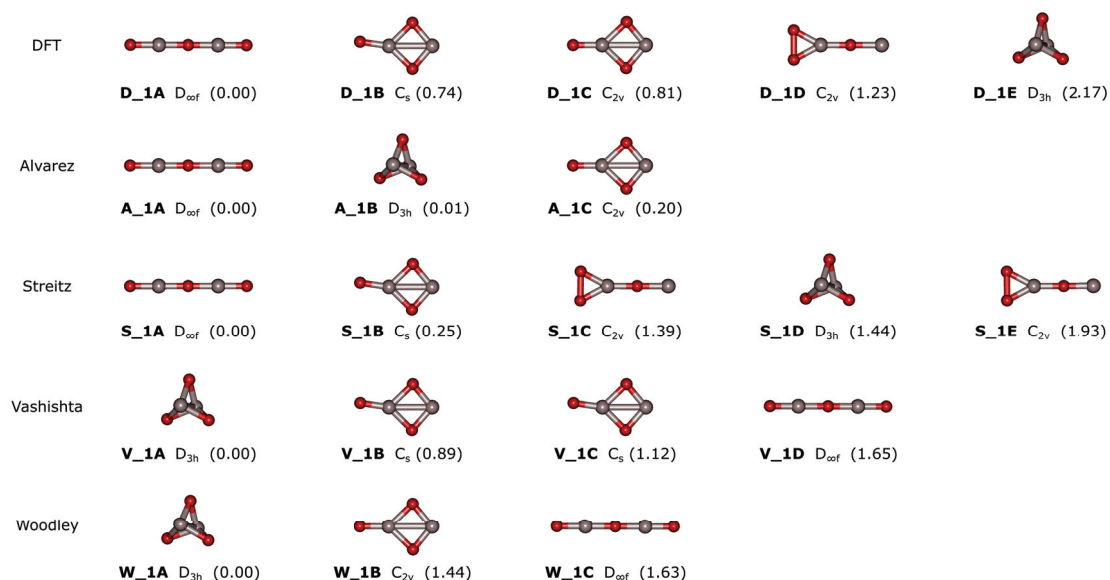


Figure C.1 – Final isomer geometries of the $(\text{Al}_2\text{O}_3)_1$ cluster calculated in DFT and with the four empirical potentials by the conformational research method. The symmetry point groups and the energy relative to the most stable structure are added. Aluminum and oxygen ions are in grey and red, respectively. * represents the structures found by the conformation research with the potentials.

Appendix C: Empirical potentials benchmarking

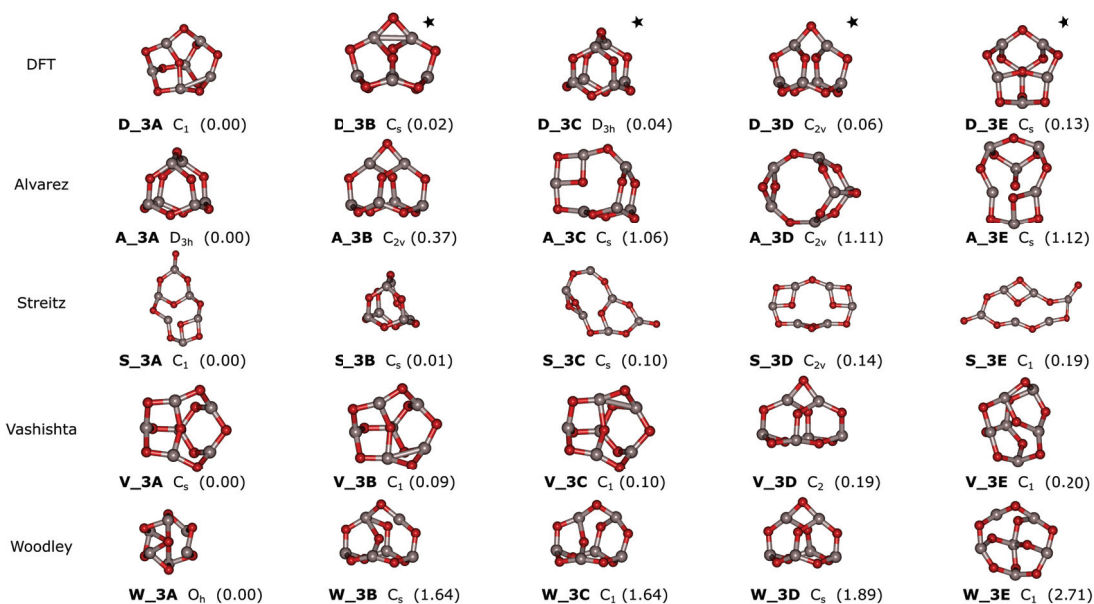


Figure C.2 – Final isomer geometries of the $(\text{Al}_2\text{O}_3)_3$ cluster calculated in DFT and with the four empirical potentials by the conformational research method. The symmetry point groups and the energy relative to the most stable structure are added. Aluminum and oxygen ions are in grey and red, respectively. * represents the structures found by the conformation research with the potentials.

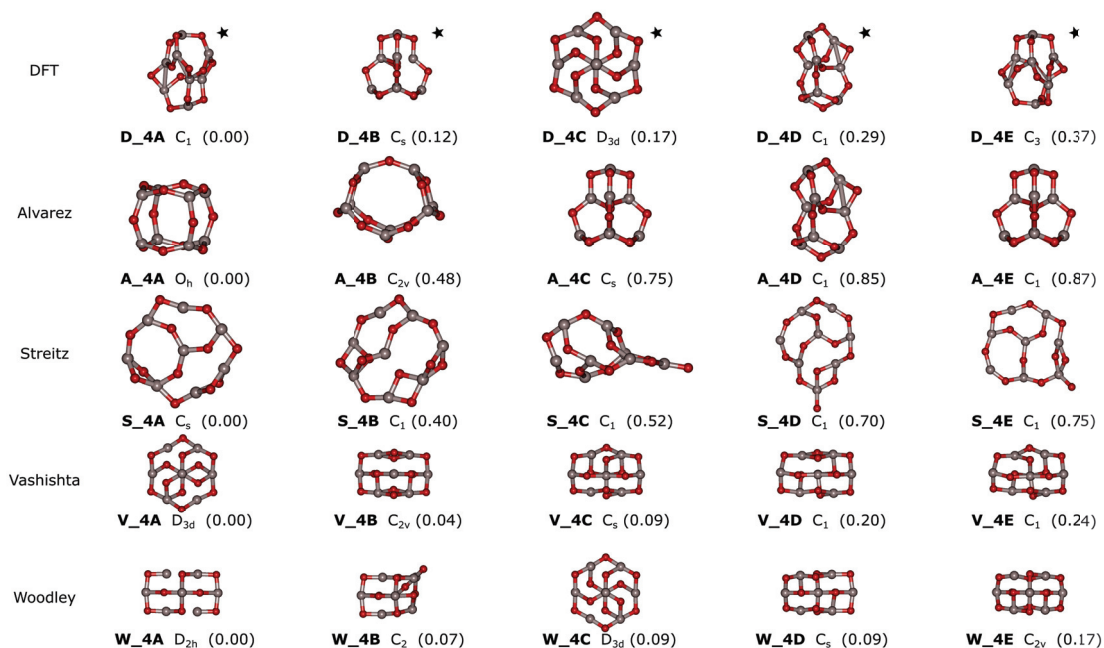


Figure C.3 – Final isomer geometries of the $(\text{Al}_2\text{O}_3)_4$ cluster calculated with the four empirical potentials by the conformational research method. The symmetry point groups and the energy relative to the most stable structure are added. Aluminum and oxygen ions are in grey and red, respectively. * represents the structures found by the conformation research with the potentials.

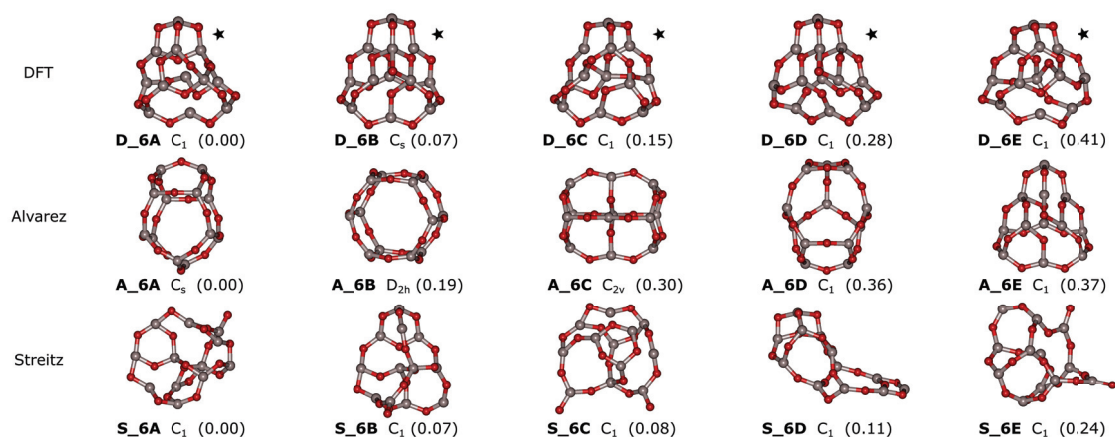


Figure C.4 – Final isomer geometries of the $(\text{Al}_2\text{O}_3)_6$ cluster calculated with the Alvarez and Streitz potentials by the conformational research method. The symmetry point groups and the energy relative to the most stable structure are added. Aluminum and oxygen ions are in grey and red, respectively. * represents the structures found by the conformation research with the potentials.

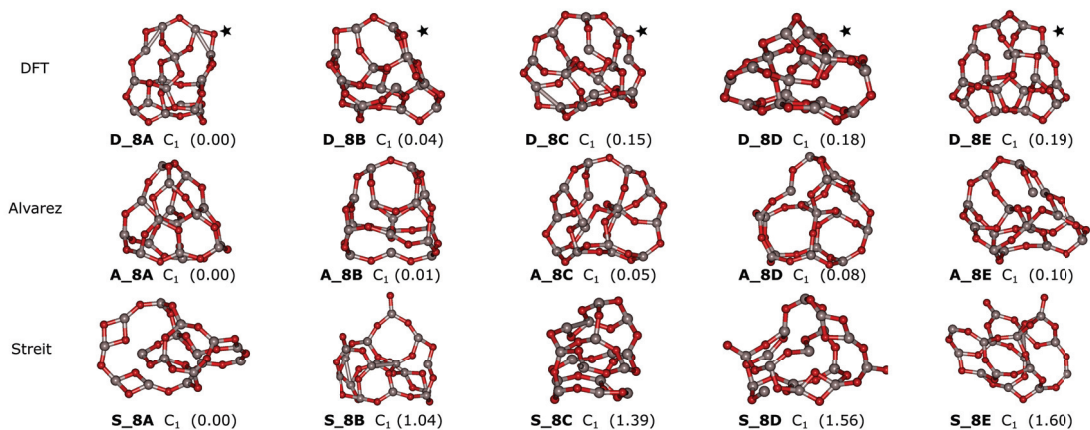


Figure C.5 – Final isomer geometries of the $(\text{Al}_2\text{O}_3)_8$ cluster calculated with the Alvarez and Streitz potentials by the conformational research method. The symmetry point groups and the energy relative to the most stable structure are added. Aluminum and oxygen ions are in grey and red, respectively. \star represents the structures found by the conformation research with the potentials.

C.2 Nanoparticles

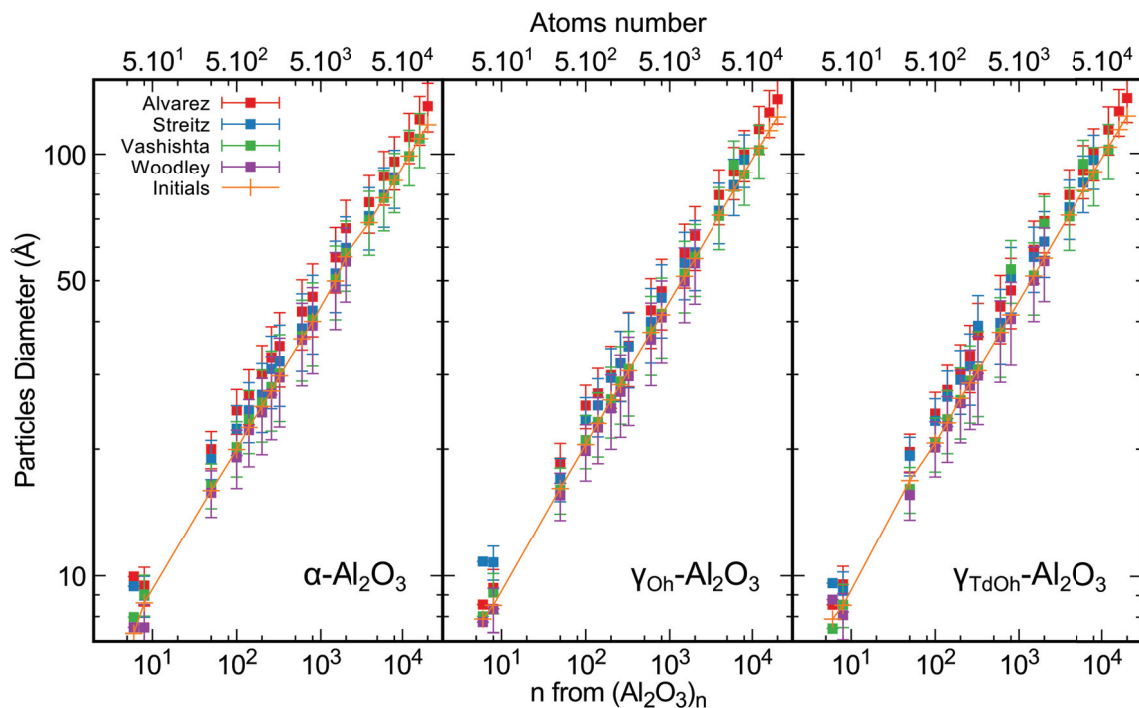


Figure C.6 – Diameters of the nanoparticles optimized by each potential from the initial starting crystal structures (orange curve) as a function of the units number n and the atoms number.

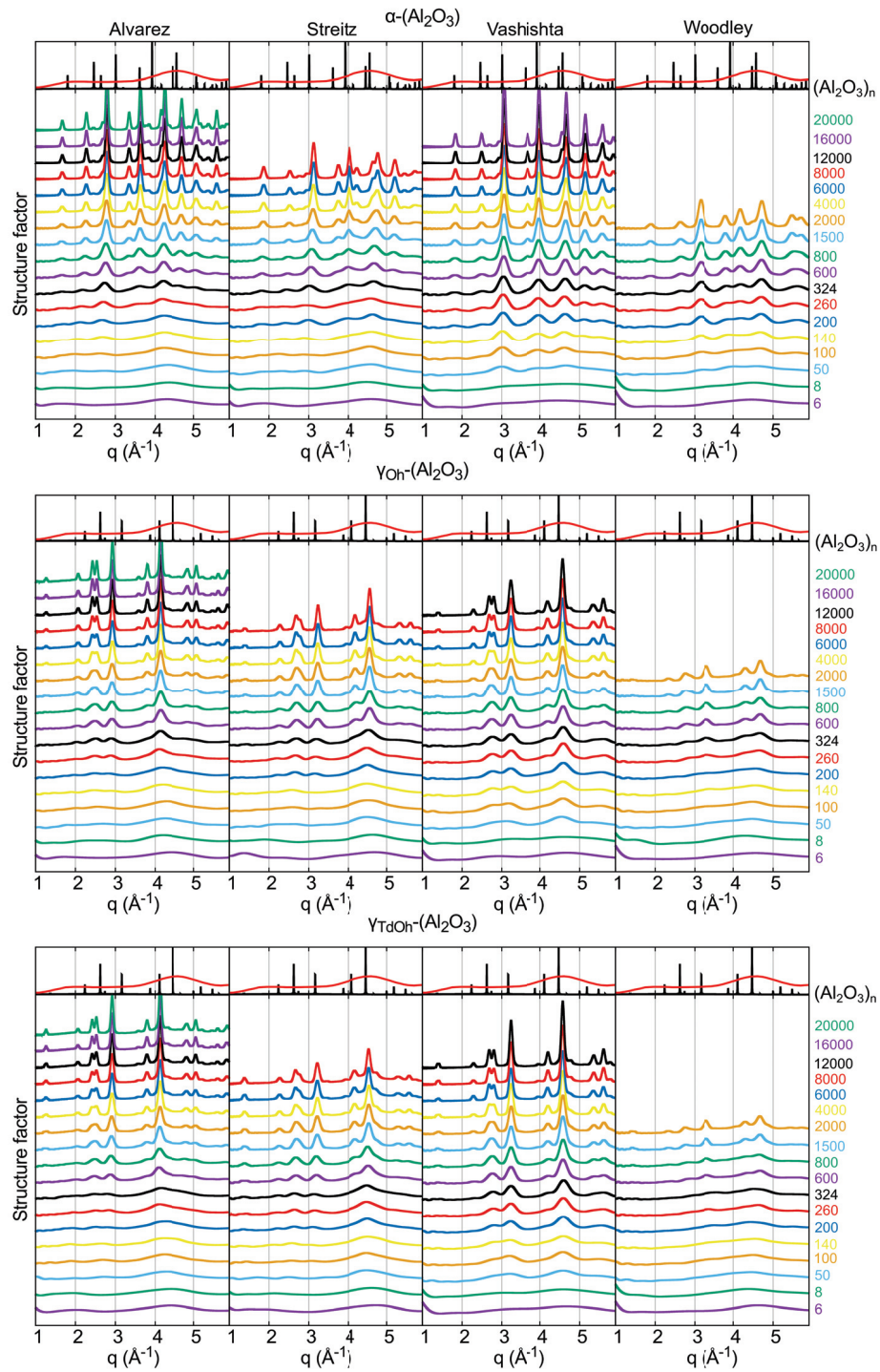


Figure C.7 – Structure factors S of the nanoparticles relaxed starting from the three crystal phases using all the potentials. For each curve, the repeat unit n is displayed on the right. Experimental data from α ³⁸² or γ ³⁸³ bulk alumina (black curve) and α - (Al_2O_3) bulk³⁸⁷ (red curve) are displayed on top of the panel according to the starting phase.

D.1 Theoretical analysis of local pressure

The technique we used to extract relevant local pressures in the Al_2O_3 systems slightly differs from classical methods, such as the Irving-Kirkwood procedure⁴²⁰. First, the Al and O atoms experience different energy interaction terms, which are responsible for local variations of the atomic pressure. To get rid of these atomic scale variations that preclude any detailed local analysis, we build P_{loc} a locally averaged pressure over small stoichiometric regions centered on Al atoms :

$$P_{loc} = P_{Al} + \sum_{i=1, n_{c,Al}} \frac{P_{O_i}}{n_{c,O_i}} \quad (\text{D.1})$$

where P_{Al} and P_{O_i} are the usual atomic pressures calculated on an Al atom and its oxygen first neighbors O_i with an average volume per atom $\frac{V}{N}$ (a cut-off of 2.3 Å has been used to define the first neighbor shell). V and N are the total volume and atom numbers, respectively. $n_{c,Al}$ and n_{c,O_i} are the coordination number of Al and O_i .

Second, the system is subdivided in shells according to its geometry thus taking into account successive regions from the surface to the center of mass. To obtain a local pressure evaluation in meaningful regions such as the inner region and the surface region, we first find the undercoordinated Al atoms from which we define the surface region. Starting from this outer shell, we define the next inner shell from the Al first neighbors of the atoms in the previous outer shell. This procedure is repeated until a shell has been attributed to all the Al atoms. This partitioning of the (0001) Al_2O_3 surface into shells is depicted in figure D.3(a).

D.2 $\Delta a/a_0$ - P - $\Delta \lambda$ relation

Pressure to structural deformation. The groups of d'Amour³⁹⁵ and Finger³⁹⁴ studied independently in 1978 the evolution of the hexagonal lattice parameters of the bulk of α -Al₂O₃ under pressure. They measured the structural deformation by performing X-ray diffraction measurements through a Diamond-Anvil Cell (DAC) apparatus. The first group worked until 9 GPa whereas the second reached 8 GPa but they sustained a non-hydrostatic pressure above 5 GPa for the same liquid medium.

Hence, we calculated the lattice deformation rates defined as:

$$\Delta X/X_0 = \frac{X_i - X_0}{X_0} \quad (\text{D.2})$$

with X_i and X_0 the lattice parameters of the pressurized and zero pressure samples, respectively. X refers to the a and c lattice parameters along the hexagonal x and z axis. The figure D.1 shows the evolution of the lattice deformation rates according to the pressure. Linear fits were adjusted with R^2 between 0.98 and 1. The averaged equation was found to be $\Delta X/X_0 = -0.00126 \times P - 0.00011$.

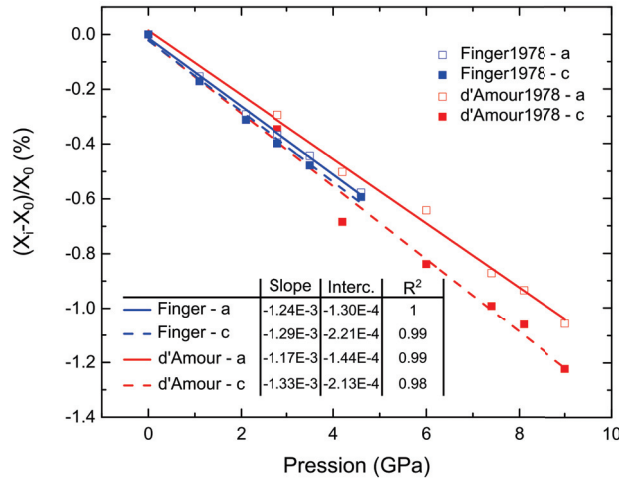


Figure D.1 – Lattice deformation rates calculated for a and c hexagonal lattice parameters over applied pressure (Data from works of d'Amour *et al.*³⁹⁵ and Finger *et al.*³⁹⁴). Data are fitted with linear curves (adjusted R^2 , slope and intercepts are indicated for each curve).

Pressure to luminescence shift. Ruby is known to present pressure dependent luminescence lines. Therefore, emission lines were recorded under controlled pressure using a Diamond Anvil Cell (DAC) apparatus. These experiments were carried out on micro- and nano- size particles before my work thesis in collaboration with Ing. Sylvie Le Floch from the Institute Lumière Matière of the University Lyon 1.

The measurements were performed using the following equipment and protocol:

-
- **DAC.** High hydrostatic pressures were applied on samples using a Chervin-type diamond anvil cell (DAC). The pressure transmitting fluid is a 16:3:1 methanol-ethanol-water mixture. Both remain hydrostatic up to 10.5 ± 0.5 GPa⁴²¹. Above 10.5 GPa, the standard deviation χ of the pressure distribution in the anvil increases linearly with the pressure P , $\chi[\text{GPa}] = 0.2 \times (P - 10.5)$. The errorbars in figure D.2 take into account this error.

 - **Raman spectroscopy.** Luminescence spectra under high pressure has been recorded using a Renishaw RM 1000 micro-Raman-spectrometer equipped with a $10\times$ objective in backscattering configuration⁴²². The excitation line was provided by a Nd:YAG laser, operating at 532.0 nm wavelength. The $10\times$ objective leads to a spot laser radius smaller than $50 \mu\text{m}$. Signal detection has been carried out by a cooled CCD camera. The silicon Raman peak is used as a reference for wavelength calibration. The shift has been measured at 520.3 cm^{-1} for each set of measurement.

 - **Calibration.** Sm:YAG displays a luminescence doublet at 16185 cm^{-1} (Y1) and 16231 cm^{-1} (Y2), whose position has a small temperature dependence, but a pressure dependence as large as that of ruby fluorescence line. Small beads of ruby of diameter $< 10\mu\text{m}$ and burst of YAG:Sm³⁺ of characteristic length $< 20\mu\text{m}$ were disposed at the center of the lower diamond of the anvil cell. The DAC was filled the transmitting fluid. Pressure was increased up to 16 GPa by steps of < 0.5 GPa, then identically decreased to the atmospheric pressure. Pressure was estimated using the Mao calibration⁴²³ of the shift of the R1 line of ruby. Raman spectra of Yag:Sm³⁺ and ruby were recorded after a wait of 30 minutes for stabilization. As Y1 and Y2 bands merge under pressure, we calibrated the Y1 line when the bands were decoupled, and the maximum after. The curve obtained from the pressure decrease shows no deviation with respect to those obtained when increasing pressure. The last spectra were acquired after the cell was open, and show perfect recovery of the position of the Y1, Y2 and Y3 lines before compression.

 - **Ruby measurements under pressure.** Dried micro and nanoparticles and a micron-sized Samarium doped yttrium aluminum garnets crystal (Sm:YAG) were placed in a metallic gasket hole ($145 \mu\text{m}$ diameter) filled with a pressure transmitting fluid. Pressures were measured from the luminescence of the Sm:YAG crystal⁴²⁴. Luminescence spectra from Sm:YAG and nano-ruby were sequentially measured from two spatially separate sample area, thanks to *in-situ* surface visualization. The linear behavior of the final luminescence shift $\Delta\lambda$ as a function of the pressure P is finally fitted below 11 GPa (Fig. D.2) and leads to: $\Delta\lambda[\text{nm}] = 0.357 \times P[\text{GPa}]$.

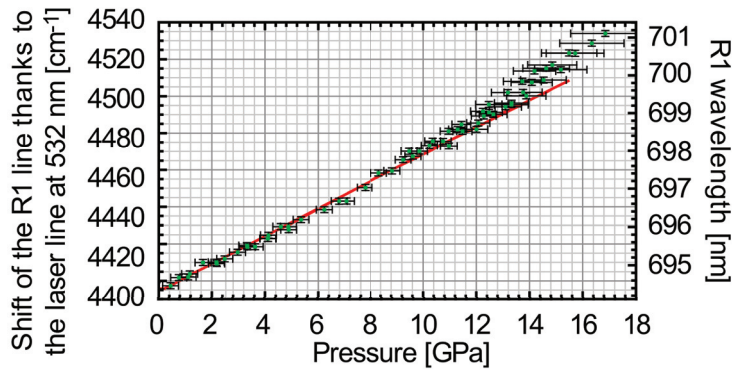


Figure D.2 – Shift of the ruby R1 line as a function of the pressure. The measured wavenumbers correspond to the shift between the R1 line and the laser exciting line (532 nm). The red curves correspond to micro-sized ruby. The green squares correspond to the nanoparticles.

D.3 SMTBQ free alumina surface

A supercell of 1800 atoms was generated ($x = 24.05537 \text{ \AA}$; $y = 24.99907 \text{ \AA}$; $z = 26.12054 \text{ \AA}$) by duplicating the hexagonal unit cell, introduced in section 4.2.3.1. A (0001) $\alpha\text{-Al}_2\text{O}_3$ surface was built by creating a vacuum space above the bulk supercell ($z = 56.1205 \text{ \AA}$) by keeping the same in-plane (x,y) dimensions. The local pressures are then computed for unrelaxed and relaxed surfaces.

The curves in figure D.3(a) give the local pressures at 0 K found in the different shells for two different (0001) Al_2O_3 surfaces : (1) A relaxed (0001) surface with in plane lattice parameters fixed to the bulk values. (2) An unrelaxed (0001) surface with in plane lattice parameters fixed to the bulk values. The zero pressure line corresponds to the bulk. The local pressures can be thus correlated to the structural modifications sustained by the surface. Figure D.3(b) shows the final bulk and surface supercells with the mean z -positions of their atomic layers.

After the cut from the bulk, mainly the surface and subsurface planes are affected and both experience negative pressure contributions that can be interpreted as a tendency to relax towards the bulk and to reduce the surface area. After relaxation with the same lattice parameters, the pressure in the surface region becomes positive, which can be explained by the outer surface Al atoms that are almost incorporated in the subsurface plane. The first interlayer thus highly relaxes (-72.7 %). This leads to a shortening of the first neighbor bonds in the in-plane directions together with an increase of the repulsive terms in this plane. This interpretation is supported by the fact that the in-plane components of the pressure represent more than 85 % of the average pressure in the surface and subsurface shells. Then, the mechanical equilibrium is easily understood as the surface tends to extend its area while the bulk contribution counter balances this effect by developing a corresponding negative pressure at around 8.5 \AA . The transition from positive to negative pressures are seen structurally by damped oscillations of the interlayers between -49.3 and 22.3 %. Finally, the pressure in the central region of the slabs recovers that of the bulk indicated by interlayers variations lower

than 2 %. The results agree with those obtained by Tétot and co-workers³⁴⁹ and confirm those of the VASP surface (section B.3).

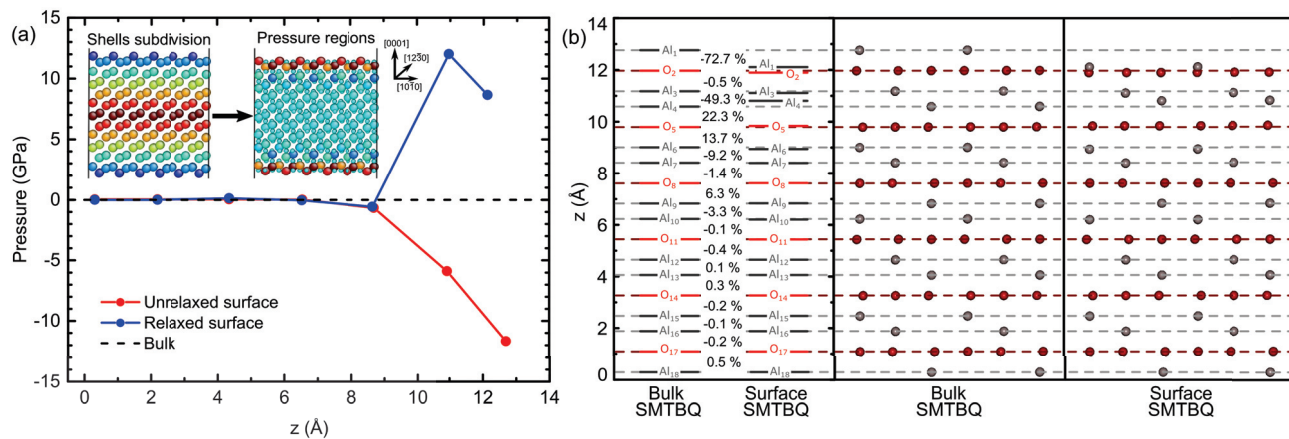


Figure D.3 – (a) Pressure profile of (0001) α -Al₂O₃ surface calculated with the SMTBQ method. The surface is subdivided in shell (left snapshot) to determine separately the local pressures (right snapshot).

D.4 VASP slabs

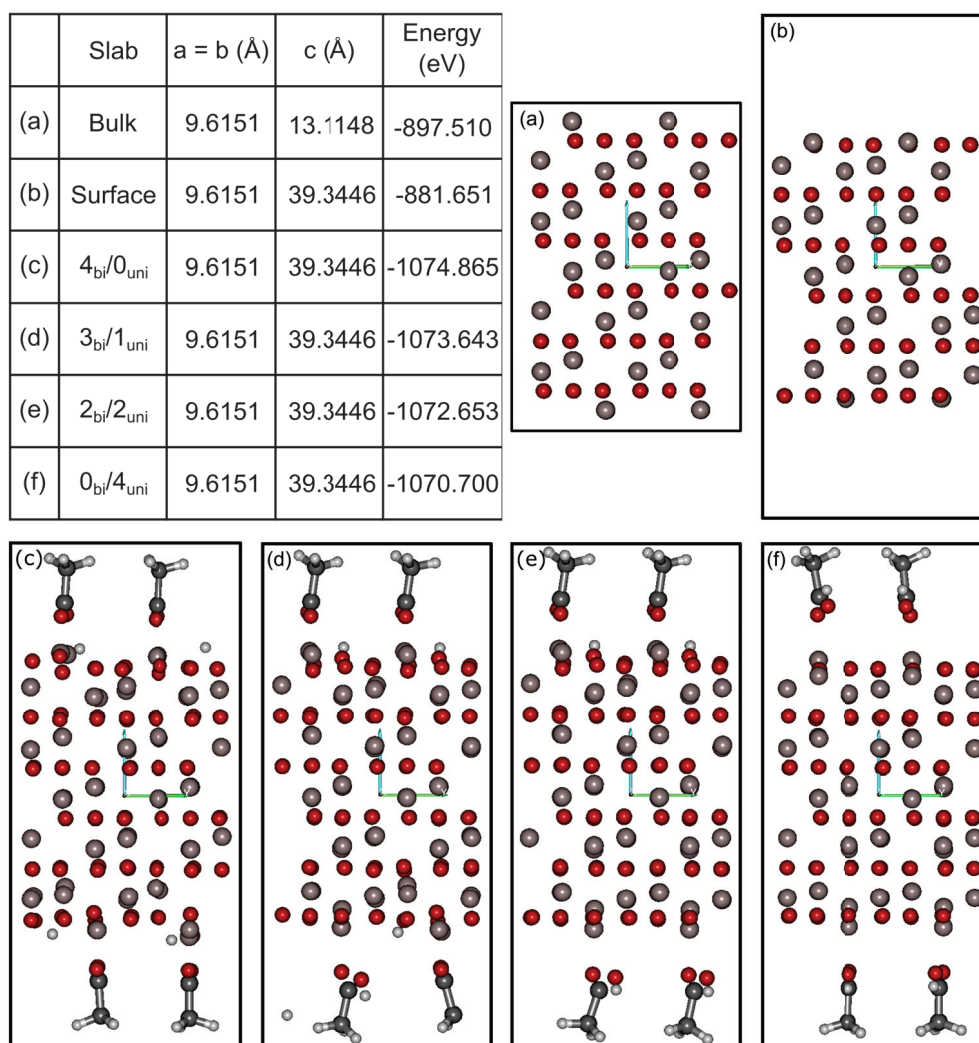


Figure D.4 – (a) Pressure profile of (0001) α -Al₂O₃ surface calculated with the SMTBQ method. The surface is subdivided in shell (left snapshot) to determine separately the local pressures (right snapshot).

- [1] J. R. Lead and K. J. Wilkinson, Aquatic Colloids and Nanoparticles: Current Knowledge and Future Trends, *Environmental Chemistry*, **2006**, 3, 159–171, doi: [10.1071/EN06025](https://doi.org/10.1071/EN06025).
- [2] R. Hough, R. Noble and M. Reich, Natural gold nanoparticles, *Ore Geology Reviews*, **2011**, 42, 55–61, doi: [10.1016/j.oregeorev.2011.07.003](https://doi.org/10.1016/j.oregeorev.2011.07.003).
- [3] J. Jeevanandam, A. Barhoum, Y. S. Chan, A. Dufresne and M. K. Danquah, Review on nanoparticles and nanostructured materials: history, sources, toxicity and regulations, *Beilstein Journal of Nanotechnology*, **2018**, 9, 1050–1074, doi: [10.3762/bjnano.9.98](https://doi.org/10.3762/bjnano.9.98).
- [4] P. Colomban, The Use of Metal Nanoparticles to Produce Yellow, Red and Iridescent Colour, from Bronze Age to Present Times in Lustre Pottery and Glass: Solid State Chemistry, Spectroscopy and Nanostructure, *Journal of Nano Research*, **2009**, 8, 109–132, doi: [10.4028/www.scientific.net/JNanoR.8.109](https://doi.org/10.4028/www.scientific.net/JNanoR.8.109).
- [5] I. Freestonen, N. Meeks, M. Sax and C. Higgitt, The Lycurgus Cup — A Roman nanotechnology, *Gold Bulletin*, **2007**, 40, 270–277, doi: [10.1007/BF03215599](https://doi.org/10.1007/BF03215599).
- [6] P. Sciau, C. Mirguet, C. Roucau, D. Chabanne and M. Schvoerer, Double Nanoparticle Layer in a 12th Century Lustreware Decoration: Accident or Technological Mastery?, *Journal of Nano Research*, **2009**, 8, 133–139, doi: [10.4028/www.scientific.net/JNanoR.8.133](https://doi.org/10.4028/www.scientific.net/JNanoR.8.133).
- [7] J. Kreuter, Nanoparticles—a historical perspective, *International Journal of Pharmaceutics*, **2007**, 331, 1–10, doi: [10.1016/j.ijpharm.2006.10.021](https://doi.org/10.1016/j.ijpharm.2006.10.021).
- [8] M. Knoll and E. Ruska, Beitrag zur geometrischen Elektronenoptik, *Annalen Der Physik*, **1932**, 404, 607–640, doi: [10.1002/andp.19324040506](https://doi.org/10.1002/andp.19324040506).
- [9] S. Mobasser and A. Firoozi, Review of Nanotechnology Applications in Science and Engineering, *J. Civil Eng. Urban*, 6, 84–93, doi: doi not available.

- [10] M. E. Vance, T. Kuiken, E. P. Vejerano, S. P. McGinnis, M. F. Hochella, D. Rejeski and M. S. Hull, Nanotechnology in the real world: Redeveloping the nanomaterial consumer products inventory, *Beilstein Journal of Nanotechnology*, **2015**, 6, 1769–1780, doi: [10.3762/bjnano.6.181](https://doi.org/10.3762/bjnano.6.181).
- [11] A. Henglein, Small-particle research: physicochemical properties of extremely small colloidal metal and semiconductor particles, *Chemical Reviews*, **1989**, 89, 1861–1873, doi: [10.1021/cr00098a010](https://doi.org/10.1021/cr00098a010).
- [12] C. Burda, X. Chen, R. Narayanan and M. A. El-Sayed, Chemistry and Properties of Nanocrystals of Different Shapes, *Chemical Reviews*, **2005**, 105, 1025–1102, doi: [10.1021/cr030063a](https://doi.org/10.1021/cr030063a).
- [13] A. Gour and N. K. Jain, Advances in green synthesis of nanoparticles, *Artificial Cells, Nanomedicine, and Biotechnology*, **2019**, 47, 844–851, doi: [10.1080/21691401.2019.1577878](https://doi.org/10.1080/21691401.2019.1577878).
- [14] B. L. Cushing, V. L. Kolesnichenko and C. J. O'Connor, Recent Advances in the Liquid-Phase Syntheses of Inorganic Nanoparticles, *Chemical Reviews*, **2004**, 104, 3893–3946, doi: [10.1021/cr030027b](https://doi.org/10.1021/cr030027b).
- [15] W. A. de Heer, The Physics of Simple Metal Clusters: Experimental Aspects and Simple Models, *Rev. Mod. Phys.*, **1993**, 65, 611–676, doi: [10.1103/RevModPhys.65.611](https://doi.org/10.1103/RevModPhys.65.611).
- [16] T. Maiman, Stimulated optical radiation in ruby, *Nature*, **1960**, 187, 493–494, doi: [10.1038/187493a0](https://doi.org/10.1038/187493a0).
- [17] E. Werwa, A. A. Seraphin, L. A. Chiu, C. Zhou and K. D. Kolenbrander, Synthesis and processing of silicon nanocrystallites using a pulsed laser ablation supersonic expansion method, *Applied Physics Letters*, **1994**, 64, 1821–1823, doi: [10.1063/1.111766](https://doi.org/10.1063/1.111766).
- [18] Y. Wang, Z. Deng, G. Fu, Y. Zhou, L. Chu and Y. Peng, The average size of Si nanoparticles prepared by pulsed laser ablation in the gas mixture of He/Ar, Ne/Ar or He/Ne, *Thin Solid Films*, **2006**, 515, 1897–1900, doi: [10.1016/j.tsf.2006.07.031](https://doi.org/10.1016/j.tsf.2006.07.031).
- [19] C. Journet and P. Bernier, Production of carbon nanotubes, *Appl. Phys. A*, 67, 1–9, doi: [10.1007/s003390050731](https://doi.org/10.1007/s003390050731).
- [20] H. W. Kroto, J. R. Heath, S. C. O'Brien, R. F. Curl and R. E. Smalley, C₆₀ : Buckminsterfullerene, *Nature*, **1985**, 318, 162–163, doi: [10.1038/318162a0](https://doi.org/10.1038/318162a0).
- [21] P. P. Patil, D. M. Phase, S. A. Kulkarni, S. V. Ghaisas, S. K. Kulkarni, S. M. Kanetkar, S. B. Ogale and V. G. Bhide, Pulsed-laser induced reactive quenching at a liquid-solid interface - aqueous oxidation of iron, *Phys. Rev. Lett.*, **1987**, 58, 238–241, doi: [10.1103/PhysRevLett.58.238](https://doi.org/10.1103/PhysRevLett.58.238).

- [22] S. B. Ogale, P. P. Patil, D. M. Phase, Y. V. Bhandarkar, S. K. Kulkarni, S. Kulkarni, S. V. Ghaisas and S. M. Kanetkar, Synthesis of metastable phases via pulsed-laser-induced reactive quenching at liquid–solid interfaces, *Phys. Rev. B*, **1987**, 36, 8237, doi: [10.1103/PhysRevB.36.8237](https://doi.org/10.1103/PhysRevB.36.8237).
- [23] Y. Lida, A. Tsuge, Y. Uwamino, H. Morikawa and T. Ishizuka, Laser ablation in a liquid-medium as a technique for solid sampling, *J. Anal. At. Spectrom.*, **1991**, 6, 541–544, doi: [10.1039/JA9910600541](https://doi.org/10.1039/JA9910600541).
- [24] A. Fojtik and A. Henglein, Laser ablation of films and suspended particles in a solvent - formation of cluster and colloid solutions, *Ber. Bunsen-Ges. Phys. Chem. Chem. Phys.*, **1993**, 97, 252–254, doi: [doi not available](#).
- [25] S. B. Ogale, A. P. Malshe, S. M. Kanetkar and S. T. Kshirsagar, Formation of diamond particulates by pulsed ruby-laser irradiation of graphite immersed in benzene, *Solid State Commun.*, **1992**, 84, 371–373, doi: [10.1016/0038-1098\(92\)90479-S](https://doi.org/10.1016/0038-1098(92)90479-S).
- [26] J. Neddersen, G. Chumanov and T. Cotton, Laser-ablation of metals - a new method for preparing SERS active colloids, *Appl. Spectrosc.*, **1993**, 47, 1959–1964, doi: [10.1366/0003702934066460](https://doi.org/10.1366/0003702934066460).
- [27] M. Prochazka, P. Mojzes, J. Stepanek, B. Vlckova and P. Y. Turpin, Probing applications of laser ablated Ag colloids in SERS spectroscopy: Improvement of ablation procedure and SERS spectral testing, *Anal. Chem.*, **1997**, 69, 5103–5108, doi: [10.1021/ac970683+](https://doi.org/10.1021/ac970683+).
- [28] A. Kruusing, Underwater and water-assisted laser processing: Part 1—general features, steam cleaning and shock processing, *Optics and Lasers in Engineering*, **2004**, 41, 307–327, doi: [10.1016/S0143-8166\(02\)00142-2](https://doi.org/10.1016/S0143-8166(02)00142-2).
- [29] D. Zhang, B. Gökce and S. Barcikowski, Laser Synthesis and Processing of Colloids: Fundamentals and Applications, *Chemical Reviews*, **2017**, 117, 3990–4103, doi: [10.1021/acs.chemrev.6b00468](https://doi.org/10.1021/acs.chemrev.6b00468).
- [30] V. Amendola and M. Meneghetti, What controls the composition and the structure of nanomaterials generated by laser ablation in liquid solution?, *Phys. Chem. Chem. Phys.*, **2013**, 15, 3027–3046, doi: [10.1039/c2cp42895d](https://doi.org/10.1039/c2cp42895d).
- [31] Z. Yan and D. B. Chrisey, Pulsed laser ablation in liquid for micro-/nanostucture generation, *Journal of Photochemistry and Photobiology C: Photochemistry Reviews*, **2012**, 13, 204–223, doi: [10.1016/j.jphotochemrev.2012.04.004](https://doi.org/10.1016/j.jphotochemrev.2012.04.004).
- [32] J. Lam, *PhD thesis*, Pulsed Laser Ablation in Liquid : towards the comprehension of the growth processes, Université Claude Bernard Lyon 1, 2015.

- [33] R. Streubel, G. Bendt and B. Gökce, Pilot-scale synthesis of metal nanoparticles by high-speed pulsed laser ablation in liquids, *Nanotechnology*, **2016**, 27, 205602–205610, doi: [10.1088/0957-4484/27/20/205602](https://doi.org/10.1088/0957-4484/27/20/205602).
- [34] R. Streubel, S. Barcikowski and B. Gökce, Continuous multigram nanoparticle synthesis by high-power, high-repetition-rate ultrafast laser ablation in liquids, *Opt. Lett.*, **2016**, 41, 1486–1489, doi: [10.1364/OL.41.001486](https://doi.org/10.1364/OL.41.001486).
- [35] A. Schwenke, P. Wagener, S. Nolte and S. Barcikowski, Influence of processing time on nanoparticle generation during picosecond-pulsed fundamental and second harmonic laser ablation of metals in tetrahydrofuran, *Applied Physics A*, **2011**, 104, 77–82, doi: [10.1007/s00339-011-6398-9](https://doi.org/10.1007/s00339-011-6398-9).
- [36] R. Streubel, S. Barcikowski and B. Gökce, Continuous multigram nanoparticle synthesis by high-power, high-repetition-rate ultrafast laser ablation in liquids, *Optics Letters*, **2016**, 41, 1486, doi: [10.1364/OL.41.001486](https://doi.org/10.1364/OL.41.001486).
- [37] C. L. Sajti, R. Sattari, B. N. Chichkov and S. Barcikowski, Gram Scale Synthesis of Pure Ceramic Nanoparticles by Laser Ablation in Liquid, *J. Phys. Chem. C*, **2010**, 114, 2421, doi: [10.1021/jp906960g](https://doi.org/10.1021/jp906960g).
- [38] A. Kanitz, J. S. Hoppius, M. Fiebrandt, P. Awakowicz, C. Esen, A. Ostendorf and E. L. Gurevich, Impact of liquid environment on femtosecond laser ablation, *Applied Physics A*, **2017**, 123, 674–680, doi: [10.1007/s00339-017-1280-z](https://doi.org/10.1007/s00339-017-1280-z).
- [39] S. Barcikowski, A. Menéndez-Manjón, B. Chichkov, M. Brikas and G. Račiukaitis, Generation of nanoparticle colloids by picosecond and femtosecond laser ablations in liquid flow, *Applied Physics Letters*, **2007**, 91, 083113–083115, doi: [10.1063/1.2773937](https://doi.org/10.1063/1.2773937).
- [40] R. Streubel, G. Bendt and B. Gökce, Pilot-scale synthesis of metal nanoparticles by high-speed pulsed laser ablation in liquids, *Nanotechnology*, **2016**, 27, 205602, doi: [10.1088/0957-4484/27/20/205602](https://doi.org/10.1088/0957-4484/27/20/205602).
- [41] S. Scaramuzza, M. Zerbetto and V. Amendola, Synthesis of Gold Nanoparticles in Liquid Environment by Laser Ablation with Geometrically Confined Configurations: Insights To Improve Size Control and Productivity, *The Journal of Physical Chemistry C*, **2016**, 120, 9453–9463, doi: [10.1021/acs.jpcc.6b00161](https://doi.org/10.1021/acs.jpcc.6b00161).
- [42] Z. Yan, R. Bao and D. B. Chrisey, Generation of Ag₂O Micro-/Nanostructures by Pulsed Excimer Laser Ablation of Ag in Aqueous Solutions of Polysorbate 80, *Langmuir*, **2011**, 27, 851–855, doi: [10.1021/la104331p](https://doi.org/10.1021/la104331p).

- [43] A. Vogel, S. Busch and U. Parlitz, Shock wave emission and cavitation bubble generation by picosecond and nanosecond optical breakdown in water, *The Journal of the Acoustical Society of America*, **1996**, 100, 148–165, doi: [10.1121/1.415878](https://doi.org/10.1121/1.415878).
- [44] A. Vogel, N. Linz, S. Freidank and G. Paltauf, Femtosecond-Laser-Induced Nanocavitation in Water: Implications for Optical Breakdown Threshold and Cell Surgery, *Physical Review Letters*, **2008**, 100, 038102–038105, doi: [10.1103/PhysRevLett.100.038102](https://doi.org/10.1103/PhysRevLett.100.038102).
- [45] A. Menéndez-Manjón, P. Wagener and S. Barcikowski, Transfer-Matrix Method for Efficient Ablation by Pulsed Laser Ablation and Nanoparticle Generation in Liquids, *The Journal of Physical Chemistry C*, **2011**, 115, 5108–5114, doi: [10.1021/jp109370q](https://doi.org/10.1021/jp109370q).
- [46] A. De Giacomo, M. Dell’Aglio, O. De Pascale and M. Capitelli, From single pulse to double pulse ns-Laser Induced Breakdown Spectroscopy under water: Elemental analysis of aqueous solutions and submerged solid samples, *Spectrochimica Acta Part B: Atomic Spectroscopy*, **2007**, 62, 721–738, doi: [10.1016/j.sab.2007.06.008](https://doi.org/10.1016/j.sab.2007.06.008).
- [47] A. De Giacomo, M. Dell’Aglio, O. De Pascale and M. Capitelli, Spectroscopic investigation of laser–water interaction beyond the breakdown threshold energy, *Spectrochimica Acta Part B: Atomic Spectroscopy*, **2007**, 62, 87–93, doi: [10.1016/j.sab.2007.01.002](https://doi.org/10.1016/j.sab.2007.01.002).
- [48] O. Lindau and W. Lauterborn, Cinematographic observation of the collapse and rebound of a laser-produced cavitation bubble near a wall, *Journal of Fluid Mechanics*, **2003**, 479, 327–348, doi: [10.1017/S0022112002003695](https://doi.org/10.1017/S0022112002003695).
- [49] S. Besner, A. V. Kabashin and M. Meunier, Fragmentation of colloidal nanoparticles by femtosecond laser-induced supercontinuum generation, *Applied Physics Letters*, **2006**, 89, 233122, doi: [10.1063/1.2402944](https://doi.org/10.1063/1.2402944).
- [50] W. Liu, O. Kosareva, I. Golubtsov, A. Iwasaki, A. Becker, V. Kandidov and S. Chin, Femtosecond laser pulse filamentation versus optical breakdown in H₂O, *Applied Physics B*, **2003**, 76, 215–229, doi: [10.1007/s00340-002-1087-1](https://doi.org/10.1007/s00340-002-1087-1).
- [51] A. Kabashin and M. Meunier, Synthesis of colloidal nanoparticles during femtosecond laser ablation of gold in water, *J. Appl. Phys.*, **2003**, 94, 7941–7943, doi: [10.1063/1.1626793](https://doi.org/10.1063/1.1626793).
- [52] K. Metwally, S. Mensah and G. Baffou, Fluence Threshold for Photothermal Bubble Generation Using Plasmonic Nanoparticles, *The Journal of Physical Chemistry C*, **2015**, 119, 28586–28596, doi: [10.1021/acs.jpcc.5b09903](https://doi.org/10.1021/acs.jpcc.5b09903).
- [53] S. Link, C. Burda, B. Nikoobakht and M. A. El-Sayed, How long does it take to melt a gold nanorod? A femtosecond pump–probe absorption spectroscopic study, *Chemical Physics Letters*, **1999**, 315, 12–18, doi: [10.1016/S0009-2614\(99\)01214-2](https://doi.org/10.1016/S0009-2614(99)01214-2).

- [54] S. Link, C. Burda, M. B. Mohamed, B. Nikoobakht and M. A. El-Sayed, Laser Photothermal Melting and Fragmentation of Gold Nanorods: Energy and Laser Pulse-Width Dependence, *The Journal of Physical Chemistry A*, **1999**, 103, 1165–1170, doi: [10.1021/jp983141k](https://doi.org/10.1021/jp983141k).
- [55] G. Gonzalez-Rubio, A. Guerrero-Martinez and L. M. Liz-Marzan, Reshaping, Fragmentation, and Assembly of Gold Nanoparticles Assisted by Pulse Lasers, *Accounts Chem. Res.*, **2016**, 49, 678–686, doi: [10.1021/acs.accounts.6b00041](https://doi.org/10.1021/acs.accounts.6b00041).
- [56] A. Pyatenko, H. Wang, N. Koshizaki and T. Tsuji, Mechanism of pulse laser interaction with colloidal nanoparticles, *Laser Photon. Rev.*, **2013**, 7, 596–604, doi: [10.1002/lpor.201300013](https://doi.org/10.1002/lpor.201300013).
- [57] D. Liu, C. Li, F. Zhou, T. Zhang, H. Zhang, X. Li, G. Duan, W. Cai and Y. Li, Rapid Synthesis of Monodisperse Au Nanospheres through a Laser Irradiation-Induced Shape Conversion, Self-Assembly and Their Electromagnetic Coupling SERS Enhancement, *Scientific Reports*, **2015**, 5, 7686–7694, doi: [10.1038/srep07686](https://doi.org/10.1038/srep07686).
- [58] S. Sakaki, H. Ikenoue, T. Tsuji, Y. Ishikawa and N. Koshizaki, Pulse-Width Dependence of the Cooling Effect on Sub-Micrometer ZnO Spherical Particle Formation by Pulsed-Laser Melting in a Liquid, *Chem. Phys. Chem.*, **2017**, 18, 1101–1107, doi: [10.1002/cphc.201601175](https://doi.org/10.1002/cphc.201601175).
- [59] F. Waag, B. Gökce, C. Kalapu, G. Bendt, S. Salamon, J. Landers, U. Hagemann, M. Heidelmann, S. Schulz, H. Wende, N. Hartmann, M. Behrens and S. Barcikowski, Adjusting the catalytic properties of cobalt ferrite nanoparticles by pulsed laser fragmentation in water with defined energy dose, *Scientific Reports*, **2017**, 7, 13161, doi: [10.1038/s41598-017-13333-z](https://doi.org/10.1038/s41598-017-13333-z).
- [60] V. Amendola and M. Meneghetti, Laser ablation synthesis in solution and size manipulation of noble metal nanoparticles, *Physical Chemistry Chemical Physics*, **2009**, 11, 3805–3821, doi: [10.1039/b900654k](https://doi.org/10.1039/b900654k).
- [61] W. T. Nichols, T. Sasaki and N. Koshizaki, Laser ablation of a platinum target in water. II. Ablation rate and nanoparticle size distributions, *Journal of Applied Physics*, **2006**, 100, 114912–114917, doi: [10.1063/1.2390641](https://doi.org/10.1063/1.2390641).
- [62] B. N. Chichkov, C. Momma and S. Nolte, Femtosecond, picosecond and nanosecond laser ablation of solids, *Appl. Phys. A*, **1996**, 63, 109–115, doi: [10.1007/BF01567637](https://doi.org/10.1007/BF01567637).
- [63] D. Perez, L. K. Béland, D. Deryng, L. J. Lewis and M. Meunier, Numerical study of the thermal ablation of wet solids by ultrashort laser pulses, *Physical Review B*, **2008**, 77, 014108–014116, doi: [10.1103/PhysRevB.77.014108](https://doi.org/10.1103/PhysRevB.77.014108).
- [64] D. Amans, M. Diouf, J. Lam, G. Ledoux and C. Dujardin, Origin of the nano-carbon allotropes in pulsed laser ablation in liquids synthesis, *J. Colloid Interface Sci.*, **2017**, 489, 114–125, doi: [10.1016/j.jcis.2016.08.017](https://doi.org/10.1016/j.jcis.2016.08.017).

-
- [65] T. Hupfeld, G. Laurens, S. Merabia, S. Barcikowski, B. Gökce, and D. Amans, Dynamics of laser-induced cavitation bubbles at a solid-liquid interface in high capillary number regimes, *Journal of Applied Physics*, Submitted,
- [66] C. Momma, B. N. Chichkov, S. Nolte, F. von Alvensleben, A. Tünnermann, H. Welling and B. Wellegehausen, Short-pulse laser ablation of solid targets, *Optics Communications*, **1996**, 129, 134–142, doi: [10.1016/0030-4018\(96\)00250-7](https://doi.org/10.1016/0030-4018(96)00250-7).
- [67] B. Y. Mueller and B. Rethfeld, Relaxation dynamics in laser-excited metals under nonequilibrium conditions, *Phys. Rev. B*, **2013**, 87, 035139, doi: [10.1103/PhysRevB.87.035139](https://doi.org/10.1103/PhysRevB.87.035139).
- [68] Z. Lin, R. A. Johnson and L. V. Zhigilei, Computational study of the generation of crystal defects in a bcc metal target irradiated by short laser pulses, *Phys. Rev. B*, **2008**, 77, 214108, doi: [10.1103/PhysRevB.77.214108](https://doi.org/10.1103/PhysRevB.77.214108).
- [69] S. K. Sundaram and E. Mazur, Inducing and probing non-thermal transitions in semiconductors using femtosecond laser pulses, *Nature Materials*, **2002**, 1, 217–224, doi: [10.1038/nmat767](https://doi.org/10.1038/nmat767).
- [70] S. I. Anisimov, Electron emission from metal surfaces exposed to ultrashort laser pulses, *Sov. Phys.-JETP*, **1974**, 39, 375–377, doi: not available.
- [71] A. Miotello and R. Kelly, Critical assessment of thermal models for laser sputtering at high fluences, *Applied Physics Letters*, **1995**, 67, 3535–3537, doi: [10.1063/1.114912](https://doi.org/10.1063/1.114912).
- [72] A. Miotello and R. Kelly, Laser-induced phase explosion: new physical problems when a condensed phase approaches the thermodynamic critical temperature, *Applied Physics A Materials Science & Processing*, **1999**, 69, S67–S73, doi: [10.1007/s003399900296](https://doi.org/10.1007/s003399900296).
- [73] A. V. Bulgakov and N. M. Bulgakova, Thermal model of pulsed laser ablation under the conditions of formation and heating of a radiation-absorbing plasma, *Quantum Electron.*, **1999**, 29, 433–437, doi: [10.1070/QE1999v029n05ABEH001503](https://doi.org/10.1070/QE1999v029n05ABEH001503).
- [74] N. Bulgakova and A. Bulgakov, Pulsed laser ablation of solids: transition from normal vaporization to phase explosion, *Applied Physics A*, **2001**, 73, 199–208, doi: [10.1007/s003390000686](https://doi.org/10.1007/s003390000686).
- [75] N. M. Bulgakova, V. P. Zhukov, A. Y. Vorobyev and C. Guo, Modeling of residual thermal effect in femtosecond laser ablation of metals: role of a gas environment, *Appl. Phys. A*, **2008**, 92, 883–889, doi: [10.1007/s00339-008-4568-1](https://doi.org/10.1007/s00339-008-4568-1).
- [76] T. Itina, J. Hermann, P. Delaporte and M. Sentis, Modeling of metal ablation induced by ultrashort laser pulses, *Thin Solid Films*, **2004**, 453–454, 513–517, doi: [10.1016/j.tsf.2003.11.124](https://doi.org/10.1016/j.tsf.2003.11.124).

- [77] T. Itina, F. Vidal, P. Delaporte and M. Sentis, Numerical study of ultra-short laser ablation of metals and of laser plume dynamics, *Appl. Phys. A*, **2004**, 79, 1089–1092, doi: [10.1007/s00339-004-2647-5](https://doi.org/10.1007/s00339-004-2647-5).
- [78] V. Mazhukin, I. Smurov, G. Flamant and C. Dupuy, Peculiarities of laser melting and evaporation of superconducting ceramics, *Thin Solid Films*, **1994**, 241, 109–113, doi: [10.1016/0040-6090\(94\)90408-1](https://doi.org/10.1016/0040-6090(94)90408-1).
- [79] M. E. Povarnitsyn, T. E. Itina, M. Sentis, K. V. Khishchenko and P. R. Levashov, Material decomposition mechanisms in femtosecond laser interactions with metals, *Phys. Rev. B*, **2007**, 75, 235414, doi: [10.1103/PhysRevB.75.235414](https://doi.org/10.1103/PhysRevB.75.235414).
- [80] M. E. Povarnitsyn, T. E. Itina, P. R. Levashov and K. V. Khishchenko, Mechanisms of nanoparticle formation by ultra-short laser ablation of metals in liquid environment, *Physical Chemistry Chemical Physics*, **2013**, 15, 3108, doi: [10.1039/c2cp42650a](https://doi.org/10.1039/c2cp42650a).
- [81] M. E. Povarnitsyn and T. E. Itina, Hydrodynamic modeling of femtosecond laser ablation of metals in vacuum and in liquid, *Applied Physics A*, **2014**, 117, 175–178, doi: [10.1007/s00339-014-8319-1](https://doi.org/10.1007/s00339-014-8319-1).
- [82] T. E. Itina, W. Marine and M. Autric, Monte Carlo simulation of pulsed laser ablation from two-component target into diluted ambient gas, *Journal of Applied Physics*, **1997**, 82, 3536–3542, doi: [10.1063/1.365672](https://doi.org/10.1063/1.365672).
- [83] T. E. Itina, A. A. Katassonov, W. Marine and M. Autric, Numerical study of the role of a background gas and system geometry in pulsed laser deposition, *Journal of Applied Physics*, **1998**, 83, 6050–6054, doi: [10.1063/1.367995](https://doi.org/10.1063/1.367995).
- [84] T. Itina, W. Marine and M. Autric, Mathematical modelling of pulsed laser ablated flows, *Applied Surface Science*, **2000**, 154-155, 60–65, doi: [10.1016/S0169-4332\(99\)00388-8](https://doi.org/10.1016/S0169-4332(99)00388-8).
- [85] B. J. Garrison and R. Srinivasan, Microscopic model for the ablative photodecomposition of polymers by far-ultraviolet radiation (193 nm), *Appl. Phys. Lett.*, **1984**, 44, 849–851, doi: [10.1063/1.94947](https://doi.org/10.1063/1.94947).
- [86] B. J. Garrison and R. Srinivasan, Laser ablation of organic polymers: Microscopic models for photochemical and thermal processes, *Journal of Applied Physics*, **1985**, 57, 2909–2914, doi: [10.1063/1.335230](https://doi.org/10.1063/1.335230).
- [87] B. J. Garrison, T. E. Itina and L. V. Zhigilei, Limit of overheating and the threshold behavior in laser ablation, *Phys. Rev. E*, **2003**, 68, 041501, doi: [10.1103/PhysRevE.68.041501](https://doi.org/10.1103/PhysRevE.68.041501).
- [88] T. E. Itina, L. V. Zhigilei and B. J. Garrison, Microscopic Mechanisms of Matrix Assisted Laser Desorption of Analyte Molecules: Insights from Molecular Dynamics Simulation, *J. Phys. Chem. B*, **2002**, 106, 303–310, doi: [10.1021/jp0127768](https://doi.org/10.1021/jp0127768).

- [89] T. E. Itina, Decomposition of rapidly expanding liquid: Molecular dynamics study, *Chemical Physics Letters*, **2008**, 452, 129–132, doi: [10.1016/j.cplett.2007.12.029](https://doi.org/10.1016/j.cplett.2007.12.029).
- [90] D. Perez and L. J. Lewis, Ablation of Solids under Femtosecond Laser Pulses, *Physical Review Letters*, **2002**, 89, 255504–255507, doi: [10.1103/PhysRevLett.89.255504](https://doi.org/10.1103/PhysRevLett.89.255504).
- [91] D. Perez and L. J. Lewis, Molecular-dynamics study of ablation of solids under femtosecond laser pulses, *Physical Review B*, **2003**, 67, 184102–184116, doi: [10.1103/PhysRevB.67.184102](https://doi.org/10.1103/PhysRevB.67.184102).
- [92] D. Perez and L. Lewis, Thermodynamic evolution of materials during laser ablation under pico and femtosecond pulses, *Applied Physics A*, **2004**, 79, 987–990, doi: [10.1007/s00339-004-2611-4](https://doi.org/10.1007/s00339-004-2611-4).
- [93] D. Perez, L. J. Lewis, P. Lorazo and M. Meunier, Ablation of molecular solids under nanosecond laser pulses: The role of inertial confinement, *Applied Physics Letters*, **2006**, 89, 141907–141909, doi: [10.1063/1.2358941](https://doi.org/10.1063/1.2358941).
- [94] P. Lorazo, L. J. Lewis and M. Meunier, Short-Pulse Laser Ablation of Solids: From Phase Explosion to Fragmentation, *Physical Review Letters*, **2003**, 91, 225502–225505, doi: [10.1103/PhysRevLett.91.225502](https://doi.org/10.1103/PhysRevLett.91.225502).
- [95] P. Lorazo, L. J. Lewis and M. Meunier, Thermodynamic pathways to melting, ablation, and solidification in absorbing solids under pulsed laser irradiation, *Physical Review B*, **2006**, 73, 134108–134129, doi: [10.1103/PhysRevB.73.134108](https://doi.org/10.1103/PhysRevB.73.134108).
- [96] C.-Y. Shih, C. Wu, M. V. Shugaev and L. V. Zhigilei, Atomistic modeling of nanoparticle generation in short pulse laser ablation of thin metal films in water, *Journal of Colloid and Interface Science*, **2017**, 489, 3–17, doi: [10.1016/j.jcis.2016.10.029](https://doi.org/10.1016/j.jcis.2016.10.029).
- [97] C.-Y. Shih, M. V. Shugaev, C. Wu and L. V. Zhigilei, Generation of Subsurface Voids, Incubation Effect, and Formation of Nanoparticles in Short Pulse Laser Interactions with Bulk Metal Targets in Liquid: Molecular Dynamics Study, *The Journal of Physical Chemistry C*, **2017**, 121, 16549–16567, doi: [10.1021/acs.jpcc.7b02301](https://doi.org/10.1021/acs.jpcc.7b02301).
- [98] C.-Y. Shih, R. Streubel, J. Heberle, A. Letzel, M. V. Shugaev, C. Wu, M. Schmidt, B. Gökce, S. Barcikowski and L. V. Zhigilei, Two mechanisms of nanoparticle generation in picosecond laser ablation in liquids: the origin of the bimodal size distribution, *Nanoscale*, **2018**, 10, 6900–6910, doi: [10.1039/C7NR08614H](https://doi.org/10.1039/C7NR08614H).
- [99] S. I. Anisimov and B. S. Luk'yanchuk, Selected problems of laser ablation theory, *Phys.-Usp.*, **2002**, 45, 293–324, doi: [10.1070/PU2002v045n03ABEH000966](https://doi.org/10.1070/PU2002v045n03ABEH000966).

- [100] Numerical Analysis of Ultrashort Laser Ablation: Application for Fabrication of Nanoparticles and Nanostructures, 2014,
- [101] L. V. Zhigilei, E. Leveugle, B. J. Garrison, Y. G. Yingling and M. I. Zeifman, Computer Simulations of Laser Ablation of Molecular Substrates, *Chem. Rev.*, **2003**, 103, 321–348, doi: [10.1021/cr010459r](https://doi.org/10.1021/cr010459r).
- [102] A. Kanitz, D. J. Förster, J. S. Hoppius, R. Weber, A. Ostendorf and E. L. Gurevich, Pump-probe microscopy of femtosecond laser ablation in air and liquids, *Appl. Surf. Sci.*, **2019**, 475, 204 – 210, doi: [10.1016/j.apsusc.2018.12.184](https://doi.org/10.1016/j.apsusc.2018.12.184).
- [103] M. Domke, S. Rapp, M. Schmidt and H. P. Huber, Ultra-fast movies of thin-film laser ablation, *Applied Physics A*, **2012**, 109, 409–420, doi: [10.1007/s00339-012-7072-6](https://doi.org/10.1007/s00339-012-7072-6).
- [104] T. Sakka, S. Iwanaga, Y. H. Ogata, A. Matsunawa and T. Takemoto, Laser ablation at solid–liquid interfaces: An approach from optical emission spectra, *The Journal of Chemical Physics*, **2000**, 112, 8645–8653, doi: [10.1063/1.481465](https://doi.org/10.1063/1.481465).
- [105] T. Sakka, K. Takatani, Y. H. Ogata and M. Mabuchi, Laser ablation at the solid-liquid interface: transient absorption of continuous spectral emission by ablated aluminium atoms, *Journal of Physics D: Applied Physics*, **2002**, 35, 65–73, doi: [10.1088/0022-3727/35/1/312](https://doi.org/10.1088/0022-3727/35/1/312).
- [106] K. Sasaki and N. Takada, Liquid-phase laser ablation, *Pure and Applied Chemistry*, **2010**, 82, 1317–1327, doi: [10.1351/PAC-CON-09-10-23](https://doi.org/10.1351/PAC-CON-09-10-23).
- [107] J. Lam, D. Amans, F. Chaput, M. Diouf, G. Ledoux, N. Mary, K. Masenelli-Varlot, V. Motto-Ros and C. Dujardin, γ -Al₂O₃ nanoparticles synthesised by pulsed laser ablation in liquids: a plasma analysis, *Phys. Chem. Chem. Phys.*, **2014**, 16, 963–973, doi: [10.1039/C3CP53748J](https://doi.org/10.1039/C3CP53748J).
- [108] M. Dell’Aglia, A. Santagata, G. Valenza, A. De Sradis and A. De Giacomo, Study of the effect of water pressure on plasma and cavitation bubble induced by Pulsed Laser Ablation in Liquid of silver and missed variations of observable nanoparticle features, *Chem. Phys. Chem.*, **2017**, 18, 1165–1174, doi: [10.1002/cphc.201601231](https://doi.org/10.1002/cphc.201601231).
- [109] T. Sakka, K. Saito and Y. H. Ogata, Emission spectra of the species ablated from a solid target submerged in liquid: vibrational temperature of C-2 molecules in water-confined geometry, *Appl. Surf. Sci.*, **2002**, 197, 246, doi: [10.1016/S0169-4332\(02\)00373-2](https://doi.org/10.1016/S0169-4332(02)00373-2).
- [110] A. Matsumoto, A. Tamura, T. Honda, T. Hirota, K. Kobayashi, S. Katakura, N. Nishi, K.-i. Amano, K. Fukami and T. Sakka, Transfer of the Species Dissolved in a Liquid into Laser Ablation Plasma: An Approach Using Emission Spectroscopy, *J. Phys. Chem. C*, **2015**, 119, 26506–26511, doi: [10.1021/acs.jpcc.5b07769](https://doi.org/10.1021/acs.jpcc.5b07769).

- [111] J. Lam, D. Amans, C. Dujardin, G. Ledoux and A.-R. Allouche, Atomistic Mechanisms for the Nucleation of Aluminum Oxide Nanoparticles, *J. Phys. Chem. A*, **2015**, 119, 8944–8949, doi: [10.1021/acs.jpca.5b05829](https://doi.org/10.1021/acs.jpca.5b05829).
- [112] M. R. Gavrilović, M. Cvejić, V. Lazic and S. Jovićević, Secondary plasma formation after single pulse laser ablation underwater and its advantages for laser induced breakdown spectroscopy (LIBS), *Physical Chemistry Chemical Physics*, **2016**, 18, 14629–14637, doi: [10.1039/C6CP01515H](https://doi.org/10.1039/C6CP01515H).
- [113] M. R. Gavrilović, Impact of the cavitation bubble on a plasma emission following laser ablation in liquid, *The European Physical Journal D*, **2017**, 71, 316–325, doi: [10.1140/epjd/e2017-80282-7](https://doi.org/10.1140/epjd/e2017-80282-7).
- [114] K. K. Kim, M. Roy, H. Kwon, J. K. Song and S. M. Park, Laser ablation dynamics in liquid phase: The effects of magnetic field and electrolyte, *Journal of Applied Physics*, **2015**, 117, 074302, doi: [10.1063/1.4913253](https://doi.org/10.1063/1.4913253).
- [115] H. Oguchi, T. Sakka and Y. H. Ogata, Effects of pulse duration upon the plume formation by the laser ablation of Cu in water, *Journal of Applied Physics*, **2007**, 102, 023306–023311, doi: [10.1063/1.2759182](https://doi.org/10.1063/1.2759182).
- [116] K. Saito, K. Takatani, T. Sakka and Y. H. Ogata, Observation of the light emitting region produced by pulsed laser irradiation to a solid–liquid interface, *Applied Surface Science*, **2002**, 197–198, 56–60, doi: [10.1016/S0169-4332\(02\)00303-3](https://doi.org/10.1016/S0169-4332(02)00303-3).
- [117] T. Sakka, H. Yamagata, H. Oguchi, K. Fukami and Y. H. Ogata, Emission spectroscopy of laser ablation plume: Composition analysis of a target in water, *Applied Surface Science*, **2009**, 255, 9576–9580, doi: [10.1016/j.apsusc.2009.04.086](https://doi.org/10.1016/j.apsusc.2009.04.086).
- [118] T. Tsuji, D.-H. Thang, Y. Okazaki, M. Nakanishi, Y. Tsuboi and M. Tsuji, Preparation of silver nanoparticles by laser ablation in polyvinylpyrrolidone solutions, *Applied Surface Science*, **2008**, 254, 5224–5230, doi: [10.1016/j.apsusc.2008.02.048](https://doi.org/10.1016/j.apsusc.2008.02.048).
- [119] A. De Giacomo, M. Dell’Aglia, A. Santagata, R. Gaudioso, O. De Pascale, P. Wagener, G. C. Messina, G. Compagnini and S. Barcikowski, Cavitation dynamics of laser ablation of bulk and wire-shaped metals in water during nanoparticles production, *Phys. Chem. Chem. Phys.*, **2013**, 15, 3083–3092, doi: [10.1039/C2CP42649H](https://doi.org/10.1039/C2CP42649H).
- [120] A. Tamura, A. Matsumoto, K. Fukami, N. Nishi and T. Sakka, Simultaneous observation of nascent plasma and bubble induced by laser ablation in water with various pulse durations, *Journal of Applied Physics*, **2015**, 117, 173304–173311, doi: [10.1063/1.4919729](https://doi.org/10.1063/1.4919729).
- [121] T. Sakka, A. Tamura, A. Matsumoto, K. Fukami, N. Nishi and B. Thornton, Effects of pulse width on nascent laser-induced bubbles for underwater laser-induced breakdown

- spectroscopy, *Spectrochimica Acta Part B: Atomic Spectroscopy*, **2014**, 97, 94–98, doi: [10.1016/j.sab.2014.05.009](https://doi.org/10.1016/j.sab.2014.05.009).
- [122] X. Mao and R. E. Russo, Invited paper Observation of plasma shielding by measuring transmitted and reflected laser pulse temporal profiles, *Applied Physics A: Materials Science & Processing*, **1996**, 64, 1–6, doi: [10.1007/s003390050437](https://doi.org/10.1007/s003390050437).
- [123] J. H. Yoo, S. H. Jeong, R. Greif and R. E. Russo, Explosive change in crater properties during high power nanosecond laser ablation of silicon, *Journal of Applied Physics*, **2000**, 88, 1638–1649, doi: [10.1063/1.373865](https://doi.org/10.1063/1.373865).
- [124] M. Amin, J. Tomko, J. Naddeo, R. Jimenez, D. Bubb, M. Steiner, J. Fitz-Gerald and S. O'Malley, Laser-assisted synthesis of ultra-small anatase TiO₂ nanoparticles, *Applied Surface Science*, **2015**, 348, 30–37, doi: [10.1016/j.apsusc.2014.12.191](https://doi.org/10.1016/j.apsusc.2014.12.191).
- [125] S. Zhu, Y. F. Lu and M. H. Hong, Laser ablation of solid substrates in a water-confined environment, *Applied Physics Letters*, **2001**, 79, 1396–1398, doi: [10.1063/1.1400086](https://doi.org/10.1063/1.1400086).
- [126] H. Jin, J.-W. Kim, J.-A. Son and J.-G. Choi, An acoustic based, laser induced breakdown method for determining the sizes and concentrations of nanoparticles, *Phys. Chem. Chem. Phys.*, **2010**, 12, 5199–5202, doi: [10.1039/b924933h](https://doi.org/10.1039/b924933h).
- [127] Y. Tomita, M. Tsubota and N. An-naka, Energy evaluation of cavitation bubble generation and shock wave emission by laser focusing in liquid nitrogen, *Journal of Applied Physics*, **2003**, 93, 3039–3048, doi: [10.1063/1.1542669](https://doi.org/10.1063/1.1542669).
- [128] A. Vogel, J. Noack, K. Nahen, D. Theisen, S. Busch, U. Parlitz, D. Hammer, G. Noojin, B. Rockwell and R. Birngruber, Energy balance of optical breakdown in water at nanosecond to femtosecond time scales, *Applied Physics B*, **1999**, 68, 271–280, doi: [10.1007/s003400050617](https://doi.org/10.1007/s003400050617).
- [129] D. Kraus, A. Ravasio, M. Gauthier, D. O. Gericke, J. Vorberger, S. Frydrych, J. Helfrich, L. B. Fletcher, G. Schaumann, B. Nagler, B. Barbrel, B. Bachmann, E. J. Gamboa, S. Göde, E. Granados, G. Gregori, H. J. Lee, P. Neumayer, W. Schumaker, T. Döppner, R. W. Falcone, S. H. Glenzer and M. Roth, Nanosecond formation of diamond and lonsdaleite by shock compression of graphite, *Nature Communications*, **2016**, 7, 10970–10975, doi: [10.1038/ncomms10970](https://doi.org/10.1038/ncomms10970).
- [130] T. Sakka, S. Masai, K. Fukami and Y. H. Ogata, Spectral profile of atomic emission lines and effects of pulse duration on laser ablation in liquid, *Spectrochimica Acta Part B: Atomic Spectroscopy*, **2009**, 64, 981–985, doi: [10.1016/j.sab.2009.07.018](https://doi.org/10.1016/j.sab.2009.07.018).
- [131] T. Tsuji, Y. Okazaki, Y. Tsuboi and M. Tsuji, Nanosecond Time-Resolved Observations of Laser Ablation of Silver in Water, *Japanese Journal of Applied Physics*, **2007**, 46, 1533–1535, doi: [10.1143/JJAP.46.1533](https://doi.org/10.1143/JJAP.46.1533).

- [132] J. Lam, J. Lombard, C. Dujardin, G. Ledoux, S. Merabia and D. Amans, Dynamical study of bubble expansion following laser ablation in liquids, *Applied Physics Letters*, **2016**, 108, 074104–074108, doi: [10.1063/1.4942389](https://doi.org/10.1063/1.4942389).
- [133] M. Dell’Aglia, R. Gaudio, O. De Pascale and A. De Giacomo, Mechanisms and processes of pulsed laser ablation in liquids during nanoparticle production, *Applied Surface Science*, **2015**, 348, 4–9, doi: [10.1016/j.apsusc.2015.01.082](https://doi.org/10.1016/j.apsusc.2015.01.082).
- [134] M. Dell’Aglia, R. Gaudio, R. ElRashedy, O. De Pascale, G. Palazzo and A. De Giacomo, Collinear double pulse laser ablation in water for the production of silver nanoparticles, *Physical Chemistry Chemical Physics*, **2013**, 15, 20868, doi: [10.1039/c3cp54194k](https://doi.org/10.1039/c3cp54194k).
- [135] A. De Giacomo, A. De Bonis, M. Dell’Aglia, O. De Pascale, R. Gaudio, S. Orlando, A. Santagata, G. S. Senesi, F. Taccogna and R. Teghil, Laser Ablation of Graphite in Water in a Range of Pressure from 1 to 146 atm Using Single and Double Pulse Techniques for the Production of Carbon Nanostructures, *The Journal of Physical Chemistry C*, **2011**, 115, 5123–5130, doi: [10.1021/jp109389c](https://doi.org/10.1021/jp109389c).
- [136] J. Tomko, S. M. O’Malley, C. Trout, J. J. Naddeo, R. Jimenez, J. C. Griepenburg, W. Soliman and D. M. Bubb, Cavitation bubble dynamics and nanoparticle size distributions in laser ablation in liquids, *Colloid Surf. A-Physicochem. Eng. Asp.*, **2017**, 522, 368–372, doi: [10.1016/j.colsurfa.2017.03.030](https://doi.org/10.1016/j.colsurfa.2017.03.030).
- [137] P. Wagener, S. Ibrahimkuty, A. Menzel, A. Plech and S. Barcikowski, Dynamics of silver nanoparticle formation and agglomeration inside the cavitation bubble after pulsed laser ablation in liquid, *Phys. Chem. Chem. Phys.*, **2013**, 15, 3068–3074, doi: [10.1039/C2CP42592K](https://doi.org/10.1039/C2CP42592K).
- [138] M.-R. Kalus, N. Bärsch, R. Streubel, E. Gökce, S. Barcikowski and B. Gökce, How persistent microbubbles shield nanoparticle productivity in laser synthesis of colloids – quantification of their volume, dwell dynamics, and gas composition, *Phys. Chem. Chem. Phys.*, **2017**, 19, 7112–7123, doi: [10.1039/C6CP07011F](https://doi.org/10.1039/C6CP07011F).
- [139] K. Sasaki, T. Nakano, W. Soliman and N. Takada, Effect of Pressurization on the Dynamics of a Cavitation Bubble Induced by Liquid-Phase Laser Ablation, *Applied Physics Express*, **2009**, 2, 046501–046503, doi: [10.1143/APEX.2.046501](https://doi.org/10.1143/APEX.2.046501).
- [140] K. Sasaki and Y. Takahashi, Discharge phenomena in a cavitation bubble induced by liquid-phase laser ablation, *Journal of Physics D: Applied Physics*, **2017**, 50, 325202, doi: [10.1088/1361-6463/aa754a](https://doi.org/10.1088/1361-6463/aa754a).
- [141] B. Kumar, D. Yadav and R. K. Thareja, Growth dynamics of nanoparticles in laser produced plasma in liquid ambient, *Journal of Applied Physics*, **2011**, 110, 074903–074910, doi: [10.1063/1.3642968](https://doi.org/10.1063/1.3642968).

- [142] W. Soliman, N. Takada and K. Sasaki, Growth Processes of Nanoparticles in Liquid-Phase Laser Ablation Studied by Laser-Light Scattering, *Applied Physics Express*, **2010**, 3, 035201–035203, doi: [10.1143/APEX.3.035201](https://doi.org/10.1143/APEX.3.035201).
- [143] M. Takeuchi and K. Sasaki, Spectrum of laser light scattered by nanoparticles in an ablation-induced cavitation bubble, *Appl. Phys. A-Mater. Sci. Process.*, **2016**, 122, 312–317, doi: [10.1007/s00339-016-9927-8](https://doi.org/10.1007/s00339-016-9927-8).
- [144] S. Ibrahimkuty, P. Wagener, A. Menzel, A. Plech and S. Barcikowski, Nanoparticle formation in a cavitation bubble after pulsed laser ablation in liquid studied with high time resolution small angle x-ray scattering, *Applied Physics Letters*, **2012**, 101, 103104, doi: [10.1063/1.4750250](https://doi.org/10.1063/1.4750250).
- [145] S. Ibrahimkuty, P. Wagener, T. d. S. Rolo, D. Karpov, A. Menzel, T. Baumbach, S. Barcikowski and A. Plech, A hierarchical view on material formation during pulsed-laser synthesis of nanoparticles in liquid, *Scientific Reports*, **2015**, 5, 16313–16323, doi: [10.1038/srep16313](https://doi.org/10.1038/srep16313).
- [146] A. Letzel, B. Gökce, P. Wagener, S. Ibrahimkuty, A. Menzel, A. Plech and S. Barcikowski, Size Quenching during Laser Synthesis of Colloids Happens Already in the Vapor Phase of the Cavitation Bubble, *The Journal of Physical Chemistry C*, **2017**, 121, 5356–5365, doi: [10.1021/acs.jpcc.6b12554](https://doi.org/10.1021/acs.jpcc.6b12554).
- [147] S. Reich, A. Letzel, A. Menzel, N. Kretzschmar, B. Gökce, S. Barcikowski and A. Plech, Early appearance of crystalline nanoparticles in pulsed laser ablation in liquids dynamics, *Nanoscale*, **2019**, 11, 6962, doi: [10.1039/C9NR01203F](https://doi.org/10.1039/C9NR01203F).
- [148] G. Marzun, J. Nakamura, X. Zhang, S. Barcikowski and P. Wagener, Size control and supporting of palladium nanoparticles made by laser ablation in saline solution as a facile route to heterogeneous catalysts, *Applied Surface Science*, **2015**, 348, 75–84, doi: [10.1016/j.apsusc.2015.01.108](https://doi.org/10.1016/j.apsusc.2015.01.108).
- [149] J.-P. Sylvestre, A. Kabashin, E. Sacher and M. Meunier, Femtosecond laser ablation of gold in water: influence of the laser-produced plasma on the nanoparticle size distribution, *Applied Physics A*, **2005**, 80, 753–758, doi: [10.1007/s00339-004-3081-4](https://doi.org/10.1007/s00339-004-3081-4).
- [150] G. Cristoforetti, E. Pitzalis, R. Spiniello, R. Ishak and M. Muniz-Miranda, Production of Palladium Nanoparticles by Pulsed Laser Ablation in Water and Their Characterization, *The Journal of Physical Chemistry C*, **2011**, 115, 5073–5083, doi: [10.1021/jp109281q](https://doi.org/10.1021/jp109281q).
- [151] J.-P. Sylvestre, S. Poulin, A. V. Kabashin, E. Sacher, M. Meunier and J. H. T. Luong, Surface Chemistry of Gold Nanoparticles Produced by Laser Ablation in Aqueous Media, *J. Phys. Chem. B*, **2004**, 108, 16864–16869, doi: [10.1021/jp047134+](https://doi.org/10.1021/jp047134+).

- [152] H. Liu, F. Chen, X. Wang, Q. Yang, H. Bian, J. Si and X. Hou, Influence of liquid environments on femtosecond laser ablation of silicon, *Thin Solid Films*, **2010**, 518, 5188–5194, doi: [10.1016/j.tsf.2010.04.043](https://doi.org/10.1016/j.tsf.2010.04.043).
- [153] H. Mustafa, D. Matthews and G. Römer, Investigation of the ultrashort pulsed laser processing of zinc at 515 nm: Morphology, crystallography and ablation threshold, *Materials & Design*, **2019**, 169, 107675, doi: [10.1016/j.matdes.2019.107675](https://doi.org/10.1016/j.matdes.2019.107675).
- [154] J. Liu, C. Liang, Z. Tian, S. Zhang and G. Shao, Spontaneous Growth and Chemical Reduction Ability of Ge Nanoparticles, *Sci Rep*, **2013**, 3, 1741, doi: [10.1038/srep01741](https://doi.org/10.1038/srep01741).
- [155] C.-C. Huang, C.-S. Yeh and C.-J. Ho, Laser Ablation Synthesis of Spindle-like Gallium Oxide Hydroxide Nanoparticles with the Presence of Cationic Cetyltrimethylammonium Bromide, *The Journal of Physical Chemistry B*, **2004**, 108, 4940–4945, doi: [10.1021/jp037427n](https://doi.org/10.1021/jp037427n).
- [156] V. K. LaMer and R. H. Dinegar, Theory, Production and Mechanism of Formation of Monodispersed Hydrosols, *Journal of the American Chemical Society*, **1950**, 72, 4847–4854, doi: [10.1021/ja01167a001](https://doi.org/10.1021/ja01167a001).
- [157] H. Wang, N. Koshizaki, L. Li, L. Jia, K. Kawaguchi, X. Li, A. Pyatenko, Z. Swiatkowska-Warkocka, Y. Bando and D. Golberg, Size-Tailored ZnO Submicrometer Spheres: Bottom-Up Construction, Size-Related Optical Extinction, and Selective Aniline Trapping, *Advanced Materials*, **2011**, 23, 1865–1870, doi: [10.1002/adma.201100078](https://doi.org/10.1002/adma.201100078).
- [158] D. Zhang, M. Lau, S. Lu, S. Barcikowski and B. Gökce, Germanium Sub-Microspheres Synthesized by Picosecond Pulsed Laser Melting in Liquids: Educt Size Effects, *Scientific Reports*, **2017**, 7, 40355, doi: [10.1038/srep40355](https://doi.org/10.1038/srep40355).
- [159] K. D. Malviya and K. Chattopadhyay, Temperature- and Size-Dependent Compositionally Tuned Microstructural Landscape for Ag-46at.% Cu Nanoalloy Prepared by Laser Ablation in Liquid, *The Journal of Physical Chemistry C*, **2016**, 120, 27699–27706, doi: [10.1021/acs.jpcc.6b09781](https://doi.org/10.1021/acs.jpcc.6b09781).
- [160] K. D. Malviya and K. Chattopadhyay, Synthesis and Mechanism of Composition and Size Dependent Morphology Selection in Nanoparticles of Ag–Cu Alloys Processed by Laser Ablation Under Liquid Medium, *The Journal of Physical Chemistry C*, **2014**, 118, 13228–13237, doi: [10.1021/jp502327c](https://doi.org/10.1021/jp502327c).
- [161] P. Wagener, J. Jakobi, C. Rehbock, V. S. K. Chakravadhanula, C. Thede, U. Wiedwald, M. Bartsch, L. Kienle and S. Barcikowski, Solvent-surface interactions control the phase structure in laser-generated iron-gold core-shell nanoparticles, *Scientific Reports*, **2016**, 6, 23352, doi: [10.1038/srep23352](https://doi.org/10.1038/srep23352).

- [162] V. Amendola, S. Scaramuzza, F. Carraro and E. Cattaruzza, Formation of alloy nanoparticles by laser ablation of Au/Fe multilayer films in liquid environment, *Journal of Colloid and Interface Science*, **2017**, 489, 18–27, doi: [10.1016/j.jcis.2016.10.023](https://doi.org/10.1016/j.jcis.2016.10.023).
- [163] P. W. Voorhees, The theory of Ostwald ripening, *Journal of Statistical Physics*, **1985**, 38, 231–252, doi: [10.1007/BF01017860](https://doi.org/10.1007/BF01017860).
- [164] S. Jendrzey, B. Gökce, V. Amendola and S. Barcikowski, Barrierless growth of precursor-free, ultrafast laser-fragmented noble metal nanoparticles by colloidal atom clusters – A kinetic in situ study, *Journal of Colloid and Interface Science*, **2016**, 463, 299–307, doi: [10.1016/j.jcis.2015.10.032](https://doi.org/10.1016/j.jcis.2015.10.032).
- [165] J. J. De Yoreo, P. U. P. A. Gilbert, N. A. J. M. Sommerdijk, R. L. Penn, S. Whitelam, D. Joester, H. Zhang, J. D. Rimer, A. Navrotsky, J. F. Banfield, A. F. Wallace, F. M. Michel, F. C. Meldrum, H. Colfen and P. M. Dove, Crystallization by particle attachment in synthetic, biogenic, and geologic environments, *Science*, **2015**, 349, 498, doi: [10.1126/science.aaa6760](https://doi.org/10.1126/science.aaa6760).
- [166] C.-H. Wu, S.-Y. Chen and P. Shen, Special grain boundaries of anatase nanocondensates by oriented attachment, *CrystEngComm*, **2014**, 16, 1459–1465, doi: [10.1039/C3CE41599F](https://doi.org/10.1039/C3CE41599F).
- [167] J. Liu, C. Liang, X. Zhu, Y. Lin, H. Zhang and S. Wu, Understanding the Solvent Molecules Induced Spontaneous Growth of Uncapped Tellurium Nanoparticles, *Scientific Reports*, **2016**, 6, 32631, doi: [10.1038/srep32631](https://doi.org/10.1038/srep32631).
- [168] M. A. Sobhan, M. J. Withford and E. M. Goldys, Enhanced Stability of Gold Colloids Produced by Femtosecond Laser Synthesis in Aqueous Solution of CTAB, *Langmuir*, **2010**, 26, 3156–3159, doi: [10.1021/la903088e](https://doi.org/10.1021/la903088e).
- [169] D. Amans, C. Malaterre, M. Diouf, C. Mancini, F. Chaput, G. Ledoux, G. Breton, Y. Guillin, C. Dujardin, K. Masenelli-Varlot and P. Perriat, Synthesis of Oxide Nanoparticles by Pulsed Laser Ablation in Liquids Containing a Complexing Molecule: Impact on Size Distributions and Prepared Phases, *J. Phys. Chem. C*, **2011**, 115, 5131–5139, doi: [10.1021/jp109387e](https://doi.org/10.1021/jp109387e).
- [170] A. Essaidi, Size Control of Gold Nanoparticles During Laser Ablation In Liquids With Different Functional Molecules, *Journal of Laser Micro/Nanoengineering*, **2013**, 8, 131–136, doi: [10.2961/jlmn.2013.02.0003](https://doi.org/10.2961/jlmn.2013.02.0003).
- [171] S. Lee, J. H. Shin and M. Y. Choi, Watching the growth of aluminum hydroxide nanoparticles from aluminum nanoparticles synthesized by pulsed laser ablation in aqueous surfactant solution, *Journal of Nanoparticle Research*, **2013**, 15, 1473, doi: [10.1007/s11051-013-1473-0](https://doi.org/10.1007/s11051-013-1473-0).
- [172] M. I. Mendivil, B. Krishnan, F. A. Sanchez, S. Martinez, J. A. Aguilar-Martinez, G. A. Castillo, D. I. Garcia-Gutierrez and S. Shaji, Synthesis of silver nanoparticles and antimony oxide

- nanocrystals by pulsed laser ablation in liquid media, *Applied Physics A*, **2013**, 110, 809–816, doi: [10.1007/s00339-012-7157-2](https://doi.org/10.1007/s00339-012-7157-2).
- [173] K. Yamada, Y. Tokumoto, T. Nagata and F. Mafuné, Mechanism of Laser-induced Size-reduction of Gold Nanoparticles as Studied by Nanosecond Transient Absorption Spectroscopy, *The Journal of Physical Chemistry B*, **2006**, 110, 11751–11756, doi: [10.1021/jp061020b](https://doi.org/10.1021/jp061020b).
- [174] C. He, T. Sasaki, Y. Shimizu and N. Koshizaki, Synthesis of ZnO nanoparticles using nanosecond pulsed laser ablation in aqueous media and their self-assembly towards spindle-like ZnO aggregates, *Applied Surface Science*, **2008**, 254, 2196–2202, doi: [10.1016/j.apsusc.2007.09.007](https://doi.org/10.1016/j.apsusc.2007.09.007).
- [175] C. Liang, T. Sasaki, Y. Shimizu and N. Koshizaki, Pulsed-laser ablation of Mg in liquids: surfactant-directing nanoparticle assembly for magnesium hydroxide nanostructures, *Chemical Physics Letters*, **2004**, 389, 58–63, doi: [10.1016/j.cplett.2004.03.056](https://doi.org/10.1016/j.cplett.2004.03.056).
- [176] Y. Ishikawa, Y. Shimizu, T. Sasaki and N. Koshizaki, Preparation of zinc oxide nanorods using pulsed laser ablation in water media at high temperature, *Journal of Colloid and Interface Science*, **2006**, 300, 612–615, doi: [10.1016/j.jcis.2006.04.005](https://doi.org/10.1016/j.jcis.2006.04.005).
- [177] Y.-Y. Fong, J. R. Gascooke, B. R. Visser, H. H. Harris, B. C. C. Cowie, L. Thomsen, G. F. Metha and M. A. Buntine, Influence of Cationic Surfactants on the Formation and Surface Oxidation States of Gold Nanoparticles Produced via Laser Ablation, *Langmuir*, **2013**, 29, 12452–12462, doi: [10.1021/la402234k](https://doi.org/10.1021/la402234k).
- [178] G. Laurens, J. Lam, A. Chemin, A. Cornet, C. Martinet, C. Dujardin, G. Ledoux, K. Lebbou, F. Chaput, B. Gökce, S. Barcikowski, T. Albaret, and D. Amans, Synthesis and characterization of nanoruby, *In preparation*,
- [179] D. Zhang, Z. Ma, M. Spasova, A. E. Yelsukova, S. Lu, M. Farle, U. Wiedwald and B. Gökce, Formation Mechanism of Laser-Synthesized Iron-Manganese Alloy Nanoparticles, Manganese Oxide Nanosheets and Nanofibers, *Particle & Particle Systems Characterization*, **2017**, 34, 1600225, doi: [10.1002/ppsc.201600225](https://doi.org/10.1002/ppsc.201600225).
- [180] H. Kwon, K. K. Kim, J. K. Song and S. M. Park, The Effects of Ambient Ions on the Growth of Gold Nanoparticles by Laser Ablation in Liquid, *Bulletin of the Korean Chemical Society*, **2014**, 35, 865–870, doi: [10.5012/bkcs.2014.35.3.865](https://doi.org/10.5012/bkcs.2014.35.3.865).
- [181] M. De Anda Villa, J. Gaudin, D. Amans, F. Boudjada, J. Bozek, R. Evaristo Grisenti, E. Lamour, G. Laurens, S. Macé, C. Nicolas, I. Papagiannouli, M. Patanen, C. Prigent, E. Robert, S. Steydli, M. Trassinelli, D. Vernhet and A. Lévy, Assessing the Surface Oxidation State of

- Free-Standing Gold Nanoparticles Produced by Laser Ablation, *Langmuir*, **2019**, 35, 11859–11871, doi: [10.1021/acs.langmuir.9b02159](https://doi.org/10.1021/acs.langmuir.9b02159).
- [182] A. Chemin, J. Lam, G. Laurens, F. Trichard, V. Motto-Ros, G. Ledoux, V. Jarý, V. Laguta, M. Nikl, C. Dujardin and D. Amans, Doping nanoparticles using pulsed laser ablation in a liquid containing the doping agent, *Nanoscale Adv.*, **2019**, doi: [10.1039/C9NA00223E](https://doi.org/10.1039/C9NA00223E).
- [183] G. Marzun, H. Bönnemann, C. Lehmann, B. Spliethoff, C. Weidenthaler and S. Barcikowski, Role of Dissolved and Molecular Oxygen on Cu and PtCu Alloy Particle Structure during Laser Ablation Synthesis in Liquids, *ChemPhysChem*, **2017**, 18, 1175–1184, doi: [10.1002/cphc.201601315](https://doi.org/10.1002/cphc.201601315).
- [184] E. Jiménez, K. Abderrafi, R. Abargues, J. L. Valdés and J. P. Martínez-Pastor, Laser-Ablation-Induced Synthesis of SiO₂-Capped Noble Metal Nanoparticles in a Single Step, *Langmuir*, **2010**, 26, 7458–7463, doi: [10.1021/la904179x](https://doi.org/10.1021/la904179x).
- [185] S. Hu, M. Tian, E. L. Ribeiro, G. Duscher and D. Mukherjee, Tandem laser ablation synthesis in solution-galvanic replacement reaction (LASiS-GRR) for the production of PtCo nanoalloys as oxygen reduction electrocatalysts, *Journal of Power Sources*, **2016**, 306, 413–423, doi: [10.1016/j.jpowsour.2015.11.078](https://doi.org/10.1016/j.jpowsour.2015.11.078).
- [186] H. Park, D. A. Reddy, Y. Kim, S. Lee, R. Ma, M. Lim and T. K. Kim, Hydrogenation of 4-nitrophenol to 4-aminophenol at room temperature: Boosting palladium nanocrystals efficiency by coupling with copper via liquid phase pulsed laser ablation, *Applied Surface Science*, **2017**, 401, 314–322, doi: [10.1016/j.apsusc.2017.01.045](https://doi.org/10.1016/j.apsusc.2017.01.045).
- [187] Y.-j. Kim, R. Ma, D. A. Reddy and T. K. Kim, Liquid-phase pulsed laser ablation synthesis of graphitized carbon-encapsulated palladium core-shell nanospheres for catalytic reduction of nitrobenzene to aniline, *Applied Surface Science*, **2015**, 357, 2112–2120, doi: [10.1016/j.apsusc.2015.09.193](https://doi.org/10.1016/j.apsusc.2015.09.193).
- [188] V. Amendola, S. Polizzi and M. Meneghetti, Free Silver Nanoparticles Synthesized by Laser Ablation in Organic Solvents and Their Easy Functionalization, *Langmuir*, **2007**, 23, 6766–6770, doi: [10.1021/la0637061](https://doi.org/10.1021/la0637061).
- [189] D. Zhang, B. Gökce, C. Notthoff and S. Barcikowski, Layered Seed-Growth of AgGe Football-like Microspheres via Precursor-Free Picosecond Laser Synthesis in Water, *Scientific Reports*, **2015**, 5, 13661, doi: [10.1038/srep13661](https://doi.org/10.1038/srep13661).
- [190] D. Zhang, J. Liu and C. Liang, Perspective on how laser-ablated particles grow in liquids, *Science China Physics, Mechanics & Astronomy*, **2017**, 60, 074201, doi: [10.1007/s11433-017-9035-8](https://doi.org/10.1007/s11433-017-9035-8).

- [191] H. Zhang, G. Duan, Y. Li, X. Xu, Z. Dai and W. Cai, Leaf-like Tungsten Oxide Nanoplatelets Induced by Laser Ablation in Liquid and Subsequent Aging, *Crystal Growth & Design*, **2012**, 12, 2646–2652, doi: [10.1021/cg300226r](https://doi.org/10.1021/cg300226r).
- [192] V. Merk, C. Rehbock, F. Becker, U. Hagemann, H. Nienhaus and S. Barcikowski, In Situ Non-DIWO Stabilization of Surfactant-Free, Plasmonic Gold Nanoparticles: Effect of Hofmeister's Anions, *Langmuir*, **2014**, 30, 4213–4222, doi: [10.1021/la404556a](https://doi.org/10.1021/la404556a).
- [193] P. Liu, Y. Liang, X. Lin, C. Wang and G. Yang, A General Strategy To Fabricate Simple Polyoxometalate Nanostructures: Electrochemistry-Assisted Laser Ablation in Liquid, *ACS Nano*, **2011**, 5, 4748–4755, doi: [10.1021/nm2007282](https://doi.org/10.1021/nm2007282).
- [194] P. Liu, C. X. Wang, X. Y. Chen and G. W. Yang, Controllable Fabrication and Cathodoluminescence Performance of High-index Facets GeO₂ Micro- and Nanocubes and Spindles upon Electrical-field-assisted Laser Ablation in Liquid, *The Journal of Physical Chemistry C*, **2008**, 112, 13450–13456, doi: [10.1021/jp802529r](https://doi.org/10.1021/jp802529r).
- [195] C. Streich, S. Koenen, M. Lelle, K. Peneva and S. Barcikowski, Influence of ligands in metal nanoparticle electrophoresis for the fabrication of biofunctional coatings, *Applied Surface Science*, **2015**, 348, 92–99, doi: [10.1016/j.apsusc.2014.12.159](https://doi.org/10.1016/j.apsusc.2014.12.159).
- [196] Y. Liang, P. Liu, J. Xiao, H. Li, C. Wang and G. Yang, A microfibre assembly of an iron-carbon composite with giant magnetisation, *Scientific Reports*, **2013**, 3, 3051, doi: [10.1038/srep03051](https://doi.org/10.1038/srep03051).
- [197] G. Gonzalez-Rubio, P. Diaz-Nunez, A. Rivera, A. Prada, G. Tardajos, J. Gonzalez-Izquierdo, L. Banares, P. Llombart, L. G. Macdowell, M. Alcolea Palafox, L. M. Liz-Marzan, O. Pena-Rodriguez and A. Guerrero-Martinez, Femtosecond laser reshaping yields gold nanorods with ultranarrow surface plasmon resonances, *Science*, **2017**, 358, 640–644, doi: [10.1126/science.aan8478](https://doi.org/10.1126/science.aan8478).
- [198] C. A. Schaumberg, M. Wollgarten and K. Rademann, Metallic Copper Colloids by Reductive Laser Ablation of Nonmetallic Copper Precursor Suspensions, *The Journal of Physical Chemistry A*, **2014**, 118, 8329–8337, doi: [10.1021/jp501123y](https://doi.org/10.1021/jp501123y).
- [199] Z. Yan, R. Bao, Y. Huang, A. N. Caruso, S. B. Qadri, C. Z. Dinu and D. B. Chrisey, Excimer Laser Production, Assembly, Sintering, and Fragmentation of Novel Fullerene-like Permalloy Particles in Liquid, *The Journal of Physical Chemistry C*, **2010**, 114, 3869–3873, doi: [10.1021/jp911566a](https://doi.org/10.1021/jp911566a).
- [200] K.-I. Saitow, Silicon Nanoclusters Selectively Generated by Laser Ablation in Supercritical Fluid, *The Journal of Physical Chemistry B*, **2005**, 109, 3731–3733, doi: [10.1021/jp0442551](https://doi.org/10.1021/jp0442551).

- [201] D. Amans, W. Cai and S. Barcikowski, Status and demand of research to bring laser generation of nanoparticles in liquids to maturity, *Applied Surface Science*, **2019**, 488, 445 – 454, doi: <https://doi.org/10.1016/j.apsusc.2019.05.117>.
- [202] J. G. Walter, S. Petersen, F. Stahl, T. Scheper and S. Barcikowski, Laser ablation-based one-step generation and bio-functionalization of gold nanoparticles conjugated with aptamers, *ChemPhysChem*, **2010**, 8, 21–31, doi: [10.1186/1477-3155-8-21](https://doi.org/10.1186/1477-3155-8-21).
- [203] S. Petersen and S. Barcikowski, In Situ Bioconjugation: Single Step Approach to Tailored Nanoparticle-Bioconjugates by Ultrashort Pulsed Laser Ablation, *Advanced Functional Materials*, **2009**, 19, 1167–1172, doi: [10.1002/adfm.200801526](https://doi.org/10.1002/adfm.200801526).
- [204] S. Mutisya, L. Franzel, B. Barnstein, T. Faber, J. Ryan and M. Bertino, Comparison of in situ and ex situ bioconjugation of Au nanoparticles generated by laser ablation, *Applied Surface Science*, **2013**, 264, 27–30, doi: [10.1016/j.apsusc.2012.09.064](https://doi.org/10.1016/j.apsusc.2012.09.064).
- [205] D. Zhang and B. Gökce, Perspective of laser-prototyping nanoparticle-polymer composites, *Applied Surface Science*, **2017**, 392, 991–1003, doi: [10.1016/j.apsusc.2016.09.150](https://doi.org/10.1016/j.apsusc.2016.09.150).
- [206] M. Flores-Castañeda, E. Camps, M. Camacho-López, S. Muhl, E. García and M. Figueroa, Bismuth nanoparticles synthesized by laser ablation in lubricant oils for tribological tests, *Journal of Alloys and Compounds*, **2015**, 643, S67–S70, doi: [10.1016/j.jallcom.2014.12.054](https://doi.org/10.1016/j.jallcom.2014.12.054).
- [207] S. Jendrzej, L. Gondecki, J. Debus, H. Moldenhauer, P. Tenberge, S. Barcikowski and B. Gökce, Tribological properties of laser-generated hard ceramic particles in a gear drive contact, *Applied Surface Science*, **2019**, 467, 811–818, doi: [10.1016/j.apsusc.2018.10.060](https://doi.org/10.1016/j.apsusc.2018.10.060).
- [208] S. Li, J. Zhang, M. G. Kibria, Z. Mi, M. Chaker, D. Ma, R. Nechache and F. Rosei, Remarkably enhanced photocatalytic activity of laser ablated Au nanoparticle decorated BiFeO₃ nanowires under visible-light, *Chemical Communications*, **2013**, 49, 5856, doi: [10.1039/c3cc40363g](https://doi.org/10.1039/c3cc40363g).
- [209] S. Kohsakowski, R. Streubel, I. Radev, V. Peinecke, S. Barcikowski, G. Marzun and S. Reichenberger, First PEM fuel cell based on ligand-free, laser-generated platinum nanoparticles, *Applied Surface Science*, **2019**, 467, 486–492, doi: [10.1016/j.apsusc.2018.10.145](https://doi.org/10.1016/j.apsusc.2018.10.145).
- [210] N. Bärsch, J. Jakobi, S. Weiler and S. Barcikowski, Pure colloidal metal and ceramic nanoparticles from high-power picosecond laser ablation in water and acetone, *Nanotechnology*, **2009**, 20, 445603, doi: [10.1088/0957-4484/20/44/445603](https://doi.org/10.1088/0957-4484/20/44/445603).
- [211] K. Y. Niu, J. Yang, S. A. Kulinich, J. Sun and X. W. Du, Hollow Nanoparticles of Metal Oxides and Sulfides: Fast Preparation via Laser Ablation in Liquid, *Langmuir*, **2010**, 26, 16652–16657, doi: [10.1021/la1033146](https://doi.org/10.1021/la1033146).

- [212] V. Amendola, P. Riello and M. Meneghetti, Magnetic Nanoparticles of Iron Carbide, Iron Oxide, Iron@Iron Oxide, and Metal Iron Synthesized by Laser Ablation in Organic Solvents, *The Journal of Physical Chemistry C*, **2011**, 115, 5140–5146, doi: [10.1021/jp109371m](https://doi.org/10.1021/jp109371m).
- [213] V. Amendola, P. Riello, S. Polizzi, S. Fiameni, C. Innocenti, C. Sangregorio and M. Meneghetti, Magnetic iron oxide nanoparticles with tunable size and free surface obtained via a “green” approach based on laser irradiation in water, *J. Mater. Chem.*, **2011**, 21, 18665–18673, doi: [10.1039/C1JM13680A](https://doi.org/10.1039/C1JM13680A).
- [214] G. Ledoux, D. Amans, C. Dujardin and K. Masenelli-Varlot, Facile and rapid synthesis of highly luminescent nanoparticles via pulsed laser ablation in liquid, *Nanotechnology*, **2009**, 20, 445605, doi: [10.1088/0957-4484/20/44/445605](https://doi.org/10.1088/0957-4484/20/44/445605).
- [215] P. Blandin, K. A. Maximova, M. B. Gongalsky, J. F. Sanchez-Royo, V. S. Chirvony, M. Sentis, V. Y. Timoshenko and A. V. Kabashin, Femtosecond laser fragmentation from water-dispersed microcolloids: toward fast controllable growth of ultrapure Si-based nanomaterials for biological applications, *J. Mat. Chem. B*, **2013**, 1, 2489–2495, doi: [10.1039/c3tb20285b](https://doi.org/10.1039/c3tb20285b).
- [216] G. L. Plautz, I. L. Graff, W. H. Schreiner and A. G. Bezerra, Evolution of size distribution, optical properties, and structure of Si nanoparticles obtained by laser-assisted fragmentation, *Appl. Phys. A-Mater. Sci. Process.*, **2017**, 123, 359, doi: [10.1007/s00339-017-0961-y](https://doi.org/10.1007/s00339-017-0961-y).
- [217] W.-J. Qin, S. A. Kulinich, X.-B. Yang, J. Sun and X.-W. Du, Preparation of semiconductor nanospheres by laser-induced phase separation, *Journal of Applied Physics*, **2009**, 106, 114318, doi: [10.1063/1.3267298](https://doi.org/10.1063/1.3267298).
- [218] J. Singh, M. Vellaikal and J. Narayan, Laser-enhanced synthesis and processing of diamond films from liquid hydrocarbons, *J. Appl. Phys.*, **1993**, 73, 4351–4356, doi: [10.1063/1.352819](https://doi.org/10.1063/1.352819).
- [219] L. Yang, P. May, L. Yin, J. Smith and K. Rosser, Growth of diamond nanocrystals by pulsed laser ablation of graphite in liquid, *Diamond and Related Materials*, **2007**, 16, 725–729, doi: [10.1016/j.diamond.2006.11.010](https://doi.org/10.1016/j.diamond.2006.11.010).
- [220] D. Liang, Z. Tian, J. Liu, Y. Ye, S. Wu, Y. Cai and C. Liang, MoS₂ nanosheets decorated with ultrafine Co₃O₄ nanoparticles for high-performance electrochemical capacitors, *Electrochimica Acta*, **2015**, 182, 376–382, doi: [10.1016/j.electacta.2015.09.085](https://doi.org/10.1016/j.electacta.2015.09.085).
- [221] M. Nath, C. N. R. Rao, R. Popovitz-Biro, A. Albu-Yaron and R. Tenne, Nanoparticles Produced by Laser Ablation of HfS₃ in Liquid Medium: Inorganic Fullerene-Like Structures of Hf₂S, *Chemistry of Materials*, **2004**, 16, 2238–2243, doi: [10.1021/cm035246s](https://doi.org/10.1021/cm035246s).

- [222] S. C. Singh, S. K. Mishra, R. K. Srivastava and R. Gopal, Optical Properties of Selenium Quantum Dots Produced with Laser Irradiation of Water Suspended Se Nanoparticles, *The Journal of Physical Chemistry C*, **2010**, 114, 17374–17384, doi: [10.1021/jp105037w](https://doi.org/10.1021/jp105037w).
- [223] Y. Liang, L. F. Zhu, P. Liu, H. B. Li, J. Xiao, X. W. Ji and G. W. Yang, Ag₂V₄O₁₁ nanostructures for highly ethanol sensitive performance, *CrystEngComm*, **2013**, 15, 6131, doi: [10.1039/c3ce40787j](https://doi.org/10.1039/c3ce40787j).
- [224] W. An, J. Miao and Z. Zhang, Effect of laser intensity on synthesis of solid solution CeTbO_{3+δ} in the liquid induced by Nd:YAG laser irradiation, *Chemical Physics Letters*, **2006**, 423, 386–389, doi: [10.1016/j.cplett.2006.04.018](https://doi.org/10.1016/j.cplett.2006.04.018).
- [225] C. Donate-Buendia, F. Froemel, M. B. Wilms, R. Streubel, J. Tenkamp, T. Hupfeld, M. Nachev, E. Goekce, A. Weisheit, S. Barcikowski, F. Walther, J. H. Schleifenbaum and B. Gökce, Oxide dispersion-strengthened alloys generated by laser metal deposition of laser-generated nanoparticle-metal powder composites, *Mater. Des.*, **2018**, 154, 360–369, doi: [10.1016/j.matdes.2018.05.044](https://doi.org/10.1016/j.matdes.2018.05.044).
- [226] E. Maurer, S. Barcikowski and B. Gökce, Process Chain for the Fabrication of Nanoparticle Polymer Composites by Laser Ablation Synthesis, *Chem. Eng. Technol.*, **2017**, 40, 1535–1543, doi: [10.1002/ceat.201600506](https://doi.org/10.1002/ceat.201600506).
- [227] D. D. Zand, Nanocomposite Fibre Fabrication via in situ Monomer Grafting and Bonding on Laser-generated Nanoparticles, *Journal of Laser Micro/Nanoengineering*, **2012**, 7, 21–27, doi: [10.2961/jlmn.2012.01.0004](https://doi.org/10.2961/jlmn.2012.01.0004).
- [228] P. Liu, H. Cui, C. X. Wang and G. W. Yang, From nanocrystal synthesis to functional nanostructure fabrication: laser ablation in liquid, *Physical Chemistry Chemical Physics*, **2010**, 12, 3942, doi: [10.1039/b918759f](https://doi.org/10.1039/b918759f).
- [229] G. W. Yang, Laser ablation in liquids: Applications in the synthesis of nanocrystals, *Prog. Mater. Sci.*, **2007**, 52, 648, doi: [10.1016/j.pmatsci.2006.10.016](https://doi.org/10.1016/j.pmatsci.2006.10.016).
- [230] L. C. Nistor, G. Epurescu, M. Dinescu and G. Dinescu, Boron nitride nano-structures produced by pulsed laser ablation in acetone, *IOP Conference Series: Materials Science and Engineering*, **2010**, 15, 012067, doi: [10.1088/1757-899X/15/1/012067](https://doi.org/10.1088/1757-899X/15/1/012067).
- [231] T. Sasaki, C. Liang, W. Nichols, Y. Shimizu and N. Koshizaki, Fabrication of oxide base nanostructures using pulsed laser ablation in aqueous solutions, *Applied Physics A*, **2004**, 79, 1489–1492, doi: [10.1007/s00339-004-2827-3](https://doi.org/10.1007/s00339-004-2827-3).
- [232] F. Bian, Y. C. Tian, R. Wang, H. X. Yang, H. Xu, S. Meng and J. Zhao, Ultrasmall Silver Nanopores Fabricated by Femtosecond Laser Pulses, *Nano Letters*, **2011**, 11, 3251–3257, doi: [10.1021/nl201529d](https://doi.org/10.1021/nl201529d).

- [233] A. Simakin, V. Voronov, G. Shafeev, R. Brayner and F. Bozon-Verduraz, Nanodisks of Au and Ag produced by laser ablation in liquid environment, *Chemical Physics Letters*, **2001**, 348, 182–186, doi: [10.1016/S0009-2614\(01\)01136-8](https://doi.org/10.1016/S0009-2614(01)01136-8).
- [234] C. He, T. Sasaki, Y. Zhou, Y. Shimizu, M. Masuda and N. Koshizaki, Surfactant-Assisted Preparation of Novel Layered Silver Bromide-Based Inorganic/Organic Nanosheets by Pulsed Laser Ablation in Aqueous Media, *Advanced Functional Materials*, **2007**, 17, 3554–3561, doi: [10.1002/adfm.200700081](https://doi.org/10.1002/adfm.200700081).
- [235] G. Yang, Laser ablation in liquids: Applications in the synthesis of nanocrystals, *Progress in Materials Science*, **2007**, 52, 648–698, doi: [10.1016/j.pmatsci.2006.10.016](https://doi.org/10.1016/j.pmatsci.2006.10.016).
- [236] L. Yang, P. W. May, L. Yin, R. Brown and T. B. Scott, Direct Growth of Highly Organized Crystalline Carbon Nitride from Liquid-Phase Pulsed Laser Ablation, *Chemistry of Materials*, **2006**, 18, 5058–5064, doi: [10.1021/cm061485e](https://doi.org/10.1021/cm061485e).
- [237] S. K. Singh, K. Kumar and S. B. Rai, Synthesis and spectroscopy of transparent colloidal solution of $\text{Gd}_2\text{O}_3:\text{Er}^{3+}, \text{Yb}^{3+}$ spherical nanocrystals by pulsed laser ablation, *Mater. Sci. Eng. B*, **2010**, 166, 180–184, doi: [10.1016/j.mseb.2009.11.018](https://doi.org/10.1016/j.mseb.2009.11.018).
- [238] S. Barcikowski, A. Hahn, A. Kabashin and B. Chichkov, Properties of nanoparticles generated during femtosecond laser machining in air and water, *Applied Physics A*, **2007**, 87, 47–55, doi: [10.1007/s00339-006-3852-1](https://doi.org/10.1007/s00339-006-3852-1).
- [239] S. Barcikowski, Picosecond and Femtosecond Laser Machining May Cause Health Risks Related to Nanoparticle Emission, *Journal of Laser Micro/Nanoengineering*, **2009**, 4, 159–164, doi: [10.2961/jlmn.2009.03.0003](https://doi.org/10.2961/jlmn.2009.03.0003).
- [240] J. Lee, S. Mahendra and P. J. J. Alvarez, Nanomaterials in the Construction Industry: A Review of Their Applications and Environmental Health and Safety Considerations, *ACS Nano*, **2010**, 4, 3580–3590, doi: [10.1021/nm100866w](https://doi.org/10.1021/nm100866w).
- [241] P. Anastas and N. Eghbali, Green Chemistry: Principles and Practice, *Chem. Soc. Rev.*, **2010**, 39, 301–312, doi: [10.1039/B918763B](https://doi.org/10.1039/B918763B).
- [242] S. Jendrzej, B. Gökce, M. Epple and S. Barcikowski, How Size Determines the Value of Gold: Economic Aspects of Wet Chemical and Laser-Based Metal Colloid Synthesis, *ChemPhysChem*, **2017**, 18, 1012–1019, doi: [10.1002/cphc.201601139](https://doi.org/10.1002/cphc.201601139).
- [243] D. Zhang, B. Gökce and S. Barcikowski, Laser Synthesis and Processing of Colloids: Fundamentals and Applications, *Chem. Rev.*, **2017**, 117, 3990–4103, doi: [10.1021/acs.chemrev.6b00468](https://doi.org/10.1021/acs.chemrev.6b00468).

- [244] P. Liu, Y. L. Cao, X. Y. Chen and G. W. Yang, Trapping High-Pressure Nanophase of Ge upon Laser Ablation in Liquid, *Crystal Growth & Design*, **2009**, 9, 1390–1393, doi: [10.1021/cg800633j](https://doi.org/10.1021/cg800633j).
- [245] A. Resano-Garcia, Y. Battie, A. Koch, A. En Naciri and N. Chaoui, Influence of the laser light absorption by the colloid on the properties of silver nanoparticles produced by laser ablation in stirred and stationary liquid, *Journal of Applied Physics*, **2015**, 117, 113103, doi: [10.1063/1.4915277](https://doi.org/10.1063/1.4915277).
- [246] M. Meseth, K. Lamine, M. Dehnen, S. Kayser, W. Brock, D. Behrenberg, H. Orthner, A. El-sukova, N. Hartmann, H. Wiggers, T. Hülser, H. Nienhaus, N. Benson and R. Schmechel, Laser-doping of crystalline silicon substrates using doped silicon nanoparticles, *Thin Solid Films*, **2013**, 548, 437–442, doi: [10.1016/j.tsf.2013.09.056](https://doi.org/10.1016/j.tsf.2013.09.056).
- [247] S. Kohsakowski, B. Gökce, R. Tanabe, P. Wagener, A. Plech, Y. Ito and S. Barcikowski, Target geometry and rigidity determines laser-induced cavitation bubble transport and nanoparticle productivity – a high-speed videography study, *Physical Chemistry Chemical Physics*, **2016**, 18, 16585–16593, doi: [10.1039/C6CP01232A](https://doi.org/10.1039/C6CP01232A).
- [248] J. Zhang, G. Chen, M. Chaker, F. Rosei and D. Ma, Gold nanoparticle decorated ceria nanotubes with significantly high catalytic activity for the reduction of nitrophenol and mechanism study, *Applied Catalysis B: Environmental*, **2013**, 132, 107–115, doi: [10.1016/j.apcatb.2012.11.030](https://doi.org/10.1016/j.apcatb.2012.11.030).
- [249] R. Intartaglia, G. Das, K. Bagga, A. Gopalakrishnan, A. Genovese, M. Povia, E. Di Fabrizio, R. Cingolani, A. Diaspro and F. Brandi, Laser synthesis of ligand-free bimetallic nanoparticles for plasmonic applications, *Phys. Chem. Chem. Phys.*, **2013**, 15, 3075–3082, doi: [10.1039/C2CP42656K](https://doi.org/10.1039/C2CP42656K).
- [250] N. Luo, X. Tian, C. Yang, J. Xiao, W. Hu, D. Chen and L. Li, Ligand-free gadolinium oxide for in vivo T1-weighted magnetic resonance imaging, *Physical Chemistry Chemical Physics*, **2013**, 15, 12235, doi: [10.1039/c3cp51530c](https://doi.org/10.1039/c3cp51530c).
- [251] E. Kymakis, G. D. Spyropoulos, R. Fernandes, G. Kakavelakis, A. G. Kanaras and E. Stratakis, Plasmonic Bulk Heterojunction Solar Cells: The Role of Nanoparticle Ligand Coating, *ACS Photonics*, **2015**, 2, 714–723, doi: [10.1021/acsp Photonics.5b00202](https://doi.org/10.1021/acsp Photonics.5b00202).
- [252] J. Zhang, D. Han, H. Zhang, M. Chaker, Y. Zhao and D. Ma, In situ recyclable gold nanoparticles using CO₂-switchable polymers for catalytic reduction of 4-nitrophenol, *Chemical Communications*, **2012**, 48, 11510, doi: [10.1039/c2cc35784d](https://doi.org/10.1039/c2cc35784d).
- [253] L. H. Li, J. Xiao, P. Liu and G. W. Yang, Super adsorption capability from amorphousization of metal oxide nanoparticles for dye removal, *Scientific Reports*, **2015**, 5, 9028, doi: [10.1038/srep09028](https://doi.org/10.1038/srep09028).

- [254] X. Xu, G. Duan, Y. Li, G. Liu, J. Wang, H. Zhang, Z. Dai and W. Cai, Fabrication of Gold Nanoparticles by Laser Ablation in Liquid and Their Application for Simultaneous Electrochemical Detection of Cd^{2+} , Pb^{2+} , Cu^{2+} , Hg^{2+} , *ACS Applied Materials & Interfaces*, **2014**, 6, 65–71, doi: [10.1021/am404816e](https://doi.org/10.1021/am404816e).
- [255] S. D. Angelov, S. Koenen, J. Jakobi, H. E. Heissler, M. Alam, K. Schwabe, S. Barcikowski and J. K. Krauss, Electrophoretic deposition of ligand-free platinum nanoparticles on neural electrodes affects their impedance in vitro and in vivo with no negative effect on reactive gliosis, *Journal of Nanobiotechnology*, **2016**, 14, 3, doi: [10.1186/s12951-015-0154-9](https://doi.org/10.1186/s12951-015-0154-9).
- [256] H. Zeng, G. Duan, Y. Li, S. Yang, X. Xu and W. Cai, Blue Luminescence of ZnO Nanoparticles Based on Non-Equilibrium Processes: Defect Origins and Emission Controls, *Advanced Functional Materials*, **2010**, 20, 561–572, doi: [10.1002/adfm.200901884](https://doi.org/10.1002/adfm.200901884).
- [257] H. Zhang, C. Liang, J. Liu, Z. Tian, G. Wang and W. Cai, Defect-Mediated Formation of Ag Cluster-Doped TiO_2 Nanoparticles for Efficient Photodegradation of Pentachlorophenol, *Langmuir*, **2012**, 28, 3938–3944, doi: [10.1021/la2043526](https://doi.org/10.1021/la2043526).
- [258] M. Zhang, X. Wang, X. Fu and Y. Xia, Performance and anti-wear mechanism of CaCO_3 nanoparticles as a green additive in poly-alpha-olefin, *Tribology International*, **2009**, 42, 1029–1039, doi: [10.1016/j.triboint.2009.02.012](https://doi.org/10.1016/j.triboint.2009.02.012).
- [259] R. Chou, A. H. Battez, J. Cabello, J. Viesca, A. Osorio and A. Sagastume, Tribological behavior of polyalphaolefin with the addition of nickel nanoparticles, *Tribology International*, **2010**, 43, 2327 – 2332, doi: <https://doi.org/10.1016/j.triboint.2010.08.006>.
- [260] S. Barcikowski, A. Plech, K. S. Suslick and A. Vogel, Materials synthesis in a bubble, *MRS Bulletin*, **2019**, 44, 382–391, doi: [10.1557/mrs.2019.107](https://doi.org/10.1557/mrs.2019.107).
- [261] W. Soliman, T. Nakano, N. Takada and K. Sasaki, Modification of Rayleigh–Plesset Theory for Reproducing Dynamics of Cavitation Bubbles in Liquid-Phase Laser Ablation, *Japanese Journal of Applied Physics*, **2010**, 49, 116202, doi: [10.1143/JJAP.49.116202](https://doi.org/10.1143/JJAP.49.116202).
- [262] R. Tanabe, T. T. Nguyen, T. Sugiura and Y. Ito, Bubble dynamics in metal nanoparticle formation by laser ablation in liquid studied through high-speed laser stroboscopic videography, *Applied Surface Science*, **2015**, 351, 327–331, doi: [10.1016/j.apsusc.2015.05.030](https://doi.org/10.1016/j.apsusc.2015.05.030).
- [263] S. Reich, P. Schönfeld, A. Letzel, S. Kohsakowski, M. Olbinado, B. Gökce, S. Barcikowski and A. Plech, Fluence Threshold Behaviour on Ablation and Bubble Formation in Pulsed Laser Ablation in Liquids, *ChemPhysChem*, **2017**, 18, 1084–1090, doi: [10.1002/cphc.201601198](https://doi.org/10.1002/cphc.201601198).
- [264] T. Tsuji, Y. Tsuboi, N. Kitamura and M. Tsuji, Microsecond-resolved imaging of laser ablation at solid–liquid interface: investigation of formation process of nano-size metal colloids, *Applied Surface Science*, **2004**, 229, 365–371, doi: [10.1016/j.apsusc.2004.02.013](https://doi.org/10.1016/j.apsusc.2004.02.013).

- [265] S. Jendrzey, B. Gökce and S. Barcikowski, Colloidal Stability of Metal Nanoparticles in Engine Oil under Thermal and Mechanical Load, *Chemical Engineering & Technology*, **2017**, 40, 1569–1576, doi: [10.1002/ceat.201600541](https://doi.org/10.1002/ceat.201600541).
- [266] A. Menéndez-Manjón, A. Schwenke, T. Steinke, M. Meyer, U. Giese, P. Wagener and S. Barcikowski, Ligand-free gold–silver nanoparticle alloy polymer composites generated by picosecond laser ablation in liquid monomer, *Applied Physics A*, **2013**, 110, 343–350, doi: [10.1007/s00339-012-7264-0](https://doi.org/10.1007/s00339-012-7264-0).
- [267] B. Lavi and A. Marmur, The exponential power law: partial wetting kinetics and dynamic contact angles, *Colloids and Surfaces A: Physicochemical and Engineering Aspects*, **2004**, 250, 409–414, doi: [10.1016/j.colsurfa.2004.04.079](https://doi.org/10.1016/j.colsurfa.2004.04.079).
- [268] D. Bonn, J. Eggers, J. Indekeu, J. Meunier and E. Rolley, Wetting and spreading, *Reviews of Modern Physics*, **2009**, 81, 739–805, doi: [10.1103/RevModPhys.81.739](https://doi.org/10.1103/RevModPhys.81.739).
- [269] J. D. Paulsen, R. Carmigniani, A. Kannan, J. C. Burton and S. R. Nagel, Coalescence of bubbles and drops in an outer fluid, *Nature Communications*, **2014**, 5, 3182, doi: [10.1038/ncomms4182](https://doi.org/10.1038/ncomms4182).
- [270] H. de Maleprade, C. Clanet and D. Quéré, Spreading of Bubbles after Contacting the Lower Side of an Aerophilic Slide Immersed in Water, *Physical Review Letters*, **2016**, 117, 094501, doi: [10.1103/PhysRevLett.117.094501](https://doi.org/10.1103/PhysRevLett.117.094501).
- [271] P. G. de Gennes, Wetting: statics and dynamics, *Reviews of Modern Physics*, **1985**, 57, 827–863, doi: [10.1103/RevModPhys.57.827](https://doi.org/10.1103/RevModPhys.57.827).
- [272] D. Legendre and M. Maglio, Numerical simulation of spreading drops, *Colloids and Surfaces A: Physicochemical and Engineering Aspects*, **2013**, 432, 29–37, doi: [10.1016/j.colsurfa.2013.04.046](https://doi.org/10.1016/j.colsurfa.2013.04.046).
- [273] T. Blake and J. Haynes, Kinetics of liquid/liquid displacement, *Journal of Colloid and Interface Science*, **1969**, 30, 421–423, doi: [10.1016/0021-9797\(69\)90411-1](https://doi.org/10.1016/0021-9797(69)90411-1).
- [274] T. Blake and J. De Coninck, The influence of solid–liquid interactions on dynamic wetting, *Advances in Colloid and Interface Science*, **2002**, 96, 21–36, doi: [10.1016/S0001-8686\(01\)00073-2](https://doi.org/10.1016/S0001-8686(01)00073-2).
- [275] R. G. Cox, The dynamics of the spreading of liquids on a solid surface. Part 1. Viscous flow, *Journal of Fluid Mechanics*, **1986**, 168, 169, doi: [10.1017/S0022112086000332](https://doi.org/10.1017/S0022112086000332).
- [276] O. V. Voinov, Hydrodynamics of wetting, *Fluid Dynamics*, **1977**, 11, 714–721, doi: [10.1007/BF01012963](https://doi.org/10.1007/BF01012963).

- [277] E. Bertrand, T. Blake and J. De Coninck, Dynamics of dewetting, *Colloids and Surfaces A: Physicochemical and Engineering Aspects*, **2010**, 369, 141–147, doi: [10.1016/j.colsurfa.2010.08.006](https://doi.org/10.1016/j.colsurfa.2010.08.006).
- [278] D. Jacqmin, Very, very fast wetting, *Journal of Fluid Mechanics*, **2002**, 455, 347–358, doi: [10.1017/S0022112001007492](https://doi.org/10.1017/S0022112001007492).
- [279] T. D. Blake, R. A. Dobson and K. J. Ruschak, Wetting at high capillary numbers, *Journal of colloid and interface science*, **2004**, 279, 198–205, doi: [10.1016/j.jcis.2004.06.057](https://doi.org/10.1016/j.jcis.2004.06.057).
- [280] J. H. Snoeijer and B. Andreotti, Moving Contact Lines: Scales, Regimes, and Dynamical Transitions, *Annual Review of Fluid Mechanics*, **2013**, 45, 269–292, doi: [10.1146/annurev-fluid-011212-140734](https://doi.org/10.1146/annurev-fluid-011212-140734).
- [281] H. van Ouwerkerk, The rapid growth of a vapour bubble at a liquid-solid interface, *International Journal of Heat and Mass Transfer*, **1971**, 14, 1415–1431, doi: [10.1016/0017-9310\(71\)90189-X](https://doi.org/10.1016/0017-9310(71)90189-X).
- [282] H. Van Ouwerkerk, Hemispherical bubble growth in a binary mixture, *Chemical Engineering Science*, **1972**, 27, 1957–1967, doi: [10.1016/0009-2509\(72\)87054-4](https://doi.org/10.1016/0009-2509(72)87054-4).
- [283] F. R. Gilmore, *The growth or collapse of a spherical bubble in a viscous compressible liquid*, California Institute of Technology Technical Report no. 26–4, 1952.
- [284] C. Rehbock, V. Merk, L. Gamrad, R. Streubel and S. Barcikowski, Size control of laser-fabricated surfactant-free gold nanoparticles with highly diluted electrolytes and their subsequent bioconjugation, *Phys. Chem. Chem. Phys.*, **2013**, 15, 3057–3067, doi: [10.1039/C2CP42641B](https://doi.org/10.1039/C2CP42641B).
- [285] G. Palazzo, G. Valenza, M. Dell’Aglio and A. De Giacomo, On the stability of gold nanoparticles synthesized by laser ablation in liquids, *Journal of Colloid and Interface Science*, **2017**, 489, 47–56, doi: [10.1016/j.jcis.2016.09.017](https://doi.org/10.1016/j.jcis.2016.09.017).
- [286] B. V. Derjaguin, N. V. Churaev and V. M. Muller, in *The Derjaguin—Landau—Verwey—Overbeek (DLVO) Theory of Stability of Lyophobic Colloids*, Springer US, Boston, MA, 1987, pp. 293–310, doi: [10.1007/978-1-4757-6639-4_8](https://doi.org/10.1007/978-1-4757-6639-4_8).
- [287] T. L. Doane, C.-H. Chuang, R. J. Hill and C. Burda, Nanoparticle ζ -Potentials, *Accounts of Chemical Research*, **2012**, 45, 317–326, doi: [10.1021/ar200113c](https://doi.org/10.1021/ar200113c).
- [288] H. Muto, K. Yamada, K. Miyajima and F. Mafuné, Estimation of Surface Oxide on Surfactant-Free Gold Nanoparticles Laser-Ablated in Water, *J. Phys. Chem. C*, **2007**, 111, 17221–17226, doi: [10.1021/jp075582m](https://doi.org/10.1021/jp075582m).

- [289] A. Lindblad, J. Söderström, C. Nicolas, E. Robert and C. Miron, A multi purpose source chamber at the PLEIADES beamline at SOLEIL for spectroscopic studies of isolated species: Cold molecules, clusters, and nanoparticles, *Review of Scientific Instruments*, **2013**, 84, 113105, doi: [10.1063/1.4829718](https://doi.org/10.1063/1.4829718).
- [290] S. Tanuma, C. J. Powell and D. R. Penn, Calculations of electron inelastic mean free paths. IX. Data for 41 elemental solids over the 50 eV to 30 keV range, *Surf. Interface Anal.*, **2011**, 43, 689–713, doi: [10.1002/sia.3522](https://doi.org/10.1002/sia.3522).
- [291] M. Trassinelli, Bayesian data analysis tools for atomic physics, *Nuclear Instruments and Methods in Physics Research Section B: Beam Interactions with Materials and Atoms*, **2017**, 408, 301–312, doi: [10.1016/j.nimb.2017.05.030](https://doi.org/10.1016/j.nimb.2017.05.030).
- [292] P. S. Bagus and G. Pacchioni, Core-level binding-energy shifts due to ionic adsorbates, *Phys. Rev. B*, **1993**, 48, 15262–15273, doi: [10.1103/PhysRevB.48.15262](https://doi.org/10.1103/PhysRevB.48.15262).
- [293] H. Zhang and J. Banfield, Thermodynamic analysis of phase stability of nanocrystalline titania, *J. Mater. Chem.*, **1998**, 8, 2073–2076, doi: [10.1039/a802619j](https://doi.org/10.1039/a802619j).
- [294] H. Zhang and J. Banfield, Understanding polymorphic phase transformation behavior during growth of nanocrystalline aggregates: Insights from TiO₂, *J. Phys. Chem. B*, **2000**, 104, 3481–3487, doi: [10.1021/jp000499j](https://doi.org/10.1021/jp000499j).
- [295] K. Zhu, M. Zhang, J. Hong and Z. Yin, Size effect on phase transition sequence of TiO₂ nanocrystal, *Mater. Sci. Eng. A-Struct. Mater. Prop. Microstruct. Process.*, **2005**, 403, 87–93, doi: [10.1016/j.msea.2005.04.029](https://doi.org/10.1016/j.msea.2005.04.029).
- [296] M. Ranade, A. Navrotsky, H. Zhang, J. Banfield, S. Elder, A. Zaban, P. Borse, S. Kulkarni, G. Doran and H. Whitfield, Energetics of nanocrystalline TiO₂, *Proc. Natl. Acad. Sci. U. S. A.*, **2002**, 99, 6476–6481, doi: [10.1073/pnas.251534898](https://doi.org/10.1073/pnas.251534898).
- [297] R. C. Garvie, Occurrence of metastable tetragonal zirconia as a crystallite size effect, *J. Phys. Chem.*, **1965**, 69, 1238, doi: [10.1021/j100888a024](https://doi.org/10.1021/j100888a024).
- [298] A. Navrotsky, Energetics of nanoparticle oxides: interplay between surface energy and polymorphism, *Geochem. Trans.*, **2003**, 4, 34–37, doi: [10.1186/1467-4866-4-34](https://doi.org/10.1186/1467-4866-4-34).
- [299] L. Chen, T. Mashimo, E. Omurzak, H. Okudera, C. Iwamoto and A. Yoshiasa, Pure Tetragonal ZrO₂ Nanoparticles Synthesized by Pulsed Plasma in Liquid, *J. Phys. Chem. C*, **2011**, 115, 9370–9375, doi: [10.1021/jp111367k](https://doi.org/10.1021/jp111367k).
- [300] G. Schimanke and M. Martin, In situ XRD study of the phase transition of nanocrystalline maghemite (γ -Fe₂O₃) to hematite (α -Fe₂O₃), *Solid State Ion.*, **2000**, 136, 1235–1240, doi: [10.1016/S0167-2738\(00\)00593-2](https://doi.org/10.1016/S0167-2738(00)00593-2).

- [301] D. Nicolas, B. Masenelli, P. Melinon, E. Bernstein, C. Dujardin, G. Ledoux and C. Esnouf, Structural transition in rare earth oxide clusters, *J. Chem. Phys.*, **2006**, 125, 171104, doi: [10.1063/1.2390693](https://doi.org/10.1063/1.2390693).
- [302] M. A. Caldwell, S. Raoux, R. Y. Wang, H. S. P. Wong and D. J. Milliron, Synthesis and size-dependent crystallization of colloidal germanium telluride nanoparticles, *J. Mater. Chem.*, **2010**, 20, 1285–1291, doi: [10.1039/b917024c](https://doi.org/10.1039/b917024c).
- [303] B. Guo and Z.-P. Luo, Particle size effect on the crystal structure of Y_2O_3 particles formed in a flame aerosol process, *J. Am. Ceram. Soc.*, **2008**, 91, 1653–1658, doi: [10.1111/j.1551-2916.2008.02341.x](https://doi.org/10.1111/j.1551-2916.2008.02341.x).
- [304] L. Botter-Jensen, N. Larsen, B. Markey and S. McKeever, $Al_2O_3:C$ as a sensitive OSL dosimeter for rapid assessment of environmental photon dose rates, *Radiat. Meas.*, **1997**, 27, 295, doi: [10.1016/S1350-4487\(96\)00124-2](https://doi.org/10.1016/S1350-4487(96)00124-2).
- [305] R. A. Forman, G. J. Piermarini, J. D. Barnett and S. Block, Pressure Measurement Made by the Utilization of Ruby Sharp-Line Luminescence, *Science*, **1972**, 176, 284–285, doi: [10.1126/science.176.4032.284](https://doi.org/10.1126/science.176.4032.284).
- [306] A. Kostyukov, M. Baronskiy, A. Rastorguev, V. Snytnikov, V. Snytnikov, A. Zhuzhgov and A. Ishchenko, Photoluminescence of Cr^{3+} in nanostructured Al_2O_3 synthesized by evaporation using a continuous wave CO_2 laser, *RSC Advances*, **2016**, 6, 2072–2078, doi: [10.1039/C5RA19455E](https://doi.org/10.1039/C5RA19455E).
- [307] I. Levin and D. Brandon, Metastable Alumina Polymorphs: Crystal Structures and Transition Sequences, *Journal of the American Ceramic Society*, **1998**, 81, 1995–2012, doi: [10.1111/j.1151-2916.1998.tb02581.x](https://doi.org/10.1111/j.1151-2916.1998.tb02581.x).
- [308] J. M. McHale, Surface Energies and Thermodynamic Phase Stability in Nanocrystalline Aluminas, *Science*, **1997**, 277, 788–791, doi: [10.1126/science.277.5327.788](https://doi.org/10.1126/science.277.5327.788).
- [309] J. M. McHale, A. Navrotsky and A. J. Perrotta, Effects of Increased Surface Area and Chemisorbed H_2O on the Relative Stability of Nanocrystalline $\gamma-Al_2O_3$ and $\alpha-Al_2O_3$, *J. Phys. Chem. B*, **1997**, 101, 603–613, doi: [10.1021/jp9627584](https://doi.org/10.1021/jp9627584).
- [310] A. H. Tavakoli, P. S. Maram, S. J. Widgeon, J. Rufner, K. van Benthem, S. Ushakov, S. Sen and A. Navrotsky, Amorphous Alumina Nanoparticles: Structure, Surface Energy, and Thermodynamic Phase Stability, *The Journal of Physical Chemistry C*, **2013**, 117, 17123–17130, doi: [10.1021/jp405820g](https://doi.org/10.1021/jp405820g).
- [311] B. Kumar and R. K. Thareja, Synthesis of nanoparticles in laser ablation of aluminum in liquid, *Journal of Applied Physics*, **2010**, 108, 064906, doi: [10.1063/1.3486517](https://doi.org/10.1063/1.3486517).

BIBLIOGRAPHY

- [312] B. Kumar and R. K. Thareja, Synthesis of aluminum oxide nanoparticles using laser ablation in liquid, *physica status solidi (c)*, **2010**, 7, 1409–1412, doi: [10.1002/pssc.200983356](https://doi.org/10.1002/pssc.200983356).
- [313] I. L. Liu, P. Shen and S. Y. Chen, H⁺ - and Al²⁺ -Codoped Al₂O₃ Nanoparticles with Spinel-Type Related Structures by Pulsed Laser Ablation in Water, *The Journal of Physical Chemistry C*, **2010**, 114, 7751–7757, doi: [10.1021/jp1002325](https://doi.org/10.1021/jp1002325).
- [314] I. L. Liu, B. C. Lin, S. Y. Chen and P. Shen, NaAlO₂ and γ -Al₂O₃ Nanoparticles by Pulsed Laser Ablation in Aqueous Solution, *The Journal of Physical Chemistry C*, **2011**, 115, 4994–5002, doi: [10.1021/jp107030h](https://doi.org/10.1021/jp107030h).
- [315] S. A. Al-Mamun, R. Nakajima and T. Ishigaki, Tuning the size of aluminum oxide nanoparticles synthesized by laser ablation in water using physical and chemical approaches, *Journal of Colloid and Interface Science*, **2013**, 392, 172–182, doi: [10.1016/j.jcis.2012.10.027](https://doi.org/10.1016/j.jcis.2012.10.027).
- [316] Y.-P. Lee, Y.-H. Liu and C.-S. Yeh, Formation of bayerite, gibbsite and boehmite particles by laser ablation, *Physical Chemistry Chemical Physics*, **1999**, 1, 4681–4686, doi: [10.1039/a905178c](https://doi.org/10.1039/a905178c).
- [317] H.-M. Kao, R.-R. Wu, T.-Y. Chen, Y.-H. Chen and C.-S. Yeh, Probing the formation process of aluminium hydroxide nanoparticles prepared by laser ablation with ²⁷Al NMR spectroscopy, *Journal of Materials Chemistry*, **2000**, 10, 2802–2804, doi: [10.1039/b004936k](https://doi.org/10.1039/b004936k).
- [318] H. Li, E. A. Ghezal, A. Nehari, G. Alombert-Goget, A. Brenier and K. Lebbou, Bubbles defects distribution in sapphire bulk crystals grown by Czochralski technique, *Opt. Mater.*, **2013**, 35, 1071, doi: [10.1016/j.optmat.2012.12.022](https://doi.org/10.1016/j.optmat.2012.12.022).
- [319] H. Li, E. A. Ghezal, G. Alombert-Goget, G. Breton, J. M. Ingargiola, A. Brenier and K. Lebbou, Qualitative and quantitative bubbles defects analysis in undoped and Ti-doped sapphire crystals grown by Czochralski technique, *Opt. Mater.*, **2014**, 37, 132, doi: [10.1016/j.optmat.2014.05.012](https://doi.org/10.1016/j.optmat.2014.05.012).
- [320] K. Nakamoto, *Infrared and Raman Spectra of Inorganic and Coordination Compounds*, Wiley: New York, 1986, p. 189.
- [321] M. Nara, H. Torii and M. Tasumi, Correlation between the Vibrational Frequencies of the Carboxylate Group and the Types of Its Coordination to a Metal Ion: An ab Initio Molecular Orbital Study, *The Journal of Physical Chemistry*, **1996**, 100, 19812–19817, doi: [10.1021/jp9615924](https://doi.org/10.1021/jp9615924).
- [322] J. E. Tackett, FT-IR characterization of metal acetates in aqueous-solution, *Appl. Spectrosc.*, **1989**, 43, 483–489, doi: [10.1366/0003702894202931](https://doi.org/10.1366/0003702894202931).

- [323] G. D. Deacon and R. J. Phillips, Relationships between the carbon-oxygen stretching frequencies of carboxylato complexes and the type of carboxylate coordination, *Coord. Chem. Rev.*, **1980**, 33, 227–250, doi: [10.1016/S0010-8545\(00\)80455-5](https://doi.org/10.1016/S0010-8545(00)80455-5).
- [324] J. P. Déry, E. F. Borra and A. M. Ritcey, Ethylene glycol ferrofluid for the fabrication of magnetically deformable liquid mirrors, *Chem. Mater.*, **2008**, 20, 6420–6426, doi: [10.1021/cm801075u](https://doi.org/10.1021/cm801075u).
- [325] O. Deutschbein, Die linienhafte Emission und Absorption der Chromphosphore. I, *Annalen der Physik*, **1932**, 406, 712–728, doi: [10.1002/andp.19324060609](https://doi.org/10.1002/andp.19324060609).
- [326] O. Deutschbein, Die linienhafte Emission und Absorption der Chromphosphore. II, *Annalen der Physik*, **1932**, 406, 729–754, doi: [10.1002/andp.19324060702](https://doi.org/10.1002/andp.19324060702).
- [327] L. Basso, F. Gorrini, M. Cazzanelli, N. Bazzanella, A. Bifone and A. Miotello, An all-optical single-step process for production of nanometric-sized fluorescent diamonds, *Nanoscale*, **2018**, 10, 5738–5744, doi: [10.1039/C7NR08791H](https://doi.org/10.1039/C7NR08791H).
- [328] H. K. Mao and P. M. Bell, High-Pressure Physics: The 1-Megabar Mark on the Ruby R1 Static Pressure Scale, *Science*, **1976**, 191, 851–852, doi: [10.1126/science.191.4229.851](https://doi.org/10.1126/science.191.4229.851).
- [329] H. K. Mao, P. M. Bell, J. W. Shaner and D. J. Steinberg, Specific volume measurements of Cu, Mo, Pd, and Ag and calibration of the ruby R_1 fluorescence pressure gauge from 0.06 to 1 Mbar, *Journal of Applied Physics*, **1978**, 49, 3276–3283, doi: [10.1063/1.325277](https://doi.org/10.1063/1.325277).
- [330] M. Born and R. Oppenheimer, Zur Quantentheorie der Molekeln, *Annalen der Physik*, **1927**, 389, 457–484, doi: [10.1002/andp.19273892002](https://doi.org/10.1002/andp.19273892002).
- [331] D. R. Hartree, The Wave Mechanics of an Atom with a non-Coulomb Central Field. Part III. Term Values and Intensities in Series in Optical Spectra, *Mathematical Proceedings of the Cambridge Philosophical Society*, **1928**, 24, 426–437, doi: [10.1017/S0305004100015954](https://doi.org/10.1017/S0305004100015954).
- [332] J. C. Slater, The Theory of Complex Spectra, *Phys. Rev.*, **1929**, 34, 1293–1322, doi: [10.1103/PhysRev.34.1293](https://doi.org/10.1103/PhysRev.34.1293).
- [333] P. Hohenberg and W. Kohn, Inhomogeneous Electron Gas, *Phys. Rev.*, **1964**, 136, B864–B871, doi: [10.1103/PhysRev.136.B864](https://doi.org/10.1103/PhysRev.136.B864).
- [334] W. Kohn and L. J. Sham, Self-Consistent Equations Including Exchange and Correlation Effects, *Phys. Rev.*, **1965**, 140, A1133–A1138, doi: [10.1103/PhysRev.140.A1133](https://doi.org/10.1103/PhysRev.140.A1133).
- [335] J. P. Perdew, K. Burke and M. Ernzerhof, Generalized Gradient Approximation Made Simple, *Phys. Rev. Lett.*, **1996**, 77, 3865–3868, doi: [10.1103/PhysRevLett.77.3865](https://doi.org/10.1103/PhysRevLett.77.3865).

- [336] A. D. Becke, Density-functional thermochemistry. III. The role of exact exchange, *The Journal of Chemical Physics*, **1993**, 98, 5648–5652, doi: [10.1063/1.464913](https://doi.org/10.1063/1.464913).
- [337] F. Bloch, Über die Quantenmechanik der Elektronen in Kristallgittern, *Zeitschrift für Physik*, **1929**, 52, 555–600, doi: [10.1007/BF01339455](https://doi.org/10.1007/BF01339455).
- [338] G. Kresse and J. Hafner, Ab initio molecular dynamics for liquid metals, *Phys. Rev. B*, **1993**, 47, 558–561, doi: [10.1103/PhysRevB.47.558](https://doi.org/10.1103/PhysRevB.47.558).
- [339] G. Kresse and J. Furthmüller, Efficiency of ab-initio total energy calculations for metals and semiconductors using a plane-wave basis set, *Computational Materials Science*, **1996**, 6, 15–50, doi: [10.1016/0927-0256\(96\)00008-0](https://doi.org/10.1016/0927-0256(96)00008-0).
- [340] G. Kresse and J. Furthmüller, Efficient iterative schemes for *ab initio* total-energy calculations using a plane-wave basis set, *Phys. Rev. B*, **1996**, 54, 11169–11186, doi: [10.1103/PhysRevB.54.11169](https://doi.org/10.1103/PhysRevB.54.11169).
- [341] J. C. Slater and G. F. Koster, Simplified LCAO Method for the Periodic Potential Problem, *Phys. Rev.*, **1954**, 94, 1498–1524, doi: [10.1103/PhysRev.94.1498](https://doi.org/10.1103/PhysRev.94.1498).
- [342] B. Aradi, B. Hourahine and T. Frauenheim, DFTB+, a Sparse Matrix-Based Implementation of the DFTB Method, *The Journal of Physical Chemistry A*, **2007**, 111, 5678–5684, doi: [10.1021/jp070186p](https://doi.org/10.1021/jp070186p).
- [343] J. E. Jones and S. Chapman, On the determination of molecular fields. -II. From the equation of state of a gas, *Proceedings of the Royal Society of London. Series A, Containing Papers of a Mathematical and Physical Character*, **1924**, 106, 463–477, doi: [10.1098/rspa.1924.0082](https://doi.org/10.1098/rspa.1924.0082).
- [344] R. A. Buckingham and J. E. Lennard-Jones, The classical equation of state of gaseous helium, neon and argon, *Proceedings of the Royal Society of London. Series A. Mathematical and Physical Sciences*, **1938**, 168, 264–283, doi: [10.1098/rspa.1938.0173](https://doi.org/10.1098/rspa.1938.0173).
- [345] M. S. Daw, S. M. Foiles and M. I. Baskes, The embedded-atom method: a review of theory and applications, *Materials Science Reports*, **1993**, 9, 251–310, doi: [https://doi.org/10.1016/0920-2307\(93\)90001-U](https://doi.org/10.1016/0920-2307(93)90001-U).
- [346] R. Lizárraga, E. Holmström, S. C. Parker and C. Arrouvel, Structural characterization of amorphous alumina and its polymorphs from first-principles XPS and NMR calculations, *Phys. Rev. B*, **2011**, 83, 094201, doi: [10.1103/PhysRevB.83.094201](https://doi.org/10.1103/PhysRevB.83.094201).
- [347] X. Krokidis, P. Raybaud, A.-E. Gobichon, B. Rebours, P. Euzen and H. Toulhoat, Theoretical Study of the Dehydration Process of Boehmite to γ -Alumina, *J. Phys. Chem. B*, **2001**, 105, 5121–5130, doi: [10.1021/jp0038310](https://doi.org/10.1021/jp0038310).

- [348] C. Ruberto, Y. Yourdshahyan and B. I. Lundqvist, Surface properties of metastable alumina: A comparative study of κ - and α -Al₂O₃, *Phys. Rev. B*, **2003**, 67, 195412, doi: [10.1103/PhysRevB.67.195412](https://doi.org/10.1103/PhysRevB.67.195412).
- [349] N. Salles, O. Politano, E. Amzallag and R. Tétot, Molecular dynamics study of high-pressure alumina polymorphs with a tight-binding variable-charge model, *Computational Materials Science*, **2016**, 111, 181–189, doi: [10.1016/j.commatsci.2015.09.017](https://doi.org/10.1016/j.commatsci.2015.09.017).
- [350] W. C. Mackrodt, R. J. Davey and S. N. Black, The morphology of α -Al₂O₃ and α -Fe₂O₃: the importance of surface relaxation, *Journal of Crystal Growth*, **1987**, 80, 441–446, doi: [10.1016/0022-0248\(87\)90093-5](https://doi.org/10.1016/0022-0248(87)90093-5).
- [351] A. D. V. I., Manassidis and M. Gillan., Structure of the (0001) surface of α -Al₂O₃ from first principles calculations, *Surface Science Letters*, **1993**, 285, 517–521, doi: [10.1016/0039-6028\(93\)90423-H](https://doi.org/10.1016/0039-6028(93)90423-H).
- [352] S. Blonski and S. H. Garofalini, Molecular dynamics simulations of α -alumina and γ -alumina surfaces, *Surface Science*, **1993**, 295, 263–274, doi: [10.1016/0039-6028\(93\)90202-U](https://doi.org/10.1016/0039-6028(93)90202-U).
- [353] L. J. Alvarez, L. E. León, J. F. Sanz, M. J. Capitán and J. A. Odriozola, Surface structure of cubic aluminum oxide, *Phys. Rev. B*, **1994**, 50, 2561–2565, doi: [10.1103/PhysRevB.50.2561](https://doi.org/10.1103/PhysRevB.50.2561).
- [354] L. J. Alvarez, L. E. Leon, J. F. Sanz, M. J. Capitan and J. A. Odriozola, Computer Simulation of γ -Al₂O₃ Microcrystal, *J. Phys. Chem.*, **1995**, 99, 17872–17876, doi: [10.1021/j100051a011](https://doi.org/10.1021/j100051a011).
- [355] H. P. Pinto, R. M. Nieminen and S. D. Elliott, *Ab initio* study of γ -Al₂O₃ surfaces, *Phys. Rev. B*, **2004**, 70, 125402, doi: [10.1103/PhysRevB.70.125402](https://doi.org/10.1103/PhysRevB.70.125402).
- [356] S. P. Adiga, P. Zapol and L. A. Curtiss, Atomistic simulations of amorphous alumina surfaces, *Phys. Rev. B*, **2006**, 74, 064204, doi: [10.1103/PhysRevB.74.064204](https://doi.org/10.1103/PhysRevB.74.064204).
- [357] G. Gutiérrez and B. Johansson, Molecular dynamics study of structural properties of amorphous Al₂O₃, *Phys. Rev. B*, **2002**, 65, 104202, doi: [10.1103/PhysRevB.65.104202](https://doi.org/10.1103/PhysRevB.65.104202).
- [358] S. Davis and G. Gutiérrez, Structural, elastic, vibrational and electronic properties of amorphous Al₂O₃ from *ab initio* calculations, *J. Phys.: Condens. Matter*, **2011**, 23, 495401, doi: [10.1088/0953-8984/23/49/495401](https://doi.org/10.1088/0953-8984/23/49/495401).
- [359] P. Vashishta, R. K. Kalia, A. Nakano and J. P. Rino, Interaction potentials for alumina and molecular dynamics simulations of amorphous and liquid alumina, *Journal of Applied Physics*, **2008**, 103, 083504, doi: [10.1063/1.2901171](https://doi.org/10.1063/1.2901171).
- [360] V. Van Hoang and S. Kun Oh, Simulation of structural properties and structural transformation of amorphous Al₂O₃, *Physica B: Condensed Matter*, **2004**, 352, 73–85, doi: [10.1016/j.physb.2004.06.057](https://doi.org/10.1016/j.physb.2004.06.057).

- [361] G. T. Nguyen, T. T. Nguyen, T. T. Nguyen and V. V. Le, Molecular dynamics simulations of pressure-induced structural and mechanical property changes in amorphous Al_2O_3 , *Journal of Non-Crystalline Solids*, **2016**, 449, 100–106, doi: [10.1016/j.jnoncrysol.2016.07.018](https://doi.org/10.1016/j.jnoncrysol.2016.07.018).
- [362] R. Ahuja, A. Belonoshko and B. Johansson, Melting and liquid structure of aluminum oxide using a molecular-dynamics simulation, *Phys. Rev. E*, **1998**, 57, 1673–1676, doi: [10.1103/PhysRevE.57.1673](https://doi.org/10.1103/PhysRevE.57.1673).
- [363] S. Ansell, S. Krishnan, J. K. R. Weber, J. J. Felten, P. C. Nordine, M. A. Beno, D. L. Price and M.-L. Saboungi, Structure of Liquid Aluminum Oxide, *Phys. Rev. Lett.*, **1997**, 78, 464–466, doi: [10.1103/PhysRevLett.78.464](https://doi.org/10.1103/PhysRevLett.78.464).
- [364] I. Manassidis and M. J. Gillan, Structure and Energetics of Alumina Surfaces Calculated from First Principles, *J American Ceramic Society*, **1994**, 77, 335–338, doi: [10.1111/j.1151-2916.1994.tb07000.x](https://doi.org/10.1111/j.1151-2916.1994.tb07000.x).
- [365] A. Marmier and S. C. Parker, *Ab initio* morphology and surface thermodynamics of $\alpha\text{-Al}_2\text{O}_3$, *Phys. Rev. B*, **2004**, 69, 115409, doi: [10.1103/PhysRevB.69.115409](https://doi.org/10.1103/PhysRevB.69.115409).
- [366] A. S. Sharipov, B. I. Loukhovitski and A. M. Starik, Theoretical study of structure and physical properties of $(\text{Al}_2\text{O}_3)_n$ clusters, *Phys. Scr.*, **2013**, 88, 058307, doi: [10.1088/0031-8949/88/05/058307](https://doi.org/10.1088/0031-8949/88/05/058307).
- [367] R. Li and L. Cheng, Structural determination of $(\text{Al}_2\text{O}_3)_n$ ($n=1-7$) clusters based on density functional calculation, *Computational and Theoretical Chemistry*, **2012**, 996, 125–131, doi: [10.1016/j.comptc.2012.07.027](https://doi.org/10.1016/j.comptc.2012.07.027).
- [368] A. B. Rahane, M. D. Deshpande and V. Kumar, Structural and Electronic Properties of $(\text{Al}_2\text{O}_3)_n$ Clusters with $n = 1-10$ from First Principles Calculations, *J. Phys. Chem. C*, **2011**, 115, 18111–18121, doi: [10.1021/jp2050614](https://doi.org/10.1021/jp2050614).
- [369] Y. Gu, N. Xu, M. Lin and K. Tan, Structures, stabilities and properties of hollow $(\text{Al}_2\text{O}_3)_n$ clusters ($n=10, 12, 16, 18, 24$ and 33): Studied with density functional theory, *Computational and Theoretical Chemistry*, **2015**, 1063, 29–34, doi: [10.1016/j.comptc.2015.03.027](https://doi.org/10.1016/j.comptc.2015.03.027).
- [370] J. Sun, T. Stirner, W. Hagston, A. Leyland and A. Matthews, A simple transferable interatomic potential model for binary oxides applied to bulk and the (0001) surface, *Journal of Crystal Growth*, **2006**, 290, 235–240, doi: [10.1016/j.jcrysgro.2005.12.076](https://doi.org/10.1016/j.jcrysgro.2005.12.076).
- [371] W. C. Mackrodt, Atomistic simulation of the surfaces of oxides, *J. Chem. Soc., Faraday Trans. 2*, **1989**, 85, 541, doi: [10.1039/f29898500541](https://doi.org/10.1039/f29898500541).
- [372] P. Hartman, The effect of surface relaxation on crystal habit: cases of corundum ($\alpha\text{-Al}_2\text{O}_3$) and hematite ($\alpha\text{-Fe}_2\text{O}_3$), *Journal of Crystal Growth*, **1989**, 96, 667–672, doi: [10.1016/0022-0248\(89\)90065-1](https://doi.org/10.1016/0022-0248(89)90065-1).

- [373] A. Erlebach, H.-D. Kurland, J. Grabow, F. A. Müller and M. Sierka, Structure evolution of nanoparticulate Fe_2O_3 , *Nanoscale*, **2015**, 7, 2960–2969, doi: [10.1039/C4NR06989G](https://doi.org/10.1039/C4NR06989G).
- [374] F. H. Streitz and J. W. Mintmire, Electrostatic potentials for metal-oxide surfaces and interfaces, *Phys. Rev. B*, **1994**, 50, 11996–12003, doi: [10.1103/PhysRevB.50.11996](https://doi.org/10.1103/PhysRevB.50.11996).
- [375] C. C. J. Roothaan, A Study of Two-Center Integrals Useful in Calculations on Molecular Structure. I, *The Journal of Chemical Physics*, **1951**, 19, 1445–1458, doi: [10.1063/1.1748100](https://doi.org/10.1063/1.1748100).
- [376] P. Vashishta, R. Kalia, J. Rino and I. Ebbsjö, Interaction potential for SiO_2 : A molecular-dynamics study of structural correlations, *Phys. Rev. B*, **1990**, 41, 12197–12209, doi: [10.1103/PhysRevB.41.12197](https://doi.org/10.1103/PhysRevB.41.12197).
- [377] L. Verlet, Computer "Experiments" on Classical Fluids. I. Thermodynamical Properties of Lennard-Jones Molecules, *Phys. Rev.*, **1967**, 159, 98–103, doi: [10.1103/PhysRev.159.98](https://doi.org/10.1103/PhysRev.159.98).
- [378] M. Matsui, A Transferable Interatomic Potential Model for Crystals and Melts in the System $\text{CaO-MgO-Al}_2\text{O}_3\text{-SiO}_2$, *Mineralogical Magazine*, **1994**, 58A, 571–572, doi: [10.1180/minmag.1994.58A.2.34](https://doi.org/10.1180/minmag.1994.58A.2.34).
- [379] G. Gutiérrez, A. Belonoshko, R. Ahuja and B. Johansson, Structural properties of liquid Al_2O_3 : A molecular dynamics study, *Phys. Rev. E*, **2000**, 61, 2723–2729, doi: [10.1088/0953-8984/23/49/495401](https://doi.org/10.1088/0953-8984/23/49/495401).
- [380] S. M. Woodley, Atomistic and electronic structure of $(\text{X}_2\text{O}_3)_n$ nanoclusters; $n=1-5$, $\text{X}=\text{B}, \text{Al}, \text{Ga}, \text{In}$ and Tl , *Proceedings of the Royal Society A: Mathematical, Physical and Engineering Sciences*, **2011**, 467, 2020–2042, doi: [10.1098/rspa.2011.0009](https://doi.org/10.1098/rspa.2011.0009).
- [381] W. H. Press, S. A. Teukolsky, W. T. Vetterling and B. P. Flannery, *Numerical Recipes 3rd Edition: The Art of Scientific Computing*, Cambridge University Press, New York, NY, USA, 3rd edn, 2007.
- [382] J. Lewis, D. Schwarzenbach and H. Flack, Electric Field Gradients and Charge Density in Corundum, $\alpha\text{-Al}_2\text{O}_3$, *Acta Cryst.*, **1982**, A38, 733–739, doi: [10.1107/S0567739482001478](https://doi.org/10.1107/S0567739482001478).
- [383] W. Guse and H. Saalfeld, X-ray characterization and structure refinement of a new cubic alumina phase ($\delta\text{-Al}_2\text{O}_3$) with spinel-type structure, *Neues Jahrb. Mineral., Monatsh.*, **1990**, 217, 733–739, doi: [doi not available](#).
- [384] E. N. Maslen, V. A. Streltsov, N. R. Streltsova, N. Ishizawa and Y. Satow, Synchrotron X-ray study of the electron density in $\alpha\text{-Al}_2\text{O}_3$, *Acta Crystallogr B Struct Sci*, **1993**, 49, 973–980, doi: [10.1107/S0108768193006901](https://doi.org/10.1107/S0108768193006901).

- [385] R. S. Zhou and R. L. Snyder, Structures and transformation mechanisms of the η , γ and θ transition aluminas, *Acta Crystallogr B Struct Sci*, **1991**, 47, 617–630, doi: [10.1107/S0108768191002719](https://doi.org/10.1107/S0108768191002719).
- [386] L. Samain, A. Jaworski, M. Edén, D. M. Ladd, D.-K. Seo, F. J. Garcia-Garcia and U. Häussermann, Structural analysis of highly porous γ -Al₂O₃, *Journal of Solid State Chemistry*, **2014**, 217, 1–8, doi: [10.1016/j.jssc.2014.05.004](https://doi.org/10.1016/j.jssc.2014.05.004).
- [387] P. Lamparter and R. Kniep, Structure of amorphous Al₂O₃, *Physica B: Condens. Matter*, **1997**, 234, 405–406, doi: [doi.org/10.1016/S0921-4526\(96\)01044-7](https://doi.org/10.1016/S0921-4526(96)01044-7).
- [388] X. W. Zhou, H. N. G. Wadley, J.-S. Filhol and M. N. Neurock, Modified charge transfer–embedded atom method potential for metal/metal oxide systems, *Physical Review B*, **2004**, 69, 035402, doi: [10.1103/PhysRevB.69.035402](https://doi.org/10.1103/PhysRevB.69.035402).
- [389] R. Shuttleworth, The Surface Tension of Solids, *Proceedings of the Physical Society. Section A*, **1950**, 63, 444–457, doi: [10.1088/0370-1298/63/5/302](https://doi.org/10.1088/0370-1298/63/5/302).
- [390] P. Muller, Elastic effects on surface physics, *Surface Science Reports*, **2004**, 54, 157–258, doi: [10.1016/j.surfrep.2004.05.001](https://doi.org/10.1016/j.surfrep.2004.05.001).
- [391] F. Fischer, T. Waitz, D. Vollath and N. Simha, On the role of surface energy and surface stress in phase-transforming nanoparticles, *Progress in Materials Science*, **2008**, 53, 481–527, doi: [10.1016/j.pmatsci.2007.09.001](https://doi.org/10.1016/j.pmatsci.2007.09.001).
- [392] V. Marichev, Current state and problems in the surface tension of solids, *Colloids and Surfaces A: Physicochemical and Engineering Aspects*, **2009**, 345, 1–12, doi: [10.1016/j.colsurfa.2009.05.004](https://doi.org/10.1016/j.colsurfa.2009.05.004).
- [393] S. Plimpton, Fast Parallel Algorithms for Short-Range Molecular Dynamics, *Journal of Computational Physics*, **1995**, 117, 1 – 19, doi: <https://doi.org/10.1006/jcph.1995.1039>.
- [394] L. W. Finger and R. M. Hazen, Crystal structure and compression of ruby to 46 kbar, *Journal of Applied Physics*, **1978**, 49, 5823–5826, doi: [10.1063/1.324598](https://doi.org/10.1063/1.324598).
- [395] H. d’Amour, D. Schiferl, W. Denner, H. Schulz and W. B. Holzapfel, High-pressure single-crystal structure determinations for ruby up to 90 kbar using an automatic diffractometer, *Journal of Applied Physics*, **1978**, 49, 4411–4416, doi: [10.1063/1.325494](https://doi.org/10.1063/1.325494).
- [396] M. Kronberg, Plastic deformation of single crystals of sapphire: Basal slip and twinning, *Acta Metallurgica*, **1957**, 5, 507 – 524, doi: [https://doi.org/10.1016/0001-6160\(57\)90090-1](https://doi.org/10.1016/0001-6160(57)90090-1).
- [397] G. Renaud, Oxide surfaces and metal/oxide interfaces studied by grazing incidence X-ray scattering, *Surf. Sci. Rep.*, **1998**, 32, 5–90, doi: [10.1016/S0167-5729\(98\)00005-3](https://doi.org/10.1016/S0167-5729(98)00005-3).

- [398] G. Henkelman, A. Arnaldsson and H. Jónsson, A fast and robust algorithm for Bader decomposition of charge density, *Computational Materials Science*, **2006**, 36, 354 – 360, doi: <https://doi.org/10.1016/j.commatsci.2005.04.010>.
- [399] J. W. Elam, C. E. Nelson, M. A. Cameron, M. A. Tolbert, and S. M. George, Adsorption of H₂O on a Single-Crystal α -Al₂O₃(0001) Surface, *J. Phys. Chem. B*, **1998**, 102, 7008, doi: [10.1021/jp981070j](https://doi.org/10.1021/jp981070j).
- [400] P. Liu, T. Kendelewicz, G. E. Brown, E. J. Nelson and S. A. Chambers, Reaction of water vapor with α -Al₂O₃(0001) and α -Fe₂O₃(0001) surfaces: synchrotron X-ray photoemission studies and thermodynamic calculations, *Surf. Sci.*, **1998**, 417, 53, doi: [10.1016/S0039-6028\(98\)00661-X](https://doi.org/10.1016/S0039-6028(98)00661-X).
- [401] J. Ahn and J. Rabalais, Composition and structure of the Al₂O₃{0001}-(1 x 1) surface, *Surf. Sci.*, **1998**, 388, 121, doi: [10.1016/S0039-6028\(97\)00383-X](https://doi.org/10.1016/S0039-6028(97)00383-X).
- [402] *Handbook of Optical Constants of Solids*, ed. E. D. Palik, Academic Press, Burlington, 1997, pp. xv – xvi, doi: [10.1016/B978-012544415-6.50000-5](https://doi.org/10.1016/B978-012544415-6.50000-5).
- [403] P. B. Johnson and R. W. Christy, Optical Constants of the Noble Metals, *Phys. Rev. B*, **1972**, 6, 4370–4379, doi: [10.1103/PhysRevB.6.4370](https://doi.org/10.1103/PhysRevB.6.4370).
- [404] S. H. Vosko, L. Wilk and M. Nusair, Accurate spin-dependent electron liquid correlation energies for local spin density calculations: a critical analysis, *Canadian Journal of Physics*, **1980**, 58, 1200–1211, doi: [10.1139/p80-159](https://doi.org/10.1139/p80-159).
- [405] J. P. Perdew and A. Zunger, Self-interaction correction to density-functional approximations for many-electron systems, *Phys. Rev. B*, **1981**, 23, 5048–5079, doi: [10.1103/PhysRevB.23.5048](https://doi.org/10.1103/PhysRevB.23.5048).
- [406] P. A. M. Dirac and F. R. H., Quantum mechanics of many-electron systems, *Proceedings of the Royal Society of London*, **1929**, 123, 714–733, doi: [10.1098/rspa.1929.0094](https://doi.org/10.1098/rspa.1929.0094).
- [407] J. P. Perdew, Accurate Density Functional for the Energy: Real-Space Cutoff of the Gradient Expansion for the Exchange Hole, *Phys. Rev. Lett.*, **1985**, 55, 1665–1668, doi: [10.1103/PhysRevLett.55.1665](https://doi.org/10.1103/PhysRevLett.55.1665).
- [408] A. D. Becke, Density-functional exchange-energy approximation with correct asymptotic behavior, *Phys. Rev. A*, **1988**, 38, 3098–3100, doi: [10.1103/PhysRevA.38.3098](https://doi.org/10.1103/PhysRevA.38.3098).
- [409] C. Lee, W. Yang and R. G. Parr, Development of the Colle-Salvetti correlation-energy formula into a functional of the electron density, *Phys. Rev. B*, **1988**, 37, 785–789, doi: [10.1103/PhysRevB.37.785](https://doi.org/10.1103/PhysRevB.37.785).

BIBLIOGRAPHY

- [410] J. C. Slater, Atomic Shielding Constants, *Phys. Rev.*, **1930**, 36, 57–64, doi: [10.1103/PhysRev.36.57](https://doi.org/10.1103/PhysRev.36.57).
- [411] W. J. Hehre, R. Ditchfield and J. A. Pople, Self—Consistent Molecular Orbital Methods. XII. Further Extensions of Gaussian—Type Basis Sets for Use in Molecular Orbital Studies of Organic Molecules, *The Journal of Chemical Physics*, **1972**, 56, 2257–2261, doi: [10.1063/1.1677527](https://doi.org/10.1063/1.1677527).
- [412] R. Krishnan, J. S. Binkley, R. Seeger and J. A. Pople, Self-consistent molecular orbital methods. XX. A basis set for correlated wave functions, *The Journal of Chemical Physics*, **1980**, 72, 650–654, doi: [10.1063/1.438955](https://doi.org/10.1063/1.438955).
- [413] H. J. Monkhorst and J. D. Pack, Special points for Brillouin-zone integrations, *Phys. Rev. B*, **1976**, 13, 5188–5192, doi: [10.1103/PhysRevB.13.5188](https://doi.org/10.1103/PhysRevB.13.5188).
- [414] J. C. Phillips and L. Kleinman, New Method for Calculating Wave Functions in Crystals and Molecules, *Phys. Rev.*, **1959**, 116, 287–294, doi: [10.1103/PhysRev.116.287](https://doi.org/10.1103/PhysRev.116.287).
- [415] D. R. Hamann, M. Schlüter and C. Chiang, Norm-Conserving Pseudopotentials, *Phys. Rev. Lett.*, **1979**, 43, 1494–1497, doi: [10.1103/PhysRevLett.43.1494](https://doi.org/10.1103/PhysRevLett.43.1494).
- [416] D. Vanderbilt, Soft self-consistent pseudopotentials in a generalized eigenvalue formalism, *Phys. Rev. B*, **1990**, 41, 7892–7895, doi: [10.1103/PhysRevB.41.7892](https://doi.org/10.1103/PhysRevB.41.7892).
- [417] P. E. Blöchl, Projector augmented-wave method, *Phys. Rev. B*, **1994**, 50, 17953–17979, doi: [10.1103/PhysRevB.50.17953](https://doi.org/10.1103/PhysRevB.50.17953).
- [418] G. Kresse and D. Joubert, From ultrasoft pseudopotentials to the projector augmented waves method, *Phys. Rev. B*, **1999**, 59, 1758, doi: [10.1103/PhysRevB.59.1758](https://doi.org/10.1103/PhysRevB.59.1758).
- [419] R. P. Feynman, Forces in Molecules, *Phys. Rev.*, **1939**, 56, 340–343, doi: [10.1103/PhysRev.56.340](https://doi.org/10.1103/PhysRev.56.340).
- [420] J. H. Irving and J. G. Kirkwood, The Statistical Mechanical Theory of Transport Processes. IV. The Equations of Hydrodynamics, *The Journal of Chemical Physics*, **1950**, 18, 817–829, doi: [10.1063/1.1747782](https://doi.org/10.1063/1.1747782).
- [421] S. Klotz, J.-C. Chervin, P. Munsch and G. Le Marchand, Hydrostatic limits of 11 pressure transmitting media, *J. Phys. D-Appl. Phys.*, **2009**, 42, 075413, doi: [10.1088/0022-3727/42/7/075413](https://doi.org/10.1088/0022-3727/42/7/075413).
- [422] T. Deschamps, C. Martinet, J. L. Bruneel and B. Champagnon, Soda-lime silicate glass under hydrostatic pressure and indentation: a micro-Raman study, *J. Phys.-Condes. Matter*, **2011**, 23, 035402, doi: [10.1088/0953-8984/23/3/035402](https://doi.org/10.1088/0953-8984/23/3/035402).

- [423] H. K. Mao, J. Xu and P. M. Bell, Calibration of the ruby pressure gauge to 800-kbar under quasi-hydrostatic conditions, *J. Geophys. Res.* , **1986**, 91, 4673, doi: [10.1029/JB091iB05p04673](https://doi.org/10.1029/JB091iB05p04673).
- [424] C. Sanchez-Valle, I. Daniel, B. Reynard, R. Abraham and C. Goutaudier, Optimization of Sm³⁺ fluorescence in Sm-doped yttrium aluminum garnet: Application to pressure calibration in diamond-anvil cell at high temperature, *J. Appl. Phys.*, **2002**, 92, 4349, doi: [10.1063/1.1509843](https://doi.org/10.1063/1.1509843).

GÉNÉRATION DE NANOPARTICULES PAR ABLATION LASER EN LIQUIDE : VERS UN MEILLEUR CONTRÔLE DE LA PHASE CRISTALLINE ET DE LA STABILITÉ COLLOÏDALE

L'intérêt des Hommes pour ce qu'ils ne pouvaient voir a toujours été source de curiosité. De l'infiniment grand à l'infiniment petit, la découverte de ces deux mondes a permis le développement technologique des sociétés. La particularité du monde nanométrique (10^{-9} m) réside dans l'apparition d'une dépendance en taille des propriétés physico-chimiques. Les propriétés originales qui en découlent, comparées à celles observées à l'échelle macroscopique, sont engendrées par l'effet de taille des nanomatériaux possédant au moins une de leurs dimensions sous le micromètre. Par exemple, l'utilisation de nanoparticules comme catalyseur pour la dégradation de monoxydes dans les gaz d'échappements automobiles, ou d'agents d'absorption localisés dans les régions tumorales en médecine, prend son importance grâce à leurs propriétés de surfaces. L'engouement industriel pour ces matériaux dans la deuxième partie du XX^{me} siècle a vu le développement de nombreuses techniques de fabrication. Parmi elles, l'ablation laser en liquide (PLAL) est une méthode récente de synthèse dites physique dont l'originalité est marquée par la production de nanoparticules en solution ayant des surfaces libres de tout contaminant. Le PLAL fait alors face à des méthodes plus répandues comme les synthèses chimiques pour lesquelles la taille et la morphologie des particules peut être finement maîtrisée, mais en utilisant des ligands.

Historiquement, l'ablation laser en liquide suit celle sous atmosphère contrôlée, après que les premiers lasers aient été construits dans les années 1960. Les premiers essais expérimentaux ont été menés au début des années 1990 afin de produire des solutions colloïdales de particules destinées à être utilisées comme échantillons dans des expériences de métrologie (méthode d'échantillonnage pour l'ICP-AES). La mise en œuvre expérimentale de l'époque, qui reste encore valide aujourd'hui, consistait à ablater une cible immergée dans un liquide. Une source laser pulsée et de haute intensité est généralement utilisée pour produire directement des solutions colloïdales de nanoparticules.

Malgré la simplicité du système expérimental et de la génération du produit final, il n'en demeure pas moins une complexité dans les mécanismes physico-chimiques se succédant sur des gammes de temps s'étalant de la femtoseconde à la centaine de microseconde.

Après l'absorption d'une impulsion laser par la cible, des phénomènes de relaxation suivent et entraînent un échauffement de la cible en quelques picosecondes. Selon la puissance laser injectée, différents régimes d'ablation peuvent être engendrés aboutissant à l'éjection de matière sous la forme d'un plasma chaud et dense. Celui-ci est composé d'espèces excitées, ions, électrons, atomes et molécules, qui lorsqu'elles se désexcitent émettent une lumière caractéristique d'un plasma. En moins d'une microseconde, l'interaction entre cette phase plasma et le solvant provoque la vaporisation de celui-ci et crée une bulle de gaz contenant majoritairement les molécules du solvant mais aussi de la matière ablatée. Cette bulle est caractérisée par une étape de croissance suivi d'une décroissance avant de s'effondrer sur la cible au bout de quelques centaines de microsecondes. Des rebonds sont souvent observés, mais la matière contenue dans la bulle (les nanoparticules) est majoritairement injectée dans le liquide lors du premier effondrement de la bulle, après seulement une centaine de microsecondes. Les particules peuvent alors interagir avec leur environnement et la solution colloïdale être amenée à "vieillir".

Cependant, la méthode reposant sur une succession de mécanismes hors équilibre, un contrôle des produits finaux est complexe par rapport à des synthèses purement chimiques. Des objets compris entre quelques nanomètres et quelques centaines de nanomètres sont finalement obtenus, souvent sous la forme d'une distribution en taille bimodale. Depuis les débuts de cette méthode, les recherches ont vocation à obtenir une meilleure maîtrise de la morphologie des particules produites ainsi qu'une stabilité des solutions colloïdales. Pour cela, de nombreux paramètres qui pilotent la synthèse peuvent être ajustés. L'enjeu de ce travail de thèse a été d'étudier et de comprendre les effets de quelques facteurs influençant la stabilité colloïdale et une sélectivité de la phase cristalline des nanoparticules synthétisées.

Le chapitre 1 décrit l'ensemble des mécanismes physico-chimiques qui se déroulent pendant l'ablation et qui amènent à la formation de particules colloïdales, en identifiant les paramètres influençant les caractéristiques du produit final. L'intérêt de cette technique pour des applications industrielles y est aussi développé, ainsi que les axes d'améliorations à explorer.

Dans le chapitre 2, nous nous sommes concentrés sur la première bulle générée par laser pour laquelle la cinétique diffère de celle de systèmes classiques de mécanique des fluides, comme l'étalement de goutte ou de bulle. Un projet en collaboration avec le groupe de Barcikowski nous a amené à étudier la cinétique de bulles induites dans des huiles à hautes viscosités. En plus de leurs grandes vitesses, ces bulles présentent des valeurs de nombres capillaires bien plus grandes que ceux de cas généraux, ce qui engendrent des cinétiques particulières.

Tout d'abord, nous avons suivi les bulles formées lors de l'ablation dans différents solvants d'une

cible d'or et d'un grenat d'oxyde de fer et d'yttrium (YIG). Des vidéos ont été enregistrées en utilisant une caméra ultra-rapide incluse dans un montage d'ombroscopie. Les images séparées d'environ $5 \mu\text{s}$ ont été analysées automatiquement par un code informatique que j'ai développé. Les caractéristiques géométriques de la bulle au cours du temps ont permis d'en déduire les nombres adimensionnels de Reynolds, de Weber et capillaire qui expriment le rapport de différentes forces s'exerçant sur la bulle. De plus, dans le cadre d'ablations réalisées dans des solvants à faibles viscosités, les quantités thermodynamiques comme la température et la pression ont été calculées en implémentant une version simplifiée de l'équation de Rayleigh-Plesset.

Tout d'abord, nous avons étudié l'effet de la puissance laser sur le comportement de la bulle produite dans de l'eau. La bulle est observée hémisphérique et ne change pas au cours de son existence. Sans surprise, en augmentant l'intensité du faisceau, plus d'énergie est déposée dans le système, plus la taille des bulles et leur temps de vie augmentent, mais la cinétique reste identique indépendamment de l'énergie déposée. Un régime inertiel domine la cinétique de la bulle au contact de l'eau.

Dans un second temps, l'eau a été remplacé par des solvants plus visqueux. Nous avons utilisé deux huiles polyoléfiniques à 100 et 1000 plus visqueuses que l'eau (en Pa.s). Les bulles produites sont visuellement différentes avec une partie haute hémisphérique au contact du solvant, similaire au cas dans l'eau, alors que la partie inférieure évolue avec l'augmentation des frottements visqueux. Nous montrons qu'un régime inertiel régit les cinétiques pour la partie supérieure de la bulle. Dans la partie inférieure, en plus de la résistance du solvant, la bulle expérimente une friction sur le solide qui limite plus largement le déplacement de la ligne de contact. Au final, en augmentant la viscosité, des régimes à hauts nombres capillaires ($Ca > 100$) sont atteints ce qui est impossible à décrire avec le modèle de Rayleigh-Plesset.

Dans un prochain travail, nous souhaitons développer un modèle unique thermodynamique. Les caractéristiques du solvant comme la viscosité devront être prises en compte afin de pouvoir décrire les cinétiques des bulles sur une large gamme de nombre capillaires.

Alors que le contrôle de la bulle peut favoriser indirectement la morphologie des nanoparticules, l'utilisation de ligands tels que des ions ou des molécules est une manière plus directe d'y parvenir. Un second projet, décrit dans le chapitre 3, a visé à étudier la stabilité colloïdale de nanoparticules d'or synthétisées dans des solutions aqueuses contenant des sels. Bien que plusieurs visions s'opposent sur l'origine des charges, la stabilité colloïdale est assurée par formation d'une double couche d'ions autour de chaque nanoparticule. En effet, les nanoparticules sont chargées en sortie de synthèses soit par un excès d'électrons emprisonnés dans les particules lors de la phase plasma, soit par l'oxydation de leur surface. Dans un milieu salin, les ions forment alors une couche globalement négative qui aboutit à une répulsion électrostatique entre les particules et permet d'éviter une agrégation.

L'effet des ions a été incontestablement prouvé ces dernières années pour des nanoparticules produites par ablation laser en liquide et encore démontré lors de ce travail. Nous avons testé plusieurs

sels à différentes concentrations. La stabilité colloïdale des solutions synthétisées a été globalement assurée pour toutes les concentrations. Celle-ci augmente légèrement avec la concentration en sel correspondant à des distributions de taille centrées autour de 10 nm pour les plus petites particules, même si une seconde population existe à plus de 100 nm. De plus, cette stabilité est maintenue dans le temps. Des mesures de contrôle pendant plus d'un mois révèlent l'efficacité de la plupart des ions à préserver l'équilibre des solutions.

Ce qui a été moins étudié dans la littérature est l'évolution de ces solutions lorsqu'elles sont concentrées en évaporant le solvant. Cette fois-ci, l'effet est plus flagrant sachant que les solutions sont en général déstabilisées lorsque la concentration en or dépasse une certaine valeur critique. Le plus surprenant vient du fait que cette instabilité survient pour n'importe quelle concentration initiale en sel. Ceci laisse présager que l'espace entre les particules qui est réduit par évaporation du solvant devient trop petite à cette concentration critique pour que la couche ionique puisse repousser efficacement les nanoparticules.

Ces études ont ainsi permis de préparer des échantillons destinés à être analysés par spectrométrie photoélectronique par rayons X (XPS) lors d'une semaine de mesures sur la ligne PLEIADES du synchrotron SOLEIL à Paris dans le cadre d'une collaboration internationale. Nous avons pu fournir des solutions de nanoparticules d'or stabilisées par des sels de NaOH et de NaBr et concentrées à plus de 1 g/L. Ces mesures effectuées sur un faisceau de nanoparticules d'or ont révélé qu'il n'y avait pas de traces d'oxydation, mettant en difficulté les mécanismes généralement décrits pour expliquer la stabilisation d'anions à la surface de l'or. Mais étonnement, la moitié de la surface des nanoparticules produites avec des sels de NaBr est recouverte par ces anions. Des calculs théoriques sont en cours de réalisations afin de mieux comprendre la chimie de surface des nanoparticules, en particulier les scénarios de complexion des anions à leur surface.

Nous nous sommes ensuite intéressés à la stabilisation des oxydes par des ligands. Dans le chapitre 4, l'oxyde d'aluminium a été notre cas d'étude pour lequel des nanoparticules plus petites que 10 nm ont été synthétisées avec l'aide de ligands. Dans ce cas, en plus d'obtenir une solution colloïdale stable et homogène avec des particules d'une taille contrôlée à environ 4 nm de diamètre, la phase cristallographique de ces nanoparticules d'alumine a ainsi été contrainte à la phase α qui est la plus stable à l'échelle macroscopique, mais métastable pour des tailles inférieures à 10 nm. Habituellement, la phase γ est favorisée thermodynamiquement à ces tailles. En produisant des nano-rubis, nous avons ouvert la voie vers la production de capteur de pression à l'échelle nanométrique. En effet, les raies de luminescence du chrome dans l'alumine en phase α sont connues pour se déplacer vers les hautes longueurs d'onde avec la pression.

Sans ligands, les nanoparticules présentent une phase amorphe pour des tailles plus petites que 4 nm. Une première transition de phase a alors lieu. La phase γ est alors favorisée pour des tailles de particules allant jusqu'à environ 12 nm, avant qu'elles soient finalement stabilisées dans la phase α de l'alumine massif. L'ajout de ligands avant la synthèse est connu pour venir stabiliser les nano-

particules en solution. Cependant, leur effet sur la structure mécanique des nanoparticules ne sont pas encore bien comprises. Pour cela, nous avons réalisé des calculs visant tout d'abord à étudier les structures cristallines de l'alumine. Un benchmark de plusieurs potentiels empiriques a été mené sur une gamme de taille de particules allant de quelques dixièmes de nanomètres jusqu'à 12 nm. Puis la structure de surface d'alumine en phase α a été étudiée avec et sans ligands à l'aide de calculs électroniques.

Tout d'abord, nous avons testé quatre potentiels empiriques développés pour l'étude de l'alumine et implémentés depuis la littérature. Les potentiels ont été appliqués à la recherche des géométries stables des clusters, ainsi qu'à l'étude des énergies de formation de nanoparticules jusqu'à 12 nm de diamètre. Finalement, le plus simple des potentiels a pu reproduire les régions de stabilité des différentes phases de l'alumine prévues par l'expérience.

Puis, la structure de ces particules sans ligands a pu être étudiée. Nous avons pu montrer que la stabilité des phases cristallines se traduit par une reconstruction atomique de la surface. Après la création d'une surface, les atomes sont sous-coordinés et cherchent à former des liaisons avec des voisins qui se trouvent en sous-surface. En s'insérant dans la structure, les atomes poussent leurs voisins et tendent ainsi à étendre la surface. Cette expansion se traduit par des pressions positives qui ont pu être calculées avec le potentiel SMTBQ implémenté dans le code LAMMPS. Cette contrainte de surface entraîne une déformation mécanique, due à la réorganisation des atomes, à partir de la surface et qui s'atténue vers le centre de la nanoparticule. En effet, le volume de cette dernière cherche à préserver la structure cristalline qui minimise son énergie en compensant l'extension de surface par une réduction des liaisons atomiques. Cette compression est reflétée par une pression négative au cœur de la nanoparticule. Ainsi, ces pressions superficielles et internes se compensent en laissant apparaître une faible pression globale.

L'effet de cette contrainte de surface est visible *via* l'épaisseur atomique qui a été déformée. Les nanoparticules apparaissent alors avec un cœur cristallin entouré d'une coquille d'amorphe. Nos calculs ont montré que l'épaisseur de cette couche est indépendante de la taille des particules. La contrainte de surface déforme de manière uniforme toute surface créant ainsi des structures totalement amorphes lorsque l'épaisseur de déformation est supérieure à la taille des nanoparticules.

Enfin, l'impact des ligands sur la structure mécanique des nanoparticules d'alumine a été prouvé par des calculs électroniques basés sur la théorie de la fonctionnelle de densité (DFT). Le code VASP a été utilisé pour simuler des surfaces d'alumine couvertes de ligands organiques. Par rapport à une surface nue, une réduction de la contrainte de surface a été estimée à un facteur d'environ 6. Nous en avons alors déduit que les ligands permettent de stabiliser les nanoparticules mécaniquement en coordonnant les atomes de surface et en réduisant donc la reconstruction de surface. Les pressions locales sont ainsi diminuées à un point où les ions de chromes dans une matrice d'alumine ne seraient pas sensibles à ces faibles déformations. Ceci expliquerait l'absence de décalage des raies de luminescence dans nos mesures. En effet, les spectres de luminescence de nos nano-rubis n'ont pas observées de décalage des pics, pourtant attendu si l'on considère l'existence d'une pression interne

de quelques GPa (c'est-à-dire un décalage de presque 1 nm).

Pour conclure, ce travail de thèse a permis de décrire une technique de synthèse prometteuse industriellement où le principal avantage réside dans le fait de produire des nanoparticules avec des surfaces libres. Seulement cet atout (absence de ligand) est aussi un inconvénient, la méthode d'ablation laser en liquide n'est pas contrôlée au point de pouvoir synthétiser des particules homogènes en taille, en forme et en phase cristalline. Nous avons pu montrer que certains facteurs permettent ou pourront permettre un meilleur contrôle de la stabilité colloïdale des solutions produites ainsi que la structure cristalline des produits finaux.

LIST OF PUBLICATIONS

1. **G. Laurens**, J. Lam, A. Chemin, A. Cornet, C. Martinet, C. Dujardin, G. Ledoux, K. Lebbou, F. Chaput, B. Gökce, S. Barcikowski, T. Albaret, and D. Amans, "Synthesis and characterization of nanoruby", *in preparation*.
2. **G. Laurens**, D. Amans, J. Lam and A.-R. Allouche, "Crystal structures and phase transitions of alumina at nanoscale : a theoretical study based on a benchmarking of empirical potentials", *Physical Review B*, *submitted*.
3. A. Lévy, M. De Anda Villa, J. Gaudin, D. Amans, **G. Laurens**, F. Boudjada, J. Bozek, R. E. Grisenti, E. Lamour, S. Macé, C. Nicolas, E. Papagiannouli, M. Patanen, C. Prigent, E. Robert, S. Steydli, M. Trassinelli and D. Vernhet, "Assessing the surface oxidation state of free-standing gold nanoparticles produced by laser ablation", *Langmuir*, **2019**, 35, 11859–11871, doi: [10.1021/acs.langmuir.9b02159](https://doi.org/10.1021/acs.langmuir.9b02159).
4. T. Hupfeld, **G. Laurens**, S. Merabia, S. Barcikowski, B. Gökce, and D. Amans, "Dynamics of laser-induced cavitation bubbles at a solid-liquid interface in high capillary number regimes", *Journal of Applied Physics*, *submitted*.
5. A. Chemin, J. Lam, **G. Laurens**, F. Trichard, V. Motto-Ros, G. Ledoux, V. Jarý, V. Laguta, M. Nikl, C. Dujardin and D. Amans, "Doping of nanoparticles using the solvent by pulsed laser ablation in liquids", *Nanoscale Advances*, doi: [10.1039/C9NA00223E](https://doi.org/10.1039/C9NA00223E).

Laser generation of nanoparticles in liquids : new insights on crystal structure control and colloidal stability.

The great interest of nanoparticles to their original physical and an chemical properties has been supported by the development of numerous methods of synthesis. In the nineties, laser generation of nanoparticles in liquids appeared, including Pulsed Laser Ablation in Liquids (PLAL). The PLAL technique enables to produce surface free particles for plenty of material and solvent combinations. However, the apparent simplicity of its implementation hides complex physico-chemical mechanisms resulting in a lack of control of the final products.

We firstly investigated the dynamics of the laser-generated bubbles for which the PLAL extreme conditions present new studied cases of bubbles dynamics not encountered in the field of fluid mechanics. Then, we aim to bring new insights into better control of the nanoparticles morphology and their colloidal stability. A straight way to tune sizes, crystal structures and the colloidal stability consists in the addition of stabilizing agents. Hence, we investigated the mechanisms of stabilization of colloidal gold using complexing ions. We also succeeded to synthesis nano-rubies, *i.e.* chromium doped corundum alumina nanoparticles, unexpected at nanoscale. The stabilization of the metastable crystal structure using ligands is explained thanks to a comprehensive theoretical approach.

Keywords : Pulsed Laser Ablation in Liquids, nanoparticles, colloidal stability, bubble dynamics, stabilizing agents, nano-rubies.

Génération de nanoparticules par ablation laser en liquide : vers un meilleur contrôle de la phase cristalline et de la stabilité colloïdale.

L'engouement pour l'originalité des propriétés physiques des nanoparticules s'est accompagné d'un développement de nombreuses méthodes de synthèse depuis un demi siècle. Parmi elles, l'ablation

laser en liquide permet de produire des nanoparticules avec des surfaces libres de tout contaminant et ce pour une multitude de combinaisons de matériaux et de solvants. Cependant, la simplicité apparente de cette technique dissimule la complexité des mécanismes physico-chimiques, ce qui entraîne actuellement un manque de contrôle des objets synthétisés.

Tout d'abord, nous nous sommes intéressés à la cinétique des bulles pour laquelle les conditions extrêmes d'ablation laser en liquide présentent des cas originaux de cinétique dans le domaine de la mécanique des fluides. Puis, ce travail de thèse vise à donner de plus amples perspectives quant à une meilleure maîtrise de la structure cristalline des nanoparticules et de la stabilité colloïdale. Une manière plus directe de contrôler la taille, la phase cristalline et la stabilité colloïdale des solutions contenant des nanoparticules consiste en l'ajout de ligands. Nous avons donc étudié les mécanismes de stabilisation de ces solutions en utilisant des ions qui se complexent aux nanoparticules d'or. Nous avons aussi réussi à synthétiser des nanoparticules de rubis (alumine dopée chrome). La stabilisation de ces nanoparticules dans une phase métastable en utilisant des ligands organiques a été expliquée par une étude théorique.

Mots clés : Ablation laser en liquide, nanoparticules, stabilité colloïdale, hydrodynamique des bulles, ligands, nano-rubis.

